Imperial College London

Reliability and Life Assessment of Engineering Structures with the Boundary Element Method

---

By

Mengke Zhuang

Thesis submitted in part fulfilment of the requirements for the degree of Doctor of Philosophy of Imperial College London

Department of Aeronautics
Faculty of Engineering
Imperial College London
2024

Declaration of Originality

I hereby confirm that the work presented in this thesis is my own. All else is appropriately referenced.

Copyright Declaration

The copyright of this thesis rests with the author. Unless otherwise indicated, its contents are licensed under a Creative Commons Attribution-Non Commercial 4.0 International Licence (CC BY-NC).

Under this licence, you may copy and redistribute the material in any medium or format. You may also create and distribute modified versions of the work. This is on the condition that: you credit the author and do not use it, or any derivative works, for a commercial purpose.

When reusing or sharing this work, ensure you make the licence terms clear to others by naming the licence and linking to the licence text. Where a work has been adapted, you should indicate that the work has been changed and describe those changes.

Please seek permission from the copyright holder for uses of this work that are not included in this licence or permitted under UK Copyright Law.

Acknowledgements

Foremost, I would like to thank my supervisors, Professor Aliabadi and Professor Sharif Khodaei, for their unwavering support, encouragement, and motivation that have been instrumental in shaping my academic journey. With a wealth of knowledge and a dedication that goes beyond their busy schedules, they have been a great source of wisdom in my pursuit of knowledge. Without their invaluable guidance and continuous feedback, the achievements presented in this thesis would have been impossible.

I am deeply thankful to the members of the SI&HM group. Both the present and previous members are a welcoming, intelligent, and dedicated group of individuals. I would like to extend special thanks to Dr. Morse, a person with a high 'reliability index', for his countless insightful discussions and generous knowledge sharing have been invaluable. The support of the entire group has provided me with the courage to persevere through challenging times. Their invitations to various activities, particularly foosball, have been a welcome respite so that I did not just stay in front of my computer and take the risk of growing obesity.

I'd also like to express my gratitude to my friends outside our group. Spending time with them has given me the opportunity to learn about various cultures, which has been a source of constant amazement. Even though we work in different research fields, Their unique perspectives and cultural insights have left an indelible mark on my academic journey.

In closing, but far from least, I extend my heartfelt gratitude to my parents. Their unwavering support, both emotionally and financially, has afforded me the privilege of pursuing knowledge without the burden of anxiety. Their constant encouragement and guidance have not only eased my academic voyage but have also broadened my horizons, allowing me to explore a world far beyond.

To all those who have contributed to this journey, I offer my deepest thanks. Your collective influence has shaped not only this research but also the scholar I have become, and for that, I am eternally grateful.

Abstract

The investigation in this thesis addresses the challenges posed by the stochastic characteristics of design parameters under complex loading conditions. The focus is on the reliability and fatigue life analysis of engineering structures. The thesis introduces innovative formulations utilizing the Dual Boundary Element Method (DBEM) to accurately evaluate key parameters, aiming to enhance the modelling accuracy of the reliability index and fatigue life for intricate structures.

Specifically, the study is concerned with fatigue life reliability analysis within shallow shell structures, presenting a novel methodology for assessing design sensitivities. The development of the Boundary Element Method-based Implicit Differentiation Method (BEM-IDM) enables the application of the First Order Reliability Method (FORM) to evaluate structural reliability. Expanding on this, a methodology for fatigue life reliability analysis using DBEM-IDM is introduced. This approach demonstrates superior efficiency in evaluating fatigue life sensitivities compared to the Finite Difference Method and Monte Carlo Simulations, resulting in significant reductions in CPU time.

Another related topic investigated involves the statistical inference of the Equivalent Initial Flaw Size Distribution (EIFSD) for both 2D anisotropic and isotropic shell structures. The assessment of EIFSD for the initial size of cracks and its impact on the remaining useful life of structures under fatigue loading is demonstrated. The Dual Boundary Element Method (DBEM) formulation is shown as a highly efficient computational tool, with Bayesian updating refining EIFSD estimates using simulated inspection data. The efficiency of the method is further improved through surrogate modelling, demonstrating its effectiveness in estimating fatigue life with significant agreement compared to actual fatigue life.

Contents

1 Introduction **19**

1.1 Boundary Element Method (BEM) . . . 21

1.2 Equivalent Initial Flaw Size (EIFS) . . . 22

1.3 Aims and Objectives . . . 23

1.4 Author's Published Work . . . 25

1.4.1 International Journals . . . 25

1.4.2 International conferences . . . 26

1.5 Thesis Overview . . . 26

2 Fundamental Concept of BEM **28**

2.1 Dual Boundary Element Method for anisotropic 2D structures . . . 30

2.1.1 Somigliana's Identities and Fundamental Solutions for Displacement and Stress 31

2.1.2 Boundary Integral Equations . . . 33

2.1.3 Numerical Implementation . . . 34

2.1.4 Dual Boundary Element Method Formulations . . . 36

2.1.5 Evaluation of the Stress Intensity Factors . . . 38

2.1.5.1 J-Integral technique . . . 38

2.1.5.2 The ratio of Relative Displacements Technique . . . 40

2.1.5.3 Crack tip stresses and displacements . . . 41

2.1.5.4 Model of Crack propagation . . . 42

2.2 Dual Boundary Element Method for Shallow Shell Structures . . . 44

2.2.1 Basic Theory of Shallow Shells . . . 46

2.2.2 Boundary Integral Equations 49
2.2.2.1 Displacement Boundary Integral Equations 49
2.2.2.2 Dual Reciprocity Method 51
2.2.2.3 Numerical Implementations 54
2.2.2.4 Stress Resultant Boundary Integral Equations 55
2.2.3 Evaluation of the Boundary Stress Resultants 56
2.2.4 Dual Boundary Element Method for Shallow Shell 58
2.2.5 Evaluation of the Stress Intensity Factors 61
2.2.5.1 The Crack Surface Displacement Extrapolation Technique (CSDE) 62
2.2.5.2 Crack Propagation Direction 64

3 Reliability Analysis of Shallow Shell Structures 65
3.1 Fundamental Concept of Reliability Analysis 69
3.1.1 Monte Carlo Simulation (MCS) 71
3.1.2 The First Order Reliability Method (FORM) 74
3.1.2.1 MPP searching Algorithm 76
3.1.2.2 Second-Order Reliability Method (SORM) 78
3.2 Methods for Calculating the Derivatives 79
3.2.1 BEM-FDM formulation 79
3.2.2 BEM-IDM Formulations for Shallow Shell Structures 80
3.2.2.1 BEM-IDM Formulations for Shallow Shell Structures with Respect to a Geometrical Variable Z_g 81
3.2.2.2 BEM-IDM Formulations for Shallow Shell Structures with Respect to Curvature Z_ρ 83
3.2.2.3 BEM-IDM Formulations for Shallow Shell Structures with Respect to Thickness Z_h 84
3.2.2.4 Evaluation of the Von Mises Stress Sensitivity and Boundary Stress Resultants Sensitivity 85
3.3 Numerical Examples 89
3.3.1 Analytical Validation of the BEM-IDM Formulation 89

3.3.2 Reliability Analysis . . . 92
3.3.3 Sensitivity Analysis . . . 95
3.3.4 Optimisation . . . 99
3.3.4.1 Numerical example 1: Circular Shallow Spherical Shell . . . 100
3.3.4.2 Numerical example 2: Shell Structure with a Window . . . 102
3.4 Conclusion . . . 107

4 Reliability Analysis of Fatigue Crack Growth in Shallow Shell Structures 109
4.1 Fundamental Concept of Fatigue Reliability Analysis . . . 111
4.2 The Implicit Differentiation Method (IDM) for Shallow Shell Structure . . . 114
4.2.1 BEM-IDM Formulations for Shallow Shell Structures with Respect to a Geometrical Variable Z_g . . . 114
4.2.2 BEM-IDM Formulations for Shallow Shell Structures with Respect to Curvature Z_ρ . . . 117
4.2.3 Evaluation of the Stress Intensity Factor Sensitivity . . . 120
4.3 Fracture Reliability analysis of cracked fuselage window structure . . . 122
4.4 Reliability analysis of shallow shell with centre hole and two cracks . . . 126
4.4.1 Sensitivity of Stress intensity factors . . . 127
4.4.2 Reliability Analysis . . . 129
4.4.3 Fracture Reliability Analysis . . . 129
4.4.4 Fatigue Reliability Assessment . . . 132
4.5 Fatigue Reliability assessment of multi-site damage problem of the shell with three holes . . . 139
4.6 Conclusion . . . 143

5 Statistical Inference of Equivalent Initial Flaw Size for Engineering Structure 147
5.1 Basic Theory of EIFS . . . 152
5.2 Concept of Fatigue Crack Growth . . . 153
5.3 Bayesian Updating Method . . . 154
5.4 Surrogate Modelling . . . 158

5.5 Inference of EIFS for 2D Anisotropic Structures . . . 162
5.5.1 Inference of EIFS for an Anisotropic Plate Structure with Window Section . 162
5.5.1.1 Simulation of Inspection Data . . . 164
5.5.1.2 Evaluation of the Surrogate Model . . . 166
5.5.1.3 Inference of EIFSD . . . 170
5.5.1.4 Parametric Study for Convergence . . . 176
5.5.1.5 Application of EIFSD to Maintenance . . . 177
5.5.2 Inference of EIFS for an Anisotropic Plate Structure with Crack emanating from a Circular Hole . . . 179
5.5.2.1 Surrogate model . . . 181
5.5.2.2 Bayesian Inference of EIFS . . . 183
5.5.2.3 Application of the inferred EIFSD . . . 185
5.5.3 Summary . . . 186
5.6 Inference of EIFS for Shallow Shell Structure . . . 187
5.6.1 Evaluation of the Surrogate Models . . . 188
5.6.2 Inference of EIFSD . . . 194
5.6.3 Summary . . . 204
5.7 Conclusion . . . 205

6 Conclusion and Future Works 207
6.1 Conclusion . . . 207
6.2 Future Works . . . 215

Bibliography 216

Appendices 234

A Fundamental Solutions and Kernels of the Boundary Element Method for Shell Structure 235
A.1 Fundamental Solutions . . . 235
A.2 Kernels . . . 237

B Particular Solutions for the Dual Reciprocity Method 239

B.1 Particular Solutions for Plane Stress . . . 240

B.2 Particular Solutions for Plate Bending . . . 241

C Probablistic Distributions and Derivatives of Limit State Function 244

C.1 Probablistic Distributions . . . 244

C.1.1 Normal Distribution . . . 244

C.1.2 Lognormal Distribution . . . 245

C.2 Derivatives of the Limit State Function . . . 246

D Derivatives of the Particular Solutions 248

D.1 Derivatives of the particular solutions with respect to geometry variables . . . 248

D.1.1 Derivatives of the particular solutions for 2D plane stress with respect to a geometrical variable . . . 249

D.1.2 Derivatives of the particular solutions for plate bending with respect to a geometrical variable . . . 250

D.2 Derivatives of the particular solutions with respect to thickness . . . 253

D.2.1 Derivatives of the particular solutions for 2D plane stress with respect to thickness . . . 254

D.2.2 Derivatives of the particular solution for plate bending with respect to thickness 254

E Derivatives of the Boundary Stress Resultants and Stress Intensity Factors 256

E.1 Derivatives of the Boundary Stress Resultants . . . 256

E.1.1 Bending stress resultant derivatives . . . 256

E.1.2 shear stress resultant derivatives . . . 257

E.2 Derivatives of the Stress Intensity Factor . . . 257

List of Figures

2.1 Figure shows the structure containing upper and lower crack surfaces labelled as Γ^+ and Γ^-. The structure's overall boundary is composed of $\Gamma = \Gamma^e + \Gamma^+ + \Gamma^-$, where Γ^e represents the outer boundary. The enclosed domain within this boundary is designated as Ω. The source points corresponding to the upper and lower crack surfaces are denoted as x^+ and x^-, respectively. 37

2.2 Crack deformation modes: Mode I Opening/Tensile mode. Mode II Sliding/ In-plane shear mode. Mode III Tearing/ Anti-plane shear mode. [1] 38

2.3 Example of circular contour path used in the J-integral technique. 40

2.4 Crack definition in the polar coordinate system. [2] 42

2.5 correction of crack extension direction [3] 43

2.6 View from inside of failure at the forward escape hatch on the port side COMET G-ALYU. [4] 45

2.7 Photo of the fuselage damage on Aloha Airline Flight 243, 1988. [5] 45

2.8 Definition of the generalised displacements and tractions and the curvatures for the shell structure in the BEM. [6] 47

2.9 Fracture modes for the shell problem. 61

2.10 Example of crack tip nodal element. 63

3.1 Example of joint Probability Density Function form by two random variables. The figure shows only the pdf corresponds to the safety region with the failure region removed (cut surface). The contour of the PDF is shown in the Z_1-Z_2 plane. The limit state function represents the boundary between the safe and failure domain. . 70

3.2 Comparison of Random sampling, Latin Hypercube sampling and Sobol sampling method of generating 50 sample points in a unit cube space. 72
3.3 Convergence of the failure probability with an increasing amount of MCS samples used. 73
3.4 Coefficient of Variation for the failure probability with an increasing amount of MCS samples used. 74
3.5 Contour of Joint pdf after the transformation into the U-space 75
3.6 MPP search algorithm. 77
3.7 SORM approximation of the limit state function. 78
3.8 Hemispherical shell under normal pressure with radius of curvature R. 90
3.9 The example features a circular shallow spherical shell with a central hole. The shell experiences a uniform pressure load applied against its curvature, in a downward direction. This shell is characterized by an inner radius of r_1 and an outer radius of r_2, along with a specified thickness h. The curvatures in both the x and y directions are represented by $\kappa_{11} = \kappa_{22} = \kappa$. 92
3.10 Effect of the uncertainties (COV) in the curvature on the Reliability index for IDM and FDM compare to the results obtained from MCS. 94
3.11 Percentage influence of the sensitivity factors of mean of the variables with varying COV in curvature. 97
3.12 Percentage influence of the sensitivity factors of standard deviation of the variables with varying COV in curvature. 98
3.13 Optimisation history from the IDM-based BEM with multiple Aluminium alloys. Three examples of shape-changing in the optimisation are presented for Aluminium 2024-T4. 102
3.14 Shell structure subjected at tension, bending and domain pressure loading. 103
3.15 Optimisation history from the IDM-based BEM with different target reliability β_{target}. 105
3.16 Optimisation results for shell design with $\beta_{target} = 2$ and $\beta_{target} = 6$. (not to scale) . 106
3.17 Sensitivity of the maximum Von Mises stress to the change in fillet radius R_2 at the optimal design of $\beta_{target} = 4$. 107

4.1 The geometry of the shallow shell fuselage window structure. The window structure consists of inner boundaries and outer boundaries with a crack initiated at point A. The loading consists of bending moment, tension and domain pressure. 123

4.2 a): The meshed of the shell using quadratic elements. b): The meshes around the crack area. Denser meshes were usED around the corner of the window so that the element size on the corner is similar size to the element size on the crack. 124

4.3 Reliability indices and the corresponding probabilities of failure evaluated at each crack length via the IDM-based FORM. 125

4.4 a): The geometry of the shallow shell structure used in the numerical example. The shallow shell configuration includes a central hole characterized by a radius of r_1 and two cracks, each with a length of a. The curvature in the x-direction is denoted as κ_{11} and κ_{22} for y-direction. The shell thickness is defined as h, and the centre hole's position along the x-axis is denoted as b_1. The outer dimensions of the shell remain constant, with a width and length of $101.6mm$. b): The boundary element mesh of the shallow shell structure. 127

4.5 A convergence test of derivatives using the Finite Difference Method (FDM) was conducted with respect to: a) thickness, b) membrane load, c) bending load, and d) domain pressure. The test investigated various ranges in the step size $\Delta Z'_g$, spanning from 0.5 to 10^{-6}. The objective of this test was to identify the step size that provides the best balance of numerical precision and stability for parameters. . 128

4.6 The graph shows the reliability index with variations in crack length (shown on the right y-axis). Additionally, an illustration of the probability of detection obtained from handheld eddy-current inspection is presented against the crack size (displayed on the left y-axis) [7]. The tolerable crack size was determined at a reliability index of $\beta = 3$, which corresponds to a crack length of $17.6mm$, as indicated by the cross on the graph. Notably, the corresponding probability of detection is measured at 86.3%. 131

4.7 The reliability index against the number of loading cycles to which the structure has been exposed (service life) is shown for LSF I (a) and LSF II (b). The results of the Monte Carlo Simulation are illustrated for both LSFs. The highest difference observed in LSF I is at the value of 3.76% at 23000 *cycles*, while in LSF II it is found at 2.40% at 16000 *cycles*. 134

4.8 The parametric analysis investigated the influence of uncertainties in the geometrical parameters on the structure's reliability. Notably, uncertainties in the thickness exhibited a more pronounced impact on reliability. This is evident from the fact that the same reliability index corresponds to a shorter service life along the thickness line. 135

4.9 The Parametric analysis of the uncertainties in the loading parameters to the reliability of the structure. Notably, uncertainties in the tension exhibited a more pronounced impact on reliability. 136

4.10 The Parametric analysis of the uncertainties in the Paris law constants to the reliability of the structure. Notably, uncertainties in the Paris law exponential term exhibited a more pronounced impact on reliability. 137

4.11 The parametric analysis of the combined effect of geometrical variables, loading parameters and Paris Law constants respectively with the same level of COV in the parameter. 138

4.12 The geometry of the shallow shell used in the second reliability analysis. The geometry comprises three holes featuring two cracks extending from opposing sides of each hole. The cracked section is denoted as region A. 140

4.13 (a): The boundary element mesh of the shallow shell used in the second reliability analysis. (b): The mesh on the centre hole and crack. Only the mesh of the middle hole is shown here, the rest of the holes were meshed in the same way. 140

4.14 The reliability index concerning the structure's service life, influenced by different curvatures of the shell structure is shown in the figure. To validate the accuracy of the findings, the results of the Monte Carlo Simulation are included for comparison. 143

5.1 A graphic demonstration of the EIFS as a model calibration parameter for a long crack growth model $g_{long}(a)$ vs. the growth of an actual initial flaw size to a crack size a_f using a short crack growth model. The area under the curve represents the number of cycles required to grow a crack [8]. 153

5.2 Monte Carlo Simulation procedure for obtaining the distribution $f_{N|\hat{\mu}_i,\hat{\sigma}_j,\mathbf{Y}}$ and hence the likelihood equation given in Eq.(5.6). 158

5.3 The BEM mesh (left) and boundary conditions (right) of the anisotropic plate used in the numerical example. The larger dots denote the end-nodes of the elements, while the smaller dots represent the centre-nodes. The initial crack is located at the middle of the right-most edge of the centre hole. The anisotropic principal axis exhibits an inclination angle denoted as α concerning the global horizontal direction. To emphasize, the region where the initial crack is situated has been demarcated as 'Region B'. 163

5.4 Sub-figure (a) shows the BEM mesh for the centre hole. Sub-figure (b) shows a zoomed-in view of the BEM mesh around the initial crack of length a_0 located at the middle of the right-most edge of the centre hole. To provide accurate results, elements were concentrated near the base of the crack. 164

5.5 Surface plots showing the results evaluated from the Kriging models for the testing dataset when $\phi = 0.19$ and $\alpha = 29.5°$. The surfaces represent the results of the Kriging models over a range of initial and intermediate crack sizes. Sub-figure (a) shows the results of K_{eff} and sub-figure (b) shows the results of N. 169

5.6 Convergence of the posterior distributions computed by Bayesian updating after using the data from 50, 100, 300, and 500 inspections. Sub-figure (a) shows the convergence for a 'good' initial guess and low uncertainties. Sub-figure (b) shows the convergence for a 'poor' initial guess and high uncertainties. 172

5.7 Convergence of the EIFSD mean and standard deviation from Bayesian Updating for the 'low' level of uncertainty. 173

5.8 Convergence of the EIFSD mean and standard deviation from Bayesian Updating for the 'high' level of uncertainty. 174

5.9 Convergence of the EIFS standard deviation estimation with respect to the number of inspection data that has been used in Bayesian Updating at high level of uncertainties. The Bayesian updating the 'poor' prior distribution is plotted only. . 175
5.10 Convergence of mean and standard deviation when consider individual uncertainty. 176
5.11 Graphical illustration of the estimation of the fatigue life distribution using the inferred EIFSD $\theta \sim lnN(\mu, \sigma)$. 177
5.12 Sub-figure (a): The boundary element mesh of the structure and the boundary conditions. Sub-figure (b): The zoom-in demonstration of the starting crack. 180
5.13 Surface plot showing the results of Kriging model evaluation comparing to the test dataset when $\psi = 0.18$ and $\alpha = 24°$. Sub-figure (a) surrogate model for K_{eff} and sub-figure (b) surrogate model for N. 182
5.14 Convergence behaviour for the 'low' level of uncertainty. 184
5.15 Convergence behaviour for the 'high' level of uncertainty. 185
5.16 a) The mesh of the high-fidelity model. b) The mesh of the low-fidelity model . . . 189
5.17 The surfaces represent the results of the K_{eff} constructed from the MF model over a range of initial and intermediate crack sizes versus the testing points (black dots) for CASE I (left) and CASE II (right). 192
5.18 The surfaces represent the results of the number of cycles N constructed from the MF model over a range of initial and intermediate crack sizes versus the testing points (black dots) for case I (left) and case II (right). 193
5.19 Simulated inspection data generated from actual EIFS vs the number of cycles required to grow the crack to $a_{det} = 20mm$. 195
5.20 CASE I: Convergence of the posterior distributions computed by Bayesian updating using the Co-Kriging model after using the data from 50, 600, 900, and 1500 inspections. a): the figure shows the convergence for a 'good' initial guess and low uncertainties (COV = 0.01). b): the figure shows the convergence for a 'poor' initial guess and high uncertainties (COV = 0.02). 197
5.21 CASE I: Convergence of the EIFSD mean and standard deviation from Bayesian Updating for the 'low' level of uncertainty using Kriging and Co-Kriging model. . . 198

5.22 CASE I: Convergence of the EIFSD mean and standard deviation from Bayesian Updating for the 'high' level of uncertainty using Kriging and Co-Kriging model. . 199

5.23 CASE II: Convergence of the posterior distributions computed by Bayesian updating using the Co-Kriging model after using the data from 50, 600, 900, and 1500 inspections. a): The figure shows the convergence for a 'good' initial guess and low uncertainties (COV = 0.01). b): The figure shows the convergence for a 'poor' initial guess and high uncertainties (COV = 0.02). 201

5.24 CASE II: Convergence of the EIFSD mean and standard deviation from Bayesian Updating for the 'low' level of uncertainty using Kriging and Co-Kriging model. . . 202

5.25 CASE II: Convergence of the EIFSD mean and standard deviation from Bayesian Updating for the 'high' level of uncertainty using Kriging and Co-Kriging model. . 203

List of Tables

3.1 Results of the derivatives of the centre deflection with respect to the radius of curvature $w_{3,R}$ obtained from the analytical solution, IDM and FDM. The derivatives are given in magnitude of 10^{-4}. Percentage differences are in [%] between the IDM and the analytical solution. 91

3.2 Results of the derivatives of the centre deflection w with respect to the thickness $w_{3,h}$ obtained from the analytical solution, IDM and FDM. Percentage differences in [%] between the IDM and the analytical solution. 91

3.3 The design variables used in the reliability analyses 93

3.4 CPU time required for the FORM, with either the IDM or the FDM. 95

3.5 The sensitivity factors obtained from the reliability analysis for $COV_\kappa = 0.1$. The table gives both the sensitivity factor and the normalised sensitivity factors. 96

3.6 Material properties of different Aluminium alloys. The Young's modulus E, Poisson's ratio ν, yield strength σ_Y and density ρ are given [9]. 101

3.7 Optimisation results from the IDM-based BEM with multiple Aluminium alloys. . . 101

3.8 Details of the shell structure parameters and random variables used in the optimisation procedure 103

3.9 Optimisation results for different target reliability indexes β_{target}. 105

4.1 Details of the shell structure parameters and random variables used in the reliability analysis. 123

4.2 The design variables used in the reliability analyses 128

4.3 Geometrical factors and uncertainties present in example 2. 141

5.1 Uncertainties presented in the crack propagation. 165
5.2 The training ranges covered by the surrogate model. 167
5.3 Model error of the K_{eff} and N surrogate models compared to the test dataset. . . . 169
5.4 Comparison of CPU time required by the kriging model and DBEM respectively. . . 170
5.5 Three levels of quality of the prior distribution that are used to represent 'good', 'moderate', and 'poor' engineering judgement. 171
5.6 Convergence of the mean and standard deviation from Bayesian updating for the 'low' level of uncertainty. 173
5.7 Convergence of the EIFSD mean and standard deviation from Bayesian Updating for the 'high' level of uncertainty. 175
5.8 The fatigue life distributions obtained using MCS with the EIFSD results from section 5.5.1.3, and with the actual EIFSD. 178
5.9 Number of cycles to failure chance of 2%. EIFS distribution inferred from the Bayesian updating and actual EIFSD were used with different levels of uncertainties. 178
5.10 Uncertainties in the parameter presented in the fatigue crack growth. 181
5.11 The statistical error in stress intensity factors and fatigue life between the actual DBEM and the surrogate model. 183
5.12 The results of the distribution of the fatigue life in the form of $lnN(\alpha, \beta)$ obtained using the Monte Carlo simulation. Assuming that the structure needs to ensure that the failure chance of less than 2%. 186
5.13 Details of the shell structure parameters and random variables used in the EIFS inference. 188
5.14 Model error of the K_{eff} for surrogate models compared to the test dataset. MAE $[MPa\sqrt{m}]$, RMSE $[MPa\sqrt{m}]$. 191
5.15 Model error of the N for surrogate models compared to the test dataset. 193
5.16 Three levels of quality of the prior distribution that are used to represent 'good', 'moderate', and 'poor' engineering judgement. 196
5.17 Convergence of the mean and standard deviation from Bayesian updating for CASE I. 200

5.18 Convergence of the mean and standard deviation from Bayesian updating for CASE II. 204

Chapter 1

Introduction

In the domain of engineering, nearly every parameter carries a certain level of inherent uncertainty. These uncertainties may arise from various sources, including human error, environmental conditions, or imperfections in manufacturing processes. Failure to account for these uncertainties can potentially lead to catastrophic structural failures. Consequently, design parameters are often treated as random variables, owing to their stochastic nature. Therefore, engineering structures are not designed with absolute certainty, but rather in consideration of probability. Managing the influence of these uncertainties while ensuring structural safety is a pivotal concern within the field of structural engineering. The criterion for evaluating a structure's capacity to maintain satisfactory performance is the probability of failure. The process of assessing this probability is known as reliability analysis, which provides engineers with a structured approach to evaluate the influence of individual parameters on the overall structural reliability. This, in turn, empowers engineers to prioritize critical factors in the design process.

Traditionally, uncertainties have been treated through a deterministic approach, wherein a standardized safety factor is assigned to all components as a safeguard against potential catastrophic failures. This approach aligns with established safety standards, which underscore the importance of risk assessment. However, it's important to note that the failure of one component does not necessarily equate to the failure of a system. In many instances, the redistribution of loads to other components allows the system to maintain its desired performance. For example, components with a lesser impact on structural safety may be assigned lower safety factors, thereby avoiding exces-

sive over-engineering. It is essential to assess the safety requirements of individual components separately, taking into account the consequences of their potential failure. Nevertheless, the deterministic approach has its limitations, particularly in its inability to provide information on the influence of individual parameters on overall system performance. In contrast, reliability analysis presents an alternative to this deterministic approach. Based on mathematical and probabilistic theory, it offers a more comprehensive understanding of structural safety. In this context, structural safety is evaluated through the computation of the reliability index, defined as the probability that the structure maintains adequate performance. Importantly, it serves as the complementary parameter to the probability of failure.

Among the diverse array of methods available for assessing structural reliability, two fundamental categories emerge: direct methods, notably, the Monte Carlo Simulation (MCS), and indirect methods, represented by the First-Order Reliability Method (FORM) and Second-Order Reliability Method (SORM). In the MCS approach, the evaluation of structural reliability involves an exhaustive exploration of all combinations of uncertainties via extensive statistical sampling. Conversely, FORM and SORM rely on mathematical approximations to estimate the reliability index. For the majority of static structural problems, FORM has proven to yield sufficiently accurate results. In comparison, SORM is able to provide higher precision but demands more extensive computational efforts. More comprehensive insights into these methodologies can be found in the following chapters.

Although it is possible to perform reliability analysis through experimental approaches, this requires substantial investments in equipment, laboratory infrastructure, and associated expenses. As such, computational modelling methods represent a more preferable and cost-effective approach. Among the commonly employed structural modelling techniques are the Finite Element Method (FEM) and the Boundary Element Method (BEM). While FEM finds broad application across various structural problems, BEM offers distinct advantages by significantly reducing computational demands, rendering it a particularly suitable choice for reliability analysis.

1.1 Boundary Element Method (BEM)

Modern engineering structures exhibit increasing complexity in terms of both their materials and geometric configurations. Computational tools such as the Finite Element Method (FEM) and the Boundary Element Method (BEM) provide engineers with the means to perform structural analyses with reasonable modelling efforts. FEM has higher popularity due to the availability of numerous commercial software packages. Nevertheless, BEM offers its unique advantages, particularly in reducing the dimensionality of structural problems. In BEM, only the structure's boundaries are required to be modelled, leading to a significant reduction in computational demand compared to methods involving domain meshing. BEM results in a smaller system of equations, facilitating efficient evaluation when assessing a structure's sensitivity to its design parameters, making it more suitable for reliability analysis.

Following the initial development of the Boundary Element Method (BEM), a specialized variant known as Dual Boundary Element Method (DBEM) emerged, primarily designed for addressing crack-related problems [10]. DBEM not only inherits the advantages of BEM but also offers the distinct capability of facilitating simple and automatic crack increment for crack growth simulations, without the need for geometry remeshing. The DBEM has found broad applications in resolving crack-related issues within anisotropic materials [11], plate structures [12], and shell configurations [13], etc. DBEM enables continuous modelling of crack surfaces, allowing for the evaluation of stress intensity factors using methods such as the J-integral or the Crack Surface Displacement Extrapolation (CSDE) technique. With its superior computational efficiency, DBEM emerges as a particularly valuable tool for scenarios requiring a high amount of crack simulations, making it a valuable tool for statistical fracture analysis and fatigue life assessment.

For an in-depth exploration of the historical evolution of the Boundary Element Method (BEM) can be found in the work of Aliabadi [6]. However, this thesis distinctively narrows its focus to the formulation of anisotropic BEM and the formulation of shear deformable shell structures. As such, a comprehensive understanding of these specific aspects is elaborated in Chapter 2.

1.2 Equivalent Initial Flaw Size (EIFS)

A common approach for studying fatigue accumulation in structures involves the estimation of their fatigue life, under the assumption that there exist initially small flaws which developed into critical fatigue sizes due to cyclic loading. This fundamental concept aligns with the USAF Airplane Damage Tolerance Requirement. Several factors contribute to the presence of these initial small flaws, including material characteristics, the manufacturing environment (in terms of corrosion or wear), and the loading conditions. Consequently, a crucial aspect is the determination of the initial flaw distribution. Therefore, it is important to determine the initial flaw distribution.

Determining the actual initial flaw size (IFS) is often challenging, and measuring the IFS for each component is impractical. According to the principles of damage tolerance design, it is assumed that the actual IFS is slightly smaller than the detectable limit of Non-Destructive Inspection (NDI) techniques [14]. Although this assumption serves as a basis for estimating fatigue life, the actual IFS is frequently much smaller than the minimum size detectable by NDI. Consequently, this results in a conservative estimate of the fatigue life, which may lead to the need for more frequent inspections than might actually be necessary. Consequently, this approach increases both maintenance costs and human effort. Therefore, it is important to accurately determine the fatigue life to establish an inspection interval that aligns with safety and economic considerations. However, determining fatigue life presents numerous challenges. Among them is the difficulty in precisely measuring the initial flaw size, particularly when dealing with very small flaws, such as the 3 μm cracks commonly measured in thin 2024-T3 sheet materials [15]. These tiny flaws often fail to be detected by conventional NDI methods. Furthermore, obtaining an appropriate model for the growth of short cracks introduces further complications, given that the propagation of such small cracks is largely influenced by the material's microstructure [16], thus increase the complexity of modelling their expansion.

To mitigate the complexities mentioned above, the concept of Equivalent Initial Flaw Size (EIFS) was introduced. EIFS, although not representing a physical entity itself, serves as a parameter for calibrating models in long crack growth, such as the Paris Law. The EIFS is typically inferred from a structure's loading history and then conducting a backward analysis to determine the crack's size at the beginning of the process. Once EIFS is determined for a given structure, it can be

extrapolated for use in analogous structures subjected to similar loading conditions, such as an entire fleet of aircraft. The EIFS emerges as an important concept within the domain of durability analysis.

As previously mentioned, EIFS is extrapolated from historical data regarding crack propagation. However, obtaining substantial real-world inspection data for a specific component has considerable challenges, and conducting experimental statistical analyses involving uncertainties is often impractical. Hence, a valid numerical approach has been adopted to simulate inspection data. Owing to the aforementioned advantages associated with DBEM, it emerges as the preferred choice for EIFS inference in crack propagation modelling.

1.3 Aims and Objectives

The main objective of the research presented in this thesis is to enhance the utilization of the boundary element method in the field of structural reliability evaluation and fatigue assessment for various structures. This encompasses the subsequent areas of focus:

1. **To develop an Implicit Differentiation-Based (IDM) Reliability Analysis for Shallow Shell Structures using the BEM.**

    - The research delves into the sensitivity analysis of shallow structures with respect to design parameters of shallow shell structures. This assessment is conducted through the derivation of direct derivatives of the BEM formulations using the Implicit Differentiation Method (IDM). Shallow shell problems are of great significance in engineering design due to their extensive application in aircraft and naval structures, owing to the advantages of low weight and high strength. The integration of reliability analysis with the BEM for shell structures has been relatively unexplored in the literature. In this work, the implicit derivatives of the BEM formulations for shear deformable shell structures with respect to geometric variables, such as curvature and thickness, are derived for the first time. The IDM is employed with the First-Order Reliability Method (FORM) to assess the reliability of shallow shell structures and the sensitivity of the reliability index to design parameters. Once the sensitivity of the structure is obtained,

it can be further employed in conjunction with Reliability-Based Design Optimization (RBDO), showcasing the practical applications of the IDM formulations.

2. **Develop the IDM formulation for cracked shell structure and perform fatigue reliability assessment using FORM.**

   - The research focuses on the evaluation of the Implicit Differentiation Method (IDM) formulation by directly differentiating the Dual Boundary Element Method (DBEM) shell formulation concerning various design parameters. The study of fatigue holds significant importance within the field of structural design, with particular emphasis on the assessment of stress intensity factors (SIFs) and their sensitivity to design parameters. Within structural engineering, fatigue reliability is a critical characteristic, quantifying the likelihood of component failure during its operational lifespan. The assessment of fatigue reliability can assist in determining optimal inspection intervals, thereby enhancing safety and cost-effectiveness. While the most relevant previous research has address reliability analysis for structures with cracks in shear deformable plates, this thesis addresses an unexplored topic by applying DBEM to reliability analysis in the context of shallow shell problems.

3. **Develop formulation for estimating the EIFS for anisotropic structures**

   - The research introduces a novel methodology for estimating the fatigue life of an anisotropic structure with uncertainties in the crack growth parameters. A noteworthy aspect of this study is its novel utilization of statistical inference to determine the Equivalent Initial Flaw Size Distribution (EIFSD) in anisotropic material using the DBEM. Estimating the fatigue life of a structural component presents a significant challenge, primarily due to the small and difficult-to-measure initial flaw size, as well as the complex growth behaviour of such flaws, particularly in anisotropic materials. To address this, the Dual Boundary Element Method (DBEM) is employed, a highly efficient computational approach for fatigue modelling. Within the existing literature, DBEM has not yet been applied to model anisotropic structures for inferring EIFSD. Once EIFSD is inferred for a given structural component, it can be extrapolated to similar components

exposed to similar loading conditions. This information is important in establishing optimal intervals for routine inspections, thus promoting safety and cost-effectiveness.

4. **Develop formulation for estimating the EIFS for shallow shell structures**

   - The work introduces an approach for inference of EIFS in shallow shell structures, accommodating uncertainties in geometrical parameters, load conditions, and parameters governing crack growth. A distinctive aspect of this study is its pioneering use of statistical inference techniques to determine the EIFSD within shallow shell structures, employing the DBEM. This application of DBEM in modelling shallow shell structures for EIFSD inference has not yet been performed in the existing literature. The complexity of the shallow shell DBEM formulation poses significant computational and dimensional challenges. To mitigate these issues, the research incorporates a Multi-fidelity surrogate model strategy, enhancing computational efficiency. The study also delves into the influence of surrogate model quality on the overall inference process, providing insights into the relationship between model precision and the efficiency of Bayesian inferences.

1.4 Author's Published Work

1.4.1 International Journals

1. Zhuang, M; Morse, L.; Sharif-Khodaei, Z.; Aliabadi, M.H.; Statistical inference of the Equivalent Initial Flaw Size Distribution for an anisotropic material with the Dual Boundary Element Method, *International Journal of Fatigue*, 158 (2022), p. 106702.

2. Zhuang, M; Morse, L.; Sharif-Khodaei, Z.; Aliabadi, M.H.; Implicit differentiation-based reliability analysis for shallow shell structures with the Boundary Element Method, *Engineering Analysis with Boundary Elements*, 156 (2023), p. 223-238.

3. Zhuang, M; Morse, L.; Sharif-Khodaei, Z.; Aliabadi, M.H.; Reliability Analysis of Fatigue Crack Growth in Shallow Shell Structures using the Dual Boundary Element Method, *Theoretical and Applied Fracture Mechanics*, (under review).

1.4.2 International conferences

1. Zhuang, M; Morse, L.; Sharif-Khodaei, Z.; Aliabadi, M.H.; Statistical Inference of Equivalent Initial Flaw Size Distribution for Fatigue Analysis of an Anisotropic Material *Proceedings of conference: International Conference of Fracture and Damage Mechanics* (FDM). Malaga, Spain. September 2022.

2. Zhuang, M; Morse, L.; Sharif-Khodaei, Z.; Aliabadi, M.H.; Reliability-based Fracture Analysis for Shallow Shell Structure with the Dual Boundary Element Method. *Proceedings of conference: International Conference of Fracture and Damage Mechanics* (FDM). London, United Kingdom. September 2023.

1.5 Thesis Overview

An overview of the structure of the rest of the thesis are listed as follows:

- **Chapter 2: Fundamental Concepts of the DBEM for Anisotropic 2D Structure, Shear Deformable Shell Structure.** This chapter will introduce the fundamental formulations used in the DBEM for both anisotropic structures and shallow shell structures. The concept of fracture mechanics will be introduced which includes the fracture modes considered for different types of structures and the strategy used in the modelling of crack propagation in DBEM. Hence, the methodology for evaluating the crack tip stress intensity factor will be introduced. The chapter also includes the fundamental concept of reliability analysis encompasses the MCS and FORM.

- **Chapter 3: Reliability Analysis of the Shallow Shell Structure.** This chapter will introduce the fundamental concept of the reliability analysis followed by the IDM formulation of the BEM for evaluating the sensitivity of the structure response with respect to design parameters. Numerical examples will be presented and the application of the obtained sensitivity formulations to the Reliability-Based Design Optimisation n (RBDO) will be discussed. The work presented in this chapter is based on article 2 in section 1.4.1.

- **Chapter 4: Reliability Analysis of Fatigue Crack Growth in Shallow Shell Structure.** This chapter will introduce the IDM formulations of the DBEM for evaluating the sensitivity of the SIFs with respect to the design parameters. Numerical examples will be presented with fracture reliability assessment and fatigue life reliability assessment. The work presented in this chapter is based on article 3 in section 1.4.1 and article 2 in section 1.4.2.

- **Chapter 5: Statistical Inference of EIFS for engineering structure.** The fundamental concept of the EIFS which included the theory of the Bayesian updating method and the application of the surrogate modelling in reducing the computational efforts. The chapter is divided into two parts, with the first part focusing on the 2D anisotropic structures with single fidelity Kriging model. The work presented in this part is based on article 1 in section 1.4.1 and article 1 in section 1.4.1. The second part investigates the inference of EIFS on a shallow shell structure with multi-fidelity Co-Kriging model.

- **Conldusion and Future Works.** This chapter will include a summary of the key founding from the work presented in this thesis and the potential further research contained is provided.

Chapter 2

Fundamental Concept of BEM

The origins of the understanding of 'fatigue' as a structural phenomenon can be traced back to the Versailles rail accident in Menudo in 1842. This catastrophic event was triggered by the failure of a locomotive axle, an incident that highlighted the critical factors of stress concentration and the effects of repeated cyclic loading. The subsequent investigation into this accident marked the beginning of a scientific inquiry into the concept of fatigue. As researchers delved deeper into the field of fracture mechanics, a more comprehensive understanding of how cyclic loading impacts structural integrity has been developed. These early explorations laid the foundation for modern structural design, with advanced numerical tools to predict the fatigue life of structures. Today, as engineering structures become increasingly complex in terms of geometry and materials, ongoing research in fatigue mechanics aims to mitigate crack propagation and establish efficient and reliable structural designs.

Structural mechanics plays a pivotal role in the analysis of crack behaviour, with the stress intensity factor serving as a crucial parameter for such investigations. While analytical solutions for stress intensity factors are readily available for structures with simple geometries and loading conditions [17], complex structures often demand the use of numerical methods. These numerical tools encompass the Finite Element Method (FEM), Virtual Element Method (VEM), and Boundary Element Method (BEM).

Among these numerical methodologies, FEM and VEM, categorized as domain mesh methods, require the meshes in the entire structure into mesh elements. In contrast, BEM presents an

intriguing alternative, characterized by a unique advantage in dimensional reduction. For 2D problems, BEM solely necessitates meshing of the line boundary, yielding smaller system matrices and reducing modelling efforts. This attribute proves particularly advantageous when requiring large amounts of simulations, such as Monte Carlo Simulations (MCS) or the First Order Reliability Method (FORM), where the computation of first-order derivatives plays a pivotal role.

Furthermore, BEM emerges as the method of preference over domain mesh methods for the analysis of crack growth. It enables the automatic tracking of crack propagation with minimal re-meshing requirements. In BEM, the re-meshing process involves only the addition of new elements at the crack tips, simplifying the modelling effort when frequent adjustments in multiple geometric and loading variables are required. This adaptability makes BEM an ideal choice for applications such as fatigue reliability analysis or optimization problems.

A complexity encountered when employing the Boundary Element Method (BEM) to address problems involving cracked bodies is the occurrence of a singular system matrix $\mathbf{A}$. This singularity arises from coincident elements along the crack surfaces. When collocating boundary elements along these surfaces, two identical rows of equations emerge. These repeated rows result in an ill-conditioned matrix $\mathbf{A}$, making it impossible to obtain a unique solution.

To address this challenge, an alternative formulation of the Boundary Element Method (BEM) has been introduced, which includes notable techniques such as the sub-region method [18] and the Dual Boundary Element Method (DBEM) [19]. In the sub-region method, the crack surface is treated as an outer boundary for each subdivided region. However, a drawback of this approach is the increase in the resulting matrix $\mathbf{A}$ size as it introduces additional boundaries, leading to increased computational demands. On the other hand, DBEM tackles the problem within a single region. The singularity issues that arise in the system are resolved by applying the displacement integral equation on one side of the crack surface and the traction integral equation on the other. This approach has demonstrated its efficiency in numerous numerical examples such as analysis of multi-site damage in nonhomogeneous structure [20], probabilistic fracture analysis with a large number of simulations [21, 22], plate bending problem [23] and dynamic crack propagation [24].

This chapter provides an overview of the BEM and the structure of the chapter is as follows: section 2.1 presents the DBEM formulations for the anisotropic structure and methods [2, 25]

for evaluating the stress intensity factor. Section 2.2 outlines the DBEM formulations for the shell structure [13, 26] and hence the methodology for evaluating the stress intensity factors. The formulations provided in this chapter are used in the later chapter as the method of numerical modelling and only a brief overview is given for the sake of completeness.

2.1 Dual Boundary Element Method for anisotropic 2D structures

The utilization of composite materials has witnessed a rapid and remarkable expansion. Composite materials have emerged as one of the most extensively utilized materials in structural design. Their primary allure lies in their ability to provide high strength and stiffness while maintaining a lightweight nature. Engineers have the flexibility to customize composite structures to precisely match the requirements of specific applications through the design of artificial composites [27]. In most cases, these materials exhibit anisotropic behaviour concerning stiffness and strength. This anisotropy underscores the importance of considering these factors when conducting structural analysis, especially in the context of fracture analysis.

The analysis of fractures in anisotropic materials has been effectively established within the FEM [28–30]. The DBEM formulation, tailored for anisotropic and composite materials, was first introduced by Sollero [2, 25]. This approach incorporated complex numbers to formulate anisotropic elastostatics for addressing mixed-mode crack problems. Over the past few decades, the development of DBEM for fracture analysis in anisotropic materials has gained significant interest within the research community. The interest has led to a range of applications, such as the study of multi-site damage in infinite plates [31], free vibration analysis [32], crack propagation prediction via shape sensitivity [33], and the study of cracks in piezoelectric materials [34]. For a more comprehensive collection of examples, one may refer to the journal "Engineering Analysis with Boundary Elements."

This section offers an introductory overview into the DBEM formulation for 2D anisotropic materials. The discussion encompasses the boundary integral equation and the methodology employed to compute the stress intensity factor. The formulations presented herein are based on the foun-

dational work of Sollero [2, 25, 35]. For a more exhaustive understanding of this methodology, one can refer to the corresponding work.

2.1.1 Somigliana's Identities and Fundamental Solutions for Displacement and Stress

This section presents the formulations of the Boundary Element Method (BEM) and the Dual Boundary Element Method (DBEM) as originally developed in the works of Aliabadi [6] and Sollero [35]. In the context of these formulations, Latin letter indices (e.g., i, j, k) are constrained to values of either 1 or 2.

The development of the boundary element integration technique for addressing elastostatic problems is rooted in the utilization of Betti's reciprocal work theorem, which applies to two self-equilibrated states. A thorough derivation of the equations can be found in the references of Aliabadi [6] and Portela [10]. Nevertheless, this section offers a brief summary of the relevant concepts.

The expression for Somigliana's identity, which characterizes displacement and tractions in the absence of body forces, can be formulated as follows:

$$u_i\left(\mathbf{z}'\right)+\int_{\Gamma} T_{ij}\left(\mathbf{z}', \mathbf{z}\right) u_j(\mathbf{z}) d\Gamma(\mathbf{z})=\int_{\Gamma} U_{ij}\left(\mathbf{z}', \mathbf{z}\right) t_j(\mathbf{z}) d\Gamma(\mathbf{z}) \tag{2.1}$$

where u_j and t_j denote the displacement and traction at the boundary, respectively. The points $\mathbf{z}'$ and $\mathbf{z}$ are introduced as the source and field points, respectively, within a complex plane, and their precise definitions are as follows:

$$\mathbf{z_k}=x_1+\mu_{\mathbf{k}} x_2, \quad \mathbf{z_k}'=x_1\prime+\mu_{\mathbf{k}} x_2\prime \tag{2.2}$$

The values of μ_k can be determined by solving the characteristic equation, which involves the utilization of the compliance matrix coefficients a_{ij}:

$$a_{11}\mu^4-2a_{16}\mu^3+\left(2a_{12}+a_{66}\right)\mu^2-2a_{26}\mu+a_{22}=0 \tag{2.3}$$

The fundamental solution, which was derived as the solution for a point source acting on an infinite anisotropic plate, plays a pivotal role in solving boundary integral equations. A comprehensive derivation of these fundamental solutions can be found in the work conducted by Sollero [2]. The fundamental solution for displacement U_{ij} and traction T_{ij} at a source point z' and a field point z is defined as:

$$\begin{aligned} U_{ij}\left(\mathbf{z}', \mathbf{z}\right) &= 2\,\mathrm{Re}\left[p_{j1}A_{i1}\ln\left(z_1 - z_1'\right) + p_{j2}A_{i2}\ln\left(z_2 - z_2'\right)\right] \\ T_{ij}\left(\mathbf{z}', \mathbf{z}\right) &= 2\,\mathrm{Re}\left[\frac{1}{\left(z_1 - z_1'\right)}q_{j1}\left(\mu_1 n_1 - n_2\right)A_{i1} + \frac{1}{\left(z_2 - z_2'\right)}q_{j2}\left(\mu_2 n_1 - n_2\right)A_{i2}\right] \end{aligned} \tag{2.4}$$

where n_j is the normal vector and

$$[p_{ik}] = \begin{bmatrix} a_{11}\mu_k^2 + a_{12} - a_{16}\mu_k \\ a_{12}\mu_k + a_{22}/\mu_k - a_{26} \end{bmatrix} \tag{2.5}$$

$$[q_{jk}] = \begin{bmatrix} \mu_1 & \mu_2 \\ -1 & -1 \end{bmatrix} \tag{2.6}$$

and complex constant matrix A_{ij} is :

$$\begin{bmatrix} 1 & -1 & 1 & -1 \\ \mu_1 & -\bar{\mu}_1 & \mu_2 & -\bar{\mu}_2 \\ p_{11} & -\bar{p}_{11} & p_{12} & -\bar{p}_{12} \\ p_{21} & -\bar{p}_{21} & p_{22} & -\bar{p}_{22} \end{bmatrix} \begin{Bmatrix} A_{i1} \\ \bar{A}_{i1} \\ A_{i2} \\ \bar{A}_{i2} \end{Bmatrix} = \begin{Bmatrix} \delta_{i2}/(2\pi i) \\ -\delta_{i1}/(2\pi i) \\ 0 \\ 0 \end{Bmatrix} \tag{2.7}$$

Where δ_{ij} denotes the Kronecker delta function, and the overbar represents the complex conjugate. The displacement gradient tensor can be derived by taking the derivative of Eq. 2.1 with respect to the source point, which can be expressed as:

$$u_{i,k}\left(\mathbf{z}'\right) + \int_\Gamma T_{ij,k}\left(\mathbf{z}', \mathbf{z}\right) u_j(\mathbf{z}) d\Gamma(\mathbf{z}) = \int_\Gamma U_{ij,k}\left(\mathbf{z}', \mathbf{z}\right) t_j(\mathbf{z}) d\Gamma(\mathbf{z}) \tag{2.8}$$

where the derivatives of the displacement and traction fundamental solution are given by:

$$\begin{aligned} U_{ij,k}\left(\mathbf{z}',\mathbf{z}\right) &= 2\,\mathrm{Re}\left[\frac{1}{z_1-z_1'}R_{k1}p_{j1}A_{i1}+\frac{1}{z_2-z_2'}R_{k2}p_{j2}A_{i2}\right] \\ T_{ij,k}\left(\mathbf{z}',\mathbf{z}\right) &= -2\,\mathrm{Re}\left[\frac{1}{\left(z_1-z_1'\right)^2}\,R_{k1}q_{j1}\left(\mu_1 n_1-n_2\right)A_{i1}+\frac{1}{\left(z_2-z_2'\right)^2}R_{k2}q_{j2}\left(\mu_2 n_1-n_2\right)A_{i2}\right] \end{aligned} \tag{2.9}$$

where

$$[R_{kl}] = \begin{bmatrix} 1 & 1 \\ \mu_1 & \mu_2 \end{bmatrix} \tag{2.10}$$

The strain is defined as $\epsilon_{ik}(z') = \frac{1}{2}[u_{i,k}(z')+u_{k,i}(z')]$. After obtaining the displacement gradient, the stress can be determined using Hooke's law for anisotropic materials, given by $\sigma_i(z') = \bar{Q}_{ij}\epsilon_j(z')$, where $\bar{Q}_{ij}$ represents the stiffness matrix. The stress integral equation can be formulated as follows:

$$\sigma_{ij}\left(\mathbf{z}'\right)+\int_\Gamma S_{kij}\left(\mathbf{z}',\mathbf{z}\right)u_k(\mathbf{z})d\Gamma(\mathbf{z}) = \int_\Gamma D_{kij}\left(\mathbf{z}',\mathbf{z}\right)t_k(\mathbf{z})d\Gamma(\mathbf{z}) \tag{2.11}$$

the corresponding kernel S_{kij} can be obtained by Hooke's law with the fundamental solution of displacement gradient in Eq.(2.9)

$$\begin{bmatrix} S_{11j}(z',z) \\ S_{22j}(z',z) \\ S_{21j}(z',z) \end{bmatrix} = -\begin{bmatrix} \bar{Q}_{11} & \bar{Q}_{12} & \bar{Q}_{16} \\ \bar{Q}_{21} & \bar{Q}_{22} & \bar{Q}_{26} \\ \bar{Q}_{16} & \bar{Q}_{26} & \bar{Q}_{66} \end{bmatrix} \begin{bmatrix} T_{1j,1}(z',z) \\ T_{2j,2}(z',z) \\ \frac{1}{2}(T_{1j,2}(z',z)+T_{2j,1}(z',z)) \end{bmatrix} \tag{2.12}$$

and

$$\begin{bmatrix} D_{11j}(z',z) \\ D_{22j}(z',z) \\ D_{21j}(z',z) \end{bmatrix} = -\begin{bmatrix} \bar{Q}_{11} & \bar{Q}_{12} & \bar{Q}_{16} \\ \bar{Q}_{21} & \bar{Q}_{22} & \bar{Q}_{26} \\ \bar{Q}_{16} & \bar{Q}_{26} & \bar{Q}_{66} \end{bmatrix} \begin{bmatrix} U_{1j,1}(z',z) \\ U_{2j,2}(z',z) \\ \frac{1}{2}(U_{1j,2}(z',z)+U_{2j,1}(z',z)) \end{bmatrix} \tag{2.13}$$

2.1.2 Boundary Integral Equations

The equations presented in Equations 2.1, 2.8, and 2.11 are applicable for any source point located within the domain Ω, i.e., $z' \in \Omega$. However, when dealing with source points situated on the boundary Γ, the boundary integral equations can be derived by considering the limit $z' \in \Gamma$.

Consequently, the displacement boundary integral equation takes the following form:

$$c_{ij}\left(z'\right)u_i\left(z'\right)+\oint_{\Gamma}T_{ij}\left(z',z\right)u_j(z)dS=\int_{\Gamma}U_{ij}\left(z',z\right)t_j(z)dS \tag{2.14}$$

where the coefficient $C_{ij}(z')=\delta_{ij}/2$ is applicable for smooth boundary 2D problems. The utilization of the Cauchy principal value integration $\oint$ is necessary due to the fact that taking the limit of the integral of the fundamental solution T_{ij} would lead to an improper integration. In a similar manner, the stress boundary integral equation can be derived as follows:

$$\frac{1}{2}\sigma_{ij}\left(\mathbf{z}'\right)+\oint\!\!\!\!\!\!=_{\Gamma}S_{kij}\left(\mathbf{z}',\mathbf{z}\right)u_k(\mathbf{z})d\Gamma(\mathbf{z})=\oint_{\Gamma}D_{kij}\left(\mathbf{z}',\mathbf{z}\right)t_k(\mathbf{z})d\Gamma(\mathbf{z}) \tag{2.15}$$

where $\oint\!\!\!\!\!\!=$ denotes the Hadamard principal value integral. The relationship between traction and stress is expressed as $t_i=\sigma_{ij}n_j$. Consequently, the traction boundary integral equation can be derived by multiplying the normal vector n_i with the equation mentioned above

$$\frac{1}{2}t_j\left(\mathbf{z}'\right)+n_i\left(\mathbf{z}'\right)\oint\!\!\!\!\!\!=_{\Gamma}S_{kij}\left(\mathbf{z}',\mathbf{z}\right)u_k(\mathbf{z})d\Gamma(\mathbf{z})=n_i\left(\mathbf{z}'\right)\oint_{\Gamma}D_{kij}\left(\mathbf{z}',\mathbf{z}\right)t_k(\mathbf{z})d\Gamma(\mathbf{z}) \tag{2.16}$$

2.1.3 Numerical Implementation

In the BEM, the structural boundaries are divided into a set of N_e discrete elements, enabling the representation of the boundary Γ as the summation of these individual elements, expressed as $\Gamma=\sum_{n=1}^{N_e}\Gamma_n$, where n denotes the enumeration of the elements. The discretized expression for the displacement integral equation can be formulated as follows:

$$c_{ij}(z')u_i\left(z'\right)+\sum_{n=1}^{N_e}\oint_{\Gamma_n}T_{ij}\left(z',z\right)u_j(z)d\Gamma_n=\sum_{n=1}^{N_e}\int_{\Gamma_n}U_{ij}\left(z',z\right)t_j(z)d\Gamma_n \tag{2.17}$$

and the discretized expression for the traction integral equation as:

$$\frac{1}{2}t_j\left(z'\right)+\mathrm{n_i}\left(z'\right)\sum_{n=1}^{N_e}\oint\!\!\!\!\!\!=_{\Gamma_n}S_{kij}\left(z',z\right)u_k(z)d\Gamma_n=\mathrm{n_i}\left(z'\right)\sum_{n=1}^{N_e}\oint_{\Gamma_n}D_{kij}\left(z',z\right)t_k(z)d\Gamma_n \tag{2.18}$$

The accuracy of the numerical approximation of boundary displacement and traction depends upon the number of nodes employed within each element. Commonly adopted types of elements encompass constant, linear, and quadratic elements. In the case of linear elements, two nodes are employed per element, resulting in a linear approximation of the displacement and traction fields. However, it is important to note that the limitation of linear elements becomes apparent when dealing with structures featuring curved geometries, as they require more elements to adequately represent the boundary. Consequently, this work employs quadratic elements throughout. The displacement and traction can be represented as a summation of nodal components utilizing the continuous quadratic element shape function, as follows:

$$u_i(\zeta) = \sum_{l=1}^{N_l} \Phi_l^n(\zeta) u_i^{nl}, \quad t_i(\zeta) = \sum_{l=1}^{N_l} \Phi_l^n(\zeta) t_i^{nl}, \quad z_k(\zeta) = \sum_{l=1}^{N_l} \Phi_l^n(\zeta) z_k^{nl} \tag{2.19}$$

N_l represents the number of nodes in element n. The variables u_i^n and t_i^n denote the displacement and traction values at node l of element n. The shape functions are denoted as Φ_l^n, and for continuous quadratic elements, these functions are expressed as follows:

$$\Phi_1^n = \frac{1}{2}\zeta(\zeta - 1), \quad \Phi_2^n = 1 - \zeta^2, \quad \Phi_3^n = \frac{1}{2}\zeta(\zeta + 1) \tag{2.20}$$

where ζ is a nondimensional local coordinate within the element, defined over the interval $-1 \leq \zeta \leq +1$. The integral in Equation 2.14 is now computed within each element with respect to the local coordinate and can be expressed as:

$$c_{ij}(\zeta') u_i(\zeta') + \sum_{n=1}^{N_e} \sum_{l=1}^{N_l} u_j^{nl} \fint_{-1}^{+1} T_{ij}(\zeta', z(\zeta)) \Phi_l^n J(\zeta) d(\zeta) = \sum_{n=1}^{N_e} \sum_{l=1}^{N_l} t_j^{nl} \int_{-1}^{+1} U_{ij}(z', z(\zeta)) \Phi_l^n J(\zeta) d(\zeta) \tag{2.21}$$

where

$$J(\zeta) = \left| \sqrt{\left(\frac{dx_1}{d\zeta}\right)^2 + \left(\frac{dx_2}{d\zeta}\right)^2} \right| = \left| \frac{d\Gamma_n}{d\zeta} \right| \tag{2.22}$$

By sequentially applying the equations outlined above to each node, a system of equations $\mathbf{Hu} = \mathbf{Gt}$ can be established to describe boundary displacements $\mathbf{u}$ and tractions $\mathbf{t}$. In this system, $\mathbf{H}$ encompasses the integrals of the fundamental solution T_{ij}, while $\mathbf{G}$ includes the integrals of the

fundamental solution U_{ij}. This equation can be rearranged into the form where the final system of equations becomes $\mathbf{Ax} = \mathbf{b}$, with $\mathbf{A}$ representing a matrix of coefficients, $\mathbf{x}$ being a vector of unknown boundary displacements and tractions, and $\mathbf{b}$ containing known boundary conditions.

2.1.4 Dual Boundary Element Method Formulations

When simulating crack propagation, the upper and lower crack surfaces are treated as coincident surfaces, meaning that their nodes share the same coordinates. This situation can lead to the formation of an ill-conditioned matrix $\mathbf{A}$ due to the introduction of two identical rows for both crack surfaces. There are several approaches to address this challenge, including the sub-region method [18] and the Dual Boundary Element Method (DBEM) [19]. The sub-region method introduces additional boundaries within the domain to separate the two crack surfaces, ensuring they do not overlap within the same domain. However, it's important to note that this method can be computationally expensive due to the additional equations that must be solved. In contrast, the DBEM offers an alternative solution. It employs two independent boundary integral equations, allowing the displacement integral equation to be applied to one crack surface while simultaneously using the traction integral equation on the other during the collocation process

Consider a geometry with a crack in Figure 2.1. S_c^+ and S_c^- denote the upper and lower surface respectively, the rest of the boundary is denoted as S^e. The total surface of the body is $\Gamma = \Gamma^e + \Gamma_c^+ + \Gamma_c^-$.

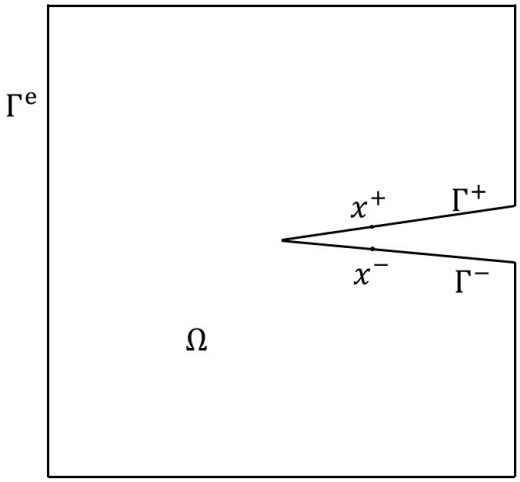


Figure 2.1: Figure shows the structure containing upper and lower crack surfaces labelled as Γ^+ and Γ^-. The structure's overall boundary is composed of $\Gamma = \Gamma^e + \Gamma^+ + \Gamma^-$, where Γ^e represents the outer boundary. The enclosed domain within this boundary is designated as Ω. The source points corresponding to the upper and lower crack surfaces are denoted as x^+ and x^-, respectively.

The displacement integral equation is used for nodal collocation on the upper surface z^+ and can be written as:

$$\frac{1}{2}u_j\left(\mathrm{z}^+\right) + \frac{1}{2}u_j\left(\mathrm{z}^-\right) + \sum_{n_e=1}^{N_e} \int\!\!\!\!\!\!- _{\Gamma_{n_e}} T_{ij}\left(z', z\right) u_j(z) d\Gamma_{n_e} = \sum_{n_e=1}^{N_e} \int_{\Gamma_{n_e}} U_{ij}\left(z', z\right) t_j(z) d\Gamma_{n_e} \tag{2.23}$$

The traction integral equation is used for collocation of the lower surface nodal points z^- and is given as follows:

$$\frac{1}{2}t_j\left(\mathrm{z}^-\right) - \frac{1}{2}t_j\left(\mathrm{z}^+\right) = n_i\left(\mathrm{z}^-\right) \sum_{n_e=1}^{N_e} \int\!\!\!\!\!\!- _{\Gamma_{n_e}} D_{kij}\left(\mathrm{z}^-, \mathrm{z}\right) t_k(\mathrm{z}) d\Gamma_{n_e} - n_i\left(\mathrm{z}^-\right) \sum_{n_e=1}^{N_e} \int\!\!\!\!\!\!= _{\Gamma_{n_e}} S_{kij}\left(\mathrm{z}^-, \mathrm{z}\right) u_k(\mathrm{z}) d\Gamma_{n_e} \tag{2.24}$$

The numerical discretization process is implemented in a manner similar to Eq.(2.21), utilizing the local coordinate ζ as presented in Eq.(2.19). Collocation is carried out following specific equations: for the upper crack surface S_c^+, Eq.(2.23) is applied; for the lower crack surface S_c^-, Eq.(2.24) is used; and for the remaining boundary nodal points, Eq.(2.21) guides the collocation. As described above, collocation is performed at all nodal points. This results in a system of equations that can be assembled into the form $\mathbf{Hu} = \mathbf{Gt}$, which is then rearranged into the matrix equation $\mathbf{Ax} = \mathbf{b}$. Note that improper integrations occur during the integration of the fundamental solution T_{ij} due

to the introduction of a singularity of order $O(1/r)$ in the integrand. To handle this singularity, the Cauchy principal value integral technique was employed. Similarly, when integrating S_{kij} and D_{kij}, singularities of order $O(1/r^2)$ and $O(1/r)$ emerge, respectively. In the case of S_{kij}, the singularity was addressed using the Hadamard principal value integral, while for D_{kij}, the Cauchy principal value integral was applied, following the same order as in the treatment of T_{ij}. The details of the treatment of the singularity in the equations were reviewed in Sollera [2] and Portela [10].

2.1.5 Evaluation of the Stress Intensity Factors

Fracture modes, as illustrated in Figure 2.2, are defined based on the relative movement of the crack surfaces. In practice, crack deformation is not confined to these fundamental fracture modes alone. Instead, cracks often experience a combination of these modes. Irwin's work [36] has established that this mixed-mode deformation can be effectively characterized through linear superposition. In the context of 2D anisotropic structure analysis, only the mixed mode involving Mode I and II was considered, while Mode III deformation was not taken into account, as the problem under consideration is strictly two-dimensional.

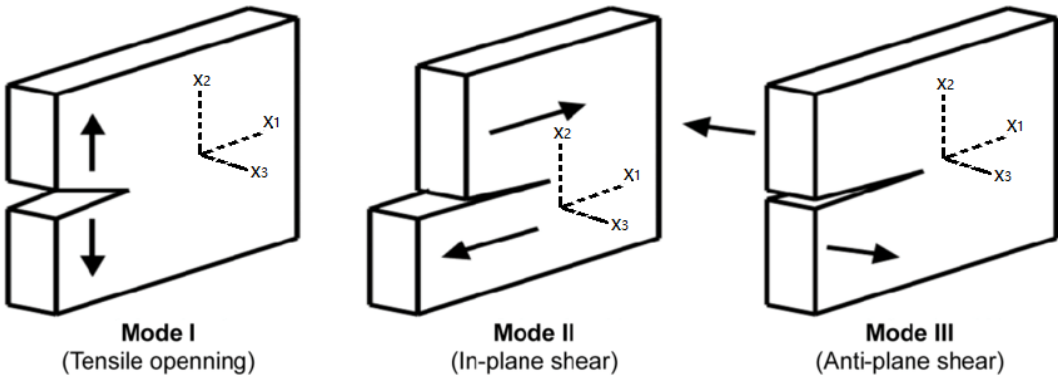


Figure 2.2: Crack deformation modes: Mode I Opening/Tensile mode. Mode II Sliding/ In-plane shear mode. Mode III Tearing/ Anti-plane shear mode. [1]

2.1.5.1 J-Integral technique

In the DBEM for the derivation of stress intensity factor, the path-independent integral approach was widely used. The J-integral is one of the viable integral methods that does not depend on the choice of intermediate integrate points on the contour. The J-integral is constructed by forming

a circular contour around the crack tip. This path is established by connecting several internal points around the crack, and by performing integration over these interior points to compute the J-integral. Further information on the construction of the J-integral path can be found in Aliabadi's comprehensive work [6].

In the case of a 2D anisotropic body, the relationship between nodal displacement near the crack tip and the stress intensity factor (SIF) can be expressed as:

$$\begin{Bmatrix} u_1 \\ u_2 \end{Bmatrix} = \sqrt{\frac{2r}{\pi}} \begin{bmatrix} D_{11} & D_{12} \\ D_{21} & D_{22} \end{bmatrix} \begin{Bmatrix} K_I \\ K_{II} \end{Bmatrix} \tag{2.25}$$

where D_{ij} is a function of anisotropic material property with the parameters given in Eq.(2.3) and 2.5.

$$\begin{aligned} D_{11} &= \mathrm{Im}\left(\tfrac{\mu_2 p_{11} - \mu_1 p_{12}}{\mu_1 - \mu_2}\right) \quad D_{12} = \mathrm{Im}\left(\tfrac{p_{11} - p_{12}}{\mu_1 - \mu_2}\right) \\ D_{21} &= \mathrm{Im}\left(\tfrac{\mu_2 p_{21} - \mu_1 p_{22}}{\mu_1 - \mu_2}\right) \quad D_{22} = \mathrm{Im}\left(\tfrac{p_{21} - p_{22}}{\mu_1 - \mu_2}\right) \end{aligned} \tag{2.26}$$

The SIF for mode I and model II are given as K_I and K_{II}.

The J-integral formulation is defined as:

$$J_k = \int_C \left(W n_k - t_j u_{j,k}\right) dC \tag{2.27}$$

where C represents an arbitrarily chosen closed contour around the crack, and n_k denotes the outward unit normal on the contour elements. The computation of traction and displacement gradient relies on the integral equations introduced in the previous section. Additionally, W represents the strain energy per unit volume and is defined as:

$$W = \frac{1}{2}\sigma_{\alpha\beta}\epsilon_{\alpha\beta} = \frac{1}{2}(\sigma_{11}\epsilon_{11} + \sigma_{22}\epsilon_{22} + \sigma_{12}\epsilon_{12}) \tag{2.28}$$

an example of contour used for the J-integral is given in Fig.2.3, where the contour path was discretized into sub-elements and Eq.(2.27) was applied to each of the elements over the contour C. For an anisotropic cracked homogeneous plate, the J-integral expressions in terms of stress

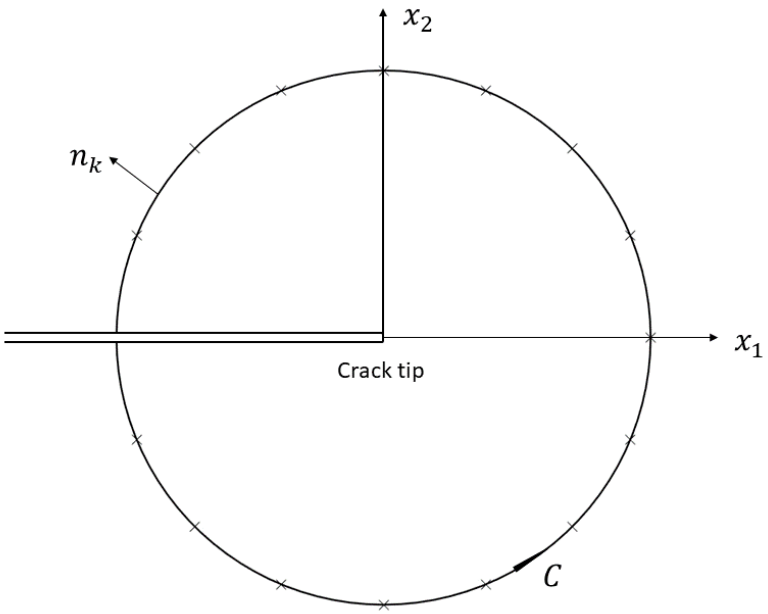


Figure 2.3: Example of circular contour path used in the J-integral technique.

intensity factors are:

$$\begin{aligned} J_1 &= \alpha_{11} K_I^2 + \alpha_{12} K_I K_{II} + \alpha_{22} K_{II}^2 \\ J_2 &= \beta_{11} K_I^2 + \beta_{12} K_I K_{II} + \beta_{22} K_{II}^2 \end{aligned} \tag{2.29}$$

where α_{ij} are given in terms of compliance matrix coefficients a_{ij} and complex roots of the characteristic equation μ_k:

$$\begin{aligned} \alpha_{11} &= -\frac{a_{22}}{2} \operatorname{Im}\left(\frac{\mu_1 + \mu_2}{\mu_1 \mu_2}\right) \\ \alpha_{22} &= \frac{a_{11}}{2} \operatorname{Im}\left(\mu_1 + \mu_2\right) \\ \alpha_{12} &= -\frac{a_{22}}{2} \operatorname{Im}\left(\frac{1}{\mu_1 \mu_2}\right) + \frac{a_{11}}{2} \operatorname{Im}\left(\mu_1 \mu_2\right) \end{aligned} \tag{2.30}$$

the definition of coefficient β_{ij} includes material properties and the detailed expression can be referred to in Sollero's work [2].

2.1.5.2 The ratio of Relative Displacements Technique

the technique of employing the ratio of relative displacement is employed to decouple the SIF for Mode I and Mode II. The expressions for relative opening and sliding displacements in terms of

the stress intensity factors are as follows:

$$\begin{aligned}\delta_1 &= 2\sqrt{\frac{2r}{\pi}}\left(D_{11}K_I + D_{12}K_{II}\right)\\ \delta_2 &= 2\sqrt{\frac{2r}{\pi}}\left(D_{21}K_I + D_{22}K_{II}\right)\end{aligned} \tag{2.31}$$

The ratio S of these relative displacements is:

$$S = \frac{\delta_2}{\delta_1} = \frac{D_{21}K_I + D_{22}K_{II}}{D_{11}K_I + D_{12}K_{II}} \tag{2.32}$$

divide the right-hand-side of the equation by K_{II} and denote the ratio of stress intensity factors as F, the expression for F is given as:

$$F = \frac{K_I}{K_{II}} = \frac{SD_{12} - D_{22}}{D_{21} - SD_{11}} \tag{2.33}$$

therefore K_I can be written as $K_I = FK_{II}$. Substitute this relation into equation (2.31) gives expression for K_{II}:

$$K_{II} = \left(\frac{J_1}{\alpha_{11}F'^2 + \alpha_{12}F + \alpha_{22}}\right)^{\frac{1}{2}} \tag{2.34}$$

2.1.5.3 Crack tip stresses and displacements

To determine the path of crack propagation and apply the fatigue criterion, information from the stress field is essential. Taking into account an infinitesimal element located within a small region around the crack tip, its centre is defined by polar coordinates (r, θ) relative to the origin located at the crack tip. An illustration of these polar coordinates is provided in Figure 2.4. The formulation of the stress field in the vicinity of the crack tip is derived based on the previous work of Sih, Paris, and Irwin [37]. Specifically, for Mode I, the stress components are expressed as follows:

$$\begin{aligned}\sigma_{11}^I &= \frac{K_I}{\sqrt{2\pi r}}\,\mathrm{Re}\left[\frac{\mu_1\mu_2}{\mu_1-\mu_2}\left(\frac{\mu_2}{\sqrt{\cos\theta+\mu_2\sin\theta}} - \frac{\mu_1}{\sqrt{\cos\theta+\mu_1\sin\theta}}\right)\right]\\ \sigma_{22}^I &= \frac{K_I}{\sqrt{2\pi r}}\,\mathrm{Re}\left[\frac{1}{\mu_1-\mu_2}\left(\frac{\mu_1}{\sqrt{\cos\theta+\mu_2\sin\theta}} - \frac{\mu_2}{\sqrt{\cos\theta+\mu_1\sin\theta}}\right)\right]\\ \sigma_{12}^I &= \frac{K_I}{\sqrt{2\pi r}}\,\mathrm{Re}\left[\frac{\mu_1\mu_2}{\mu_1-\mu_2}\left(\frac{1}{\sqrt{\cos\theta+\mu_1\sin\theta}} - \frac{1}{\sqrt{\cos\theta+\mu_2\sin\theta}}\right)\right]\end{aligned} \tag{2.35}$$

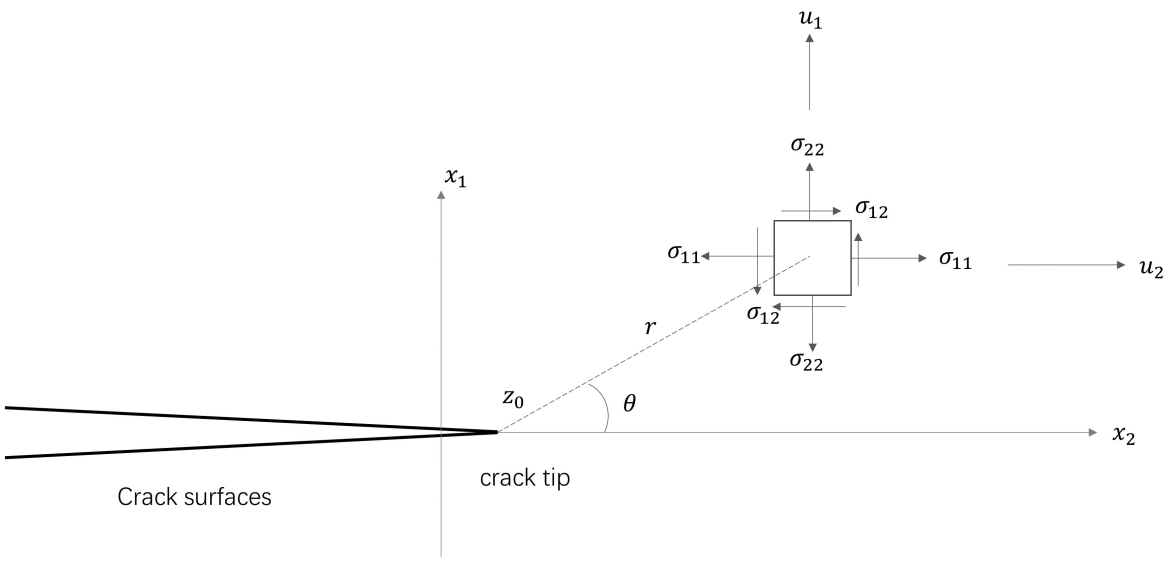


Figure 2.4: Crack definition in the polar coordinate system. [2]

For Mode II deformation, the stresses are given as:

$$\begin{aligned}
\sigma_{11}^{II} &= \frac{K_{II}}{\sqrt{2\pi r}} \operatorname{Re}\left[\frac{1}{\mu_1-\mu_2}\left(\frac{\mu_2^2}{\sqrt{\cos\theta+\mu_2\sin\theta}}-\frac{\mu_1^2}{\sqrt{\cos\theta+\mu_1\sin\theta}}\right)\right] \\
\sigma_{22}^{II} &= \frac{K_{II}}{\sqrt{2\pi r}} \operatorname{Re}\left[\frac{1}{\mu_1-\mu_2}\left(\frac{1}{\sqrt{\cos\theta+\mu_2\sin\theta}}-\frac{1}{\sqrt{\cos\theta+\mu_1\sin\theta}}\right)\right] \\
\sigma_{12}^{II} &= \frac{K_{II}}{\sqrt{2\pi r}} \operatorname{Re}\left[\frac{1}{\mu_1-\mu_2}\left(\frac{\mu_1}{\sqrt{\cos\theta+\mu_1\sin\theta}}-\frac{\mu_2}{\sqrt{\cos\theta+\mu_2\sin\theta}}\right)\right]
\end{aligned} \tag{2.36}$$

The evaluation of mixed-mode deformation involves the superposition of the individual modes. This is achieved by summing the stress components corresponding to Mode I and Mode II. Consequently, the stress fields around the crack tip can be expressed as follows:

$$\sigma_{ij} = \sigma_{ij}^{I} + \sigma_{ij}^{II} \tag{2.37}$$

2.1.5.4 Model of Crack propagation

In this study, the determination of the crack propagation path relies on the application of the maximum circumferential stress criterion. It is assumed that the crack propagates in the direction where the maximum circumferential stress occurs. In polar coordinates, the expression for

circumferential stress $\sigma_{\theta\theta}$, as defined in [2], is provided as follows:

$$\sigma_{\theta\theta} = \sigma_{11} \sin^2\theta + \sigma_{22} \cos^2\theta - 2\sigma_{12} \sin\theta \cos\theta \tag{2.38}$$

where σ_{ij} represents the stresses at the crack tip. The circumferential stress can be determined by combining Equations 2.35, 2.36, and 2.37, resulting in an expression in terms of θ, K_I, K_{II}, and the known material properties μ_k. Since the SIF can be determined using the methodology introduced earlier, the circumferential stress becomes a function solely of θ. The propagation angle θ can be identified as the value corresponding to the maximum magnitude of $\sigma_{\theta\theta}$.

The direction of crack propagation, as determined from Equation 2.38, remains independent of the crack increment size Δa. This implies that the uniqueness of the crack propagation path cannot be guaranteed when employing different increment sizes. Consequently, a correction procedure must be applied to predict the actual crack path. This correction procedure can be summarized as follows, in accordance with [3]:

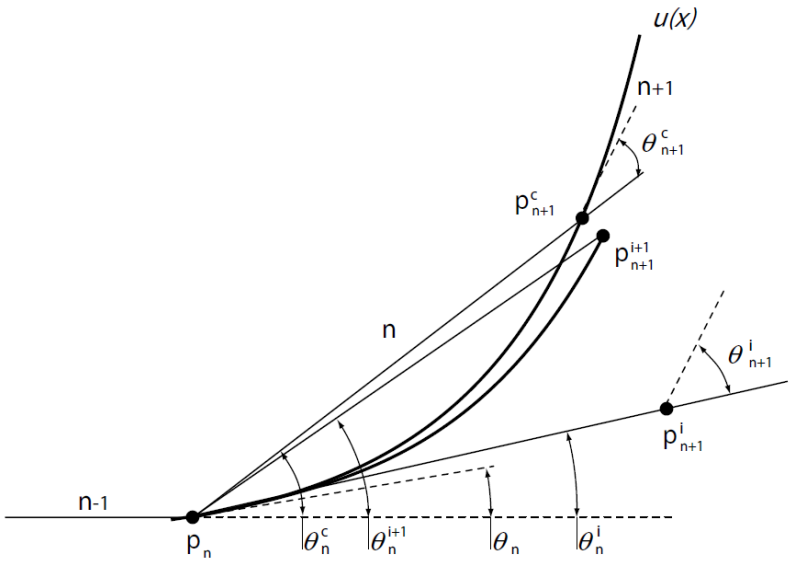


Figure 2.5: correction of crack extension direction [3]

1. For the 1st iteration only: Evaluate the angle θ_n ($\theta_n^i = \theta_n$) at crack tip P_n using the maximum circumferential stress criterion (Eq. 2.38) and extend the crack by the length Δa to P_{n+1}^i.

2. Evaluate the stress intensity factor and hence the angle θ_{n+1}^i at crack tip P_{n+1}^i using the maximum circumferential stress criterion (Eq. 2.38).

3. Calculate the corrected direction by applying the following equation:

$$\tan(\theta_n^{i+1}) = \frac{1}{2}\Big[\tan(\theta_n) + \tan(\theta_n^i + \theta_{n+1}^i)\Big] \tag{2.39}$$

4. Repeat steps 2 and 3 while $|\Delta\theta_n^i| > \beta$, where $\beta = 0.1°$.

2.2 Dual Boundary Element Method for Shallow Shell Structures

Between the 1940s and 1950s, the aircraft and ship industry witnessed a series of unexpected failures. Prior to this period, cracks were often regarded as insignificant parameters with minimal impact on large structures. However, these incidents drove a significant shift towards the study of fracture mechanics. One of the most infamous aviation accidents during this time was the 1954 crash of the COMET G-ALYU, documented in [4]. The aircraft crashed into the island of Ela merely 20 minutes after takeoff. In subsequent fatigue investigations, the primary cause of this catastrophic failure was traced back to fatigue within the pressurized cabin. The failure was observed to propagate longitudinally along the fuselage during water pressure fatigue tests, as illustrated in Fig. 2.6.

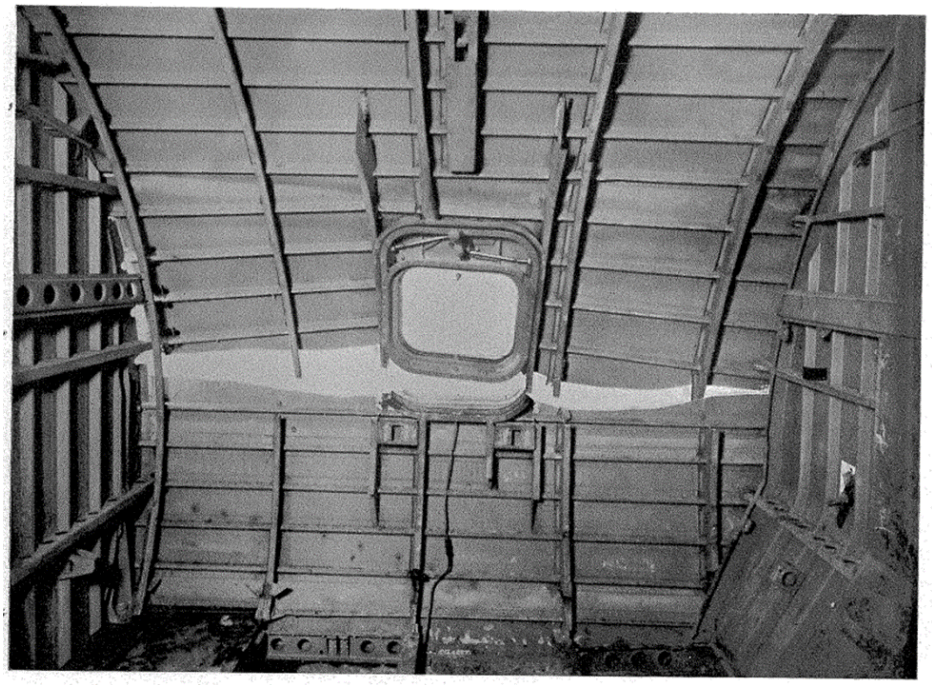


Figure 2.6: View from inside of failure at the forward escape hatch on the port side COMET G-ALYU. [4]

Another noteworthy incident is the Aloha Airline Flight 243 in 1988, where an unexpected explosive decompression occurred. The primary damage involved the loss of a significant portion of the fuselage structure, as shown in Fig. 2.7. This damage resulted from the failure of the lap splice at the stringer, leading to multi-site damage at the rivet locations, as detailed in [38]. Following these incidents, extensive research has been conducted to gain a deeper understanding of the structural behaviour of damaged fuselage panels.



Figure 2.7: Photo of the fuselage damage on Aloha Airline Flight 243, 1988. [5]

A common approach when investigating complex structures like the fuselage is to simplify them into more manageable structures. In the case of the fuselage, the corresponding simplified structure is often considered to be the shallow shell structure. Shallow shell problems are an important subject in engineering design processes, owing to the widespread use of shallow shells in aircraft and naval structures due to their favourable attributes of low weight and high strength.

The shallow shell formulations of the BEM were first developed by Dirgantara and Aliabadi [13,26] for bending problems in shallow shell structures, drawing from the classic theory [39] and Reissner's theory for thin elastic shells [40], which considered transverse normal stress and transverse shear deformation. Reissner's plate theory was pivotal in deriving the fundamental solutions, with the Dual Reciprocity Method (DRM) [41] employed to transfer the domain integrals to boundary integrals. This approach has found applications across various works, such as the analysis of assembled plate structures [42], addressing buckling concerns in shallow shells [43], and the study of composite shallow shell structures [44]. Additionally, fatigue assessments have been conducted using the DBEM formulations, encompassing problems such as crack propagation in cortical bone [45], the analysis of pressurized shells [46], and dynamic fracture assessments in plates [24, 47].

This section introduces the formulation of the Dual Boundary Element Method (DBEM) for shallow shell structures, encompassing the method of evaluating the Stress Intensity Factors (SIFs).

2.2.1 Basic Theory of Shallow Shells

he classical theory of shallow elastic shells is comprehensively discussed in [39]. Building upon this classical framework, Naghdi [48] and Reissner [40] extended the theory of shallow shells to encompass transverse normal stress and shear deformation. The subsequent development of boundary integral equations was conducted by Lu and Huang [49], along with the introduction of the Dual Reciprocal method by Wen [41], played pivotal roles in the transformation of domain integral equations into boundary integral equations. This section provides an overview of the Boundary Element Method (BEM) formulations that have been developed specifically for shallow shell structures, drawing from the work presented in [13]. In this section, Latin letter indices (e.g., i, j, k) span the range from 1 to 3, while Greek letter indices (e.g., α, β) encompass the range from 1 to 2.

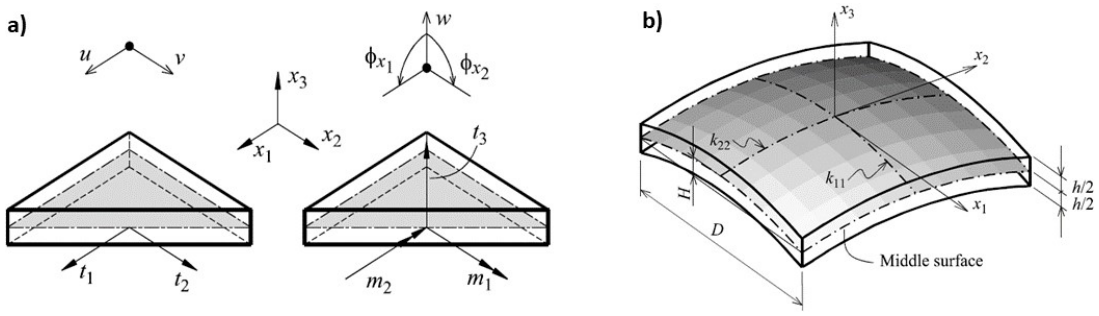


Figure 2.8: Definition of the generalised displacements and tractions and the curvatures for the shell structure in the BEM. [6]

Consider the shell structure with a thickness denoted as h, as illustrated in Fig. 2.8. The principal curvatures of the shell are represented as $\kappa_{11} = 1/R_1$ and $\kappa_{22} = 1/R_2$, where R_1 and R_2 represent the radii of curvature of the shell in the x_1 and x_2 directions, respectively, while $\kappa_{12} = \kappa_{21} = 0$. The shell is considered as thin if

$$max(\frac{h}{R}) \leq \frac{1}{20} \tag{2.40}$$

In the shear deformable shell theory, the Cartesian coordinate system in the $x_1 - x_2$ plane is positioned on the middle plane, representing the projection of points originating from the middle plane ($x_3 = 0$). The top surface is positioned at $x_3 = +h/2$, while the bottom surface is located at $x_3 = -h/2$. In this context, the conventional stress components are replaced with parameters referred to as stress resultants.

The generalized displacement and tractions in this study are defined as follows: w_α represents the rotations in the x_1 and x_2 directions (denoted as ϕ_{x1} and ϕ_{x2}, respectively), w_3 corresponds to the out-of-plane displacement normal to the middle surface. Furthermore, u_α is employed to denote the in-plane displacements in the x_1 and x_2 directions, labelled as u and v in the figure, respectively. The parameters p_α are introduced to characterize the bending tractions resulting from stress couples (m_1 and m_2), while p_3 denotes the shear traction due to the shear stress resultant. Lastly, t_1 and t_2 are employed to represent the traction caused by the membrane stress resultant in the x_1 and x_2 directions, respectively.

The membrane stress resultants $N_{\alpha\beta}$ and shear stress resultants Q_α are defined as force per unit length and are given as

$$N_{\alpha\beta} = \int_{-h/2}^{+h/2} (1 + \frac{x_3}{R_\gamma}) \sigma_{\alpha\beta} dx_3 \tag{2.41}$$

$$Q_\alpha = \int_{-h/2}^{+h/2} (1 + \frac{x_3}{R_\gamma}) \sigma_{\alpha 3} dx_3 \tag{2.42}$$

where $\gamma \neq \alpha$. The bending stress resultants $M_{\alpha\beta}$ are defined as bending and twisting moments per unit length and are given as

$$M_{\alpha\beta} = \int_{-h/2}^{+h/2} (1 + \frac{x_3}{R_\gamma}) x_3 \sigma_{\alpha\beta} dx_3 \tag{2.43}$$

The membrane stress resultants are assumed to be uniform over the thickness, while the bending and shear stress resultants are varied through the thickness [50]. To obtain the stress components, the following relationship can be employed

$$\begin{aligned} (1 + \frac{x_3}{R_\gamma}) \sigma_{\alpha\beta} &= \frac{1}{h} N_{\alpha\beta} + \frac{12 x_3}{h^3} M_{\alpha\beta}; \quad \begin{cases} \gamma = \beta & \alpha \neq \beta \\ \gamma \neq \beta & \alpha = \beta \end{cases} \\ (1 + \frac{x_3}{R_\gamma}) \sigma_{\alpha 3} &= \frac{3}{2h} \left[1 - \left(\frac{2x_3}{h} \right)^2 \right] Q_\alpha; \quad \gamma \neq \alpha \end{aligned} \tag{2.44}$$

The generalised traction components at a boundary point can be evaluated from the stress resultants using the outward normal vector n_β on the boundary by

$$\begin{aligned} p_\alpha &= M_{\alpha\beta} n_\beta \\ p_3 &= Q_\alpha n_\alpha \\ t_\alpha &= N_{\alpha\beta} n_\beta \end{aligned} \tag{2.45}$$

The equilibrium equation for the shallow shell problem considers the domain load q_i acting on the middle plane can be written in terms of the stress resultants as

$$M_{\alpha\beta,\beta} - Q_\alpha = 0 \tag{2.46}$$

$$Q_{\alpha,\alpha} - \kappa_{\alpha\beta} N_{\alpha\beta} + q_3 = 0 \tag{2.47}$$

$$N_{\alpha\beta,\beta} + q_\alpha = 0 \tag{2.48}$$

where q_i is the domain load acting over the middle plane. The stress resultants can be written in terms of the displacement by the following relation

$$M_{\alpha\beta} = D\frac{1-\nu}{2}\left(w_{\alpha,\beta} + w_{\beta,\alpha} + \frac{2\nu}{1-\nu} w_{\gamma,\gamma}\delta_{\alpha\beta}\right) \tag{2.49}$$

$$Q_\alpha = C(w_\alpha + w_{3,\alpha}) \tag{2.50}$$

$$N_{\alpha\beta} = B\frac{1-\nu}{2}\left(u_{\alpha,\beta} + u_{\beta,\alpha} + \frac{2\nu}{1-\nu} u_{\gamma,\gamma}\delta_{\alpha\beta}\right) + B\left[(1-\nu)\kappa_{\alpha\beta} + \nu\delta_{\alpha\beta}\kappa_{\phi\phi}\right] w_3 \tag{2.51}$$

where E denotes Young's modulus and ν for the Poisson's ratio. The tension stiffness $B = Eh/(1-\nu^2)$, bending stiffness $D = Eh^3/[12(1-\nu^2)]$ and the shear stiffness $C = [D(1-\nu)\lambda^2]/2$ with $\lambda = \sqrt{10}/h$.

2.2.2 Boundary Integral Equations

The derivation of the boundary integral equation for shallow shell structures follows a methodology similar to that presented in Section 2.1. The foundational framework encompassing boundary integral equations and fundamental solutions was first introduced by Weeen [51]. For conciseness, only the relevant equations are provided in this section, while the comprehensive derivation can be referenced in the works of Dirgantara [13, 26].

2.2.2.1 Displacement Boundary Integral Equations

The displacement integral equations for rotations, w_1 and w_2, and out-of-plane displacement, w_3, is:

$$\begin{aligned}
&c_{ij}(x')\, w_j(x') + \oint_\Gamma P^*_{ij}(x', x)\, w_j(x) d\Gamma(x) = \int_\Gamma W^*_{ij}(x', x)\, p_j(x) d\Gamma(x) \\
&- \int_\Omega W^*_{i3}(x', X)\, \kappa_{\alpha\beta} B \frac{1-\nu}{2}\left[u_{\alpha,\beta}(X) + u_{\beta,\alpha}(X) + \frac{2\nu}{1-\nu} u_{\phi,\phi}(X)\delta_{\alpha\beta}\right] d\Omega(X) \\
&- \int_\Omega W^*_{i3}(x', X)\, \kappa_{\alpha\beta} B\left((1-\nu)\kappa_{\alpha\beta} + \nu\delta_{\alpha\beta}\kappa_{\phi\phi}\right) w_3(X) d\Omega(X) \\
&+ \int_\Omega W^*_{i3}(x', X)\, q_3(X) d\Omega(X)
\end{aligned} \tag{2.52}$$

and the displacement integral equations for in-plane displacements, u_1 and u_2, are:

$$\begin{aligned} & c_{\theta\alpha}\left(x'\right) u_\alpha\left(x'\right) + \fint_\Gamma T_{\theta\alpha}^{*(i)}\left(x', x\right) u_\alpha(x) d\Gamma(x) \\ & + \int_\Gamma U_{\theta\alpha}^{*}\left(x', x\right) B\left[\kappa_{\alpha\beta}(1-\nu) + \nu\delta_{\alpha\beta}\kappa_{\phi\phi}\right] w_3(x) n_\beta(x) d\Gamma(x) \\ & - \int_\Omega U_{\theta\alpha}^{*}\left(x', X\right) B\left[\kappa_{\alpha\beta}(1-\nu) + \nu\delta_{\alpha\beta}\kappa_{\phi\phi}\right] w_{3,\beta}(X) d\Omega(X) \\ & = \int_\Gamma U_{\theta\alpha}^{*}\left(x', x\right) t_\alpha(x) d\Gamma(x) + \int_\Omega U_{\theta\alpha}^{*}\left(x', X\right) q_\alpha(X) d\Omega(X) \end{aligned} \tag{2.53}$$

with

$$c_{ij}(x') = \begin{cases} \frac{1}{2}\delta_{ij} & x' \in \Gamma \\ 1 & X' \in \Omega \end{cases} \tag{2.54}$$

In the provided equations, the symbol $\fint$ denotes the Cauchy principal value integral. In this context, x' and x refer to the source and field points, respectively, with $x \in \Gamma$ representing field points on the boundary and $X \in \Omega$ representing points within the domain. Notably, W_{ij}^* and $U_{\theta\alpha}^*$ represent fundamental solutions for displacements, while P_{ij}^* and $T_{\theta\alpha}^{*(i)}$ denotes the fundamental solutions for tractions. The detailed and explicit expressions of these fundamental solutions are outlined in Appendix A.

It is noteworthy that the terms q_α and q_3 denote membrane body forces and domain pressure forces, respectively. The study presented in this work exclusively focuses on the loading condition characterized by a uniform domain load $q_3 = \text{constant}$ and $q_\alpha = 0$. Consequently, the last integral in Eq. (2.53) vanishes. The last integral in Eq. (2.52) can be reformulated and transformed into a boundary integral through the application of the divergence theorem:

$$\int_\Omega W_{i3}^{*}\left(x', X\right) q_3(X) d\Omega(X) = q_3 \int_\Omega W_{i3}^{*}\left(x', X\right) d\Omega(X) = q_3 \int_\Gamma V_{i,\alpha}^{*}\left(x', x\right) d\Gamma(x) \tag{2.55}$$

where $V_{i,\phi\phi}^* = W_{i3}^*$. The expression for $V_{i,\alpha}^*$ is given in Appendix A. The remaining domain integral in Eq.(2.52), (2.53) can be transformed into boundary integral by the Dual Reciprocity Technique [52].

2.2.2.2 Dual Reciprocity Method

This section presented the Dual Reciprocity Method for transforming the domain integrals into boundary integral equations. The formulations and solutions presented are based on the derivation provided in the work of Wen [41]. Consider the case when the domain force $q_\alpha = 0$, the displacement boundary integral equations that are given in Eq. (2.52) and (2.53) contains six domain integrals.

$$\begin{aligned} I_1^D &= \int_\Omega W_{i3}^* w_3 d\Omega, \quad I_2^D = \int_\Omega W_{i3}^* \tfrac{\partial u_1}{\partial x_1} d\Omega \\ I_3^D &= \int_\Omega W_{i3}^* \tfrac{\partial u_2}{\partial x_2} d\Omega, \quad I_4^D = \int_\Omega W_{i3}^* q_3 d\Omega \\ I_5^D &= \int_\Omega U_{\alpha 1}^* \tfrac{\partial w_3}{\partial x_1} d\Omega, \quad I_6^D = \int_\Omega U_{\alpha 2}^* \tfrac{\partial w_3}{\partial x_2} d\Omega \end{aligned} \tag{2.56}$$

rewriting Eq.(2.52), (2.53) with expanding the coefficient terms related to the curvature $\kappa_{\alpha\beta}$ and substitute in with the domain integral in Eq.(2.56)

$$\begin{aligned} &c_{ij}(x')\, w_j(x') + \oint_\Gamma P_{ij}^*(x', x)\, w_j(x) d\Gamma(x) = \int_\Gamma W_{ij}^*(x', x)\, p_j(x) d\Gamma(x) \\ &- B(\kappa_{11} + \nu\kappa_{22}) I_2^D - B(\nu\kappa_{11} + \kappa_{22}) I_3^D \\ &- B(\kappa_{11}^2 + \kappa_{22}^2 + 2\nu\kappa_{11}\kappa_{22}) I_1^D + I_4^D \end{aligned} \tag{2.57}$$

and

$$\begin{aligned} &c_{\theta\alpha}(x')\, u_\alpha(x') + \oint_\Gamma T_{\theta\alpha}^{*(i)}(x', x)\, u_\alpha(x) d\Gamma(x) \\ &+ \int_\Gamma U_{\theta\alpha}^*(x', x)\, B\left[\kappa_{\alpha\beta}(1-\nu) + \nu\delta_{\alpha\beta}\kappa_{\phi\phi}\right] w_3(x) n_\beta(x) d\Gamma(x) \\ &- B(\kappa_{11} + \nu\kappa_{22}) I_5^D - B(\nu\kappa_{11} + \kappa_{22}) I_6^D \\ &= \int_\Gamma U_{\theta\alpha}^*(x', x)\, t_\alpha(x) d\Gamma(x) \end{aligned} \tag{2.58}$$

The domain integrals can be solved by pairs of particular solutions using the radial basis functions $F(r_m)$, where the displacement for a 2D problem can be approximated using the following form

$$u_\alpha(x_1, x_2) = \sum_{m=1}^{M} F(r_m)\alpha_m \tag{2.59}$$

where $r_m = \mid x_\alpha - \hat{x}_\alpha^m \mid = \sqrt{(x_1 - \hat{x}_1^m)^2 + (x_2 - \hat{x}_2^m)^2}$ with $\hat{\mathbf{x}} = (\hat{x}_1^m, \hat{x}_2^m)$ are the interpolation points located on boundary or domain. M denotes the total number of interpolation points and α_m is

the interpolating coefficients. Written in matrix form, the coefficients α_m can be found by:

$$\boldsymbol{\alpha} = \mathbf{F}^{-1}\mathbf{u}_\alpha \tag{2.60}$$

where $\mathbf{u}_\alpha = [u_{\alpha 1}, u_{\alpha 2}, ..., u_{\alpha M}]^T$. $\mathbf{F}$ is obtained by computing the radial basis functions at each pair of interpolation points and takes the form of

$$\mathbf{F} = \begin{bmatrix} F(\mid \mathbf{x}_{\alpha 1} - \mathbf{x}_{\alpha 1} \mid) & F(\mid \mathbf{x}_{\alpha 1} - \mathbf{x}_{\alpha 2} \mid) & ... & F(\mid \mathbf{x}_{\alpha 1} - \mathbf{x}_{\alpha M} \mid) \\ F(\mid \mathbf{x}_{\alpha 2} - \mathbf{x}_{\alpha 1} \mid) & F(\mid \mathbf{x}_{\alpha 2} - \mathbf{x}_{\alpha 2} \mid) & ... & F(\mid \mathbf{x}_{\alpha 2} - \mathbf{x}_{\alpha M} \mid) \\ . & . & ... & . \\ . & . & ... & . \\ F(\mid \mathbf{x}_{\alpha M} - \mathbf{x}_{\alpha 1} \mid) & F(\mid \mathbf{x}_{\alpha M} - \mathbf{x}_{\alpha 2} \mid) & ... & F(\mid \mathbf{x}_{\alpha M} - \mathbf{x}_{\alpha M} \mid) \end{bmatrix} \tag{2.61}$$

differentiating Eq.2.59 with respect to the interpolating points x_α, the derivatives of the displacement can be found as

$$\frac{\partial u_\alpha(x_1, x_2)}{\partial x_\alpha} = \sum_{m=1}^{M} \frac{\partial F(r_m)}{\partial x_\alpha}\alpha_m \tag{2.62}$$

The particular solutions were derived such that they satisfy the equilibrium equation of shear deformable shallow shell structures.

Taking a pair of particular solutions $[F(r_m), \hat{w}^3_{mk}, \hat{p}^3_{mk}]$ where the radial basis function $F(r_m) = 1 + r_m$, the domain internal equations I_1^D and I_4^D can be approximated as:

$$\begin{aligned} I_1^D = \sum_{m=1}^{M} \Bigg[& c_{ik}\left(\mathbf{x}'\right)\hat{w}^3_{mk}\left(\mathbf{x}'\right) - \int_\Gamma W^*_{ik}\left(\mathbf{x}', \mathbf{x}\right)\hat{p}^3_{mk}(\mathbf{x})d\Gamma(\mathbf{x}) \\ & + \oint_\Gamma P^*_{ik}\left(\mathbf{x}', \mathbf{x}\right)\hat{w}^3_{mk}(\mathbf{x})d\Gamma(\mathbf{x}) \Bigg] \mathbf{F}^{-1} w_3 \end{aligned} \tag{2.63}$$

$$\begin{aligned} I_4^D = \sum_{m=1}^{M} \Bigg[& c_{ik}\left(\mathbf{x}'\right)\hat{w}^3_{mk}\left(\mathbf{x}'\right) - \int_\Gamma W^*_{ik}\left(\mathbf{x}', \mathbf{x}\right)\hat{p}^3_{mk}(\mathbf{x})d\Gamma(\mathbf{x}) \\ & + \oint_\Gamma P^*_{ik}\left(\mathbf{x}', \mathbf{x}\right)\hat{w}^3_{mk}(\mathbf{x})d\Gamma(\mathbf{x}) \Bigg] \mathbf{F}^{-1} q_3 \end{aligned} \tag{2.64}$$

Similarly, taking a pair of particular solutions $[F(r_m), \hat{w}^{\alpha}_{mk}, \hat{p}^{\alpha}_{mk}]$ where the radial basis function $\partial F(r_m)/\partial x_\alpha = x_\alpha/r$, the domain internal equations I^D_2 and I^D_3 can be approximated as:

$$I^D_2 = \sum_{m=1}^{M} \left[c_{ik}\left(\mathbf{x}'\right) \hat{w}^1_{mk}\left(\mathbf{x}'\right) - \int_\Gamma W^*_{ik}\left(\mathbf{x}', \mathbf{x}\right) \hat{p}^1_{mk}(\mathbf{x}) d\Gamma(\mathbf{x}) + \cancel{\int}_\Gamma P^*_{ik}\left(\mathbf{x}', \mathbf{x}\right) \hat{w}^1_{mk}(\mathbf{x}) d\Gamma(\mathbf{x}) \right] \mathbf{F}^{-1} u_1 \tag{2.65}$$

$$I^D_3 = \sum_{m=1}^{M} \left[c_{ik}\left(\mathbf{x}'\right) \hat{w}^2_{mk}\left(\mathbf{x}'\right) - \int_\Gamma W^*_{ik}\left(\mathbf{x}', \mathbf{x}\right) \hat{p}^2_{mk}(\mathbf{x}) d\Gamma(\mathbf{x}) + \cancel{\int}_\Gamma P^*_{ik}\left(\mathbf{x}', \mathbf{x}\right) \hat{w}^2_{mk}(\mathbf{x}) d\Gamma(\mathbf{x}) \right] \mathbf{F}^{-1} u_2 \tag{2.66}$$

taking a pair of particular solutions $[F(r_m), \hat{u}^1_{m\alpha}, \hat{t}^1_{m\alpha}]$ where the radial basis function $\partial F(r_m)/\partial x_1 = x_1/r$, the domain internal equations I^D_5 can be approximated as:

$$I^D_5 = \sum_{m=1}^{M} \left[c_{\alpha\beta}\left(\mathbf{x}'\right) \hat{u}^1_{m\beta}\left(\mathbf{x}'\right) - \int_\Gamma U^*_{\alpha\beta}\left(\mathbf{x}', \mathbf{x}\right) \hat{t}^1_{m\beta}(\mathbf{x}) d\Gamma(\mathbf{x}) + \cancel{\int}_\Gamma T^*_{\alpha\beta}\left(\mathbf{x}', \mathbf{x}\right) \hat{u}^1_{m\beta}(\mathbf{x}) d\Gamma(\mathbf{x}) \right] \mathbf{F}^{-1} w_3 \tag{2.67}$$

and for $[F(r_m), \hat{u}^2_{m\alpha}, \hat{t}^2_{m\alpha}]$ where the radial basis function $\partial F(r_m)/\partial x_2 = x_2/r$, the domain internal equations I^D_6 can be approximated as:

$$I^D_6 = \sum_{m=1}^{M} \left[c_{\alpha\beta}\left(\mathbf{x}'\right) \hat{u}^2_{m\beta}\left(\mathbf{x}'\right) - \int_\Gamma U^*_{\alpha\beta}\left(\mathbf{x}', \mathbf{x}\right) \hat{t}^2_{m\beta}(\mathbf{x}) d\Gamma(\mathbf{x}) + \cancel{\int}_\Gamma T^*_{\alpha\beta}\left(\mathbf{x}', \mathbf{x}\right) \hat{u}^2_{m\beta}(\mathbf{x}) d\Gamma(\mathbf{x}) \right] \mathbf{F}^{-1} w_3 \tag{2.68}$$

the M number of interpolation points were evenly distributed in the domain and are referred to as DRM points in the following sections. The particular solutions ($\hat{u}^{\gamma}_{m\alpha}$, $\hat{t}^{\gamma}_{m\alpha}$) are derived from solving the Galerkin vector for 2D plane stress, and ($\hat{w}^{i}_{m\alpha}$, $\hat{p}^{i}_{m\alpha}$) for plate bending problem, obtained through the implementation of radial basis functions. Detailed expressions for these particular solutions can be found in the Appendix B.

2.2.2.3 Numerical Implementations

Similar to the anisotropic BEM formulation, the boundary of a given structure can be discredited into total N_e elements and each element n contains N_l nodal points. The local coordinate system within element n is defined such that $\zeta \in [-1, +1]$ and the shape function at l node is denoted as Φ_l. The Jacobian is defined in the same way as given in Eq.(2.22). The discretisation form of Eq.(2.69) and (2.70) can be written as:

$$\begin{aligned} & c_{ij}\left(x'\right) w_j\left(x'\right) + \sum_{n=1}^{N_e}\sum_{l=1}^{N_l} w_j^{nl} \fint_{-1}^{+1} P_{ij}^*\left(x', x(\zeta)\right) \Phi_l J_n(\zeta) d\zeta \\ & = \sum_{n=1}^{N_e}\sum_{l=1}^{N_l} p_j^{nl} \int_{-1}^{+1} W_{ij}^*\left(x', x(\zeta)\right) \Phi_l J_n(\zeta) d\zeta \\ & - B(\kappa_{11} + \nu\kappa_{22}) I_2^D - B(\nu\kappa_{11} + \kappa_{22}) I_3^D \\ & - B(\kappa_{11}^2 + \kappa_{22}^2 + 2\nu\kappa_{11}\kappa_{22}) I_1^D + I_4^D \end{aligned} \tag{2.69}$$

and

$$\begin{aligned} & c_{\theta\alpha}\left(x'\right) u_\alpha\left(x'\right) + \sum_{n=1}^{N_e}\sum_{l=1}^{N_l} u_\alpha^{nl} \fint_{-1}^{+1} T_{\theta\alpha}^{*(i)}\left(x', x(\zeta)\right) \Phi_l J_n(\zeta) d\zeta \\ & + \sum_{n=1}^{N_e}\sum_{l=1}^{N_l} B\left[\kappa_{\alpha\beta}(1-\nu) + \nu\delta_{\alpha\beta}\kappa_{\phi\phi}\right] w_3^{nl} n_\beta^{nl} \int_{-1}^{+1} U_{\theta\alpha}^*\left(x', x(\zeta)\right) \Phi_l J_n(\zeta) d\zeta \\ & - B(\kappa_{11} + \nu\kappa_{22}) I_5^D - B(\nu\kappa_{11} + \kappa_{22}) I_6^D \\ & = \sum_{n=1}^{N_e}\sum_{l=1}^{N_l} t_\alpha^{nl} \int_{-1}^{+1} U_{\theta\alpha}^*\left(x', x(\zeta)\right) \Phi_l J_n(\zeta) d\zeta \end{aligned} \tag{2.70}$$

For continuous quadratic elements, the shape functions are defined as given in Eq.(2.19). Semi-discontinuous elements are used for the discretisation at the corner to avoid the discontinuity of the traction since the corners do not have a distinct normal vector. The shape function for semi-discontinuous elements that are located at the local coordinate of $\zeta = -2/3, 0, +1$ are defined as

$$\Phi_1^{s1} = \frac{9}{10}\zeta(\zeta - 1), \quad \Phi_2^{s1} = -\frac{3}{2}(\zeta - 1)(\zeta + \frac{2}{3}), \quad \Phi_3^{s1} = \frac{6}{10}\zeta(\zeta + \frac{2}{3}) \tag{2.71}$$

And the shape function for semi-discontinuous elements that are located at the local coordinate of $\zeta = -1, 0, +2/3$ are defined as

$$\Phi_1^{s1} = \frac{6}{10}\zeta(\zeta - \frac{2}{3}), \quad \Phi_2^{s1} = -\frac{3}{2}(\zeta + 1)(\zeta - \frac{2}{3}), \quad \Phi_3^{s1} = \frac{9}{10}\zeta(\zeta + 1) \tag{2.72}$$

In addition, for discrimination around the crack tip, special crack tip elements that have been proposed in [53] are used.

2.2.2.4 Stress Resultant Boundary Integral Equations

The stress resultant boundary integral equation can be evaluated using the stress resultant - displacement relationship in Eq.(2.49), (2.50), (2.51). The integral equation for stress resultant can be found as

$$\begin{aligned}\frac{1}{2}M_{\alpha\beta}(\mathbf{x}') &+ \fint_\Gamma P^*_{\alpha\beta\gamma}(\mathbf{x}', \mathbf{x})\, w_\gamma(\mathbf{x}) d\Gamma(\mathbf{x}) + \int_\Gamma P^*_{\alpha\beta 3}(\mathbf{x}', \mathbf{x})\, w_3(\mathbf{x}) d\Gamma(\mathbf{x}) \\ &= \fint_\Gamma W^*_{\alpha\beta\gamma}(\mathbf{x}', \mathbf{x})\, p_\gamma(\mathbf{x}) d\Gamma(\mathbf{x}) + \int_\Gamma W^*_{\alpha\beta 3}(\mathbf{x}', \mathbf{x})\, p_3(\mathbf{x}) d\Gamma(\mathbf{x}) \\ &+ \int_\Omega W^*_{\alpha\beta 3}(\mathbf{X}', \mathbf{x})\, q_3^* d\Omega(\mathbf{X})\end{aligned} \tag{2.73}$$

and

$$\begin{aligned}\frac{1}{2}Q_\beta(\mathbf{X}') &+ \int_\Gamma P^*_{3\beta\gamma}(\mathbf{X}', \mathbf{x})\, w_\gamma(\mathbf{x}) d\Gamma(\mathbf{x}) + \fint_\Gamma P^*_{3\beta 3}(\mathbf{X}', \mathbf{x})\, w_3(\mathbf{x}) d\Gamma(\mathbf{x}) \\ &= \int_\Gamma W^*_{3\beta\gamma}(\mathbf{X}', \mathbf{x})\, p_\gamma(\mathbf{x}) d\Gamma(\mathbf{x}) + \int_\Gamma W^*_{3\beta 3}(\mathbf{X}', \mathbf{x})\, p_3(\mathbf{x}) d\Gamma(\mathbf{x}) \\ &+ \int_\Omega W^*_{3\beta 3}(\mathbf{X}', \mathbf{X})\, q_3^* d\Omega(\mathbf{X})\end{aligned} \tag{2.74}$$

and

$$\begin{aligned}&\frac{1}{2}N_{\alpha\beta}(\mathbf{X}') + \fint_\Gamma T^{(i)*}_{\alpha\beta\gamma}(\mathbf{X}', \mathbf{x})\, u_\gamma(\mathbf{x}) d\Gamma(\mathbf{x}) \\ &+ \fint_\Gamma U^*_{\alpha\beta\gamma}(\mathbf{X}', \mathbf{x})\, B\left[k_{\alpha\gamma}(1-\nu) + \nu\delta_{\alpha\gamma}k_{\phi\phi}\right] w_3(\mathbf{x}) n_\gamma(\mathbf{x}) d\Gamma(\mathbf{x}) \\ &= \fint_\Gamma U^*_{\alpha\beta\gamma}(\mathbf{X}', \mathbf{x})\, t_\gamma(\mathbf{x}) d\Gamma(\mathbf{x}) \\ &+ \int_\Omega U^*_{\alpha\beta\gamma}(\mathbf{X}', \mathbf{X})\, q_\gamma^* d\Omega(\mathbf{X}) + B\left[(1-\nu)k_{\alpha\beta} + \nu\delta_{\alpha\beta}k_{\phi\phi}\right] w_3(\mathbf{X}')\end{aligned} \tag{2.75}$$

where $q_3^* = q_3 - B(\kappa_{11} + \nu\kappa_{22})u_{1,1} - B(\nu\kappa_{11} + \kappa_{22})u_{2,2} - B(\kappa_{11}^2 + \kappa_{22}^2 + 2\nu\kappa_{11}\kappa_{22})w_3$ and $q_\alpha^* = q_\alpha + B\left[(1-\nu)k_{\alpha\beta} + \nu\delta_{\alpha\beta}k_{\phi\phi}\right] w_{3,\beta}$. The symbol $\fint$ denotes the Hadamard principal value integral.

The kernels $W^*_{i\beta k}$ and $P^*_{i\beta k}$ are determined through the first derivative of the fundamental solution W^*_{ij} and P^*_{ij}, while the kernels $U^*_{\alpha\beta\gamma}$ and $T^{(i)*}_{\alpha\beta\gamma}$ are derived from the first derivative of the fundamental solution $U^*_{\theta\alpha}$ and $T^{(i)*}_{\theta\alpha}$. Detailed expressions for these kernels are provided in the Appendix A. The matrix representation of the results of the collocation employed in the Boundary Element Method (BEM) is denoted as $\mathbf{Hu} = \mathbf{Gt}$, with $\mathbf{H}$ and $\mathbf{G}$ representing as the coefficient matrices. In this context, $\mathbf{u}$ and $\mathbf{t}$ represent vectors comprising both known and unknown boundary displacements and tractions. A rearrangement of this equation, wherein all the unknowns are aggregated into $\mathbf{X}$ and all the known boundary displacements and tractions are encompassed in $\mathbf{F}$, which yields the following expression for the system of equations

$$\mathbf{AX} = \mathbf{F} \tag{2.76}$$

2.2.3 Evaluation of the Boundary Stress Resultants

The determination of local stress resultants relies on transformation of the global displacement to local system. At a given boundary point x', the generalized displacement and traction in the local coordinate system are represented as $(\hat{w}_i, \hat{u}_\theta)$ and $(\hat{p}_i, \hat{t}_\theta)$, respectively. The conversion of global paramters into the local coordinate system were conducted by incorporating the rotational matrix $\hat{e_{ij}}$, where

$$\hat{e}_{ij} = \begin{bmatrix} n_1 & n_2 & 0 \\ -n_2 & n_1 & 0 \\ 0 & 0 & 1 \end{bmatrix} \tag{2.77}$$

The local traction and displacement can be evaluated by

$$\begin{aligned} \hat{w}_i &= \hat{e}_{ij} w_j \quad & \hat{u}_\theta &= \hat{e}_{\theta\gamma} u_\gamma \\ \hat{p}_i &= \hat{e}_{ij} p_j \quad & \hat{t}_\theta &= \hat{e}_{\theta\gamma} t_\gamma \end{aligned} \tag{2.78}$$

The global displacement and traction were obtained by solving the system of boundary integral equations in Eq.(2.76). The local bending stress resultants can be found using Eq.(2.49) and are

defined as:

$$\begin{aligned}\hat{M}_{1\alpha} &= \hat{p}_\alpha \\ \hat{M}_{22} &= \nu\hat{p}_1 + D(1-\nu^2)\hat{w}_{2,2}\end{aligned} \tag{2.79}$$

Once the local bending stress resultants are obtained, the global bending stress resultants can be evaluated using the rotation matrix as:

$$M_{\alpha\beta} = \hat{e}_{\theta\alpha}\hat{e}_{\gamma\beta}\hat{M}_{\theta\gamma} \tag{2.80}$$

The membrane stress resultants are defined such that:

$$\begin{aligned}\hat{N}_{1\alpha} &= \hat{t}_\alpha \\ \hat{N}_{22} &= \nu\hat{t}_1 + B(1-\nu^2)\hat{u}_{2,2} + B(1-\nu^2)\hat{\kappa}_{22}\hat{w}_3\end{aligned} \tag{2.81}$$

where the local curvature can be found by $\hat{\kappa}_{22} = n_2^2\kappa_{11} + n_1^2\kappa_{22}$. The global membrane stress resultant can be found by using the rotation matrix:

$$N_{\alpha\beta} = \hat{e}_{\theta\alpha}\hat{e}_{\gamma\beta}\hat{N}_{\theta\gamma} \tag{2.82}$$

The shear stress resultant can be evaluated as:

$$\begin{aligned}\hat{Q}_1 &= \hat{p}_3 \\ \hat{Q}_2 &= D\frac{1-\nu}{2}\lambda^2(\hat{w}_2 + \hat{w}_{3,2})\end{aligned} \tag{2.83}$$

The global shear stress resultant at a boundary point is therefore

$$Q_\alpha = \hat{e}_{\beta\alpha}\hat{Q}_\beta \tag{2.84}$$

Note that in the above equations, the derivatives of the displacement are required to be computed. The displacement can be approximated through the utilization of the shape function Φ^{n_l} in an element by

$$\hat{w}_j = \Phi^{n_l}\hat{w}_j^{n_l} \quad \hat{u}_\theta = \Phi^{n_l}\hat{u}_\theta^{n_l} \tag{2.85}$$

The definition of the element shape function aligns with the previous section. Consequently, the evaluation of displacement derivatives entails the transformation of the global generalized displacement into the local coordinate system. Subsequently, the approximations of these derivatives are facilitated through the utilization of the element shape function, as follows

$$\begin{aligned}\hat{w}_{i,2} &= \frac{\partial \Phi^{n_l}}{\partial \zeta} \hat{e_{ij}} w_j^{n_l} \frac{\partial \zeta}{\partial x_2(x')} \\ \hat{u}_{\theta,2} &= \frac{\partial \Phi^{n_l}}{\partial \zeta} \hat{e_{\theta\gamma}} u_\gamma^{n_l} \frac{\partial \zeta}{\partial x_2(x')}\end{aligned} \tag{2.86}$$

where $\frac{\partial \zeta}{\partial x_2(x')} = 1/J(x')$. The stress components can be evaluated from the stress resultants as given in Eq.(2.44). The maximum stresses occur at the top and bottom surfaces where $x_3 = \pm h/2$. Therefore, the maximum stress is evaluated on the top surface of the shell in this work.

2.2.4 Dual Boundary Element Method for Shallow Shell

The Dual Boundary Element Method was employed for the fracture analysis of the shear deformable shell. As described in Sec.2.1, the boundary can be separated as $\Gamma = \Gamma^e + \Gamma^+ + \Gamma^-$. The DBEM uses the displacement integral equation for collocations on the upper crack surface and the traction integral equation for the collocation on the lower crack surface. The displacement integral equations for the collocation on the upper surface $x^+ \in \Gamma^+$ are:

$$\begin{aligned}&\frac{1}{2} w_j\left(x^+\right) + \frac{1}{2} w_j\left(x^-\right) + \fint_\Gamma P_{ij}^*\left(x^+, x\right) w_j(x) d\Gamma(x) \\ &= \int_\Gamma W_{ij}^*\left(x^+, x\right) p_j(x) d\Gamma(x) \\ &- \int_\Omega W_{i3}^*\left(x^+, X\right) \kappa_{\alpha\beta} B \frac{1-\nu}{2} \left[u_{\alpha,\beta}(X) + u_{\beta,\alpha}(X) + \frac{2\nu}{1-\nu} u_{\phi,\phi}(X) \delta_{\alpha\beta}\right] d\Omega(X) \\ &- \int_\Omega W_{i3}^*\left(x^+, X\right) \kappa_{\alpha\beta} B \left((1-\nu)\kappa_{\alpha\beta} + \nu \delta_{\alpha\beta} \kappa_{\phi\phi}\right) w_3(X) d\Omega(X) \\ &+ \int_\Omega W_{i3}^*\left(x^+, X\right) q_3(X) d\Omega(X)\end{aligned} \tag{2.87}$$

and

$$\begin{aligned}
&\frac{1}{2}u_\alpha\left(x^+\right)+\frac{1}{2}u_\alpha\left(x^-\right)+\oint_\Gamma T^*_{\theta\alpha}\left(x^+,x\right)u_\alpha(x)d\Gamma(x)\\
&+\int_\Gamma U^*_{\theta\alpha}\left(x^+,x\right)B\left[\kappa_{\alpha\beta}(1-\nu)+\nu\delta_{\alpha\beta}\kappa_{\phi\phi}\right]w_3(x)n_\beta(x)d\Gamma(x)\\
&-\int_\Omega U^*_{\theta\alpha}\left(x^+,X\right)B\left[\kappa_{\alpha\beta}(1-\nu)+\nu\delta_{\alpha\beta}\kappa_{\phi\phi}\right]w_{3,\beta}(X)d\Omega(X)\\
&=\int_\Gamma U^*_{\theta\alpha}\left(x^+,x\right)t_\alpha(x)d\Gamma(x)+\int_\Omega U^*_{\theta\alpha}\left(x^+,X\right)q_\alpha(X)d\Omega(X)
\end{aligned}\tag{2.88}$$

The traction integral equations can be evaluated by multiplying the outward normal vector on the boundary $n_\beta(x^-)$ (Eq.(2.45)) to the stress resultant equations given in Eq.(2.73), (2.74), (2.75). Therefore, the collocation on the lower crack surface $x^-\in\Gamma^-$ can be written as:

$$\begin{aligned}
&\frac{1}{2}p_\alpha\left(x^-\right)-\frac{1}{2}p_\alpha\left(x^+\right)+n_\beta\left(x^-\right)\oint_\Gamma P^*_{\alpha\beta\gamma}\left(x^-,x\right)w_\gamma(x)d\Gamma(x)\\
&+n_\beta\left(x^-\right)\oint_\Gamma P^*_{\alpha\beta3}\left(x^-,x\right)w_3(x)d\Gamma(x)\\
&=n_\beta\left(x^-\right)\oint_\Gamma W^*_{\alpha\beta\gamma}\left(x^-,x\right)p_\gamma(x)d\Gamma(x)+n_\beta\left(x^-\right)\int_\Gamma W^*_{\alpha\beta3}\left(x^-,x\right)p_3(x)d\Gamma(x)\\
&-n_\beta(x^-)\int_\Omega\kappa_{\theta\psi}B\frac{1-v}{2}\left(u_{\theta,\psi}(X)+u_{\psi,\theta}(X)+\frac{2v}{1-\nu}u_{\phi,\phi}(X)\delta_{\theta\psi}\right)\\
&\times W^*_{\alpha\beta3}(x^-,X)d\Omega(X)\\
&-n_\beta\left(x^-\right)\int_\Omega\kappa_{\theta\psi}B\left((1-v)\kappa_{\theta\psi}+v\delta_{\theta\psi}\kappa_{\phi\phi}\right)w_3(X)W^*_{\alpha\beta3}\left(x^-,X\right)d\Omega(X)\\
&+n_\beta\left(x^-\right)\int_\Omega W^*_{\alpha\beta3}\left(x^-,X\right)q_3d\Omega(X)
\end{aligned}\tag{2.89}$$

and

$$\begin{aligned}
&\frac{1}{2}p_3\left(x^-\right)-\frac{1}{2}p_3\left(x^+\right)+n_\beta\left(x^-\right)\oint_\Gamma P^*_{3\beta\gamma}\left(x^-,x\right)w_\gamma(x)d\Gamma(x)\\
&+n_\beta\left(x^-\right)\oint_\Gamma P^*_{3\beta3}\left(x^-,x\right)w_3(x)d\Gamma(x)\\
&=n_\beta\left(x^-\right)\int_\Gamma W^*_{3\beta\gamma}\left(x^-,x\right)p_\gamma(x)d\Gamma(x)+n_\beta\left(x^-\right)\oint_\Gamma W^*_{3\beta3}\left(x^-,x\right)p_3(x)d\Gamma(x)\\
&-n_\beta(x^-)\int_\Omega\kappa_{\theta\psi}B\frac{1-\nu}{2}\left(u_{\theta,\psi}(X)+u_{\psi,\theta}(X)+\frac{2\nu}{1-\nu}u_{\phi,\phi}(X)\delta_{\theta\psi}\right)W^*_{3\beta3}\left(x^-,X\right)d\Omega(X)\\
&-n_\beta\left(x^-\right)\int_\Omega\kappa_{\theta\psi}B\left((1-\nu)\kappa_{\theta\psi}+\nu\delta_{\theta\psi}\kappa_{\phi\phi}\right)w_3(X)W^*_{3\beta3}\left(x^-,X\right)d\Omega(X)\\
&+n_\beta\left(x^-\right)\int_\Omega W^*_{3\beta3}\left(x^-,X\right)q_3d\Omega(X)
\end{aligned}\tag{2.90}$$

and

$$\begin{aligned}
&\frac{1}{2}t_\alpha\left(x^-\right) - \frac{1}{2}t_\alpha\left(x^+\right) + n_\beta\left(x^-\right)\fint_\Gamma T^*_{\alpha\beta\gamma}\left(x^-,x\right)u_\gamma(x)d\Gamma(x) \\
&+ n_\beta\left(x^-\right)\fint_\Gamma U^*_{\alpha\beta\gamma}\left(x^-,x\right)B\left[\kappa_{\theta\psi}(1-\nu)+\nu\delta_{\theta\psi}\kappa_{\phi\phi}\right]w_3(x)n_\psi(x)d\Gamma(x) \\
&- n_\beta\left(x^-\right)\int_\Omega U^*_{\alpha\beta\gamma}\left(x^-,X\right)B[\kappa_{\theta\psi}(1-\nu)+\nu\delta_{\theta\psi}\kappa_{\phi\phi}]w_{3,\beta}(X)d\Omega(X) \\
&= n_\beta\left(x^-\right)\fint_\Gamma U^*_{\alpha\beta\gamma}\left(x^-,x\right)t_\gamma(x)d\Gamma(x) + n_\beta\left(x^-\right)\int_\Omega U^*_{\alpha\beta\gamma}(x^-,X)q_\gamma d\Omega(X) \\
&+ \frac{1}{2}n_\beta\left(x^-\right)B\left[(1-\nu)\kappa_{\theta\psi}+\nu\delta_{\theta\psi}\kappa_{\phi\phi}\right]w_3\left(x^-\right)
\end{aligned} \tag{2.91}$$

Eq. (2.87) to (2.88) and Eq. (2.89) to (2.91) serve as the integral equations governing displacement and traction for collocation on the upper and lower boundaries of the crack, respectively. For the remaining boundaries denoted as Γ^e, collocation can be effectively performed by employing the boundary integral equations presented in Eq. (2.52) and (2.53).

It is important to note that Eq. (2.87) to (2.91) encompass the domain integral $\int_\Omega$. This domain integral can be transformed into a boundary integral via the application of the Dual Reciprocity Method (DRM). This process involves the utilization of the particular solutions, namely, ($\hat{u}^\gamma_{m\alpha}$, $\hat{t}^\gamma_{m\alpha}$), which are derived from solving the Galerkin vector for 2D plane stress, and ($\hat{w}^i_{m\alpha}$, $\hat{p}^i_{m\alpha}$) for plate bending problem, obtained through the implementation of radial basis functions. Detailed expressions for these particular solutions can be found in the Appendix B.

In order to address the improper integration that appears in the boundary integral equations, specialized regularization techniques were employed. Specifically, the terms such as $W^*_{\alpha\beta3}$, $W^*_{3\beta\gamma}$, and $Q^*_{3\beta}$ exhibit a singularity of order $O(\ln(r))$, denoting a weak singularity that can be effectively managed through the Telles transformation.

Moreover, integration of the terms P^*_{ij}, $T^*_{\theta\alpha}$, $P^*_{\alpha\beta3}$, $P^*_{3\beta\gamma}$, $W^*_{\alpha\beta\gamma}$, $W^*_{3\beta3}$, $P^*_{\alpha\beta\gamma}$ arises a strong singularity of order $O(1/r)$. This strong singularity can be appropriately addressed using the singularity subtraction method, based on the first term of Taylor expansion around the singularity point. Subsequently, the singularity term can be integrated analytically, with the aid of the Cauchy principal value.

Furthermore, the integration of $T^{(i)*}_{\alpha\beta\gamma}$ introduces a hypersingular term of order $O(1/r^2)$. The singularity subtraction method remains applicable in this case, incorporating both the first and second terms of the Taylor expansion around the singularity. Allowing for analytical integration via the

Hadamard principal value.

Lastly, for the remaining terms, namely, $P^*_{\alpha\beta\gamma}$ and $P^*_{3\beta3}$, which exhibit a singularity of order $O(1/r^2 + \ln(r))$, the separation approach is applied, effectively separating the hypersingular and weakly singular components and the corresponding regularization approach can be applied.

Comprehensive insights into the DRM formulation and the treatment of singularity are provided in the references [13] and [41].

2.2.5 Evaluation of the Stress Intensity Factors

Five fracture modes were taken into consideration for the shell problem. Among these modes, two are associated with membrane loads, while the remaining three are attributed to the effects of bending moment and shear load, as illustrated in Fig. 2.9.

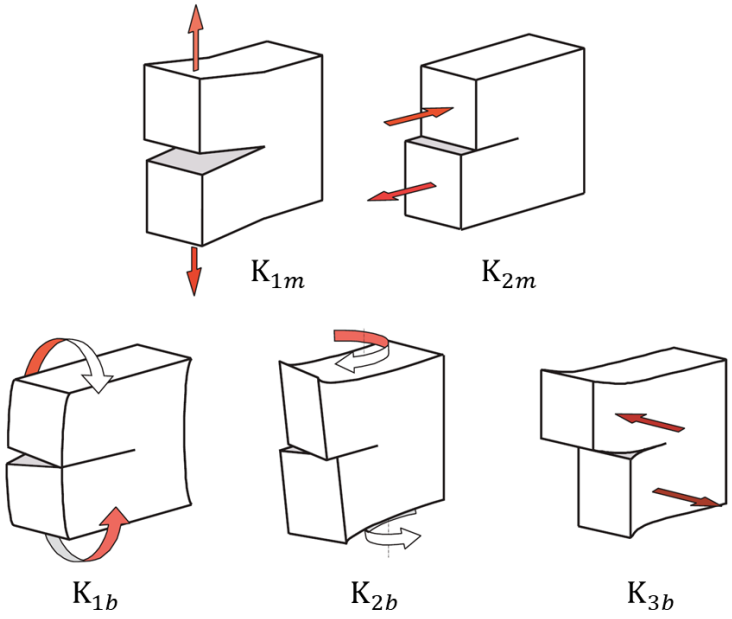


Figure 2.9: Fracture modes for the shell problem.

where the subscript m represents the membrane stress resultant intensity factors, while b denotes the bending stress resultant intensity factors. The formulation of stress intensity factors (SIFs) involves a coupling between the membrane stress resultant intensity factors and the bend-

ing stress resultant intensity factors through curvature, resulting in the following relationship:

$$\begin{aligned}
[1+\frac{x_3}{2}(\frac{1}{R_1}+\frac{1}{R_2})]K_I &= \frac{1}{h}K_{1m}+\frac{6}{h^2}K_{1b} \\
[1+\frac{x_3}{2}(\frac{1}{R_1}+\frac{1}{R_2})]K_{II} &= \frac{1}{h}K_{2m}+\frac{6}{h^2}K_{2b} \\
[1+\frac{x_3}{2}(\frac{1}{R_1}+\frac{1}{R_2})]K_{III} &= \frac{3}{2h}\left[1-\left(\frac{2x_3}{h}\right)^2\right]K_{3b}
\end{aligned} \tag{2.92}$$

Analysis has revealed that the maximum stress intensity factors (SIFs) were located at the upper and lower surfaces of the shell. In this work, the maximum SIF were evaluated at the upper surface by substituting $x_3 = h/2$ in the above equation. The crack surface displacement extrapolation technique (CSDE) has been employed in this study to assess the stress intensity factor at the crack tip.

2.2.5.1 The Crack Surface Displacement Extrapolation Technique (CSDE)

The stress intensity factor K can be expressed in relation to the displacements present on the crack surfaces adjacent to the crack tip, as follows:

$$\{K\} = \frac{1}{\sqrt{r}}[C]\{\Delta w\} \tag{2.93}$$

$$\{K\} = \begin{Bmatrix} K_{1b} \\ K_{2b} \\ K_{3b} \\ K_{1m} \\ K_{2m} \end{Bmatrix}, \quad \{\Delta w\} = \begin{Bmatrix} \Delta\phi_2 \\ \Delta\phi_1 \\ \Delta w_3 \\ \Delta u_2 \\ \Delta u_1 \end{Bmatrix} \tag{2.94}$$

where

$$\begin{Bmatrix} \Delta\phi_2 \\ \Delta\phi_1 \\ \Delta w_3 \\ \Delta u_2 \\ \Delta u_1 \end{Bmatrix} = \begin{Bmatrix} \phi_2 \\ \phi_1 \\ w_3 \\ u_2 \\ u_1 \end{Bmatrix}_{\theta=180^\circ} - \begin{Bmatrix} \phi_2 \\ \phi_1 \\ w_3 \\ u_2 \\ u_1 \end{Bmatrix}_{\theta=-180^\circ} \tag{2.95}$$

ϕ_α is the rotation in x and y direction respectively. w_3 is the out-of-plane displacement and u_α are the in-plane displacements in the x and y direction respectively. and

$$[\mathbf{C}] = \begin{bmatrix} \frac{Eh^3}{48}\sqrt{\frac{\pi}{2}} & 0 & 0 & 0 & 0 \\ 0 & \frac{Eh^3}{48}\sqrt{\frac{\pi}{2}} & 0 & 0 & 0 \\ 0 & 0 & \frac{5Eh}{24(1+\nu)}\sqrt{\frac{\pi}{2}} & 0 & 0 \\ 0 & 0 & 0 & \frac{Eh}{8}\sqrt{2\pi} & 0 \\ 0 & 0 & 0 & 0 & \frac{Eh}{8}\sqrt{2\pi} \end{bmatrix} \tag{2.96}$$

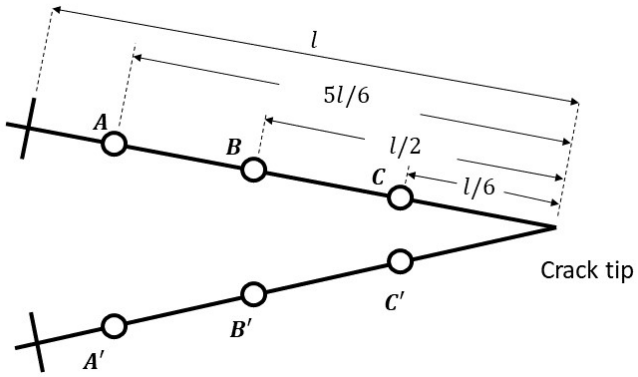


Figure 2.10: Example of crack tip nodal element.

An illustration of the crack tip element is presented in Figure 2.10. The crack tip stress intensity factors can be extrapolated from $\{K\}^{AA'}$ and $\{K\}^{BB'}$ by substituting the boundary displacements and rotation using equation 2.93, where:

$$\begin{aligned} \{K\}^{AA'} &= \sqrt{\frac{6}{5l}}[\mathbf{C}]\left(\{w\}^{A} - \{w\}^{A'}\right) \\ \{K\}^{BB'} &= \sqrt{\frac{2}{l}}[\mathbf{C}]\left(\{w\}^{B} - \{w\}^{B'}\right) \end{aligned} \tag{2.97}$$

where l is the crack tip element length. The value of the stress intensity factor at the crack tip can be extrapolated as:

$$\{K\}^{tip} = \frac{r_{AA'}}{r_{AA'} - r_{BB'}}\left(\{K\}^{BB'} - \frac{r_{BB'}}{r_{AA'}}\{K\}^{AA'}\right) \tag{2.98}$$

where $r_{AA'} = 5l/6$ and $r_{BB'} = l/2$. It is worth noting that the selection of points AA' BB' does

not necessarily need to take the same values as provided above. The stress intensity factors at the crack tip can be extrapolated from any point within the crack tip element by substituting the corresponding distance from the crack tip.

2.2.5.2 Crack Propagation Direction

Based on the stress intensity factors (SIFs) formulation provided in Eq.(2.92), it can be derived that the bending stress resultants vanish on the middle plane ($x_3 = 0$). Consequently, it is only the membrane stress resultants that exert an influence on the direction of crack propagation.
For the shell problem, the crack is assumed to propagate in the direction of maximum principal stress, where the direction θ can be determined by solving:

$$K_{Im} sin\theta + K_{IIm}(3cos\theta - 1) = 0 \tag{2.99}$$

The iterative scheme as described in the previous section 2.1 can be used to model the crack propagation.

Chapter 3

Reliability Analysis of Shallow Shell Structures

In structural analysis, modelling serves not only to faithfully replicate the physical behaviour of a structure but also it strives to construct a streamlined and viable model that can effectively incorporate uncertainties associated with geometry and loading parameters. The methods for developing such models have been elaborated in the previous chapter, while the main topic of this and the subsequent chapters is the application of these models for reliability analysis and fatigue life prediction.

In general, every engineering parameter carries an inherent level of uncertainty in its value. This uncertainty can arise from various sources, such as human error, environmental variables, and the imperfections inherent in manufacturing processes. Failing to account for these uncertainties can potentially lead to catastrophic structural failures. In the field of probability analysis, parameters are treated as having a certain degree of uncertainty, represented by probability distributions. This marks the difference from traditional approaches like the factor of safety, which measures structural safety in a deterministic way, such that variables related to the structures, loadings, and strength are assigned with an unknown conservative value about which there is no uncertainty. The consequence of this traditional approach is often an over-engineering of structures, as it treats parameters in a rigidly deterministic manner, offering limited insights into how individual parameters influence the overall system performance. In contrast, reliability analysis has emerged as a

tailored approach to address the stochastic nature of variables in the design process. Structural safety is determined through the calculation of the reliability index, which measures the probability of failure. This process involves defining a performance criterion for a structure and assessing the likelihood of successfully meeting this criterion.

The response of a structure to applied loads depends on both the material strength and the magnitude of the applied load. Whether this response aligns with the desired outcome depends on the specific requirements that the structure must meet. These requirements are termed limit states [54] and are categorized into three main types: 1) ultimate limit state, 2) serviceability limit state, and 3) fatigue limit state. The ultimate limit state predominantly concerns the loss of load-carrying capacity and often includes analyses related to phenomena like buckling. The serviceability limit state, meanwhile, focuses on excessive responses that, while not leading to structural failure, are often characterized by excessive deflection, permanent deformation, or the occurrence of cracks. The fatigue limit state, in contrast, is defined by the accumulation of damage within the structure under the influence of repeated loads [55]. In the context of the reliability analysis conducted in this work, the primary emphasis is on limit state type 2 in this chapter and type 3 in the subsequent chapter.

The application of reliability techniques to structural problems has been conducted by the research community with a diverse array of methods. Notable examples include the application of reliability analysis to diverse domains such as nano-structures [56], corrosion in pipelines [57], and bimaterial cracked structures [58]. In the field of reliability analysis, methodologies can be broadly classified into two categories: direct and indirect methods. Direct methods, such as Monte Carlo Simulations (MCS) [59], have been widely utilized. MCS entails the exploration of possible uncertainties through extensive sampling. Furthermore, the fusion of such sampling techniques with meta-modelling methods [60] has significantly contributed to enhancing computational efficiency. Indirect techniques, FORM and SORM, on the other hand, are approaches that rely on approximating the Limit State Function (LSF), which defines the boundary between the failure and safe regions of a structure. In FORM, the LSF is approximated through a first-order Taylor expansion, while SORM employs a second-order Taylor expansion for this purpose. For a more comprehensive insight into these methodologies, detailed information can be available in [6]. In

this study, FORM has been employed as the method for evaluating the reliability index of the structure, thereby providing a means to predict the probability of failure.

In the field of reliability analysis, the First-Order Reliability Method (FORM) has found extensive application. Notably, the Finite Element Method (FEM) has enjoyed extensive use with examples such as [61,62]. Moreover, the Boundary Element Method (BEM), characterized by its advantages in dimension reduction, has seen a growing adoption over recent decades. The BEM simplifies the problem by necessitating only the modelling of the outer boundaries of a structure, thereby reducing the system's dimension. The incorporation of reliability analysis and the BEM has found application across various domains, including addressing sensitivity issues in acoustic systems [63], assessing the impact of heat sensitivity of metals [64], resolving contact problems [65, 66], and plate bending problems [67]. The scope of reliability analysis extends beyond traditional safety design, encompassing applications in sensitivity analysis and design optimization processes. For instance, in [68], the Advanced First-Order Second Moment (AFOSM) method was applied to address 2D elastic problems, featuring analytically derived sensitivities. Moreover, reliability analysis has found extensive use in shape optimization problems that incorporate the BEM, including topology optimization challenges [69] and 2D anisotropic shape optimization problems [70].

When it comes to calculating the probability of failure using the First-Order Reliability Method (FORM), the sensitivity of the limit state function is required to be evaluated. This process involves determining how the response of the structure changes with respect to variations in design variables or loading conditions. In rare instances, these derivatives or sensitivities can be explicitly derived from the limit state function, as demonstrated in references such as [71, 72]. More commonly, numerical methods are employed to compute these derivatives. Various approaches have been utilized to determine the derivatives, including linearizing the limit state function and conducting **red**the Finite Difference Method (FDM) with Monte Carlo Simulations (MCS) to determine the sensitivity of the failure probability to the design parameters, or alternatively, employing surrogate models as discussed in [73] to replace the numerical model in the MCS. In [74], the derivatives were calculated using both the FDM and the Probabilistic Finite Element Method (PFEM). Notably, the Implicit Differentiation Method (IDM) has been developed to provide analytical derivatives of boundary integral equations within the Boundary Element Method (BEM), and details can be

found in [75]. Examples of practical applications can be found in [76–78].

Notable work on the application of the Boundary Element Method (BEM) in reliability analysis using both MCS and the First-Order Reliability Method (FORM) are elaborated in [76]. In this work, reliability analysis was conducted on a 2D electrostatic rectangular plate with a central aperture under uniaxial loading. The first-order sensitivities were determined using the Implicit Differentiation Method (IDM). The results exhibited a good agreement between the outcomes derived from FORM and those from MCS. The study took into consideration uncertainties associated with material properties and geometric variables. Similar applications can also be explored in [78], with specific relevance to the domain of shape optimization for plate structures [79].

Modern engineering structures, such as cylindrical walls, domes, and aircraft fuselages, are often best described as shell structures. These structural designs are well-suited for withstanding high loads, primarily experiencing membrane loading, all the while maintaining a lightweight profile. Thin or shallow shells, in particular, find widespread application due to their advantageous weight characteristics. Despite their application in engineering, the literature exploring reliability analysis with the Boundary Element Method (BEM) for shell structures is relatively limited. Notable examples include [80], which investigates shell truss structures using MCS, in [81], which incorporates surrogate modelling and reliability analysis for pressurized shells, and [82], which focuses on laminate composite shells. The most relevant work to date has concentrated on plate structures with the BEM, as demonstrated in [83] for plate bending problems and assembled plate structures in [84]. Notably, there have been no prior studies involving the reliability analysis of shell structures utilizing the BEM.

The primary innovation introduced in this chapter lies in the derivation of direct derivatives of the Boundary Element Method (BEM) formulations specifically applied to shallow-shell structures. This work represents the first time of these direct derivatives derived using an Implicit Differentiation Method (IDM). The utilization of IDM, coupled with the inherent advantages of the BEM, positions it as a highly efficient tool for structural reliability analysis. To validate the IDM, the sensitivities of structural responses for a shell structure, as determined by IDM, will be compared against sensitivities obtained through an analytical solution and those derived via the Finite Difference Method (FDM). Furthermore, an additional novel aspect of this study entails conducting

reliability analyses and Reliability-Based Design Optimization (RBDO) for a more complex shell structure, accounting for uncertainties related to geometry, material properties, and loading conditions. Both IDM and FDM will be deployed to assess the reliability index.

3.1 Fundamental Concept of Reliability Analysis

In reliability analysis, the probabilistic space defined by the random variables $\mathbf{Z}$ can be thought of as divided into two distinct domains: a safe region characterized by $g(\mathbf{Z}) > 0$ and a failure region where $g(\mathbf{Z}) < 0$. Where g is the limit state function (LSF). The function $g(\mathbf{Z}) = 0$ is the performance boundary that separates these regions. The LSF or performance function is typically constructed in terms of the structural resistance R and the structural demand $G(\mathbf{Z})$. Common examples of structural resistance include parameters such as yield strength, maximum allowable stress, or deflection. Mathematically, the performance function or limit state function (LSF) can be expressed as:

$$g(\mathbf{Z}) = R - G(\mathbf{Z}) \tag{3.1}$$

The probability of failure is defined as the probability that the performance function $g(\mathbf{Z}) \leq 0$ such that:

$$P_F = P\{g(\mathbf{Z}) < 0\} = \int_{g(\mathbf{Z})<0} f_Z(\mathbf{Z}) dZ \tag{3.2}$$

the reliability is defined by

$$P_R = 1 - P_F = P\{g(\mathbf{Z}) > 0\} = \int_{g(\mathbf{Z})>0} f_Z(\mathbf{Z}) dZ \tag{3.3}$$

In the given equation, P_F represents the failure probability while its complement P_R denotes the reliability, expressed as $1-P_F$. The equation involves an integration process over the domain where the function $g(\mathbf{Z}) > 0$. To facilitate a visual understanding of these integrations, these integrations can be visualized through the application of a Joint Probability Density Function (PDF) involving two random variables, as illustrated in Figure 3.1. The probability can be determined by computing the volume beneath the PDF surface $f_Z(\mathbf{Z})$, which corresponds to the region where $g(\mathbf{Z}) > 0$ for

reliability or $g(\mathbf{Z}) < 0$ for failure probability.

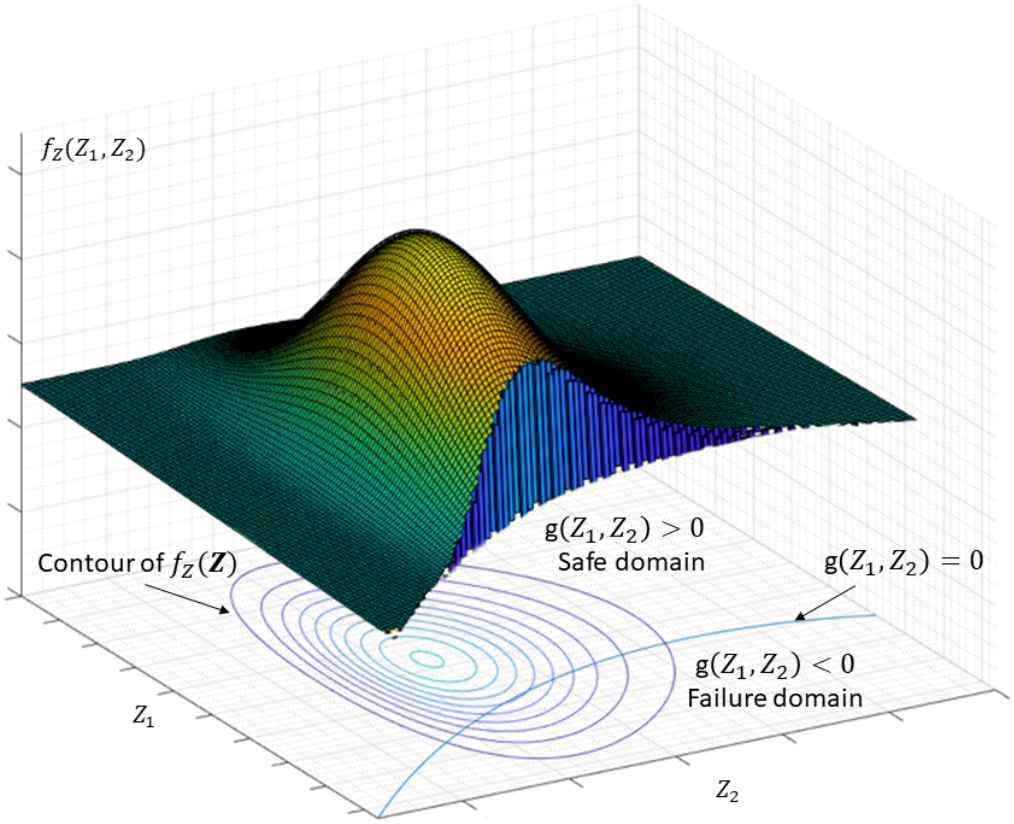


Figure 3.1: Example of joint Probability Density Function form by two random variables. The figure shows only the pdf corresponds to the safety region with the failure region removed (cut surface). The contour of the PDF is shown in the Z_1-Z_2 plane. The limit state function represents the boundary between the safe and failure domain.

Evaluating this integral can pose considerable challenges, particularly when dealing with a multidimensional design variable vector. There are three distinct methods available for the evaluation of the integrals presented in Eq. (3.2) and (3.3):

- Direct Integration: this requires analytical expression of the limit stat function, however, for complicated structural problems, the analytical solution is usually not available due to the high dimensionality.

- Approximation of Numerical Solution: Monte Carlo Simulation.

- Transformation of the Integrand and approximate the limit state function: methods that rely

on transforming the integrand to standard normal space where an iterative scheme can be applied for searching the approximate solution, hence avoiding the integration. This includes FORM, and SORM.

3.1.1 Monte Carlo Simulation (MCS)

Monte Carlo Simulation (MCS) entails the sampling of the possible value of each individual random variable, denoted as Z_i, followed by simulating the structural response based on the combination of these sampled variables. This process is iterated numerous times, and responses that result in the limit state being exceeded ($g(\mathbf{Z}) < 0$) are considered as 'failure'. Assuming that a total of N_{MCS} simulations have been carried out, the probability of failure can be calculated by:

$$p_f = \frac{n_{g(\mathbf{Z})<0}}{N_{MCS}} \tag{3.4}$$

where n is the number of failure responses observed during the repeated experiment trials. There are two main steps involved in the MCS includes:

1. Sampling the random variables Z_i
2. Determine the suitable number of N_{MCS} to have a reasonable estimation of p_f.

As it is impractical to obtain an infinite amount of sampling data, sampling methods are designed with the primary objective of achieving effective space-filling capabilities to ensure that the sample data effectively represents the entire parameter domain. In the case of simple problems characterized by a limited number of variables, conventional sampling methods such as random sampling are viable options. However, as the dimensionality of the problem increases, the computational demands associated with traditional random sampling methods become prohibitively high in order to generate a sufficient number of samples that adequately cover the entire domain defined by these variables. Alternatively, more sophisticated sampling strategies with Quasi-random nature, such as Latin Hypercube or Sobol sampling methods, can be deployed to address this issue. **red**Examples to demonstrate the space-filling capability of the three methods using 50 sampled points are given in Figure 3.2, where the samplings were generated by the MATLAB build-in func-

tions, namely, *rand* for random sampling, *lhsdesign* for Latin hypercube sampling and *sobolset* for Sobol sampling.

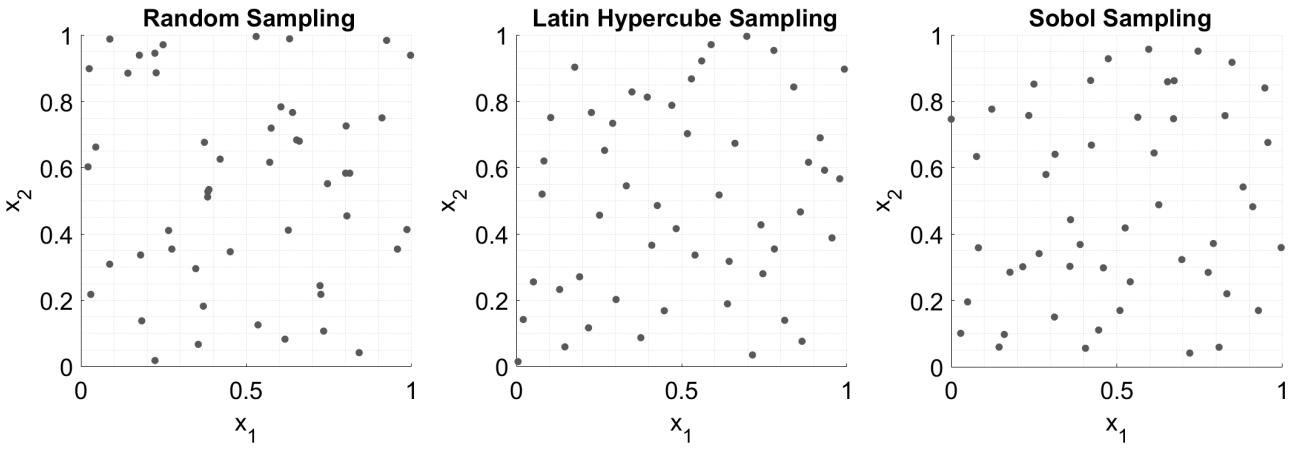


Figure 3.2: Comparison of Random sampling, Latin Hypercube sampling and Sobol sampling method of generating 50 sample points in a unit cube space.

It can be seen that both the Latin Hypercube sampling and Sobol sampling methods provide better space-filling ability compared to random sampling such that the points are more spread out evenly over the design space. Extensive research studies have been conducted to assess the efficiency of these two methods. Comprehensive information about the specific sampling techniques and the comparative analyses can be found in the following references: [85], [86], and [87]. Based on these investigations, it has been established that the Sobol sampling exhibits superior performance, particularly in terms of computational efficiency. Consequently, the Sobol sampling method has been chosen for Monte Carlo Simulation in this study. The Latin Hypercube sampling has been used for sampling in training the surrogate model as will be introduced in a later Chapter. The Sobol sampling procedure was implemented using the Matlab function *sobolset* and the Latin Hypercube sampling was implemented using the SUMO toolbox [88] with build in command for ranking and finding the optimal space-filling sampling strategy.

The appropriate number of simulations needed is determined by assessing the convergence of the probability of failure. This is accomplished by progressively increasing the number of simulations and monitoring the behavior of how the probability of failure, denoted as p_f, evolves with this increasing sample size. An illustrative example of how p_f changes with increasing N_{MCS} is given in Figure 3.3.

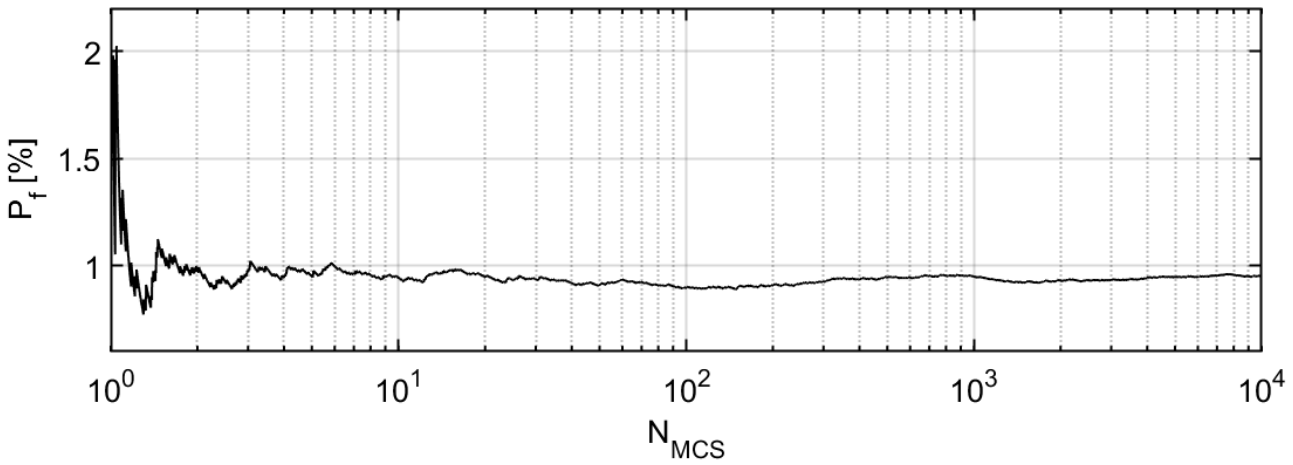


Figure 3.3: Convergence of the failure probability with an increasing amount of MCS samples used.

As the number of simulations increases, the probability of failure (p_f) tends to stabilize around a particular value. This phenomenon can be quantified and monitored using the coefficient of variation (COV). The COV is defined as the ratio of the standard deviation (σ_{p_f}) to the mean value (μ_{p_f}).

$$COV = \frac{\sigma_{p_f}}{\mu_{p_f}} \tag{3.5}$$

A lower COV reflects a decrease in the variability of the estimated failure probability. The degree of convergence required can be determined based on the desired COV. Figure 3.4 offers a visual representation of how the COV changes with an increase in the number of simulations, signified as N_{MCS}. The reduction in COV as N_{MCS} increases signifies that the probability of failure, p_f, is approaching convergence, resulting in decreased variation.

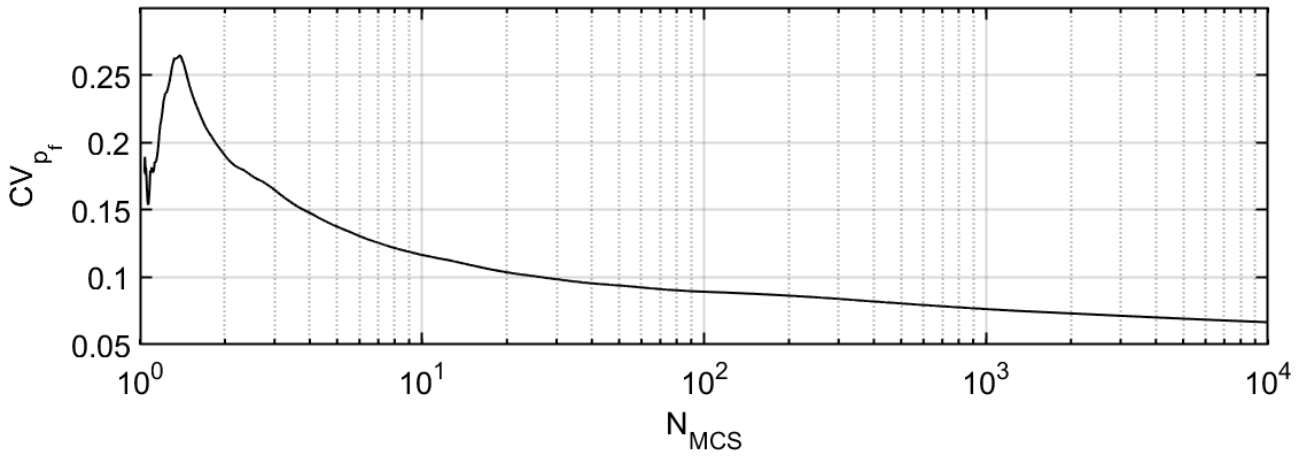


Figure 3.4: Coefficient of Variation for the failure probability with an increasing amount of MCS samples used.

3.1.2 The First Order Reliability Method (FORM)

The primary objective of the First Order Reliability Method (FORM) is to determine the reliability index, a crucial parameter that quantifies a structure's capacity to maintain safety throughout its operational lifespan. This index is linked to the probability of failure, providing a quantitative measure of the potential risk of structural collapse. To address the challenge associated with the evaluation of the integrals presented in Eq. (3.2) and (3.3), the FORM technique employs a transformation of the random variables into a standardized coordinate system known as the U-space. This transformation is achieved using the Rosenblatt transformation, which is described in [89]. As a result of this transformation, the variables within the U-space have a mean of 0 and a standard deviation of 1. The transformation can be represented as follows:

$$U_i = \Phi^{-1}\left[f_{Z_i}(Z_i)\right] \tag{3.6}$$

The transformations of various distribution types have been detailed, with particular emphasis on the normal distribution and the lognormal distribution. It's important to note that throughout this thesis, only these two distributions were taken into consideration, and their corresponding transformations can be found in the Appendix C. Following the transformation process, the Joint Probability Density Function (PDF) exhibits contour lines that take on the form of concentric cir-

cles, as demonstrated in Figure 3.5. These contours display a more regular pattern when compared to the original contour shown in Figure 3.1.

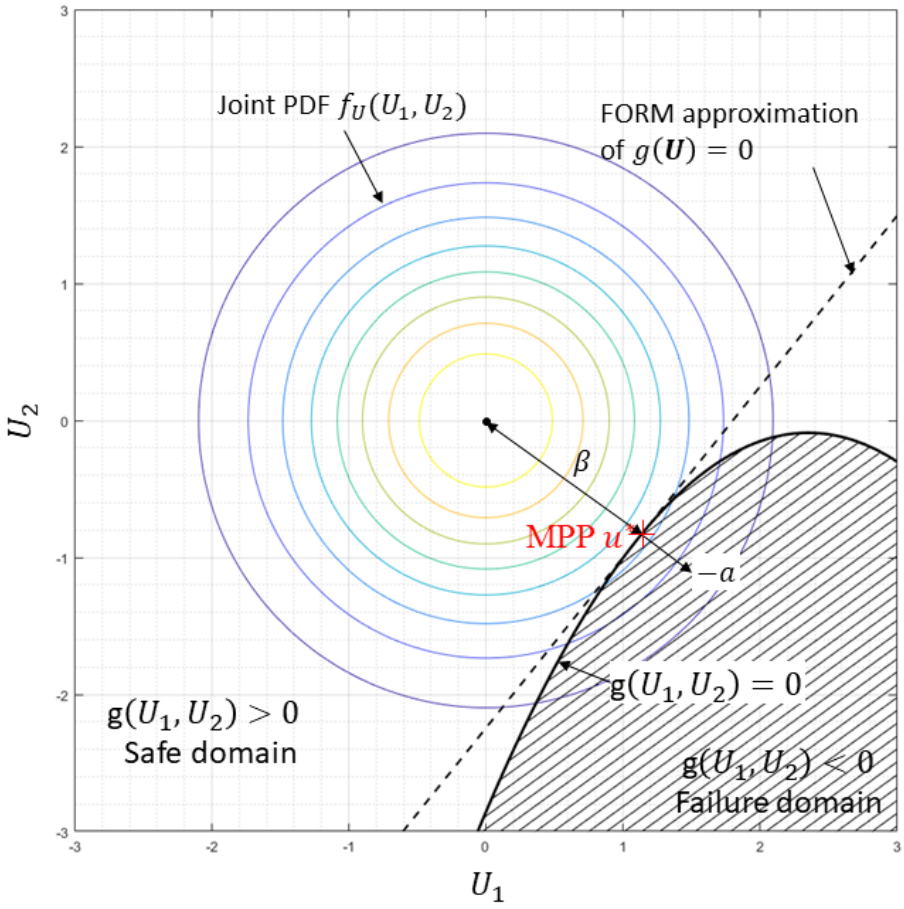


Figure 3.5: Contour of Joint pdf after the transformation into the U-space

Consequently, Eq. 3.2 is transformed into the **U**-space as:

$$P_F = P\{g(\mathbf{U}) \leq 0\} = \int_{g(\mathbf{U})\leq 0} f_U(\mathbf{U}) dU \tag{3.7}$$

The integration boundary i.e. LSF can be approximated by the first-order Taylor expansion. The FORM used linear approximation of the LSF as shown in Figure3.5 such that

$$g(\mathbf{U}) \approx g(\mathbf{u}^*) + \nabla g(\mathbf{u}^*)(\mathbf{U} - \mathbf{u}^*) \tag{3.8}$$

where u^* is the expansion point and $\nabla g(\mathbf{u}^*)$ is the gradient of $g(\mathbf{U})$ which defined as:

$$\nabla g(\mathbf{u}^*) = \left(\frac{\partial g(\mathbf{U})}{\partial U_1}, \frac{\partial g(\mathbf{U})}{\partial U_2}, ..., \frac{\partial g(\mathbf{U})}{\partial U_n} \right) \Bigg|_{\mathbf{u}^*} \tag{3.9}$$

To minimize the loss of accuracy resulting from the approximation, it is ideal to expand the approximation around the point that exerts the most influence on the integration. Further away from this critical point, the integration's impact diminishes. This pivotal point, known as the Most-Probable Point (MPP), is characterized by several key features. Notably, the MPP is situated at the shortest distance from the origin of the U-space, marked by $\beta = \| u^* \|$. Furthermore, it holds the highest probability density, making it the primary contributor to the integration. The specific location of the MPP is designated as u^* and is highlighted in Figure 3.5.

3.1.2.1 MPP searching Algorithm

In the process of locating the Most-Probable Point (MPP), an iterative gradient-based method known as the Hasofer-Lind-Rackwitz-Fiessler (HLRF) algorithm, as documented in [90] and [91], was employed. The formulation of this algorithm is derived based on the first-order Taylor expansion approximation, as outlined in Eq. (3.8). The recursive search process for the MPP is illustrated in the flowchart presented in Figure 3.6. The MPP at the k^{th} iteration is denoted as U^k, where

$$U^k = -\beta^k \mathbf{a}^k \tag{3.10}$$

where $\beta^k = \| U^k \|$ is the reliability index and is the magnitude of vector U^k and $\mathbf{a}^k$ is defined as

$$\mathbf{a}^k = \frac{\nabla g(\mathbf{U^k})}{\| \nabla g(\mathbf{U^k}) \|} \tag{3.11}$$

the vector $\mathbf{a}^k$ can be considered as a unit normal vector of the gradient and can be visualized in Figure3.5.

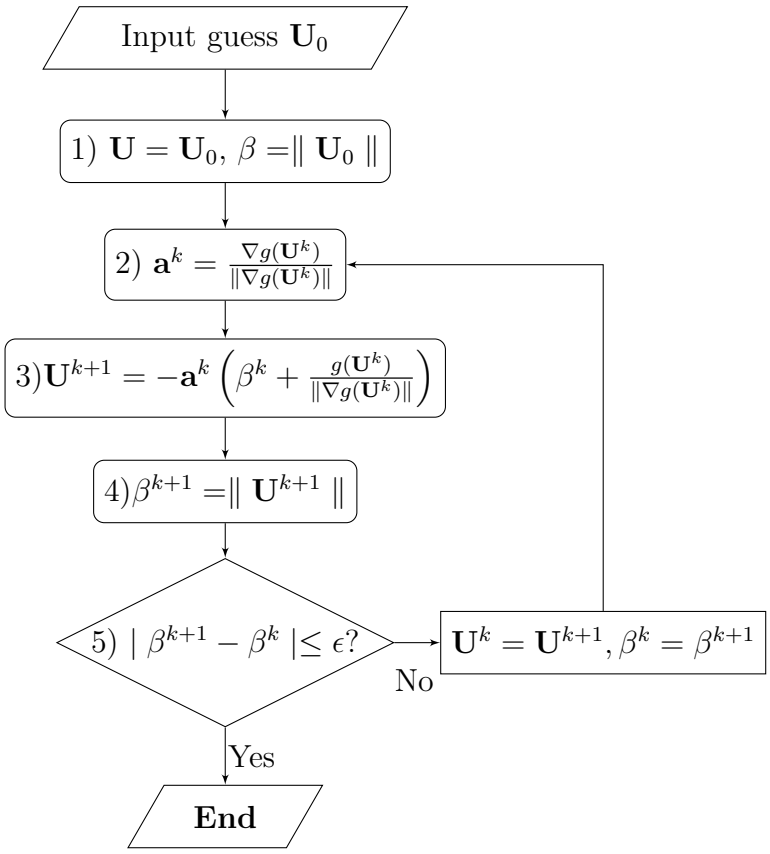


Figure 3.6: MPP search algorithm.

The algorithm requires an initial guess of the MPP location denoted as $U_0 = (U_1^0, U_2^0, ..., U_m^0)$, where m represents the number of variables in the limit state function. Typically, the mean values of the variables are chosen as the initial guess, resulting in $U_0 = (0, 0, ..., 0)$ in the U-space.

In step 5) of the MPP search procedure, the convergence of the reliability index, β, is verified, with an error tolerance of $\epsilon = 1 \times 10^{-2}$ being used.

In step 3), it is essential to obtain the response of the Limit State Function (LSF), denoted as $g(\mathbf{U^k})$. As previously discussed, the Boundary Element Method (BEM) serves as an effective tool for structural analysis and is thus employed to evaluate $g(\mathbf{U^k})$.

In step 2) involves the evaluation of the first-order derivative of the LSF. Commonly used methods for this purpose include the Improved Derivative Method (IDM) and the Finite Difference Method (FDM). Detailed formulations for these methods can be found in the following section.

Once the Most-Probable Point (MPP) is identified, the probability of failure and reliability can be computed as follows:

$$P_R = 1 - P_F = 1 - \Phi(-\beta) = \Phi(\beta) \tag{3.12}$$

where Φ is the standardised cumulative distribution function.

3.1.2.2 Second-Order Reliability Method (SORM)

A brief discussion of the Second Order Reliability Method (SORM) is provided here, as it typically yields more accurate results in comparison to the First Order Reliability Method (FORM). However, it's important to note that SORM is inherently more complex and demands greater computational resources. FORM has certain inherent limitations, primarily tied to the assumption that the exactness of the probability of failure depends on the linearity or near-linearity of the limit state function in the variable space, as demonstrated in Figure 3.7.

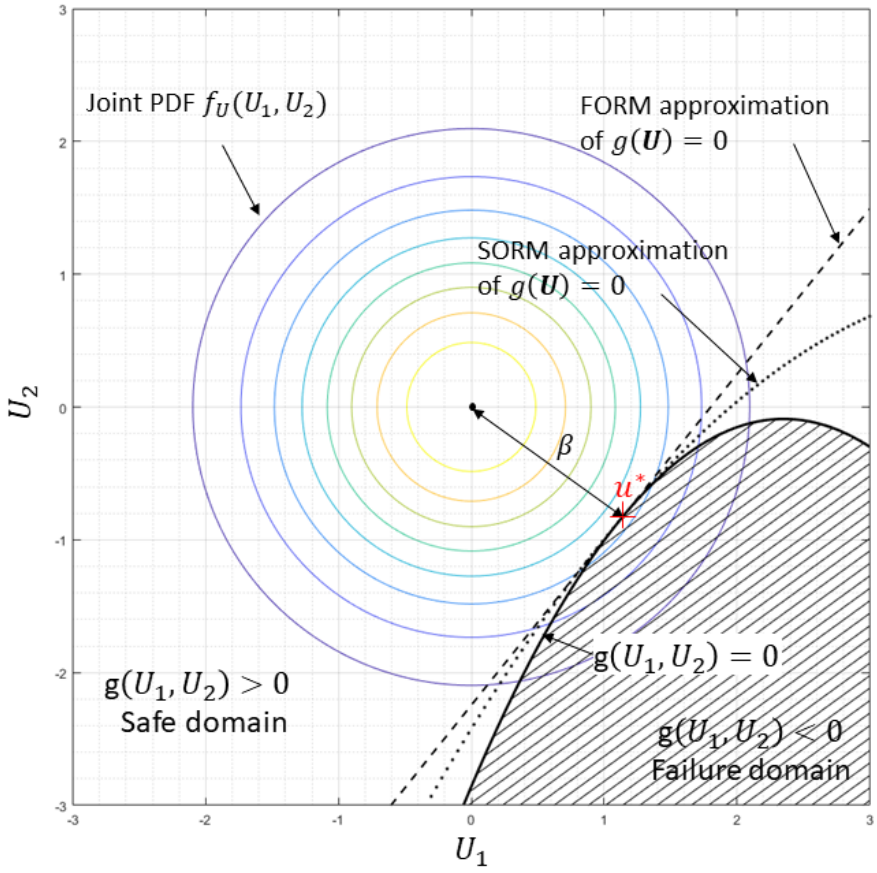


Figure 3.7: SORM approximation of the limit state function.

To enhance the accuracy of the First Order Reliability Method (FORM) results, methods such as the Second-Order Reliability Method (SORM) are preferred. SORM approximates the limit state function using a second-order Taylor expansion. It's important to note that SORM, in contrast to FORM, employs a second-order Taylor expansion for approximating the performance

function. Consequently, the approximation of the performance function differs from that presented in Eq. (3.8).

$$g(\mathbf{U}) \approx g(\mathbf{u}^*) + \nabla g(\mathbf{u}^*)(\mathbf{U} - \mathbf{u}^*)^T + \frac{1}{2}(\mathbf{U} - \mathbf{u}^*)\mathbf{H}(\mathbf{u}^*)(\mathbf{U} - \mathbf{u}^*)^T \tag{3.13}$$

where $\mathbf{H}(\mathbf{u}^*)$ is the Hessian matrix.

The First Order Reliability Method (FORM), when applied to problems involving multiple variables, requires the computation of first-order derivatives of the limit state function, resulting in an increased computational demand. This demand is even more pronounced for the Second-Order Reliability Method (SORM), where the calculation of second-order derivatives becomes a significant contributor to the computational cost.

However, it's important to note that while employing SORM does lead to an escalation in computational demand, as second-order derivatives must be computed in each reliability analysis, it is a trade-off for improved accuracy. In situations characterized by highly nonlinear limit state functions, convergence issues have been observed in Reliability-Based Design Optimization (RBDO). Nevertheless, the FORM has proven to be sufficiently accurate for the majority of static structures.

3.2 Methods for Calculating the Derivatives

In section 3.1.2, two methods for evaluating the derivatives necessary for approximating the Limit State Function (LSF) were discussed: the Implicit-Differentiation Method (IDM) and the Finite-Difference Method (FDM). The FDM is relatively straightforward to implement as it primarily relies on a finite difference scheme. However, the accuracy of the FDM is greatly influenced by the choice of the step size, and it often requires a prior convergence test to determine the optimal step size. In contrast, the IDM provides a more robust solution by directly deriving the derivatives from the formulations of the Boundary Element Method (BEM).

3.2.1 BEM-FDM formulation

The FDM involves estimation of the first-order derivatives of the LSF $g(\mathbf{Z})$ with respect to change in variables $\mathbf{Z}_i, i = 1, 2, ..., m$ where m is the numbers of variables that influence the LSF. The

derivatives for FDM can be expressed as:

$$\frac{\partial g(\mathbf{Z})}{\partial Z_i} = \frac{g(Z_i + \Delta Z_i, \mathbf{X}) - g(Z_i - \Delta Z_i, \mathbf{X})}{2\Delta Z_i} \tag{3.14}$$

In the presented expressions, ΔZ_i stands for the step size, while $\mathbf{X}$ represents the set of remaining variables, with Z_i excluded. It's important to note that the choice of step size significantly impacts the accuracy of the calculated derivatives. To address this, the step size was adaptively chosen based on the magnitude of the variable Z_i, resulting in $\Delta Z_i = Z_i \Delta Z_i'$, where $\Delta Z_i'$ denotes the normalized step size. The identification of the most suitable normalized step size involved a series of convergence tests to select the optimal value.

3.2.2 BEM-IDM Formulations for Shallow Shell Structures

The BEM-IDM formulation has been previously utilized for deriving derivatives in several earlier works, as documented in references such as [92], [93], [94], and [79]. Previous research efforts have primarily focused on developing the BEM-IDM formulation for various 2D problems and plate bending problems. Notably, while an IDM formulation was established for these cases, an IDM formulation for shallow shell structures had not yet been developed.

This section aims to introduce the IDM formulation of a shallow shell structure using the Boundary Element Method (BEM). The IDM results were initially validated by comparing them to analytical solutions and outcomes obtained through the Finite-Difference Method (FDM) for simple geometries. Subsequently, the IDM was applied to complex structures for reliability analysis, and the outcomes were compared against results obtained through the FDM-FORM and Monte Carlo Simulations (MCS).

As discussed in Chapter 2, the boundary integral equations are formulated based on the collocation of boundary nodal points. Consequently, only the parameters influencing the coordinates of these boundary nodal points were considered when deriving sensitivities using IDM. The first step in IDM involves approximating the derivatives of the boundary nodal point coordinates with respect

to changes in variables. This approximation can be determined by applying the FDM:

$$\frac{\partial x_{\alpha}^{n_e n_l}}{\partial Z_i} = x_{\alpha,m}^{n_e n_l} = \frac{x_{\alpha}^{n_e n_l}(Z_i + \Delta Z_i) - x_{\alpha}^{n_e n_l}(Z_i - \Delta Z_i)}{2\Delta Z_i} \tag{3.15}$$

where $x_{\alpha}^{n_e n_l}$ is the α coordinate of nodal point n_l in element n_e, hence the first order derivative of the boundary nodal point of an element n_e can be found by applying the shape function Φ defined in Eq.(2.19)

$$x_{\alpha,m}^{n_e}(\zeta) = \sum_{n_l=1}^{M} \Phi_{n_l}^{n_e}(\zeta) x_{\alpha,m}, \tag{3.16}$$

3.2.2.1 BEM-IDM Formulations for Shallow Shell Structures with Respect to a Geometrical Variable Z_g

This section introduces the BEM-IDM formulations for shallow shell structures with respect to certain design variables. The focus here is on presenting the derivatives of the displacement integral equations, represented by Eq. (2.52) to Eq. (2.53), with respect to a geometrical variable Z_g (e.g., shell width, length, radius, etc.). These derivatives can be expressed as follows

$$\begin{aligned}
&c_{ij}\left(x'\right) w_{j,g}\left(x'\right) + \int_{\Gamma} \left[P_{ij,g}^{*}\left(x', x\right) w_j(x) + P_{ij}^{*}\left(x', x\right) w_{j,g}(x)\right] d\Gamma(x) \\
&= \int_{\Gamma} \left[W_{ij,g}^{*}\left(x', x\right) p_j(x) + W_{ij}^{*}\left(x', x\right) p_{j,g}(x) d\Gamma(x)\right. \\
&- \int_{\Omega} W_{i3,g}^{*}\left(x', X\right) \kappa_{\alpha\beta} B \frac{1-\nu}{2} \left[u_{\alpha,\beta}(X) + u_{\beta,\alpha}(X) + \frac{2\nu}{1-\nu} u_{\phi,\phi}(X)\delta_{\alpha\beta}\right] d\Omega(X) \\
&- \int_{\Omega} W_{i3}^{*}\left(x', X\right) \kappa_{\alpha\beta} B \frac{1-\nu}{2} \left[u_{\alpha,\beta g}(X) + u_{\beta,\alpha g}(X) + \frac{2\nu}{1-\nu} u_{\phi,\phi g}(X)\delta_{\alpha\beta}\right] d\Omega(X) \\
&- \int_{\Omega} W_{i3,g}^{*}\left(x', X\right) \kappa_{\alpha\beta} B \left((1-\nu)\kappa_{\alpha\beta} + \nu\delta_{\alpha\beta}\kappa_{\phi\phi}\right) w_3(X) d\Omega(X) \\
&- \int_{\Omega} W_{i3}^{*}\left(x', X\right) \kappa_{\alpha\beta} B \left((1-\nu)\kappa_{\alpha\beta} + \nu\delta_{\alpha\beta}\kappa_{\phi\phi}\right) w_{3,g}(X) d\Omega(X) \\
&+ \int_{\Omega} \left[W_{i3,g}^{*}\left(x', X\right) q_3(X) + W_{i3}^{*}\left(x', X\right) q_{3,g}(X)\right] d\Omega(X)
\end{aligned} \tag{3.17}$$

and

$$
\begin{aligned}
&c_{\theta\alpha}\left(x'\right)u_{\alpha,g}\left(x'\right)+\oint_{\Gamma}\left[T^{*}_{\theta\alpha,g}\left(x',x\right)u_{\alpha}(x)+T^{*}_{\theta\alpha}\left(x',x\right)u_{\alpha,g}(x)\right]d\Gamma(x)\\
&+\int_{\Gamma}U^{*}_{\theta\alpha,g}\left(x',x\right)B\left[\kappa_{\alpha\beta}(1-\nu)+\nu\delta_{\alpha\beta}\kappa_{\phi\phi}\right]w_{3}(x)n_{\beta}(x)d\Gamma(x)\\
&+\int_{\Gamma}U^{*}_{\theta\alpha}\left(x',x\right)B\left[\kappa_{\alpha\beta}(1-\nu)+\nu\delta_{\alpha\beta}\kappa_{\phi\phi}\right]\left(w_{3,g}(x)n_{\beta}(x)+w_{3}(x)n_{\beta,g}(x)\right]d\Gamma(x)\\
&-\int_{\Omega}U^{*}_{\theta\alpha,g}\left(x',X\right)B\left[\kappa_{\alpha\beta}(1-\nu)+\nu\delta_{\alpha\beta}\kappa_{\phi\phi}\right]w_{3,\beta}(X)d\Omega(X)\\
&-\int_{\Omega}U^{*}_{\theta\alpha}\left(x',X\right)B\left[\kappa_{\alpha\beta}(1-\nu)+\nu\delta_{\alpha\beta}\kappa_{\phi\phi}\right]w_{3,\beta g}(X)d\Omega(X)\\
&=\int_{\Gamma}\left[U^{*}_{\theta\alpha,g}\left(x',x\right)t_{\alpha}(x)+U^{*}_{\theta\alpha}\left(x',x\right)t_{\alpha,g}(x)\right]d\Gamma(x)\\
&+\int_{\Omega}\left[U^{*}_{\theta\alpha,g}\left(x',X\right)q_{\alpha}(X)+U^{*}_{\theta\alpha}\left(x',X\right)q_{\alpha,g}(X)\right]d\Omega(X)
\end{aligned}
\tag{3.18}
$$

The definitions of the terms used in the equations are consistent with those presented in Eq. (2.52) and Eq. (2.53), where the notation $()_{,g}$ denotes the derivatives with respect to Z_g. Detailed expressions for the derivatives of the fundamental solutions can be found in Morse's work [83] for plate bending problems. These same expressions are applicable to shell structures. Additionally, it's worth noting that in Chapter 2, DRM coopering particular solutions are required to transfer the domain integral to boundary integral, expressions for the derivatives of the particular solutions for the DRM are introduced for the first time in this work and can be referenced in Appendix D.

The system of equations for the IDM-based BEM formulations is $\mathbf{H}_{,\mathbf{g}}\mathbf{u}+\mathbf{H}\mathbf{u}_{,\mathbf{g}}=\mathbf{G}_{,\mathbf{g}}\mathbf{t}+\mathbf{G}\mathbf{t}_{,\mathbf{g}}$, where the definitions of the terms $\mathbf{H}$, $\mathbf{G}$, $\mathbf{t}$, $\mathbf{u}$ are the same in the Section 2.2.2. The terms $\mathbf{H}_{,\mathbf{g}}$, $\mathbf{G}_{,\mathbf{g}}$, $\mathbf{t}_{,\mathbf{g}}$, $\mathbf{u}_{,\mathbf{g}}$ are the derivatives of these terms. Therefore, the system of equations can be rearranged as:

$$
\mathbf{A}\mathbf{X}_{,\mathbf{g}}=\mathbf{F}_{,\mathbf{g}}-\mathbf{A}_{,\mathbf{g}}\mathbf{X} \tag{3.19}
$$

The matrices $\mathbf{A}$ and $\mathbf{X}$ can be derived from Eq. (2.76). Therefore, the focus is primarily on evaluating the right-hand side of the equation. The boundary integral equations for displacement and traction are computed with respect to the nodal coordinates of collocation points and field points. The derivatives of these integral equations are linked to changes in nodal coordinates. Hence, when a change in the geometrical variable Z_g does not result in corresponding changes in

the nodal coordinates of both the collocation point and field point on a boundary, as described in Eq. (3.16) ($x^{n_e}_{\alpha,m} = 0$), the entries in $\mathbf{X}_{,\mathbf{g}}$ become zero. Consequently, the entries in $\mathbf{A}_{,\mathbf{g}}$ associated with this condition do not necessitate computation, resulting in a reduction in the computational cost of the Implicit-Differentiation Method (IDM).

3.2.2.2 BEM-IDM Formulations for Shallow Shell Structures with Respect to Curvature Z_ρ

In this work, derivatives of the shallow shell Boundary Element Method (BEM) formulations with respect to curvature Z_ρ were derived in a procedure similar to the approach described in the previous section. The curvatures considered in this research encompass only the curvatures in the x_1 and x_2 directions, with $\kappa_{11} \neq 0$, $\kappa_{22} \neq 0$, and $\kappa_{12} = \kappa_{21} = 0$. Consequently, the variable ρ can only take on the values of κ_{11} or κ_{22}. The derivatives of the curvature can be simplified as $\kappa_{\alpha\beta,\rho} = \delta_{\alpha\rho}\delta_{\beta\rho}$.The change in geometrical parameters does not affect the values of the curvature, therefore for simplification, denote the constant term $C_{\kappa 1} = B\left((1-\nu)\kappa_{\alpha\beta} + \nu\delta_{\alpha\beta}\kappa_{\phi\phi}\right)$.
The derivatives of the displacement integral equations related to rotations and out-of-plane displacement with respect to the curvature Z_ρ are expressed as:

$$
\begin{aligned}
& c_{ij}\left(x'\right) w_{j,\rho}\left(x'\right) + \oint_\Gamma P^*_{ij}\left(x', x\right) w_{j,\rho}(x) d\Gamma(x) = \int_\Gamma W^*_{ij}\left(x', x\right) p_{j,\rho}(x) d\Gamma(x) \\
& - \int_\Omega W^*_{i3}\left(x', X\right) \kappa_{\alpha\beta,\rho} B \frac{1-\nu}{2} \left[u_{\alpha,\beta}(X) + u_{\beta,\alpha}(X) + \frac{2\nu}{1-\nu} u_{\phi,\phi}(X)\delta_{\alpha\beta} \right] d\Omega(X) \\
& - \int_\Omega W^*_{i3}\left(x', X\right) \kappa_{\alpha\beta} B \frac{1-\nu}{2} \left[u_{\alpha,\beta\rho}(X) + u_{\beta,\alpha\rho}(X) + \frac{2\nu}{1-\nu} u_{\phi,\phi\rho}(X)\delta_{\alpha\beta} \right] d\Omega(X) \\
& - \int_\Omega W^*_{i3}\left(x', X\right) \left[\kappa_{\alpha\beta,\rho} C_{\kappa 1} w_3(X) + \kappa_{\alpha\beta} C_{\kappa 1,\rho} w_3(X) + \kappa_{\alpha\beta} C_{\kappa 1} w_{3,\rho}(X) \right] d\Omega(X) \\
& + \int_\Omega W^*_{i3}\left(x', X\right) q_{3,\rho}(X) d\Omega(X)
\end{aligned}
\tag{3.20}
$$

where $C_{\kappa 1,\rho} = B\left[\kappa_{\alpha\beta,\rho}(1-\nu) + \nu\delta_{\alpha\beta}\kappa_{\phi\phi,\rho}\right]$. The derivatives of the in-plane displacement integral equation are:

$$\begin{aligned} & c_{\theta\alpha}\left(x'\right) u_{\alpha,\rho}\left(x'\right) + \oint_{\Gamma} T^{*(i)}_{\theta\alpha}\left(x', x\right) u_{\alpha,\rho}(x) d\Gamma(x) \\ & + \int_{\Gamma} U^{*}_{\theta\alpha}\left(x', x\right)\left[C_{\kappa 1,\rho} w_3(x) + C_{\kappa 1} w_{3,\rho}(x)\right] n_{\beta}(x) d\Gamma(x) \\ & - \int_{\Omega} U^{*}_{\theta\alpha}\left(x', X\right)\left[C_{\kappa 1,\rho} w_{3,\beta}(X) + C_{\kappa 1} w_{3,\beta\rho}(X)\right] d\Omega(X) \\ & = \int_{\Gamma} U^{*}_{\theta\alpha}\left(x', x\right) t_{\alpha,\rho}(x) d\Gamma(x) + \int_{\Omega} U^{*}_{\theta\alpha}\left(x', X\right) q_{\alpha,\rho}(X) d\Omega(X) \end{aligned} \tag{3.21}$$

The formation of the system of equations can be evaluated in a similar way as in section 3.2.2:

$$\mathbf{A}\mathbf{X}_{,\rho} = \mathbf{F}_{,\rho} - \mathbf{A}_{,\rho}\mathbf{X} \tag{3.22}$$

It's important to note that a change in curvature does not induce any changes in the nodal coordinates of the source and field points. However, it does result in modifications in the integration term, particularly with regard to curvature-related coefficients. Given that the particular solutions do not incorporate curvature-related coefficients, the derivatives of the particular solutions with respect to curvature are effectively zero. As a result, the sole aspect requiring an update in the system of equations is the term associated with the curvature coefficient.

3.2.2.3 BEM-IDM Formulations for Shallow Shell Structures with Respect to Thickness Z_h

In this study, the derivatives of the shallow shell Boundary Element Method (BEM) formulations concerning the shell thickness Z_h were derived. This derivation process is conducted similarly to the IDM formulation for plate thickness derivatives proposed in [79]. However, it is important to note that an additional curvature-related term is introduced into the boundary integral equations for shallow shell structure compared to the plate formulation.

The derivatives of the displacement integral equations for rotations and out-of-plane displacements,

with respect to the thickness variable Z_h, are expressed as:

$$
\begin{aligned}
&c_{ij}\left(x'\right) w_{j,h}(x') + \fint_{\Gamma} \left[P^*_{ij,h}\left(x', x\right) w_j(x) + P^*_{ij}\left(x', x\right) w_{j,h}(x)\right] d\Gamma(x) \\
&= \int_{\Gamma} \left[W^*_{ij,h}\left(x', x\right) p_j(x) + W^*_{ij}\left(x', x\right) p_{j,h}(x)\right] d\Gamma(x) \\
&- \int_{\Omega} \left[W^*_{i3,h}\left(x', X\right) B + W^*_{i3}\left(x', X\right) B_{,h}\right] \kappa_{\alpha\beta} \frac{1-\nu}{2} \left[u_{\alpha,\beta}(X) + u_{\beta,\alpha}(X) + \frac{2\nu}{1-\nu} u_{\phi,\phi}(X)\delta_{\alpha\beta}\right] d\Omega(X) \\
&- \int_{\Omega} W^*_{i3}\left(x', X\right) \kappa_{\alpha\beta} B \frac{1-\nu}{2} \left[u_{\alpha,\beta h}(X) + u_{\beta,\alpha h}(X) + \frac{2\nu}{1-\nu} u_{\phi,\phi}(X)\delta_{\alpha\beta h}\right] d\Omega(X) \\
&- \int_{\Omega} W^*_{i3}\left(x', X\right) \kappa_{\alpha\beta} B \left((1-\nu)\kappa_{\alpha\beta} + \nu\delta_{\alpha\beta}\kappa_{\phi\phi}\right) w_{3,h}(X) d\Omega(X) \\
&- \int_{\Omega} \left[W^*_{i3,h}\left(x', X\right) B + W^*_{i3}\left(x', X\right) B_{,h}\right] \kappa_{\alpha\beta} \left((1-\nu)\kappa_{\alpha\beta} + \nu\delta_{\alpha\beta}\kappa_{\phi\phi}\right) w_3(X) d\Omega(X) \\
&+ \int_{\Omega} W^*_{i3,h}\left(x', X\right) q_3(X) d\Omega(X)
\end{aligned}
\tag{3.23}
$$

The derivative of the in-plane displacement integral equations are:

$$
\begin{aligned}
&c_{\theta\alpha}\left(x'\right) u_{\alpha,h}\left(x'\right) + \fint_{\Gamma} \left[T^{*(i)}_{\theta\alpha,h}\left(x', x\right) u_{\alpha}(x) + T^{*(i)}_{\theta\alpha}\left(x', x\right) u_{\alpha,h}(x)\right] d\Gamma(x) \\
&+ \int_{\Gamma} \left[U^*_{\theta\alpha,h}\left(x', x\right) B + U^*_{\theta\alpha}\left(x', x\right) B_{,h}\right] \left[\kappa_{\alpha\beta}(1-\nu) + \nu\delta_{\alpha\beta}\kappa_{\phi\phi}\right] w_3(x) n_{\beta}(x) d\Gamma(x) \\
&+ \int_{\Gamma} U^*_{\theta\alpha}\left(x', x\right) B \left[\kappa_{\alpha\beta}(1-\nu) + \nu\delta_{\alpha\beta}\kappa_{\phi\phi}\right] w_{,h}(x) n_{\beta}(x) d\Gamma(x) \\
&- \int_{\Omega} \left[U^*_{\theta\alpha,h}\left(x', X\right) B + U^*_{\theta\alpha}\left(x', X\right) B_{,h}\right] \left[\kappa_{\alpha\beta}(1-\nu) + \nu\delta_{\alpha\beta}\kappa_{\phi\phi}\right] w_{3,\beta}(X) d\Omega(X) \\
&- \int_{\Omega} U^*_{\theta\alpha}\left(x', X\right) B \left[\kappa_{\alpha\beta}(1-\nu) + \nu\delta_{\alpha\beta}\kappa_{\phi\phi}\right] w_{3,\beta h}(X) d\Omega(X) \\
&= \int_{\Gamma} \left[U^*_{\theta\alpha,h}\left(x', x\right) t_{\alpha}(x) + U^*_{\theta\alpha}\left(x', x\right) t_{\alpha,h}(x)\right] d\Gamma(x) \\
&+ \int_{\Omega} U^*_{\theta\alpha,h}\left(x', X\right) q_{\alpha}(X) d\Omega(X)
\end{aligned}
\tag{3.24}
$$

3.2.2.4 Evaluation of the Von Mises Stress Sensitivity and Boundary Stress Resultants Sensitivity

In this section, the derivatives of the boundary stress resultants are presented, which were discussed in the previous section, concerning geometrical variables, curvature, and thickness. The derivatives of the bending stress resultants $M_{\alpha\beta}$ and shear stress resultants Q_{α} for plates have been previously derived in the existing literature with respect to the geometrical variables [79, 95, 96] and thickness

[79]. These equations can be equally applied to shells. However, it's worth noting that the derivatives of the membrane stress resultants $N_{\alpha\beta}$ for shells differ from those for plates. The derivatives of the membrane stress resultants $N_{\alpha\beta}$ for shells are presented for the first time in this work.

The derivatives of the bending stress resultants $M_{\alpha\beta}$, as outlined in Eq. (2.79), with respect to a geometrical variable Z_g, can be computed as:

$$\begin{aligned} \hat{M}_{1\alpha,g} &= \hat{p}_{\alpha,g} \\ \hat{M}_{22,g} &= \nu \hat{M}_{11,g} + D\left(1-\nu^2\right)\hat{\chi}_{22,g} \end{aligned} \tag{3.25}$$

where

$$\hat{\chi}_{22,g} = \frac{1}{J(\zeta)}\left[e_{2\alpha,g}\sum\left(\hat{w}_\alpha\left(\frac{dN(\zeta)}{d\zeta}\right)\right) - J_{,g}(\zeta)\hat{\chi}_{22} + e_{2\alpha}\sum\left(\hat{w}_{\alpha,g}\left(\frac{dN(\zeta)}{d\zeta}\right)\right]\right. \tag{3.26}$$

The above equation is summed over the nodal point of each element, for simplification, the above and below equations do not include the nodal and element index. For a detailed representation of the summation refer to the work by Morse [79]. The derivatives of the shearing stress resultants $Q_{\alpha\beta}$, as outlined in Eq. (2.83), with respect to a geometrical variable Z_g, can be computed as:

$$\begin{aligned} \hat{Q}_{1,g} &= \hat{p}_{3,g} \\ \hat{Q}_{2,g} &= \frac{D(1-\nu)\lambda^2}{2}\left[w_{2,g} + \frac{1}{J(\zeta)}\sum\left(w_{3,g}\left(\frac{dN(\zeta)}{d\zeta}\right)\right) - \frac{J_{,g}(\zeta)}{J^2(\zeta)}\sum\left(w_3\left(\frac{dN(\zeta)}{d\zeta}\right)\right)\right] \end{aligned} \tag{3.27}$$

The derivatives of the membrane stress resultants $N_{\alpha\beta}$, as outlined in Eq. (2.81), with respect to a geometrical variable Z_g, can be computed as:

$$\begin{aligned} \hat{N}_{1\alpha,g} &= \hat{t}_{\alpha,g} \\ \hat{N}_{22,g} &= \frac{1}{1-\nu}\left[\nu\hat{t}_{1,g} + \frac{Eh}{1+v}\hat{\varepsilon}_{22,g}\right] + B\left(\nu\kappa_{11}+\kappa_{22}\right)\hat{w}_{3,g} \end{aligned} \tag{3.28}$$

where

$$\hat{\varepsilon}_{22,g} = \frac{1}{J(\zeta)}\left[e_{2\alpha,g}\sum\left(\hat{u}_\alpha\left(\frac{dN(\zeta)}{d\zeta}\right)\right) - J_{,g}(\zeta)\hat{\varepsilon}_{22} + e_{2\alpha}\sum\left(\hat{u}_{\alpha,g}\left(\frac{dN(\zeta)}{d\zeta}\right)\right]\right. \tag{3.29}$$

The corresponding IDM formulations for stress couples $\sigma_{\alpha\beta}$ in Eq.(2.44) with respect to Z_g at the top surface $x_3 = h/2$ can be derived as:

$$\begin{aligned}\sigma_{\alpha\beta,g} &= \left(\frac{1}{h}N_{\alpha\beta,g} + \frac{b}{h^2}M_{\alpha\beta,g}\right) / \left(1 + \frac{h}{2}\kappa_\gamma\right) \\ \sigma_{\alpha 3,g} &= \frac{3}{2h}Q_{\alpha,g} / \left(1 + \frac{h}{2}\kappa_\gamma\right)\end{aligned} \tag{3.30}$$

The derivatives of the bending stress resultants $M_{\alpha\beta}$, as outlined in Eq. (2.79), with respect to a curvature Z_ρ, can be computed as:

$$\begin{aligned}\hat{M}_{1\alpha,\rho} &= \hat{p}_{\alpha,\rho} \\ \hat{M}_{22,\rho} &= \nu\hat{M}_{11,\rho} + D\left(1-\nu^2\right)\hat{\chi}_{22,\rho}\end{aligned} \tag{3.31}$$

where

$$\hat{\chi}_{22,\rho} = \frac{e_{2\alpha}}{J(\zeta)}\sum\left(\hat{w}_{\alpha,\rho}\left(\frac{dN(\zeta)}{d\zeta}\right)\right) \tag{3.32}$$

The derivatives of the shearing stress resultants Q_α, as outlined in Eq. (2.83), with respect to a geometrical variable Z_ρ, can be computed as:

$$\begin{aligned}\hat{Q}_{1,\rho} &= \hat{p}_{3,\rho} \\ \hat{Q}_{2,\rho} &= \frac{D(1-\nu)\lambda^2}{2}\left[w_{2,\rho} + \frac{1}{J(\zeta)}\sum\left(w_{3,\rho}\left(\frac{dN(\zeta)}{d\zeta}\right)\right)\right]\end{aligned} \tag{3.33}$$

The derivatives of the membrane stress resultant in Eq.(2.81) with respect to a curvature Z_ρ can be evaluated as:

$$\begin{aligned}\hat{N}_{1\alpha,\rho} &= \hat{t}_{\alpha,\rho} \\ \hat{N}_{22,\rho} &= \frac{1}{1-v}\left[v\hat{t}_{1,\rho}\frac{Eh}{1+v}\hat{\epsilon}_{22,\rho}\right] + B\left(\nu\kappa_{11,\rho} + \kappa_{22,\rho},\right)\hat{w}_3 + B\left(\nu\kappa_{11} + \kappa_{22}\right)\hat{w}_{3,\rho}\end{aligned} \tag{3.34}$$

where

$$\hat{\varepsilon}_{22,\rho} = \frac{e_{2\alpha}}{J(\zeta)}\sum_{i=1}^{M}\left(\hat{u}_{\alpha,\rho}\left(\frac{dN(\zeta)}{d\zeta}\right)\right) \tag{3.35}$$

The corresponding IDM formulations for stress couples $\sigma_{\alpha\beta}$ in Eq.(2.44) with respect to Z_ρ at the

top surface can be derived as:

$$\begin{aligned}\sigma_{\alpha\beta,\rho} &= \left(\frac{1}{h}N_{\alpha\beta,\rho} + \frac{6}{h^2}M_{\alpha\beta,\rho}\right) / \left(1 + \frac{h}{2}\kappa_\gamma\right) - \sigma_{\alpha\beta}h/(2 + h\kappa_\gamma) \\ \sigma_{\alpha 3,\rho} &= \frac{3}{2h}Q_{\alpha,\rho} / \left(1 + \frac{h}{2}\kappa_\gamma\right) - \sigma_{\alpha 3}h/(2 + h\kappa_\gamma)\end{aligned} \tag{3.36}$$

The derivatives of the bending stress resultants in Eq.(2.79) with respect to thickness Z_h can be evaluated as:

$$\begin{aligned}\hat{M_{1\alpha,h}} &= \hat{p}_{\alpha,h} \\ \hat{M_{22,h}} &= \nu\hat{M_{11,h}} + D_{,h}\left(1-\nu^2\right)\hat{\chi}_{22} + D\left(1-\nu^2\right)\hat{\chi}_{22,h}\end{aligned} \tag{3.37}$$

where

$$\hat{\chi}_{22,h} = \frac{e_{2\alpha}}{J(\zeta)}\sum\left(\hat{w}_{\alpha,h}\left(\frac{dN(\zeta)}{d\zeta}\right)\right) \tag{3.38}$$

The derivatives of the shearing stress resultants in Eq.(2.83) with respect to thickness Z_h can be evaluated as:

$$\begin{aligned}\hat{Q_{1,h}} &= \hat{p_{3,h}} \\ \hat{Q}_{2,h} &= \frac{D_{,h}(1-\nu)\lambda^2}{2}\left[w_2 + \frac{1}{J(\zeta)}\sum\left(w_3\left(\frac{dN(\zeta)}{d\zeta}\right)\right)\right] \\ &+ \frac{2D(1-\nu)\lambda\lambda_{,h}}{2}\left[w_2 + \frac{1}{J(\zeta)}\sum\left(w_3\left(\frac{dN(\zeta)}{d\zeta}\right)\right)\right] \\ &+ \frac{D(1-\nu)^2}{2}\left[w_{2,h} + \frac{1}{J(\zeta)}\sum\left(w_{3,h}\left(\frac{dN(\zeta)}{d\zeta}\right)\right)\right]\end{aligned} \tag{3.39}$$

The derivatives of the membrane stress resultants in Eq.(2.81) with respect to thickness Z_h can be evaluated as:

$$\begin{aligned}\hat{N}_{1\alpha,h} &= \hat{t}_{\alpha,h} \\ \hat{N}_{22,h} &= \frac{1}{1-v}\left[\nu\hat{t}_{1,h} + \frac{Eh}{1+v}\hat{\varepsilon}_{22,h} + \frac{E}{1+v}\hat{\varepsilon}_{22}\right] + B\left(\nu\kappa_{11} + \kappa_{22}\right)\hat{w}_{3,h} + B_{,h}\left(v\kappa_{11} + \kappa_{22}\right)\hat{w}_3\end{aligned}$$

where

$$\hat{\varepsilon}_{22,h} = \frac{e_{2\alpha}}{J(\zeta)}\sum_{i=1}^{M}\left(\hat{u}_{\alpha,h}\left(\frac{dN(\zeta)}{d\zeta}\right)\right) \tag{3.40}$$

The corresponding IDM formulations for stress couples $\sigma_{\alpha\beta}$ in Eq.(2.44) with respect to Z_h at

the top surface can be derived as:

$$\begin{aligned}\sigma_{\alpha\beta,h} &= \left(\frac{6}{h^2}M_{\alpha\beta,h} + \frac{1}{h}N_{11,h} - \frac{12}{h^3}M_{\alpha\beta} - \frac{1}{h^2}N_{\alpha\beta}\right) / \left(1 + \frac{h}{2}\kappa_\gamma\right) - \sigma_{\alpha\beta}\kappa_\gamma/(2 + h\kappa_\gamma) \\ \sigma_{\alpha 3,h} &= \frac{3}{2}Q_{\alpha,h}/(1 + \frac{h}{2}\kappa_\gamma) - \sigma_{\alpha 3}/h - \sigma_{\alpha 3}\kappa_\gamma/(2 + h\kappa_\gamma)\end{aligned} \tag{3.41}$$

where $\kappa_\gamma = 1/R_\gamma$. The detailed IDM formulations for $M_{\alpha\beta,g}$, $M_{\alpha\beta,\rho}$, $M_{\alpha\beta,h}$ and $Q_{\alpha,g}$, $Q_{\alpha,\rho}$, and $Q_{\alpha,h}$ can be found in Appendix E.

The IDM formulations for the Von Mises stress can therefore be derived as:

$$\sigma_{v,m} = \frac{1}{2\sigma_v}\left[(\sigma_{11} - \sigma_{22})(\sigma_{11,m} - \sigma_{22,m}) + \sigma_{22}\sigma_{22,m} + \sigma_{11}\sigma_{11,m} + 12(\sigma_{23}\sigma_{23,m} + \sigma_{31}\sigma_{31,m} + \sigma_{12}\sigma_{12,m})\right] \tag{3.42}$$

where the subscript "$,m$" indicates a derivative with respect to a geometrical variable, curvature, or thickness.

3.3 Numerical Examples

The proposed BEM-IDM formulations are applied in numerical examples in this section, each demonstrating their application in reliability analysis. To commence, Section 3.3.1 provides a validation of the proposed derivatives against the analytical solution. Here, the IDM is compared against an analytical example featuring a hemispherical dome, serving as a verification of the formulation's accuracy. Section 3.3.2 delves into a more complex shell structure employed for reliability analysis, presenting also the results of the sensitivity analysis. Building on the insights gained from this sensitivity analysis, Section 3.3.4 details an optimization procedure performed based on the results. In the last numerical example, involving additional geometrical parameters was used with Reliability-based Design Optimization (RBDO). This example further illustrates the practical applications of the BEM-IDM formulations.

3.3.1 Analytical Validation of the BEM-IDM Formulation

Validation of the accuracy of the derived BEM-IDM formulations for sensitivity calculations is a fundamental requirement. To commence this validation process, the IDM results are first compared

with an analytical solution, as outlined in [97]. The focus of this validation is a hemispherical shell subjected to normal pressure. The hemispherical shell is simply supported along the edge of its circular base and is characterized by a radius of curvature R and a thickness h, and it experiences a uniform pressure of $p = 10\,\mathrm{kN/m^2}$ in the out-of-plane direction. The material properties of the shell are defined by a Young's modulus of $E = 2.0 \times 10^7\,\mathrm{kN/m^2}$ and a Poisson's ratio of $\nu = 0.1$. The curvature of the shell is calculated as $\kappa_{11} = \kappa_{22} = 1/R$. The geometric configuration is visually represented in Figure 3.8.

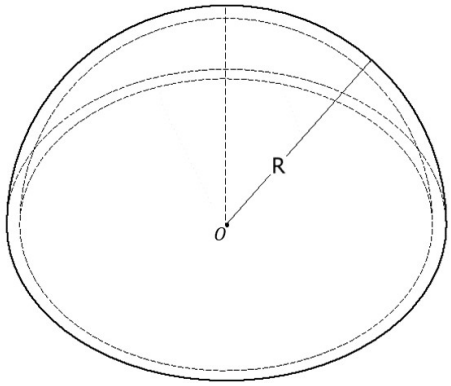


Figure 3.8: Hemispherical shell under normal pressure with radius of curvature R.

The out-of-plane displacement at the center of the shell is given by

$$w_3 = (1-\nu)pR^2/2Eh \tag{3.43}$$

The derivatives of the out-of-plane displacement at the center of the shell concerning the radius of curvature R and the thickness h are detailed as follows::

$$w_{3,R} = (1-\nu)pR/Eh; \quad w_{3,h} = -(1-\nu)pR^2/2Eh^2 \tag{3.44}$$

The BEM model is constructed with 48 quadratic elements positioned along the boundaries, coupled with 49 DRM points distributed uniformly throughout the domain. To validate the model, the out-of-plane displacement obtained from BEM was compared to that derived from the analytical solution. Additionally, derivatives were computed using both the Finite Difference Method (FDM) and the Implicit Differentiation Method (IDM) across different values of h/R. For the

FDM implementation, a normalized step size of $\Delta Z'_g = 0.01$ was used. To assess the accuracy of the model, the percentage difference between the analytical solution and the IDM/FDM solutions was calculated. The results for $w_{3,R}$ and $w_{3,h}$ are presented in Tables 3.1 and 3.2, respectively.

Table 3.1: Results of the derivatives of the centre deflection with respect to the radius of curvature $w_{3,R}$ obtained from the analytical solution, IDM and FDM. The derivatives are given in magnitude of 10^{-4}. Percentage differences are in [%] between the IDM and the analytical solution.

h/R	R	h	Analytical	IDM	FDM	% diff
1/100	5000	50	0.450	0.454	0.454	0.980
1/200	5000	25	0.900	0.901	0.901	0.147
1/500	12500	25	2.25	2.25	2.25	0.169
1/1000	25000	25	4.50	4.51	4.51	0.241
1/5000	125000	25	22.5	22.6	22.6	0.407

Table 3.2: Results of the derivatives of the centre deflection w with respect to the thickness $w_{3,h}$ obtained from the analytical solution, IDM and FDM. Percentage differences in [%] between the IDM and the analytical solution.

h/R	R	h	Analytical	IDM	FDM	% diff
1/100	5000	50	-2.25E-03	-2.19E-03	-2.19E-03	2.61
1/200	5000	25	-9.00E-03	-8.90E-03	-8.90E-03	1.09
1/500	12500	25	-5.63E-02	-5.62E-02	-5.62E-02	0.01
1/1000	25000	25	-2.25E-01	-2.26E-01	-2.26E-01	0.24
1/5000	125000	25	-5.63E+00	-5.65E+00	-5.65E+00	0.46

Tables 3.1 and 3.2 show that the differences between IDM and the analytical solution is minimal, with a magnitude less than 1% for $w_{3,R}$ and less than 3% for $w_{3,h}$. Furthermore, the results obtained from the Finite Difference Method (FDM) and IDM exhibit only minor differences, suggesting that IDM holds the same level of accuracy as the FDM. Nevertheless, it's important to highlight that the FDM requires a convergence test for choosing the optimal step size, whereas IDM, avoids the use of step size, emerges as a more robust alternative. In summation, the IDM formulations have been effectively validated against the analytical solution, showcasing good accuracy and robustness.

3.3.2 Reliability Analysis

To exemplify the application of the IDM formulation with the First-Order Reliability Method (FORM), a numerical example involving a clamped circular shallow spherical shell was used. In this example, a range of geometrical parameters and material properties were treated as random variables. The geometric configuration of the shell is shown in Figure 3.9.

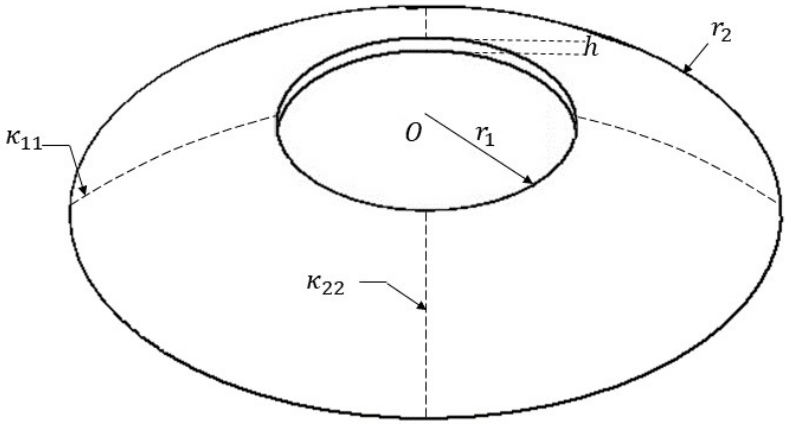


Figure 3.9: The example features a circular shallow spherical shell with a central hole. The shell experiences a uniform pressure load applied against its curvature, in a downward direction. This shell is characterized by an inner radius of r_1 and an outer radius of r_2, along with a specified thickness h. The curvatures in both the x and y directions are represented by $\kappa_{11} = \kappa_{22} = \kappa$.

The outer boundary of the shell is clamped, and the shell is subjected to a uniform pressure load. The shell is comprised of Aluminum 6061-T6 with a Young's modulus of $E = 68.9\,\text{GPa}$, a Poisson's ratio of $\nu = 0.33$, and a yield strength of $\sigma_y = 276\,\text{MPa}$, as documented in [9]. The shell is characterized by a thickness h, and its curvatures in the x and y directions are denoted as κ_{11} and κ_{22}, respectively. In this example, spherical shell are considered, meaning that $\kappa_{11} = \kappa_{22} = \kappa$. In the context of the First-Order Reliability Method (FORM), various variables are classified as random. These include the inner radius r_1 and the outer radius r_2 of the shell boundaries, the shell thickness h, the Poisson's ratio ν, the curvature κ, and the loading conditions p. Detailed descriptions of these random variables are available in Table 3.3. Additionally, the Coefficient of Variation (COV) of the curvature is included as a variable, representing different levels of manufacturing uncertainty.

The BEM model used to represent the shell structure is constructed with a total of 64 quadratic

elements. Within this configuration, 32 elements were used to discretise the inner boundary, while the remaining 32 elements were used to discretise the outer boundary. Additionally, the model incorporates 64 DRM points, which have been evenly distributed throughout the domain.

Table 3.3: The design variables used in the reliability analyses

Z_i	X_i	Parameter	Description	Distribution	Mean	COV
Z_1	X_1	r_1	Inner radius	Normal	$0.5m$	0.1
Z_2	X_2	r_2	Outer radius	Normal	$5m$	0.1
Z_3	X_3	κ	Curvature in x direction	Normal	$0.005m^{-1}$	COV_κ
Z_4	X_4	h	Shell thickness	Normal	$0.05m$	0.05
Z_5	X_5	ν	Poisson's ratio	Normal	0.3	0.05
Z_6	X_6	p	Domain pressure	Normal	$0.025MPa$	0.2

The failure criterion for the shell is established in a manner that ensures the maximum Von Mises stress within the shell remains below the yield strength of the material. In this context, the Limit State Function (LSF) takes the following form:

$$g(\mathbf{Z}) = \sigma_y - \sigma_v^{max}(\mathbf{X}) \tag{3.45}$$

where σ_y is the yield strength and σ_v^{max} is the maximum Von Mises stress. The vector $\mathbf{Z}$ contains the design variables that can influence the value of g where $\mathbf{Z} = (r_1, r_2, \kappa, h, \nu, p, \sigma_y)$ and $\mathbf{X}$ consist of the design variables in $\mathbf{Z}$ without the yield strength $\mathbf{X} = (r_1, r_2, \kappa, h, \nu, p)$.

In the context of the First-Order Reliability Method (FORM), it becomes necessary to evaluate the sensitivity of $g(\mathbf{Z})$ with respect to the design parameter Z_i. To achieve this, the IDM formulation is implemented, involving the computation of direct derivatives for boundary integral equations established in terms of both source and field points. Conducting the IDM requires estimating the derivatives of the nodal coordinates at the collocation points as given in Section 3.2.2.

Sensitivities for the geometrical variables $Z_1 - Z_4$ were evaluated using the BEM-IDM, while for the non-geometrical variables $Z_5 - Z_6$, sensitivities were derived through BEM-FDM with a step size of $\Delta Z_g' = 5 \times 10^{-4}$. The investigation encompassed a range of possible values for the coefficient of variation (COV_κ) for curvature, which takes the value from 0.02 to 0.2.

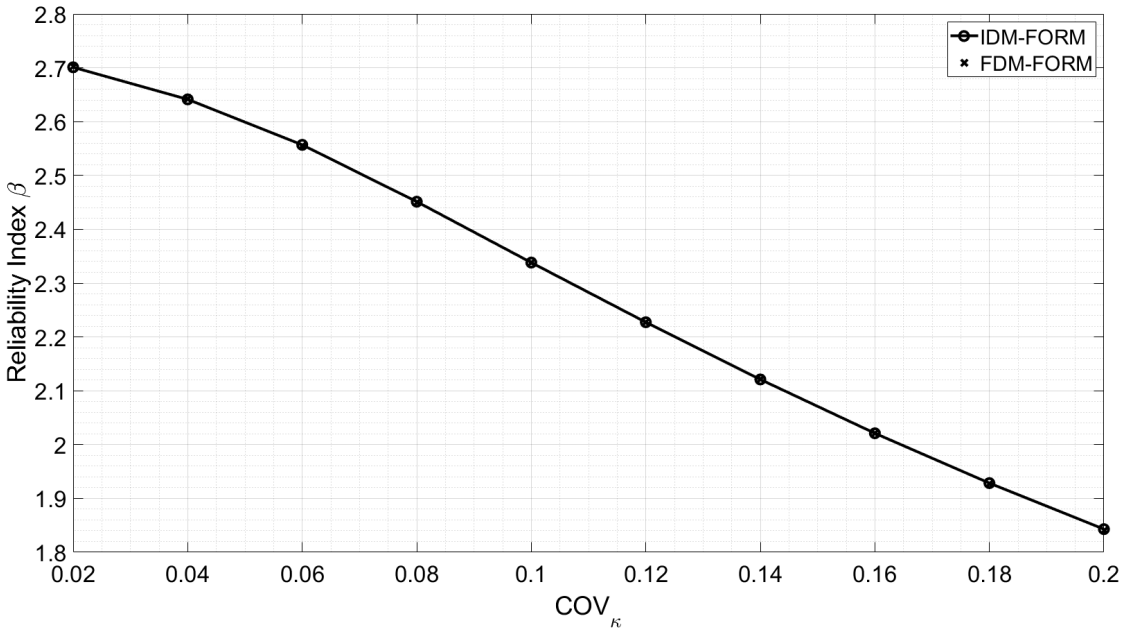


Figure 3.10: Effect of the uncertainties (COV) in the curvature on the Reliability index for IDM and FDM compare to the results obtained from MCS.

The influence of the coefficient of variation (COV_κ) on the overall structural reliability is illustrated in Figure 3.10. Notably, as COV_κ increases, the reliability of the structure decreases. This inverse relationship underscores the fact that higher uncertainties are associated with an increased probability of structural failure. Comparing the results obtained from the IDM-FORM and the FDM-FORM shows only minor differences, with the maximum difference observed at 0.11% for $COV_\kappa = 0.2$.

However, the IDM-FORM demonstrates superior computational efficiency when compared to the FDM-FORM. This efficiency is particularly evident in the CPU times presented in Table 3.4, where the IDM proves to be 35% faster than the FDM for evaluating one derivative with respect to one design parameter. While the absolute reduction in CPU time is relatively modest (0.86 seconds), this gain becomes significant when the differentiation step needs to be performed numerous times, particularly in gradient-based optimization procedures. The IDM's efficiency advantage is further underscored by the fact that it does not necessitate the use of a step size, in contrast to the FDM. Consequently, the findings establish the IDM developed in this work as a more efficient alternative to the FDM for sensitivity calculations.

Table 3.4: CPU time required for the FORM, with either the IDM or the FDM.

Method	CPU time (s) per derivative
FDM	2.41
IDM	1.55

3.3.3 Sensitivity Analysis

Reliability analysis plays an important role in the assessment of structural integrity and safety. The results can be used for conducting sensitivity analyses, with the aid in the identification of the most influential design parameters for enhancing safety. As the complexity of systems increases, along with the number of random variables affecting structural response, managing all variables becomes progressively challenging. Therefore, the emphasis shifts towards recognizing and effectively managing only the most critical variables. To assess the impact of parameter uncertainty on overall reliability, reliability sensitivity analyses are employed. These analyses enable a detailed exploration of how individual parameters exert their influence on the probability of system failure The directional vector $\mathbf{a}$, as calculated in Eq. (3.11), represents the sensitivity of the standardized limit state function at the design point u^* to changes in the parameter vector u. The practical implication of this sensitivity results is that, when the sensitivity with respect to a parameter u_i is low, it suggests that precise estimation of this parameter may not be necessary. In simpler terms, parameters with minimal sensitivity to the limit state can be effectively treated as deterministic values without considering the uncertainties. This approach can significantly simplify the problem, enabling engineers to concentrate their efforts on the most crucial parameters.

A sensitivity factor is defined as the rate of change in the probability of structural failure concerning a specific distribution parameter, such as μ or σ, associated with a given random variable. In the context of this research, the sensitivity factors were evaluated at the design point (MPP). This analysis encompassed a diverse range of values for the COV in the curvature, denoted as COV_κ. For the random variables conforming to a normal distribution, it is possible to compute the sensitivity factor relating to either the mean or standard deviation through the methodology outlined in Xiaoping's work [98].

$$S_{\mu_i} = \frac{\partial P_f}{\partial \mu_i} = \phi(-\beta)\frac{u_i^*}{\beta\sigma_i}; \quad S_{\sigma_i} = \frac{\partial P_f}{\partial \sigma_i} = \phi(-\beta)\frac{(u_i^*)^2}{\beta\sigma_i} \tag{3.46}$$

Where β represents the reliability index that is evaluated at the MPP, while $\phi(-\beta)$ denotes the probability density function for a standard normal distribution, specifically evaluated at the value of $-\beta$. In addition, u_i^* corresponds to the U-space value of the i^{th} design variable.

It is noteworthy that the sensitivity factors obtained through the equation presented in (3.46), denoted as S_{μ_i} and S_{σ_i}, differ in units, therefore the direct comparison is impractical. In order to mitigate this issue, a dimensionless transformation process has been implemented, as elaborated in the authoritative work of Saltelli [99] such that the dimensionless sensitivity results for different parameters can be comparable to each other.

$$\widetilde{S}_{\mu_i} = \frac{\mu_i}{P_f}\frac{\partial P_f}{\partial \mu_i}; \quad \widetilde{S}_{\sigma_i} = \frac{\sigma_i}{P_f}\frac{\partial P_f}{\partial \sigma_i} \tag{3.47}$$

where $\widetilde{S}_{\mu_i}$ and $\widetilde{S}_{\sigma_i}$ denotes the sensitivity of the failure probability with respect to the mean and standard deviation of the distribution, respectively. The results of the sensitivity factors evaluated at the MPP at $COV_\kappa = 0.1$ are given in Table 3.5. Table 3.5 offers insights into the sensitivity

Table 3.5: The sensitivity factors obtained from the reliability analysis for $COV_\kappa = 0.1$. The table gives both the sensitivity factor and the normalised sensitivity factors.

Sensitivity	S_{μ_i}	$\widetilde{S}_{\mu_i}$	Sensitivity	S_{σ_i}	$\widetilde{S}_{\sigma_i}$
$\partial P_f/\partial \mu_{r_1}$	-0.018	-0.93	$\partial P_f/\partial \sigma_{r_1}$	0.0015	0.0076
$\partial P_f/\partial \mu_{r_2}$	0.011	5.49	$\partial P_f/\partial \sigma_{r_2}$	0.0051	0.26
$\partial P_f/\partial \mu_\kappa$	-25.65	-13.24	$\partial P_f/\partial \sigma_\kappa$	29.67	1.53
$\partial P_f/\partial \mu_h$	-3.38	-17.45	$\partial P_f/\partial \sigma_h$	2.58	0.67
$\partial P_f/\partial \mu_\nu$	0.077	2.38	$\partial P_f/\partial \sigma_\nu$	0.0080	0.012
$\partial P_f/\partial \mu_p$	4.03	10.40	$\partial P_f/\partial \sigma_p$	7.32	3.78

factors associated with various structural parameters. Notably, the sign of the sensitivity factor for the mean values of the outer radius, Poisson's ratio, and pressure load is positive. This observation implies that an increase in these mean values correlates with an increased probability of structural failure Conversely, negative sensitivity factors indicate the inverse relationship. This aligns with the expectations; for example, a decrease in curvature values tends to transform the structure into one a near-flat plate, which inherently offers less resistance to downward pressure. Similarly, a thicker shell exhibits greater capacity to withstand higher pressure forces.

Furthermore, it's noteworthy that all sensitivity factors related to the standard deviation exhibit

positive signs. This is consistent with the expectation that greater uncertainties in the variables are likely to correspond to an increased likelihood of structural failure.

Sensitivity analysis serves as a valuable tool in the design process. Nevertheless, in situations involving a multitude of variables, identifying those with the most pronounced influence on reliability can be a challenging task. To address this, the percentage importance of each of the random variables can be computed, as elaborated in the reference by Niu [100].

$$\lambda_{\mu_i} = \frac{|\widetilde{S}_{\mu_i}|}{\sum |\widetilde{S}_{\mu_i}|} \times 100\%; \qquad \lambda_{\sigma_i} = \frac{|\widetilde{S}_{\sigma_i}|}{\sum |\widetilde{S}_{\sigma_i}|} \times 100\%; \tag{3.48}$$

where λ_{μ_i} and λ_{σ_i} represent the percentage contribution of each distribution parameter to the overall sensitivity. The graphical representation of these percentage sensitivity factors for a variety of variables, encompassing different values of COV_κ, is presented in Figures 3.11 and 3.12 for the means and standard deviations, respectively.

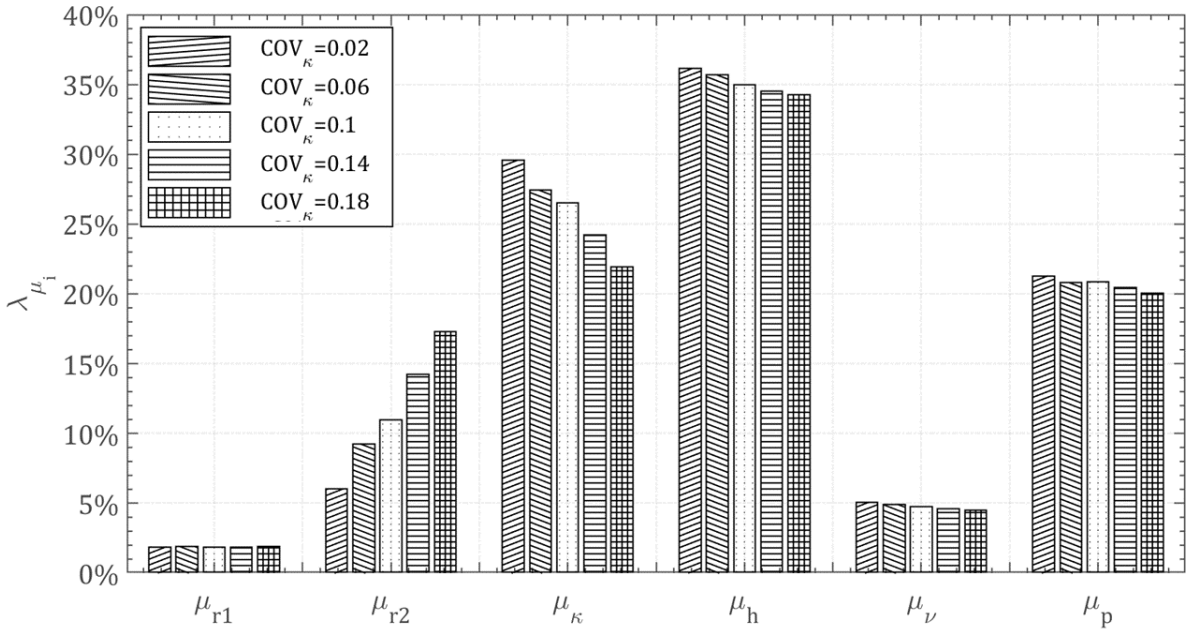


Figure 3.11: Percentage influence of the sensitivity factors of mean of the variables with varying COV in curvature.

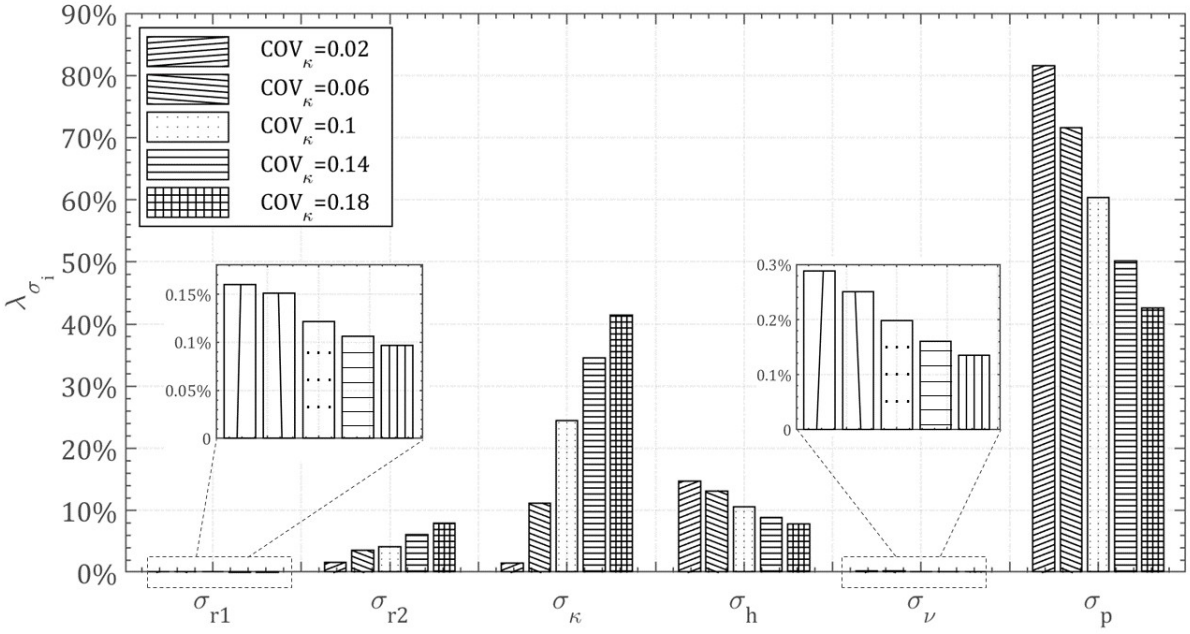


Figure 3.12: Percentage influence of the sensitivity factors of standard deviation of the variables with varying COV in curvature.

Based on the results shown in the figures. Notably, the mean and standard deviation of both the inner radius r_1 and Poisson's ratio ν exhibit considerably smaller effects on sensitivity compared to other parameters. In contrast, the geometric variables, specifically curvature κ and thickness h carry a notably higher influence on the failure probability. Among all the parameters under consideration, the standard deviation of the applied uniform pressure, denoted as σ_p emerges as the most impactful parameter. However, as COV_κ increases, the standard deviation of the curvature, σ_κ, approaches a similar level of impact.

In summary, these findings suggest that enhancing the reliability of the shallow shell structure, as illustrated in Figure 3.9, more focus should be paid on the curvature and thickness. This emphasis is given as these parameters exert a substantial influence on the probability of structural failure and are also relatively easier to control compared to non-geometric factors like the applied pressure. Furthermore, more accurate quantification of uncertainties associated with the applied pressure load is crucial, given that the standard deviation in the pressure load significantly impacts the failure probability.

3.3.4 Optimisation

Structural design consists not only the critical considerations of ensuring the strength, serviceability, and safety of a construction but also the economic aspects tied to constructing such a structure. Increasing the safety standards of a structure frequently entails an elevating in manufacturing costs, while efforts to economize often require compromises on structural safety. The balance between safety and cost underscores the complexity in structural design. Over the past two decades, significant attention has been dedicated to the development of design optimization methodologies under various uncertainties in the parameter.

In the domain of structural analysis, multiple optimization methods has found application. These encompass deterministic design optimization [101], Possibility-Based Design Optimization (PBDO) [102], Reliability-based Design Optimization (RBDO) [103], and life cycle and risk optimization [104]. Among these, RBDO has gained greater attention for shape optimization. Within RBDO, two formats of the problem are widely used: the Performance Measure Approach (PMA) and the Reliability Index Approach (RIA). The key distinction between these two approaches lies in their optimization strategies. In PMA, the objective is to minimize a complex function subject to straightforward constraints, whereas RIA involves the minimization of a simple function constrained by complex conditions. PMA has emerged as the more robust choice, demonstrating superior convergence performance compared to RIA. Moreover, to enhance the stability and convergence rate in RBDO, the Hybrid Mean Value Method, as detailed in the work by Youn [103], has been effectively incorporated in the optimisation of the following example.

In the previous two examples, the IDM formulation played a pivotal role in assessing the response sensitivities of structural systems. The IDM formulations were first validated with an analytical example and subsequently expanded to a more complex structure. The latter example served the purpose of identifying the most influential design parameters.

To underscore the practical applicability of IDM formulations, two optimization examples were performed, both involving shape optimization facilitated by the innovative IDM formulation developed within this research. The first optimization concentrated on the shape optimization of a circular shell structure considering only the crucial parameters, as identified in the sensitivity analysed in Section 3.3.3. The second optimization example was considerably more complicated,

focusing on optimizing the shape of an aircraft fuselage structure, characterized by a significantly greater number of design parameters compared to the former example.

This process of optimisation allows engineers to maximize or minimize a performance function while satisfying the constraints and requirements of the structure. Given that the sensitivities have been calculated via the FORM in using the BEM-IDM formulation, gradient-based design optimization methods become the method of choice. In practice, these optimization tasks were executed using MATLAB's nonlinear multi-variable function solver 'fmincon' with the constraint gradient evaluated by the IDM-BEM formulation and the optimisation algorithm 'trust-region-reflective' was chosen.

3.3.4.1 Numerical example 1: Circular Shallow Spherical Shell

The first optimization example centers on the enhancement of a circular shell structure with a central hole, as previously discussed in Section 3.3.3 Figure 3.9. The primary objective in this optimization is to minimize the mass of the shell, provided that the maximum Von Mises stress remains below a specified threshold. Based on the sensitivity analysis expounded in Section 3.3.3, the outer radius r_2, curvature κ, and thickness h emerge as the parameters with the most substantial influence on the maximum Von Mises stress within the structure. Consequently, the design parameters under consideration for this optimization problem are limited to the vector $\mathbf{d} = [r_2, \kappa, h]$, while all other parameters are held constant at their mean values. Thus, the optimization problem can be defined as follows:

$$\begin{aligned} &\text{Minimise:} && Mass(\mathbf{d}) \\ &\text{Subject to:} && \mathbf{d}^L \leq \mathbf{d} \leq \mathbf{d}^U, \quad \mathbf{d} \in \mathbf{R}^3 \\ & && \sigma_v^{max} \leq \sigma_Y / S \end{aligned} \tag{3.49}$$

Where σ_v^{max} denotes the maximum Von Mises stress present in the structure, σ_Y represents the yield strength, and S is the safety factor, maintaining a constant value of 1.5. The optimization process begins with an initial design denoted as $\mathbf{d}_0 = [5, 0.05, 0.5]$. Design constraints are imposed through

lower and upper bounds, defined as $\mathbf{d}^L = [4.5, 0.001, 0.01]$ and $\mathbf{d}^U = [5.5, 0.01, 0.1]$, respectively. The optimisation procedure is considered to achieve convergence when the change in $Mass(\mathbf{d})$ is less than 0.01%, and σ_v^{max} falls at or below σ_Y/S within a 0.01% of error. To comprehensively investigate the influence of yield strength on optimization results, various materials are considered, including Aluminum 6061-T6, 2024-T4, 7075-T6, and 7075-T7. Material properties for these alloys are detailed in Table3.6, and the mass calculations are conducted using the design variables $\mathbf{d}$ combined with the corresponding density. The initial design is characterized by a volume of $3.889m^3$. The expectation is that when materials with higher yield strength are employed, a lighter mass in the optimized design can be achieved.

Table 3.6: Material properties of different Aluminium alloys. The Young's modulus E, Poisson's ratio ν, yield strength σ_Y and density ρ are given [9].

Material	E $[GPa]$	ν	σ_Y $[MPa]$	ρ $[kgm^{-3}]$
Aluminium 6061-T6	68.9	0.33	276	2700
Aluminium 2024-T4	73.1	0.33	324	2780
Aluminium 7050-T7	71.7	0.33	469	2830
Aluminium 7075-T6	71.7	0.33	503	2810

The optimization outcomes for each of the specified materials are presented in Table 3.7. Additionally, the convergence history is graphically depicted in Figure 3.13. Evidently, the optimization process has successfully led to a reduction in the volume of the structure when compared to the initial design. The results notably underscore that the utilization of materials with higher yield strength, for example for Aluminum 7075-T6, indeed leads to the final design of lighter mass. This outcome aligns with the earlier expectations discussed.

Table 3.7: Optimisation results from the IDM-based BEM with multiple Aluminium alloys.

Material	σ_Y $[MPa]$	Optimal Volume	Optimal Mass	r_2 $[m]$	κ $[m^{-1}]$	h $[m]$
Aluminium 6061-T6	276	1.31 m^3	3536.3 kg	4.621	0.00802	0.0197
Aluminium 2024-T4	324	1.13 m^3	3133.6 kg	4.500	0.00882	0.0179
Aluminium 7050-T7	469	0.961 m^3	2719.8 kg	4.501	0.00781	0.0153
Aluminium 7075-T6	503	0.956 m^3	2687.7 kg	4.539	0.00677	0.0150

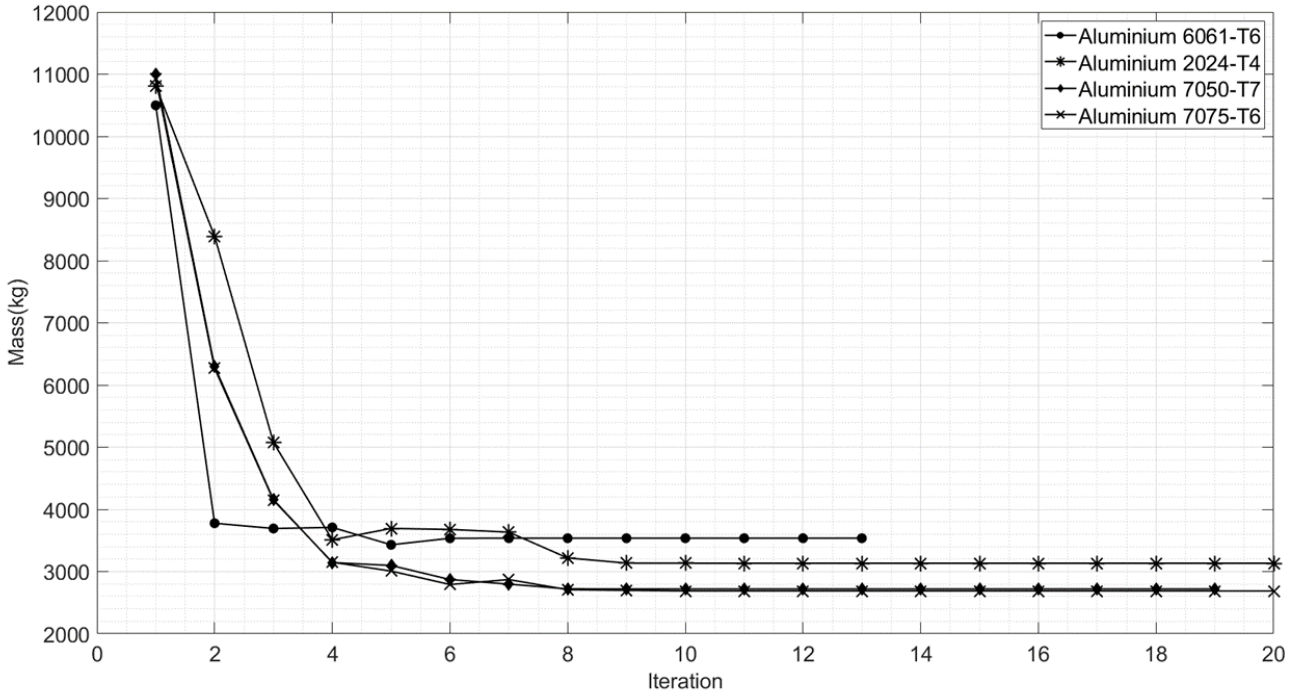


Figure 3.13: Optimisation history from the IDM-based BEM with multiple Aluminium alloys. Three examples of shape-changing in the optimisation are presented for Aluminium 2024-T4.

3.3.4.2 Numerical example 2: Shell Structure with a Window

The second example serves as a demonstration of the application of the BEM-IDM for Reliability-Based Design Optimization (RBDO). The RBDO is a well-established field in structural engineering which centred around the optimization of structures while accounting for uncertainties in design parameters to achieve a predetermined level of reliability. This area has been the subject of extensive research in the literature [78, 79, 105, 106].

The structure featuring a simply supported shell structure with a window section was used for the RBDO, as showcased in Figure3.14. The structure is constructed using Aluminum 6061-T6 and is exposed to boundary tension, bending, and domain pressure. The geometry of the shell is defined by the parameters $\mathbf{X} = [W_1, L_1, R_1, W_2, L_2, R_2, h, \kappa]$, and the design variables considered in the optimization process are $\mathbf{d} = [W_2, L_2, R_2, h, \kappa]$. Furthermore, it's essential to underscore the presence of random variables affecting loading and material properties. These random variables encompass bending moment M, tension N, domain pressure P, and yield strength σ_Y. Detailed information pertaining to these variables is tabulated in Table3.8.

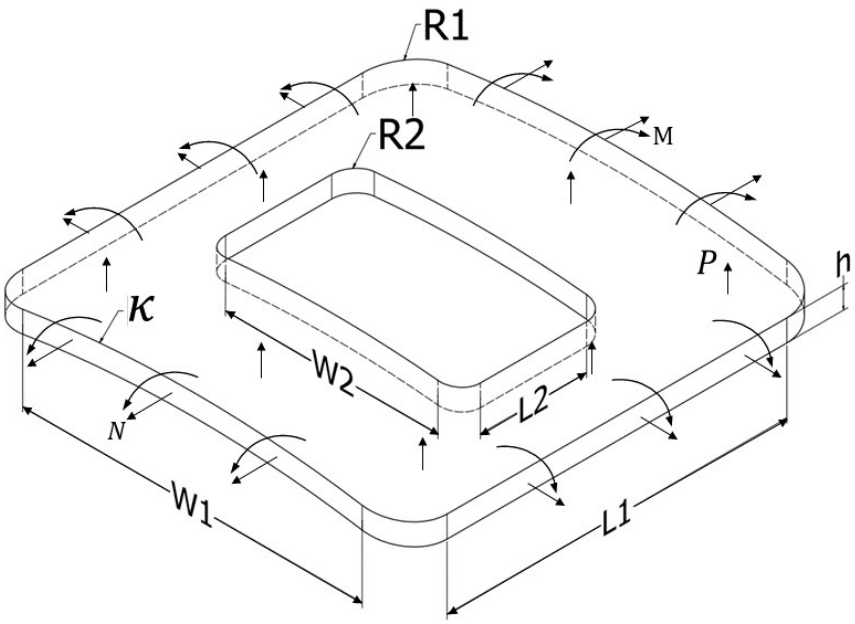


Figure 3.14: Shell structure subjected at tension, bending and domain pressure loading.

Table 3.8: Details of the shell structure parameters and random variables used in the optimisation procedure .

Variable	Description	Mean	CoV	Units
W_1	Outer width	1	0	m
L_1	Outer length	1	0	m
R_1	Outer radius	0.1	0	m
W_2	Inner width	0.5	0.01	m
L_2	Inner length	0.25	0.01	m
R_2	Inner radius	0.05	0.01	m
h	Thickness	0.05	0.01	m
κ	Curvature	0.1	0.01	m^{-1}
N	Boundary traction	0.9	0.1	MNm^{-1}
M	Boundary moment	0.01	0.1	MN
P	Domain pressure	0.056	0.1	MPa
σ_Y	Yield stress	276	0.1	MPa

The BEM mesh of this structure is composed of 112 quadratic elements on the boundaries and 78 DRM points in the domain. The optimisation problem is defined such that the mass is to be

minimised while a specific target reliability index β_{target} is reached.

$$\begin{aligned} &\text{Minimise:} && Mass(\mathbf{d}) \\ &\text{Subject to:} && \mathbf{d}^L \leq \mathbf{d} \leq \mathbf{d}^U, \quad \mathbf{d} \in \mathbf{R}^5 \\ & && g(\mathbf{Z}) \leq 0 \qquad\qquad (\parallel u \parallel = \beta_{target}) \end{aligned} \tag{3.50}$$

where the limit state function is defined as:

$$g(\mathbf{Z}) = \sigma_v^{max}(\mathbf{Q}) - \sigma_Y \tag{3.51}$$

where $\mathbf{Z} = [W_2, L_2, R_2, h, \kappa, M, N, P, \sigma_Y]$ and $\mathbf{Q} = [W_2, L_2, R_2, h, \kappa, M, N, P]$. The mass of the structure is computed using the parameters in $\mathbf{X}$ and a density value of $\rho = 2700\,\mathrm{kg/m^3}$. In the optimization equation mentioned above, two constraints were taken into account: 1) The equality constraint, denoted by $|u| = \beta_{target}$, was assessed using an 'inverse' FORM approach. This approach allows for the calculation of the corresponding design point given a specific β_{target} value. 2) The inequality constraint, expressed as $g(\mathbf{Z}) \leq 0$, required the computation of constraint gradients. These gradients were calculated using the IDM-BEM formulations.

The initial design is expressed as $\mathbf{d}_0 = [0.5, 0.25, 0.05, 0.05, 0.1]$, with lower and upper bounds defined as $\mathbf{d}^L = 0.8\mathbf{d}_0$ and $\mathbf{d}^U = 1.2\mathbf{d}_0$. Notably, a broader range of design variation is prescribed for R_2, denoted as $\mathbf{d}^L_{R_2} = 0.03$ and $\mathbf{d}^U_{R_2} = 0.07$.

The optimization process for the shell structure was conducted with a range of target reliability indices β_{target}. A higher β_{target} represents a lower probability of failure. The variation in β_{target} corresponds to different safety requirements for potential applications. The expected outcome is that, as the safety requirements become more stringent (signified by higher β_{target} values), the mass of the optimized design is likely to increase.

Table 3.9: Optimisation results for different target reliability indexes β_{target}.

β_{target}	W_2	L_2	R_2	h	κ	mass $[kg]$	β_{FORM}	P_f (%)
Initial design	0.5	0.25	0.05	0.05	0.1	165.1	3.651	0.01311
2	0.4970	0.2892	0.06956	0.04006	0.1179	125.4	2.008	2.232
3	0.4050	0.2771	0.06967	0.04008	0.1192	130.4	3.014	0.1289
4	0.4012	0.2064	0.06976	0.04279	0.1196	143.9	4.006	0.003088
5	0.4002	0.2009	0.06996	0.04856	0.1199	163.6	5.001	2.852e-05
6	0.4007	0.2027	0.06983	0.05739	0.1196	193.3	6.003	9.805e-08

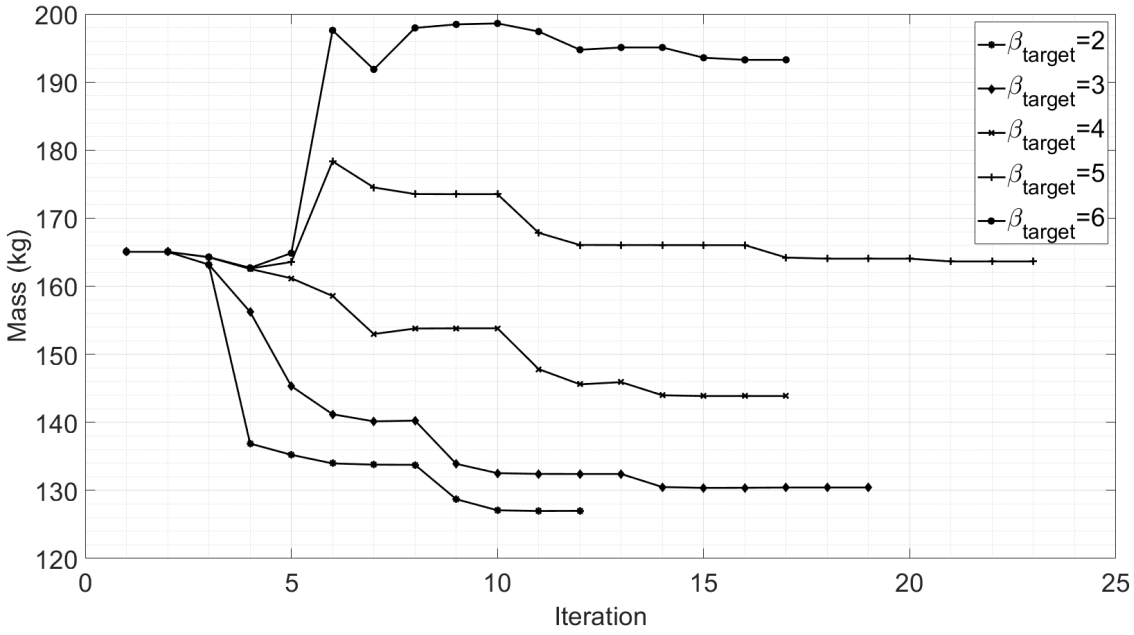


Figure 3.15: Optimisation history from the IDM-based BEM with different target reliability β_{target}.

The results of the optimisation for different target reliability indexes β_{target} are given in the Table3.9 and the iteration history of the optimisation is shown in Figure3.15. To verify that the optimal design is meeting the target reliability index, the true reliability index β_{FORM} was evaluated using the FORM. It can be seen that the error between the β_{target} and β_{FORM} is less than 0.47%, meaning that β_{target} and β_{FORM} are in very good agreement. As the target reliability index increases, the optimal mass is higher which matches the expectation discussed earlier. The optimal geometry for $\beta_{target} = 2$ and $\beta_{target} = 6$ is shown in Figure3.16. As β_{target} increases, optimal design becomes thicker and has higher curvature, the radius of the fillet is also larger and the 'window' section is smaller.

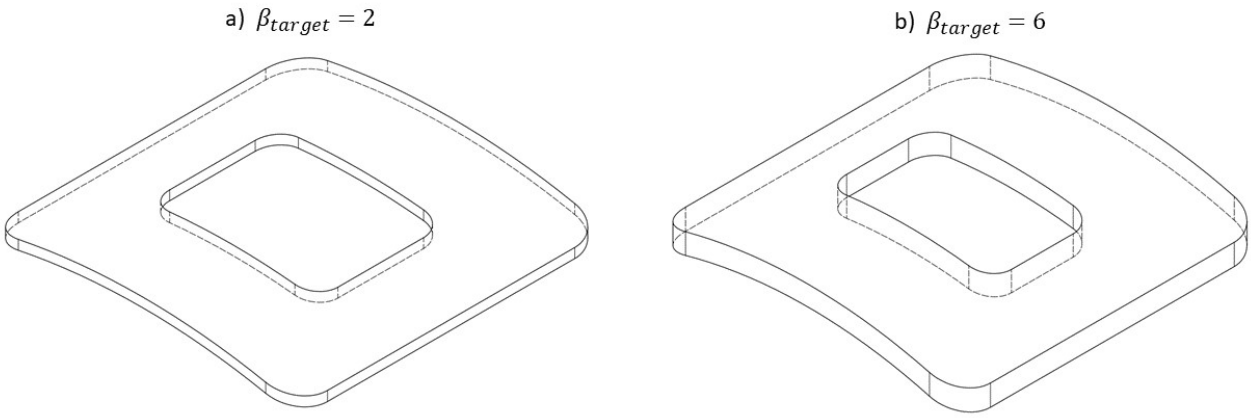


Figure 3.16: Optimisation results for shell design with $\beta_{target} = 2$ and $\beta_{target} = 6$. (not to scale)

The location of the maximum Von Mises stress is often found to concentrated at the corner of the window. Consequently, exploring the sensitivity of the maximum Von Mises stress with respect to the fillet radius R_2 becomes of particular significance. Sensitivity analysis is thoughtfully conducted at a specific reliability level (i.e., a fixed β_{target}) to evaluate the sensitivity of the maximum Von Mises stress with variations in the fillet radius.

The derivatives of the maximum Von Mises stress concerning changes in the fillet radius are distinctly portrayed in Figure3.17, where other variables are taken the value obtained by the obtained optimal design parameters for $\beta_{target} = 4$. It's essential to highlight that, while the design variables remain fixed at the optimal results given in Table3.9, the focus is on varying the value of R_2. Evidently, the maximum Von Mises stress showcases varying levels of sensitivity to changes in the fillet radius. Notably, when a larger R_2 is employed in the design, the maximum Von Mises stress tends to exhibit lower sensitivity. Importantly, the reliability index maintains close alignment with the target reliability index.

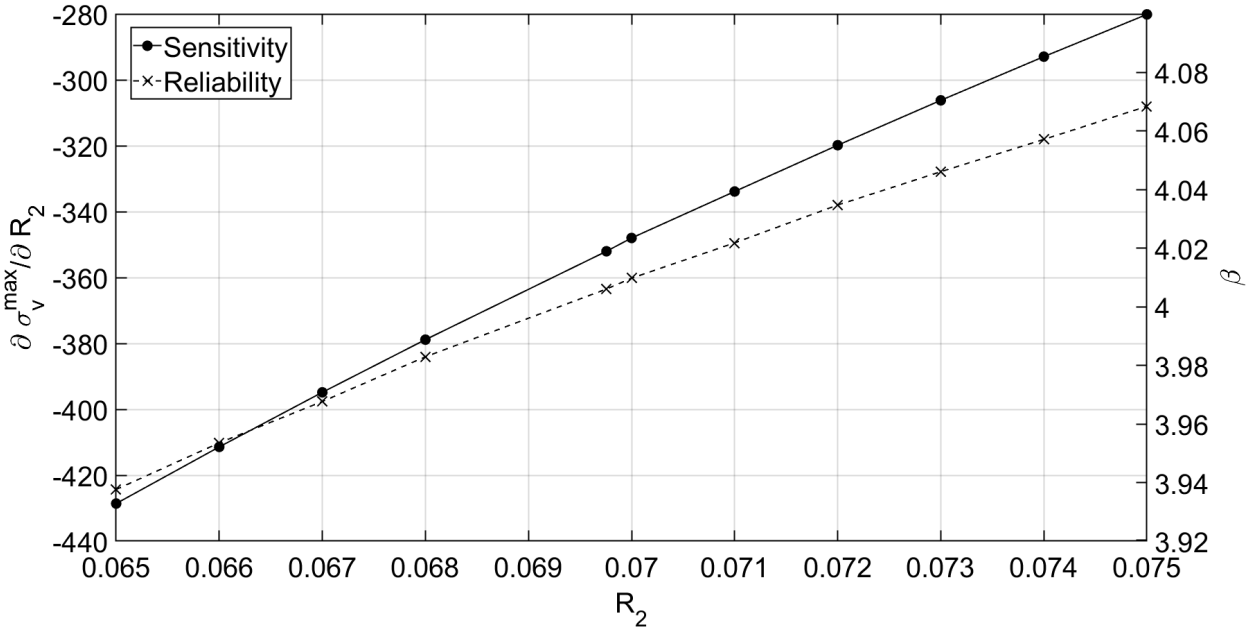


Figure 3.17: Sensitivity of the maximum Von Mises stress to the change in fillet radius R_2 at the optimal design of $\beta_{target} = 4$.

3.4 Conclusion

This chapter has introduced a novel methodology for conducting reliability analyses using the newly developed Boundary Element Method-based Implicit Differentiation Method (BEM-IDM) tailored for shallow shell structures. Notably, the chapter presents the BEM-IDM formulations for deriving the response sensitivities concerning variations in geometric parameters, curvature, and thickness.

The exact derivatives extracted from the BEM formulations were derived and coupled with the First-Order Reliability Method (FORM) to evaluate the reliability of shell structures. The IDM formulation allows the evaluation of the sensitivity of the failure criterion concerning changes in random variables. The IDM formulations were verified first against an analytical example featuring a hemispherical shell. The results showed good agreement with the analytical solution, with a maximum difference of 2.61%. Subsequently, the IDM formulations were used with the FORM for the analysis of a structure characterized by a circular shallow shell with an inner hole subjected to uniform pressure. In this analysis, geometric variables, material properties, and applied pressure were all treated as random variables. A specific focus was placed on investigating the influence

of variation in curvature uncertainties on the reliability of the structure, which, in turn, revealed that increased uncertainty in curvature corresponded to a higher probability of structural failure.

Furthermore, it's worth highlighting that the IDM results exhibited a high degree of alignment with the outcomes produced by the FDM-FORM. The differences between the two methods remained notably small, with a maximum deviation of 0.11%.

The sensitivity analysis was performed, effectively applying the newly developed BEM-IDM to analyse the impact of various variables on the reliability of the structure. The insights derived from this analysis underscored the importance of managing uncertainties associated with geometrical variables and more accurately determining uncertainties associated with pressure loads.

In a demonstration of practical applications, this chapter effectively employed the BEM-IDM as a gradient-based optimization procedure. The objective of this optimization was to minimize mass while preserving a high level of safety. The study encompassed a diverse range of materials with varying yield strengths, aimed at investigating the impact of yield strength on the optimization solutions. A notable revelation was that the utilization of stronger materials resulted in the optimization of structures with lower mass.

Furthermore, a shape optimization using Reliability-Based Design Optimization (RBDO) was performed. The results show that increasing the targeted reliability index led to a corresponding increase in the mass of the structure in order to fulfil the stringent safety requirements.

Chapter 4

Reliability Analysis of Fatigue Crack Growth in Shallow Shell Structures

Fatigue, as a mode of structural failure, remains one of the most commonly observed issues in engineering structural problems. This phenomenon is frequently encountered in engineering practice [107]. The significance of accurately assessing structural reliability has been on the rise, particularly within the field of structural integrity assessment. This interest is further emphasised in the field of aircraft structural engineering, where the demand for exceptionally high reliability is essential, given that a significant proportion of structural failures can be attributed to fatigue crack growth [108]. Consequently, the need to perform fatigue reliability has taken great interest in the research community. It's worth noting that this chapter primarily focuses on the fatigue limit state within the shallow shell structures. The following section provides a concise review of fatigue reliability analysis, with a particular emphasis on fracture mechanics.

Shallow shell problems hold a significant interest within engineering design processes, primarily due to the extensive utilization of shallow shells in aircraft and naval structures. Their appeal lies in the advantageous combination of low weight and high strength. In this context, fatigue is of high interest in the structural design. The assessment of stress intensity factors (SIFs) and the variations in design parameters represent crucial subjects in the domain of failure analysis. The field of reliability analysis, especially concerning cracked structures, has witnessed an increased research interest. Notably, a substantial portion of the existing literature leans towards indirect

approaches to reliability analysis, with Finite Element Method (FEM) being a favoured methodology [109–111]. For instance, the reliability of aircraft panels has been a subject of substantial attention, as exemplified by studies such as [112], where a wing surface panel featuring multi-site damage was considered with the initial crack lengths treated as uncertainties followed by the RBDO to determine an optimal inspection interval. Another example is presented in [113], where the reliability of a stiffened panel was estimated through a combination of Monte Carlo Simulation (MCS) and the First-Order Reliability Method (FORM), accounting for the influence of inspections. Furthermore, the extensive review by White [114] comprehensively covers various formulations for assessing the probability of failure employing the FEM. This review encompasses diverse risk assessments conducted for different aircraft, including examples like the F16 and F/A-18.

While previous research has effectively utilized the Finite Element Method (FEM) for reliability analysis, the application of shallow shell Dual Boundary Element Method (DBEM) in the context of fatigue reliability analysis has received relatively limited attention. However, several noteworthy works have emerged that demonstrate the coupling of the Boundary Element Method (BEM) in fatigue reliability analysis. For instance, in the field of railway engineering, a study proposed in [115] assessed the fatigue reliability of a railway steel component to determine its design service life. Additionally, probabilistic damage analysis for a fuselage panel, incorporating microelements in the mesh of the domain, was explored in [116]. Furthermore, a different approach involved the application of the spline fictitious boundary element method (SFBEM) coupled with the response surface method (RSM) for 2D plate structures, as illustrated in [117]. In the domain of defect identification, stochastic inverse BEM (SIBEM) was employed in [118] to determine defect parameters and locations. This information was then applied to the First Order Second Moment method to evaluate the reliability index. Notably, the work by Leonel [119] advanced the understanding of 2D plane structures by evaluating derivatives of the DBEM using the finite difference method (FDM). Subsequently, the First-Order Reliability Method (FORM) was applied to evaluate failure probabilities. In the research presented by Morse [83], a comprehensive analysis was conducted on a plate subjected to the combined effects of bending, tension, and domain load, featuring a centre slant crack. The study employed both the Implicit Differentiation Method (IDM) and the

FDM to derive the sensitivity of crack tip Stress Intensity Factors (SIFs). Additionally, Huang [77] introduced a novel approach for sensitivity evaluation, focusing on derivatives with respect to the local coordinate system, providing an accurate means to account for directional changes during crack propagation. Similar methodologies were applied in the work by the same author [120].

Despite the existing research in this domain, a comprehensive study addressing the application of the DBEM to reliability analysis for shallow shell problems remains a notable gap in the existing literature. This study aims to build upon the foundations laid by Morse [83] and Huang [77], with the objective of formulating a DBEM-based Implicit Differentiation Method (IDM) tailored to the shallow shell problems, hence enabling a precise evaluation of Sensitivity of Stress Intensity Factors (SIFs). Within this framework, the study focuses on a fatigue reliability assessment utilizing the First-Order Reliability Method (FORM). This assessment explicitly considers the uncertainties inherent in fatigue crack growth. The insights derived from this fatigue reliability assessment have the potential to inform real-world engineering scenarios, aiding in the determination of a structure's service life or the establishment of appropriate inspection intervals.

The chapter structure unfolds as follows: Section 4.1 introduces the fatigue reliability analysis and model of fatigue crack growth using the Paris Law. Section 4.2 outlines the derivatives of the DBEM formulations. In Section 4.3, a numerical example featuring a cracked fuselage window structure is presented to demonstrate the application in fracture reliablity analysis. In 4.4, a numerical case study is presented, featuring a shell structure with two cracks and a central hole in the reliability analysis. The results of the reliability analysis are presented. A third numerical example in section 4.5 involving more complex geometry was used for fatigue life reliability assessment to further illustrate possible practical applications of the DBEM-IDM formulations. A comparison of results obtained from FORM and MCS is provided. Further elaboration on the formulation of stress intensity factor derivatives can be found in the Appendix E.

4.1 Fundamental Concept of Fatigue Reliability Analysis

The methodology and algorithm employed for locating the Most Probable Point (MPP) and subsequently assessing the structure's reliability align with the principles introduced in the previous chapter. In this section, the focus is on the core concepts related to structures subject to fatigue

limit states and provides an overview of the process for conducting reliability analysis in the context of fatigue reliability assessment.

Within the domain of fracture mechanics, stress intensity factors play a pivotal role in characterizing the stress field around a crack tip. The critical stress intensity factor associated with fracture behaviour is known as the fracture toughness, denoted as K_{IC}. However, determining K_{IC} is susceptible to various sources of error, including measurement errors, microstructural variability, and variability between specimens, as discussed in [121]. Consequently, K_{IC} must be considered as a random variable. This acknowledgement leads to the expression of the limit state in terms of fracture tolerance.

$$g(\mathbf{Z_1}) = K_{IC} - K_{eff}(\mathbf{Z_1}) \tag{4.1}$$

where $\mathbf{Z_1}$ encompasses the design factors capable of influencing the Stress Intensity Factor (SIF) at the crack tip. As previously introduced in Chapter 2, the effective stress intensity factor around the crack tip, denoted as K_{eff}, can be computed using the Crack Surface Displacement Extrapolation technique (CSDE).

The expression for the fatigue life N of a structure is typically a function of design parameters, loads, and crack growth parameters. However, it's important to note that even if these factors are treated as deterministic values, fatigue crack growth remains inherently stochastic, as discussed in [121]. Hence, reliability analysis is well-suited for addressing such problems marked by substantial uncertainties. The fatigue life, quantified in terms of the number of cyclic loads, can be expressed as follows:

$$N = N(\mathbf{Z_2}) \tag{4.2}$$

where $\mathbf{Z_2}$ contains the design factors that can influence the fatigue life of a structure. The probability of failure can therefore be defined as the probability of the service life N_s exceeding the fatigue life of the structure such that

$$p_f = p(N < N_s) \tag{4.3}$$

consequently, the fatigue limit state function can be written as

$$g(\mathbf{Z_2}) = N(\mathbf{Z_2}) - N_s \tag{4.4}$$

The Paris Law which developed from empirical results has found its wide application in evaluating the fatigue life N, where the crack growth rate da/dN is found to be

$$\frac{da}{dN} = C(\Delta K)^{m_p} \tag{4.5}$$

where a is the crack length, C and m_p are called Paris coefficient and exponent respectively. ΔK is the stress intensity factor range defined as

$$\Delta K = K_{max} - K_{min} = (1 - R)K_{max} \tag{4.6}$$

where $R = \sigma_{min}/\sigma_{max}$ (where σ_{min} and σ_{max} are the minimum and maximum applied stresses respectively). Both C and m in Eq. (4.5) are dependent on the material used, where C has depends on the stress ratio that follows Walker's equation

$$C = \frac{C_0}{(1 - R)^{m_p(1-\gamma)}} \tag{4.7}$$

where γ is the coefficient of the Walker's equation, represents how strongly the stress ratio affects the crack growth rate and C_0 is the interception point when R=0. Once the crack growth rate is determined, the fatigue life can be evaluated by

$$N = \int_{a_0}^{a} \frac{1}{da/dN} da \tag{4.8}$$

where a_0 is an initial crack length, and a is a final crack length.

4.2 The Implicit Differentiation Method (IDM) for Shallow Shell Structure

As mentioned in the previous chapter, the methods for evaluating the derivatives involve IDM and FDM, where FDM follows the same formulation. The IDM formulations for boundary integral equations were outlined in the previous chapter. This chapter only focused on the IDM formulation of the DBEM in section 2.2.4 and hence is outlined in the following.

4.2.1 BEM-IDM Formulations for Shallow Shell Structures with Respect to a Geometrical Variable Z_g

The changing in geometrical parameters does not affect the values of the curvature, therefore for simplification, denote the constant term $C_{\kappa 1} = B\left((1-\nu)\kappa_{\alpha\beta} + \nu\delta_{\alpha\beta}\kappa_{\phi\phi}\right)$. The derivatives of the DBEM displacement integral equations applied for collocations on the upper crack surfaces (as given in equations 2.87 to 2.88):

$$\begin{aligned}
&\frac{1}{2}w_{j,g}\left(x^{+}\right) + \frac{1}{2}w_{j,g}\left(x^{-}\right) + \fint_{\Gamma}\left[P^{*}_{ij,g}w_j + P^{*}_{ij}w_{j,g}\right]d\Gamma \\
&= \int_{\Gamma}\left[W^{*}_{ij,g}p_j + W^{*}_{ij}p_{j,g})\right]d\Gamma \\
&- \int_{\Omega} W^{*}_{i3,g}\kappa_{\alpha\beta}B\frac{1-\nu}{2}\left[u_{\alpha,\beta} + u_{\beta,\alpha} + \frac{2\nu}{1-\nu}u_{\phi,\phi}\delta_{\alpha\beta}\right]d\Omega \\
&- \int_{\Omega} W^{*}_{i3}\kappa_{\alpha\beta}B\frac{1-\nu}{2}\left[u_{\alpha,\beta g} + u_{\beta,\alpha g} + \frac{2\nu}{1-\nu}u_{\phi,\phi g}\delta_{\alpha\beta}\right]d\Omega \\
&- \int_{\Omega}\left[W^{*}_{i3,g}\kappa_{\alpha\beta}C_{\kappa 1}w_3 + W^{*}_{i3}\kappa_{\alpha\beta}C_{\kappa 1}w_{3,g}\right]d\Omega \\
&+ \int_{\Omega}\left[W^{*}_{i3,g}q_3 + W^{*}_{i3}q_{3,g}\right]d\Omega
\end{aligned} \tag{4.9}$$

and

$$\begin{aligned}
&\frac{1}{2}u_{\alpha,g}\left(x^{+}\right) + \frac{1}{2}u_{\alpha,g}\left(x^{-}\right) + \fint_{\Gamma}\left[T^{*}_{\theta\alpha,g}u_\alpha + T^{*}_{\theta\alpha}u_{\alpha,g}\right]d\Gamma \\
&+ \int_{\Gamma}\left[U^{*}_{\theta\alpha,g}C_{\kappa 1}w_3 n_\beta + U^{*}_{\theta\alpha}C_{\kappa 1}w_{3,g}n_\beta + U^{*}_{\theta\alpha}C_{\kappa 1}w_3 n_{\beta,g}\right]d\Gamma \\
&- \int_{\Omega}\left[U^{*}_{\theta\alpha,g}C_{\kappa 1}w_{3,\beta} + U^{*}_{\theta\alpha}C_{\kappa 1}w_{3,\beta g}\right]d\Omega \\
&= \int_{\Gamma}\left[U^{*}_{\theta\alpha,g}t_\alpha + U^{*}_{\theta\alpha}t_{\alpha,g}\right]d\Gamma + \int_{\Omega}\left[U^{*}_{\theta\alpha,g}q_\alpha + U^{*}_{\theta\alpha}q_{\alpha,g}\right]d\Omega
\end{aligned} \tag{4.10}$$

similarly, denote that $C_{\kappa 2} = B\left((1-\nu)\kappa_{\theta\psi} + \nu\delta_{\theta\psi}\kappa_{\phi\phi}\right)$, the derivatives of the DBEM traction integral equations for collocations on the lower crack surfaces (equation 2.89 - 2.91) are:

$$
\begin{aligned}
&\frac{1}{2}p_{\alpha,g}\left(x^{-}\right) - \frac{1}{2}p_{\alpha,g}\left(x^{+}\right) + n_{\beta,g}\left(x^{-}\right)\oint_{\Gamma} P^{*}_{\alpha\beta\gamma}w_{\gamma}d\Gamma \\
&+ n_{\beta}\left(x^{-}\right)\oint_{\Gamma}\left[P^{*}_{\alpha\beta\gamma,g}w_{r} + P^{*}_{\alpha\beta\gamma}w_{\gamma,g}\right]d\Gamma \\
&+ n_{\beta,g}\left(x^{-}\right)\oint_{\Gamma} P^{*}_{\alpha\beta 3}w_{3}d\Gamma + n_{\beta}\left(x^{-}\right)\int_{\Gamma}\left[P^{*}_{\alpha\beta 3,g}w_{3} + P^{*}_{\alpha\beta 3}w_{3,g}\right]d\Gamma \\
&= n_{\beta,g}\left(x^{-}\right)\oint_{\Gamma} W^{*}_{\alpha\beta\gamma}p_{\gamma}d\Gamma + n_{\beta}(x^{-})\oint_{\Gamma}\left[W^{*}_{\alpha\beta\gamma,g}p_{\gamma} + W^{*}_{\alpha\beta\gamma}p_{\gamma,g}\right]d\Gamma \\
&+ n_{\beta,g}\left(x^{-}\right)\int_{\Gamma} W^{*}_{\alpha\beta 3}p_{3}d\Gamma + n_{\beta}\left(x^{-}\right)\int_{\Gamma}\left[W^{*}_{\alpha\beta 3,g}p_{3} + W^{*}_{\alpha\beta 3}p_{3,g}\right]d\Gamma \\
&- n_{\beta,g}\left(x^{-}\right)\int_{\Omega}\kappa_{\theta\psi}B\frac{1-\nu}{2}\left(u_{\theta,\psi} + u_{\psi,\theta} + \frac{2\nu}{1-\nu}u_{\phi,\phi}\delta_{\theta\psi}\right)W^{*}_{\alpha\beta 3}d\Omega \\
&- n_{\beta}\left(x^{-}\right)\int_{\Omega}\kappa_{\theta\psi}B\frac{1-\nu}{2}\left(u_{\theta,\psi g} + u_{\psi,\theta g} + \frac{2\nu}{1-\nu}u_{\phi,\phi g}\delta_{\theta\psi}\right)W^{*}_{\alpha\beta 3}d\Omega \\
&- n_{\beta}(x^{-})\int_{\Omega}\kappa_{\theta\psi}B\frac{1-\nu}{2}\left(u_{\theta,\psi} + u_{\psi,\theta} + \frac{2\nu}{1-\nu}u_{\phi,\phi}\delta_{\theta\psi}\right)W^{*}_{\alpha\beta 3,g}d\Omega \\
&- n_{\beta,g}\left(x^{-}\right)\int_{\Omega}\kappa_{\theta\psi}C_{\kappa 2}w_{3}W^{*}_{\alpha\beta 3}d\Omega \\
&- n_{\beta}\left(x^{-}\right)\int_{\Omega}\kappa_{\theta\psi}C_{\kappa 2}\left[w_{3,g}W^{*}_{\alpha\beta 3} + w_{3}W^{*}_{\alpha\beta 3,g}\right]d\Omega \\
&+ n_{\beta,g}\left(x^{-}\right)\int_{\Omega} W^{*}_{\alpha\beta 3}q_{3}d\Omega + n_{\beta}\left(x^{-}\right)\int_{\Omega}\left[W^{*}_{\alpha\beta 3,g}q_{3} + W^{*}_{\alpha\beta 3}q_{3,g}\right]d\Omega
\end{aligned}
\tag{4.11}
$$

and

$$
\begin{aligned}
&\frac{1}{2}p_{3,g}\left(x^{-}\right)-\frac{1}{2}p_{3,g}\left(x^{+}\right)+n_{\beta,g}\left(x^{-}\right)\oint_{\Gamma}P^{*}_{3\beta\gamma}w_{\gamma}d\Gamma\\
&+n_{\beta}\left(x^{-}\right)\oint_{\Gamma}\left[P^{*}_{3\beta\gamma,g}w_{\gamma}+P^{*}_{3\beta\gamma}w_{\gamma,g}\right]d\Gamma\\
&+n_{\beta,g}\left(x^{-}\right)\oint_{\Gamma}P^{*}_{3\beta3}w_{3}d\Gamma(x)+n_{\beta}\left(x^{-}\right)\oint_{\Gamma}\left[P^{*}_{3\beta3,g}w_{3}+P^{*}_{3\beta3}w_{3,g}\right]d\Gamma\\
&=n_{\beta,g}\left(x^{-}\right)\int_{\Gamma}W^{*}_{3\beta\gamma}p_{\gamma}d\Gamma+n_{\beta}\left(x^{-}\right)\int_{\Gamma}\left[W^{*}_{3\beta\gamma,g}p_{\gamma}+W^{*}_{3\beta3}p_{\gamma,g}\right]d\Gamma\\
&+n_{\beta,g}\left(x^{-}\right)\oint_{\Gamma}W^{*}_{3\beta3}p_{3}d\Gamma+n_{\beta}\left(x^{-}\right)\oint_{\Gamma}\left[W^{*}_{3\beta3,g}p_{3}+W^{*}_{3\beta3}p_{3,g}\right]d\Gamma\\
&-n_{\beta,g}\left(x^{-}\right)\int_{\Omega}\kappa_{\theta\psi}B\frac{1-\nu}{2}\left(u_{\theta,\psi}(X)+u_{\psi,\theta}+\frac{2\nu}{1-\nu}u_{\phi,\phi}\delta_{\theta\psi}\right)W^{*}_{3\beta3}d\Omega\\
&-n_{\beta}\left(x^{-}\right)\int_{\Omega}\kappa_{\theta\psi}B\frac{1-\nu}{2}\left[\left(u_{\theta,\psi g}+u_{\psi,\theta g}+\frac{2\nu}{1-\nu}u_{\phi,\phi g}\delta_{\theta\psi}\right)W^{*}_{3\beta3}\right.\\
&\left.+\left(u_{\theta,\psi}+u_{\psi,\theta}(X)+\frac{2\nu}{1-\nu}u_{\phi,\phi}\delta_{\theta\psi}\right)W^{*}_{3\beta3,g}\right]d\Omega\\
&-n_{\beta,g}\left(x^{-}\right)\int_{\Omega}\kappa_{\theta\psi}C_{\kappa2}w_{3}W^{*}_{3\beta3}d\Omega\\
&-n_{\beta}\left(x^{-}\right)\int_{\Omega}\kappa_{\theta\psi}C_{\kappa2}\left[w_{3,g}W^{*}_{3\beta3}+w_{3}W^{*}_{3\beta3,g}\right]d\Omega\\
&+n_{\beta,g}\left(x^{-}\right)\int_{\Omega}W^{*}_{3\beta3}q_{3}d\Omega+n_{\beta}\left(x^{-}\right)\int_{\Omega}\left[W^{*}_{3\beta3,g}q_{3}+W^{*}_{3\beta3}q_{3,g}\right]d\Omega
\end{aligned}
\tag{4.12}
$$

and

$$
\begin{aligned}
&\frac{1}{2}t_{\alpha,g}\left(x^{-}\right)-\frac{1}{2}t_{\alpha,g}\left(x^{+}\right)+n_{\beta,g}\left(x^{-}\right)\oint_{\Gamma}T^{*}_{\alpha\beta\gamma}u_{\gamma}d\Gamma\\
&+n_{\beta}\left(x^{-}\right)\oint_{\Gamma}\left[T^{*}_{\alpha\beta\gamma,g}u_{\gamma}+T^{*}_{\alpha\beta\gamma}u_{\gamma,g}\right]d\Gamma\\
&+n_{\beta,g}(x^{-})\oint_{\Gamma}U^{*}_{\alpha\beta\gamma}C_{\kappa2}w_{3}n_{\psi}(x)d\Gamma+n_{\beta}(x^{-})\oint_{\Gamma}U^{*}_{\alpha\beta\gamma,g}C_{\kappa2}w_{3}n_{\psi}d\Gamma\\
&+n_{\beta}\left(x^{-}\right)\oint_{\Gamma}U^{*}_{\alpha\beta\gamma}C_{\kappa2}\left[w_{3,g}n_{\psi}(x)+w_{3}n_{\psi,g}\right]d\Gamma\\
&-n_{\beta,g}\left(x^{-}\right)\int_{\Omega}U^{*}_{\alpha\beta\gamma}C_{\kappa2}w_{3,\beta}d\Omega\\
&-n_{\beta}\left(x^{-}\right)\int_{\Omega}\left[U^{*}_{\alpha\beta\gamma,g}C_{\kappa2}w_{3,\beta}+U^{*}_{\alpha\beta\gamma}C_{\kappa2}w_{3,\beta g}\right]d\Omega\\
&=n_{\beta,g}\left(x^{-}\right)\oint_{\Gamma}U^{*}_{\alpha\beta\gamma}t_{\gamma}d\Gamma+n_{\beta}\left(x^{-}\right)\oint_{\Gamma}\left[U^{*}_{\alpha\beta\gamma,g}t_{\gamma}+U^{*}_{\alpha\beta\gamma}t_{\gamma,g}\right]d\Gamma\\
&+n_{\beta,g}\left(x^{-}\right)\int_{\Omega}U^{*}_{\alpha\beta\gamma}q_{\gamma}d\Omega+n_{\beta}\left(x^{-}\right)\int_{\Omega}\left[U^{*}_{\alpha\beta\gamma,g}q_{\gamma}+U^{*}_{\alpha\beta\gamma}q_{\gamma,g}\right]d\Omega\\
&+\frac{1}{2}n_{\beta,g}\left(x^{-}\right)C_{\kappa2}w_{3}\left(x^{-}\right)+\frac{1}{2}n_{\beta}\left(x^{-}\right)C_{\kappa2}w_{3,g}\left(x^{-}\right)
\end{aligned}
\tag{4.13}
$$

The system of equations for the IDM-based BEM formulations is $\mathbf{H}_{,\mathbf{g}}\mathbf{u} + \mathbf{H}\mathbf{u}_{,\mathbf{g}} = \mathbf{G}_{,\mathbf{g}}\mathbf{t} + \mathbf{G}\mathbf{t}_{,\mathbf{g}}$, where the definitions of the terms $\mathbf{H}$, $\mathbf{G}$, $\mathbf{t}$, $\mathbf{u}$ are the same in the section 2.2.2. The terms $\mathbf{H}_{,\mathbf{g}}$, $\mathbf{G}_{,\mathbf{g}}$, $\mathbf{t}_{,\mathbf{g}}$, $\mathbf{u}_{,\mathbf{g}}$ are the derivatives of these terms. Therefore, the system of equations can be rearranged as:

$$\mathbf{A}\mathbf{X}_{,\mathbf{g}} = \mathbf{F}_{,\mathbf{g}} - \mathbf{A}_{,\mathbf{g}}\mathbf{X} \tag{4.14}$$

The matrices $\mathbf{A}$ and $\mathbf{X}$ can be obtained from Eq.(2.76). Therefore, only the right-hand side of the equation needs to be evaluated. The boundary integral equations for displacement and traction are computed in terms of the nodal coordinates of the collocation points and the field points. The derivatives of the integral equations are functions of the changes in the nodal coordinates as can be seen in Appendix **??**. Therefore if the change in the geometrical variable Z_g does not produce a change in the nodal coordinates of both the collocation point and field point on a boundary, the corresponding entries in $\mathbf{X}_{,\mathbf{g}}$ will be zero. Consequently, the entries in $\mathbf{A}_{,\mathbf{g}}$ corresponding to this case do not need to be calculated, thereby reducing the computational cost of the IDM.

4.2.2 BEM-IDM Formulations for Shallow Shell Structures with Respect to Curvature Z_ρ

The derivatives of the DBEM displacement integral equation for collocations on the upper crack surface with respect to curvature are as follows:

$$\begin{aligned}
&\frac{1}{2}w_{j,\rho}\left(x^{+}\right) + \frac{1}{2}w_{j,\rho}\left(x^{-}\right) + \oint_{\Gamma} P^{*}_{ij}w_{j,\rho}d\Gamma \\
&= \int_{\Gamma} W^{*}_{ij}p_{j,\rho}d\Gamma \\
&- \int_{\Omega} W^{*}_{i3}\kappa_{\alpha\beta,\rho}B\frac{1-\nu}{2}\left[u_{\alpha,\beta} + u_{\beta,\alpha} + \frac{2\nu}{1-\nu}u_{\phi,\phi}\delta_{\alpha\beta}\right]d\Omega \\
&- \int_{\Omega} W^{*}_{i3}\kappa_{\alpha\beta}B\frac{1-\nu}{2}\left[u_{\alpha,\beta\rho} + u_{\beta,\alpha\rho} + \frac{2\nu}{1-\nu}u_{\phi,\phi\rho}\delta_{\alpha\beta}\right]d\Omega \\
&- \int_{\Omega} W^{*}_{i3}\left[\kappa_{\alpha\beta,\rho}C_{\kappa 1}w_3 + \kappa_{\alpha\beta}C_{\kappa 1,\rho}w_3 + \kappa_{\alpha\beta}C_{\kappa 1}w_{3,\rho}\right]d\Omega \\
&+ \int_{\Omega} W^{*}_{i3}q_{3,\rho}d\Omega
\end{aligned} \tag{4.15}$$

and

$$\begin{aligned}
&\frac{1}{2}u_{\alpha,\rho}\left(x^{+}\right)+\frac{1}{2}u_{\alpha,\rho}\left(x^{-}\right)+\oint_{\Gamma}T^{*}_{\theta\alpha}u_{\alpha,\rho}d\Gamma\\
&+\int_{\Gamma}U^{*}_{\theta\alpha}\left[C_{\kappa 1,\rho}w_{3}+C_{\kappa 1}w_{3,\rho}\right]n_{\beta}d\Gamma\\
&-\int_{\Omega}U^{*}_{\theta\alpha}\left[C_{\kappa 1,\rho}w_{3,\beta}+C_{\kappa 1}w_{3,\beta\rho}\right]d\Omega\\
&=\int_{\Gamma}U^{*}_{\theta\alpha}t_{\alpha,\rho}d\Gamma+\int_{\Omega}U^{*}_{\theta\alpha}q_{\alpha,\rho}d\Omega
\end{aligned}\tag{4.16}$$

where $C_{\kappa 1,\rho}=B\left[\kappa_{\alpha\beta,\rho}(1-\nu)+\nu\delta_{\alpha\beta}\kappa_{\phi\phi,\rho}\right]$.

The derivatives of the DBEM traction integral equation for collocations on the lower crack surface with respect to the curvature is:

$$\begin{aligned}
&\frac{1}{2}p_{\alpha,\rho}\left(x^{-}\right)-\frac{1}{2}p_{\alpha,\rho}\left(x^{+}\right)+n_{\beta}\left(x^{-}\right)\oint_{\Gamma}P^{*}_{\alpha\beta\gamma}w_{\gamma,\rho}d\Gamma\\
&+n_{\beta}\left(x^{-}\right)\oint_{\Gamma}P^{*}_{\alpha\beta 3}w_{3,\rho}d\Gamma\\
&=n_{\beta}\left(x^{-}\right)\oint_{\Gamma}W^{*}_{\alpha\beta\gamma}p_{\gamma,\rho}d\Gamma+n_{\beta}\left(x^{-}\right)\int_{\Gamma}W^{*}_{\alpha\beta 3}p_{3,\rho}d\Gamma\\
&-n_{\beta}(x^{-})\int_{\Omega}\kappa_{\theta\psi,\rho}B\frac{1-v}{2}\left(u_{\theta,\psi}+u_{\psi,\theta}+\frac{2v}{1-\nu}u_{\phi,\phi}\delta_{\theta\psi}\right)W^{*}_{\alpha\beta 3}d\Omega\\
&-n_{\beta}(x^{-})\int_{\Omega}\kappa_{\theta\psi}B\frac{1-v}{2}\left(u_{\theta,\psi\rho}+u_{\psi,\theta\rho}+\frac{2v}{1-\nu}u_{\phi,\phi\rho}\delta_{\theta\psi}\right)W^{*}_{\alpha\beta 3}d\Omega\\
&-n_{\beta}\left(x^{-}\right)\int_{\Omega}\left[\kappa_{\theta\psi,\rho}C_{\kappa 2}w_{3}+\kappa_{\theta\psi}C_{\kappa 2,\rho}w_{3}+\kappa_{\theta\psi}C_{\kappa 2}w_{3,\rho}\right]W^{*}_{\alpha\beta 3}d\Omega\\
&+n_{\beta}\left(x^{-}\right)\int_{\Omega}W^{*}_{\alpha\beta 3}q_{3,\rho}d\Omega
\end{aligned}\tag{4.17}$$

and

$$\begin{aligned}
&\frac{1}{2}p_{3,\rho}\left(x^{-}\right)-\frac{1}{2}p_{3,\rho}\left(x^{+}\right)+n_{\beta}\left(x^{-}\right)\oint_{\Gamma}P^{*}_{3\beta\gamma}w_{\gamma,\rho}d\Gamma\\
&+n_{\beta}\left(x^{-}\right)\oint_{\Gamma}P^{*}_{3\beta3}w_{3,\rho}d\Gamma\\
&=n_{\beta}\left(x^{-}\right)\int_{\Gamma}W^{*}_{3\beta\gamma}p_{\gamma,\rho}d\Gamma+n_{\beta}\left(x^{-}\right)\oint_{\Gamma}W^{*}_{3\beta3}p_{3,\rho}d\Gamma\\
&-n_{\beta}(x^{-})\int_{\Omega}\kappa_{\theta\psi,\rho}B\frac{1-\nu}{2}\left(u_{\theta,\psi}+u_{\psi,\theta}+\frac{2\nu}{1-\nu}u_{\phi,\phi}\delta_{\theta\psi}\right)W^{*}_{3\beta3}d\Omega\\
&-n_{\beta}(x^{-})\int_{\Omega}\kappa_{\theta\psi}B\frac{1-\nu}{2}\left(u_{\theta,\psi\rho}+u_{\psi,\theta\rho}+\frac{2\nu}{1-\nu}u_{\phi,\phi\rho}(X)\delta_{\theta\psi}\right)W^{*}_{3\beta3}d\Omega\\
&-n_{\beta}\left(x^{-}\right)\int_{\Omega}\left[\kappa_{\theta\psi,\rho}C_{\kappa2}w_{3}+\kappa_{\theta\psi}C_{\kappa2,\rho}w_{3}+\kappa_{\theta\psi}C_{\kappa2}w_{3,\rho}\right]W^{*}_{3\beta3}d\Omega\\
&+n_{\beta}\left(x^{-}\right)\int_{\Omega}W^{*}_{3\beta3}q_{3,\rho}d\Omega
\end{aligned}\tag{4.18}$$

and

$$\begin{aligned}
&\frac{1}{2}t_{\alpha,\rho}\left(x^{-}\right)-\frac{1}{2}t_{\alpha,\rho}\left(x^{+}\right)+n_{\beta}\left(x^{-}\right)\oint_{\Gamma}T^{*}_{\alpha\beta\gamma}u_{\gamma,\rho}d\Gamma\\
&+n_{\beta}\left(x^{-}\right)\oint_{\Gamma}U^{*}_{\alpha\beta\gamma}\left[C_{\kappa2,\rho}w_{3}+C_{\kappa2}w_{3,\rho}\right]n_{\psi}d\Gamma\\
&-n_{\beta}\left(x^{-}\right)\int_{\Omega}U^{*}_{\alpha\beta\gamma}\left[C_{\kappa2,\rho}w_{3,\beta}+C_{\kappa2}w_{3,\beta\rho}\right]d\Omega\\
&=n_{\beta}\left(x^{-}\right)\oint_{\Gamma}U^{*}_{\alpha\beta\gamma}t_{\gamma,\rho}d\Gamma+n_{\beta}\left(x^{-}\right)\int_{\Omega}U^{*}_{\alpha\beta\gamma}q_{\gamma,\rho}d\Omega\\
&+\frac{1}{2}n_{\beta}\left(x^{-}\right)\left[C_{\kappa2,\rho}w_{3}\left(x^{-}\right)+C_{\kappa2}w_{3,\rho}\left(x^{-}\right)\right]
\end{aligned}\tag{4.19}$$

where $C_{\kappa2}=B\left((1-\nu)\kappa_{\theta\psi,\rho}+\nu\delta_{\theta\psi,\rho}\kappa_{\phi\phi,\rho}\right)$. In terms of the formation of the system matrix, the sensitivity of the SIFs is the same as for the derivative with respect to a geometrical variable.

4.2.3 Evaluation of the Stress Intensity Factor Sensitivity

The sensitivity of the stress intensity factors with respect to certain geometrical variables or curvature can be derived from the above equation. The derivatives of $\{K\}$ can be expressed as:

$$\begin{aligned}
K_{1b,g} &= \frac{Eh^3}{48\sqrt{r}}\sqrt{\frac{\pi}{2}}\left\{\Delta\phi_{2,g} - \frac{r_{,g}}{2r}\Delta\phi_2\right\} \\
K_{2b,g} &= \frac{Eh^3}{48\sqrt{r}}\sqrt{\frac{\pi}{2}}\left\{\Delta\phi_{1,g} - \frac{r_{,g}}{2r}\Delta\phi_1\right\} \\
K_{3b,g} &= \frac{5Eh}{24(1+\nu)\sqrt{r}}\sqrt{\frac{\pi}{2}}\left\{\Delta w_{3,g} - \frac{r_{,g}}{2r}\Delta w_3\right\} \\
K_{1m,g} &= \frac{Eh\sqrt{2\pi}}{8\sqrt{r}}\left\{\Delta u_{2,g} - \frac{r_{,g}}{2r}\Delta u_2\right\} \\
K_{2m,g} &= \frac{Eh\sqrt{2\pi}}{8\sqrt{r}}\left\{\Delta u_{1,g} - \frac{r_{,g}}{2r}\Delta u_1\right\}
\end{aligned} \tag{4.20}$$

by applying the extrapolation in Eq. (2.98), the sensitivities of the stress intensity factors are:

$$\{K\}_{,g}^{tip} = RRB_{,g}\{K\}^{BB'} + RRB\{K\}_{,g}^{BB'} - RRA_{,g}\{K\}^{AA'} - RRA\{K\}_{,g}^{AA'} \tag{4.21}$$

where

$$\begin{aligned}
RRA &= \frac{r_{BB'}}{r_{AA'} - r_{BB'}} \qquad RRB = \frac{r_{AA'}}{r_{AA'} - r_{BB'}} \\
RRA_{,g} &= \frac{r_{BB',g}}{r_{AA'} - r_{BB'}} - \frac{r_{BB'}(r_{AA',g} - r_{BB',g})}{(r_{AA'} - r_{BB'})^2} \\
RRB_{,g} &= \frac{r_{AA',g}}{r_{AA'} - r_{BB'}} - \frac{r_{AA'}(r_{AA',g} - r_{BB',g})}{(r_{AA'} - r_{BB'})^2}
\end{aligned} \tag{4.22}$$

The sensitivities of the maximum stress intensity factors were taken into consideration. The maximum SIFs were found at both the upper and lower surfaces of the shell. For this study, the SIF at the upper surface was considered, and the maximum SIF across the thickness of the shell is given by:

$$\begin{aligned}
[1 + \frac{h}{4}(\frac{1}{R_1} + \frac{1}{R_2})]K_I^{max} &= \frac{1}{h}K_{1m} + \frac{6}{h^2}K_{1b} \\
[1 + \frac{h}{4}(\frac{1}{R_1} + \frac{1}{R_2})]K_{II}^{max} &= \frac{1}{h}K_{2m} + \frac{6}{h^2}K_{2b} \\
[1 + \frac{h}{4}(\frac{1}{R_1} + \frac{1}{R_2})]K_{III}^{max} &= \frac{3}{2h}K_{3b}
\end{aligned} \tag{4.23}$$

Note that the curvature-related term is introduced there $T_R = [1 + \frac{h}{4}(\frac{1}{R_1} + \frac{1}{R_2})]$. The maximum SIF of K for different fracture modes can be found by dividing the term T_R. The derivatives of the maximum SIF can be found by:

$$\begin{aligned}
[1 + \frac{h}{4}(\frac{1}{R_1} + \frac{1}{R_2})]K_{I,g}^{max} &= \frac{1}{h}K_{1m,g} + \frac{6}{h^2}K_{1b,g} \\
[1 + \frac{h}{4}(\frac{1}{R_1} + \frac{1}{R_2})]K_{II,g}^{max} &= \frac{1}{h}K_{2m,g} + \frac{6}{h^2}K_{2b,g} \\
[1 + \frac{h}{4}(\frac{1}{R_1} + \frac{1}{R_2})]K_{III,g}^{max} &= \frac{3}{2h}K_{3b,g}
\end{aligned} \tag{4.24}$$

Similarly, $K_{,g}^{max}$ for different fracture modes can be found by dividing the term T_R. The corresponding individual maximum SIF for different fracture modes are denoted as K_{Im},K_{IIm},K_{Ib},K_{IIb},K_{IIIb}. The derivatives of the maximum SIF with respect to curvature and thickness are given in Appendix E. The effective SIF can be calculated by considering the contribution from both the bending and tension stresses.

$$K_{eff} = \sqrt{EG_{eff}} \tag{4.25}$$

where G_{eff} is the effective energy release rate

$$G_{eff} = G_1 + \alpha(G_2 + G_3 + G_4 + G_5) \tag{4.26}$$

$$\alpha = \sqrt{\frac{|\Delta K_{Ib}|}{|\Delta K_{Ib}| + |\Delta K_{Im}|}} \tag{4.27}$$

the energy release rate components were defined as:

$$\begin{aligned}
G_1 = \frac{K_{Im}^2}{E}, \quad G_2 = \frac{K_{IIm}^2}{E}, \quad G_3 = \frac{\pi K_{Ib}^2}{3E}, \\
G_4 = \frac{\pi K_{IIb}^2}{E}, \quad G_5 = \frac{8\pi(1+\nu)K_{IIIb}^2}{5E}
\end{aligned} \tag{4.28}$$

the derivatives of the effective SIF with respect to the change in some geometrical variable can be calculated as:

$$K_{eff,g} = \frac{E}{2K_{eff}}G_{eff,g} \tag{4.29}$$

and the derivatives of the energy release rate components are:

$$\begin{aligned} G_{1,g} &= \frac{2}{E} K_{Im} K_{Im,g} \\ G_{2,g} &= \frac{2}{E} K_{IIm} K_{IIm,g} \\ G_{3,g} &= \frac{2\pi}{3E} K_{Ib} K_{Ib,g} \\ G_{4,g} &= \frac{2\pi}{E} K_{IIb} K_{IIb,g} \\ G_{5,g} &= \frac{16(1+\nu)\pi}{5E} K_{IIIb} K_{IIIb,g} \end{aligned} \tag{4.30}$$

where

$$\alpha_{,g} = \frac{1}{2\alpha} \frac{|\Delta K_{Ib,g}|(|\Delta K_{Ib}| + |\Delta K_{Im}|) - |\Delta K_{Ib}|(|\Delta K_{Ib,g}| + |\Delta K_{Im,g}|)}{(|\Delta K_{Ib}| + |\Delta K_{Im}|)^2} \tag{4.31}$$

The derivatives of the stress intensity factors with respect to the curvature and thickness were derived using the same method. The detailed formulation is shown in Appendix E.

4.3 Fracture Reliability analysis of cracked fuselage window structure

A numerical investigation was conducted on a fuselage window structure featuring a crack subjected to membrane, bending, and uniform pressure loads. The structure is composed of Aluminium 6061-T6 and is modelled using 40 quadratic elements for the outer boundaries and 48 quadratic elements for the inner boundaries. The initial crack is represented by 4 elements, and a total of 78 DRM points, uniformly distributed within the domain, were employed. To model crack propagation, 2 quadratic elements are incrementally added to the tip of the propagating crack on both the upper and lower surfaces.

Figure 4.1 illustrates the geometry of the structure, highlighting region A as the location of the crack, initiated at the corner of the window frame, which typically experiences the highest stress concentration. The length of the initial crack was set as with a length of $0.02m$. The outer geometries were considered as fixed where $W_1 = 1m$, $L_1 = 1m$ and $R_1 = 0.1m$. The mesh configuration of the structure is presented in Figure 4.2(a), while a detailed view of the mesh

around the crack is presented in Figure 4.2(b). The mesh density near the crack area is increased to ensure that the mesh size around the corner is comparable to that on the crack surface.

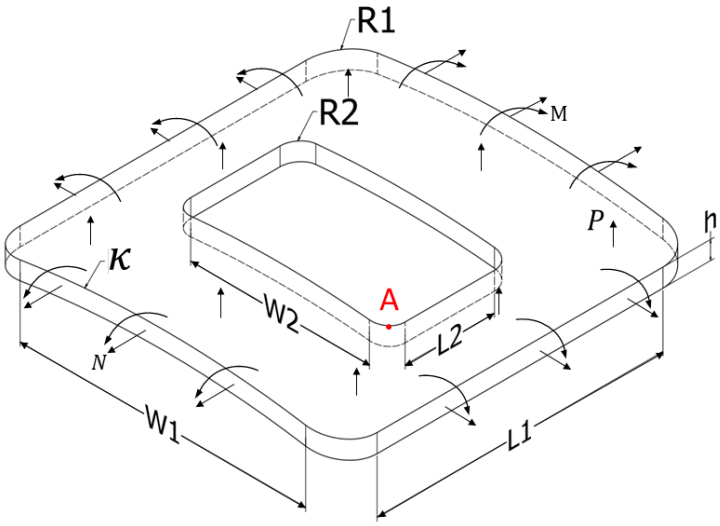


Figure 4.1: The geometry of the shallow shell fuselage window structure. The window structure consists of inner boundaries and outer boundaries with a crack initiated at point A. The loading consists of bending moment, tension and domain pressure.

Table 4.1: Details of the shell structure parameters and random variables used in the reliability analysis.

Z_i	U_i	Parameter	Description	Distribution	Mean	COV
Z_1	U_1	W_2	Inner width	Lognormal	$0.5m$	0.01
Z_2	U_2	L_2	Inner length	Lognormal	$0.25m$	0.01
Z_3	U_3	R_2	Inner radius	Lognormal	$0.05m$	0.01
Z_4	U_4	h	Thickness	Lognormal	$0.05m$	0.01
Z_5	U_5	κ	Curvature	Lognormal	$0.1m^{-1}$	0.01
Z_6	U_6	N	Boundary traction	Lognormal	$0.8\ MNm^{-1}$	0.1
Z_7	U_7	M	Boundary moment	Lognormal	$0.01\ MN$	0.1
Z_8	U_8	P	Domain pressure	Lognormal	$0.01\ MNPa$	0.1
Z_9	U_9	K_{IC}	Fracture toughness	Deterministic	$29\ MNPa$	
Z_{10}	U_{10}	a_0	Initial crack length at A	Deterministic	$0.02\ m$	

In the context of reliability analysis, it is necessary to define the limit state function, which relates the structural resistance to a specific loading condition, as discussed in Section 3.1.2. The LSF is subsequently assessed by applying the FORM to the limit state function. In this study, the limit state function is formulated in terms of the crack tip SIF and fracture toughness. Specifically, the limit state function is defined to ensure that the crack tip SIF remains below the fracture

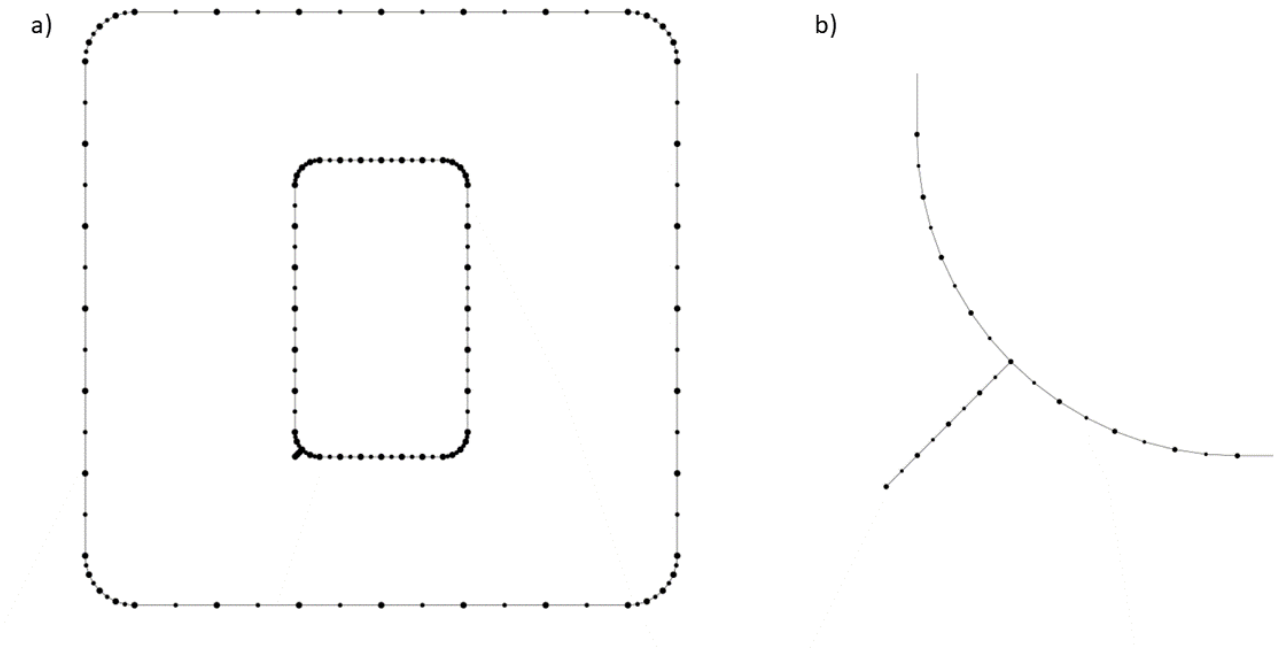


Figure 4.2: a): The meshed of the shell using quadratic elements. b): The meshes around the crack area. Denser meshes were usED around the corner of the window so that the element size on the corner is similar size to the element size on the crack.

toughness value. It is expected that as the crack size increases, the reliability diminishes.

A suitable LSF in terms of the failure criteria used in this work is:

$$g(\mathbf{Z}) = K_{IC} - K_{eff}(\mathbf{X}) \tag{4.32}$$

where K_{IC} is the fracture toughness and K_{eff} is the effective stress intensity factor. The vector $\mathbf{Z}$ contains the design variables that can influence the value of g where $\mathbf{Z} = (W_2, L_2, R_2, h, \kappa, N, M, P, K_{IC})$ and $\mathbf{X}$ consist of the design variables in $\mathbf{Z}$ without the fracture toughness $\mathbf{X} = (W_2, L_2, R_2, h, \kappa, N, M, P)$. The distribution of the above design variables is given in Table. 4.1.

In FORM, the sensitivity of $g(\mathbf{Z})$ with respect to design parameter Z_i is needed. The derivatives of the nodal coordinate with respect to the Z_i can be evaluated analytically in the DBEM-IDM. Variables $Z_1 - Z_3, Z_5$ are geometrical variables and the sensitivities were evaluated analytically using the DBEM-IDM. While the sensitivities with respect to the non-geometrical variables $Z_4, Z_6 - Z_8$ were evaluated using the DBEM-FDM with a step size of $\Delta Z_g' = 1 \times 10^{-2}$. The reliability analysis was conducted over a range of crack lengths. It is expected that the longer the crack propagates, the structure will have lower reliability.

The results of the reliability index against the length of the crack are given in Fig.4.3. The reliability index decreases as the crack length extended which is within the expectation as the structure tends to be more unstable when a larger crack exists. The MPP search algorithm converged successfully in three iterations, and the computational time for evaluating one reliability index was 2475.2 s. As a validation, the results obtained from the IDM-FORM were compared with the results obtained from 40,000 MCS. The computational time required for the MCS was 3.0788×10^7 s. The results are in good agreement with a maximum difference of 2.99% found in a crack length of $0.0725m$.

These outcomes highlight the reliability and accuracy of the proposed IDM-FORM approach, providing an efficient alternative to MCS for evaluating reliability indices in shallow shell structures with cracks.

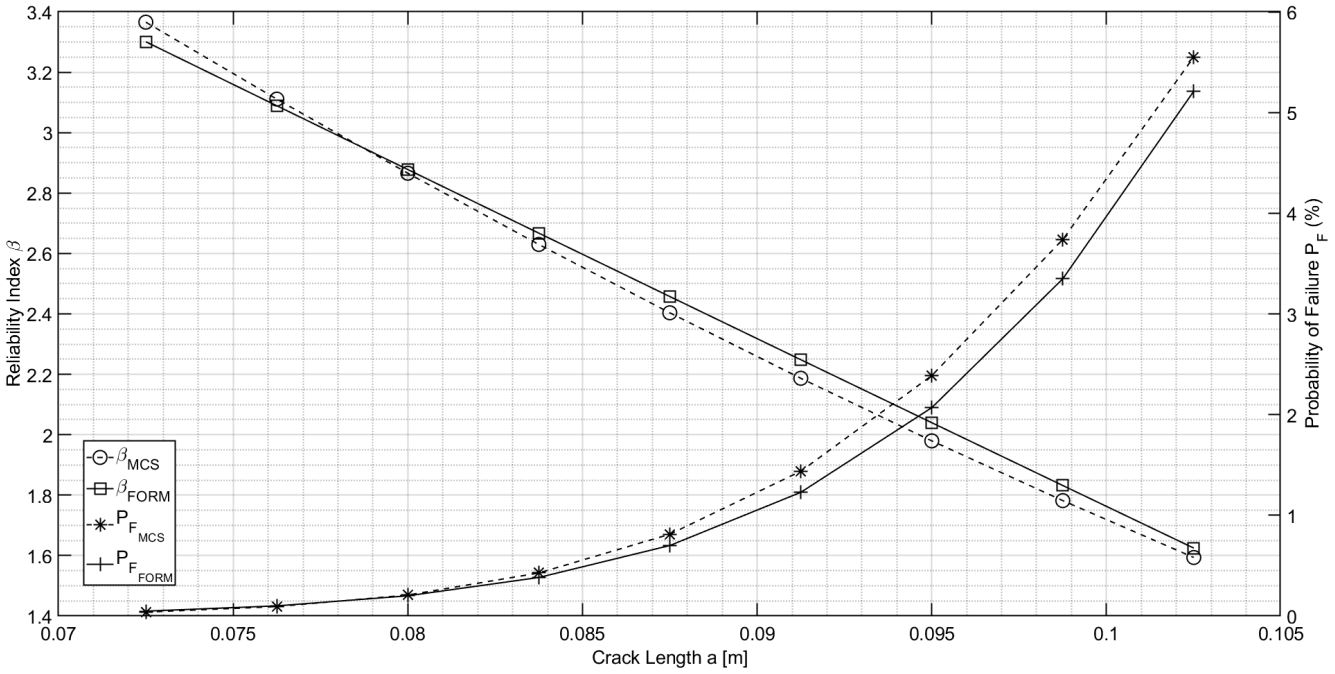


Figure 4.3: Reliability indices and the corresponding probabilities of failure evaluated at each crack length via the IDM-based FORM.

4.4 Reliability analysis of shallow shell with centre hole and two cracks

In this section, an example involves a shallow shell featuring a central hole and two cracks examined. The results obtained from the reliability analysis were compared with those obtained from Monte Carlo Simulations (MCS) to verify the accuracy of the proposed approach.

A numerical example featuring a shallow shell with a central hole and two cracks subjected to a combination of membrane, bending, and uniform pressure loads was investigated. The material of the shell is Aluminium 2024-T4. The geometry of the shallow shell is shown in Figure 4.4a). The shallow shell configuration includes a central hole characterized by a radius of r_1 and two cracks, each with a length of a. A deterministic initial crack length $a_0 = 5.08mm$ was considered. The curvature in the x-direction is denoted as κ_{11} and κ_{22} for y-direction. The shell thickness is defined as h, and the centre hole's position along the x-axis is denoted as b_1. The outer dimensions of the shell remain constant, with a width and length of $101.6mm$. The structural model was discretized using 32 quadratic elements on the outer boundaries, and 32 quadratic elements on the cracks and the central hole (with 8 elements allocated for each crack). Overall 64 DRM points were used and evenly distributed in the domain. The mesh of the boundary nodal points and DRM points is shown in Figure 4.4b). The shell, with a thickness of $2.54mm$, was subjected to tension, bending, and uniform domain pressure loads applied to the top and bottom boundaries. The sensitivity of stress intensity factors was evaluated via both the DBEM-based IDM and the DBEM-based FDM. The example is split into two parts. In the first part, a fracture reliability analysis was performed, with the fracture toughness taken as the failure criterion. The aim is to obtain a critical crack length. The second part involved a fatigue reliability assessment, utilizing the determined critical crack length to deduce the structure's service life.

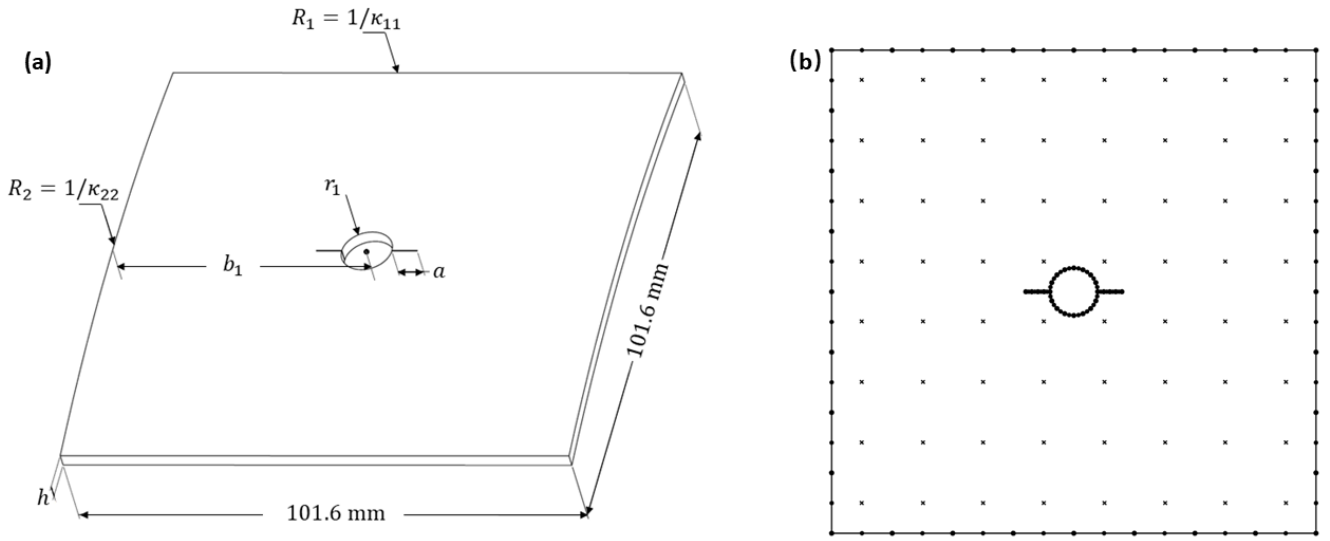


Figure 4.4: a): The geometry of the shallow shell structure used in the numerical example. The shallow shell configuration includes a central hole characterized by a radius of r_1 and two cracks, each with a length of a. The curvature in the x-direction is denoted as κ_{11} and κ_{22} for y-direction. The shell thickness is defined as h, and the centre hole's position along the x-axis is denoted as b_1. The outer dimensions of the shell remain constant, with a width and length of $101.6mm$. b): The boundary element mesh of the shallow shell structure.

4.4.1 Sensitivity of Stress intensity factors

The parameters employed to assess the Sensitivity of the SIFs are detailed in Table 4.2. The evaluation of the sensitivity of the SIF with respect to each parameter were conducted using both the DBEM-FDM and DBEM-IDM and the crack surface displacements extrapolation technique (CSDE) at different crack lengths.

For the DBEM-FDM, the derivative can be evaluated using Eq. (3.14) with an optimal step size denoted as $\Delta Z'_g$ was determined through a convergence test. A range spanning from 0.5 to 10^{-6} was investigated. Larger step sizes influence the precision of the derivatives, while very small step sizes may introduce substantial rounding errors. The optimal step size was selected within the range of $\Delta Z'_g$ that yielded stable and accurate derivative solutions. The results of the convergence test for selecting an optimal step size are illustrated in Figure 4.5. The data indicates that excessively large or small step sizes lead to significant errors in the results. An optimal balance between precision and stability was found within the range of $\Delta Z'_g = 10^{-2} - 10^{-4}$. Consequently, a step size of $\Delta Z'_g = 5 \times 10^{-2}$ was chosen for subsequent examples.

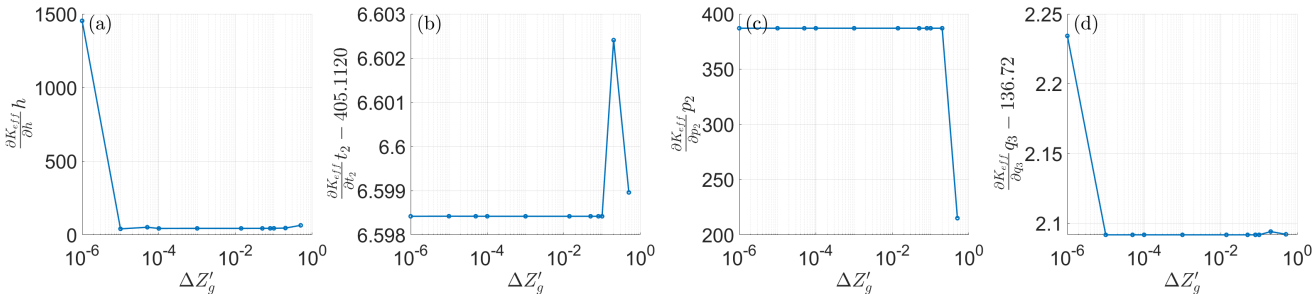


Figure 4.5: A convergence test of derivatives using the Finite Difference Method (FDM) was conducted with respect to: a) thickness, b) membrane load, c) bending load, and d) domain pressure. The test investigated various ranges in the step size $\Delta Z'_g$, spanning from 0.5 to 10^{-6}. The objective of this test was to identify the step size that provides the best balance of numerical precision and stability for parameters.

Table 4.2: The design variables used in the reliability analyses

Z_i	U_i	Parameter	Description	Distribution	Mean	COV
Z_1	U_1	r_1	Radius of the centre hole	Lognormal	$5mm$	0.02
Z_2	U_2	b_1	x-coordinate of the centre hole	Lognormal	$50.8mm$	0.02
Z_3	U_3	κ_{11}	curvature in x direction	Lognormal	$0.03m^{-1}$	0.1
Z_4	U_4	κ_{22}	curvature in y direction	Lognormal	$0.3m^{-1}$	0.1
Z_5	U_5	h	thickness	Lognormal	$2.54mm$	0.02
Z_6	U_6	t_2	membrane traction	Lognormal	$400Nmm^{-1}$	0.05
Z_7	U_7	p_2	bending load	Lognormal	$800N$	0.05
Z_8	U_8	q_3	uniform domain load	Lognormal	$0.15MPa$	0.05
Z_9	U_9	K_{IC}	Fracture toughness	Lognormal	$36.12MPa$ [122]	0.075
Z_{10}	U_{10}	C_0	Paris law Constant	Lognormal	$1.42 \times 10^{-11} \frac{m/cycle}{(MPa\sqrt{m})^{m_p}}$	0.02
Z_{11}	U_{11}	m_p	Paris law exponent	Lognormal	3.59	0.02

The growth of cracks was considered along the horizontal direction only. Geometric variables included the radius and the x-coordinate of the centre hole, with the aim to account for the potential impact of manufacturing uncertainties on SIFs. The variation in the x-coordinate of the centre hole introduces an antisymmetric in terms of the SIF in each crack tip. Therefore, the crack with a higher SIF is chosen and the corresponding derivatives were evaluated in each reliability analysis. The curvature varied more significantly in the y-direction, with a coefficient of variation (COV) set at 0.1. This choice is supported by previous literature [123], underlining its validity for the present study. Additionally, the uncertainty in the fracture toughness was introduced with a lognormal distribution characterized by a COV of 0.075, following established work [124]. The uncertainties in the geometrical parameters, loading and Pairs Law parameters were assigned

according to the previous literature [125–129].

4.4.2 Reliability Analysis

In the reliability analysis, it is essential to formulate the limit state function based on the structural resistance to a given loading condition, as introduced in Section 3.1.2. Subsequently, the reliability can be assessed using the FORM based on the limit state function. In this section, two reliability analyses were performed. The first analysis entails a limit state function formulated in terms of crack tip stress intensity factors and fracture toughness. This formulation ensures that the crack tip SIF remains below the fracture toughness threshold. It is anticipated that the reliability decreases with an increase in the crack size. This reliability analysis is coupled with the probability of detection to establish a permissible crack size, denoted as a_t, while satisfying the given safety criteria. The second reliability analysis was performed with a limit state function defined by the service life of the structure and the cumulative loading cycles required to reach the determined permissible crack size a_t from the first reliability analysis. This analysis accommodates uncertainties inherent in crack growth parameters, which play a vital role in determining an appropriate inspection service interval.

4.4.3 Fracture Reliability Analysis

The first analysis entails a limit state function formulated in terms of crack tip stress intensity factors and fracture toughness. A suitable LSF in terms of the failure criteria used in this work is [130]:

$$g(\mathbf{Z}) = K_{IC} - K_{eff}(\mathbf{X}) \tag{4.33}$$

where K_{IC} denotes the fracture toughness and K_{eff} denotes the effective stress intensity factor. The vector $\mathbf{Z}$ comprises the design variables that exert influence on the value of $g(\mathbf{Z})$, represented as $\mathbf{Z} = (r_1, b_1, \kappa_{11}, \kappa_{22}, h, t_2, p_2, q_3, K_{IC})$, while $\mathbf{X}$ includes the design variables within $\mathbf{Z}$ excluding the fracture toughness, expressed as $\mathbf{X} = (r_1, b_1, \kappa_{11}, \kappa_{22}, h, t_2, p_2, q_3)$. The distributions of these design variables are detailed in Table 4.2. The derivatives of K_{eff} with respect to the design variables were evaluated using the formulation introduced in Section 4.2.3 and Appendix E.

The derivatives of the nodal coordinates with respect to Z_i can be computed analytically using the DBEM-IDM. Among these variables, Z_1 to Z_4 are geometrical variables, and their sensitivities were analytically evaluated using the DBEM-IDM. Conversely, the sensitivities with respect to non-geometrical variables Z_5 to Z_{11} were evaluated using the DBEM-FDM with a step size of $\Delta Z'_g = 5 \times 10^{-2}$. The reliability analysis was carried out over a range of crack lengths. It's anticipated that as the crack propagates, the structure's reliability will decrease.

In the context of tolerance design and considering routine inspection, the tolerable crack size should be chosen to be both below the critical crack size according to a safety criterion while remaining sufficiently to be detectable by inspection techniques [131]. In the reliability analysis, the tolerable crack size can be determined by a required reliability index β, which varies based on the specific application of the structure. Prescribed reliability indices can often be found in standard data sheets, such as the Eurocode - Basis of Structural Design. In this example, targeting reliability of $\beta = 3$ was selected, which is within the range of minimum reliability indices recommended for structures under fatigue limit state conditions.

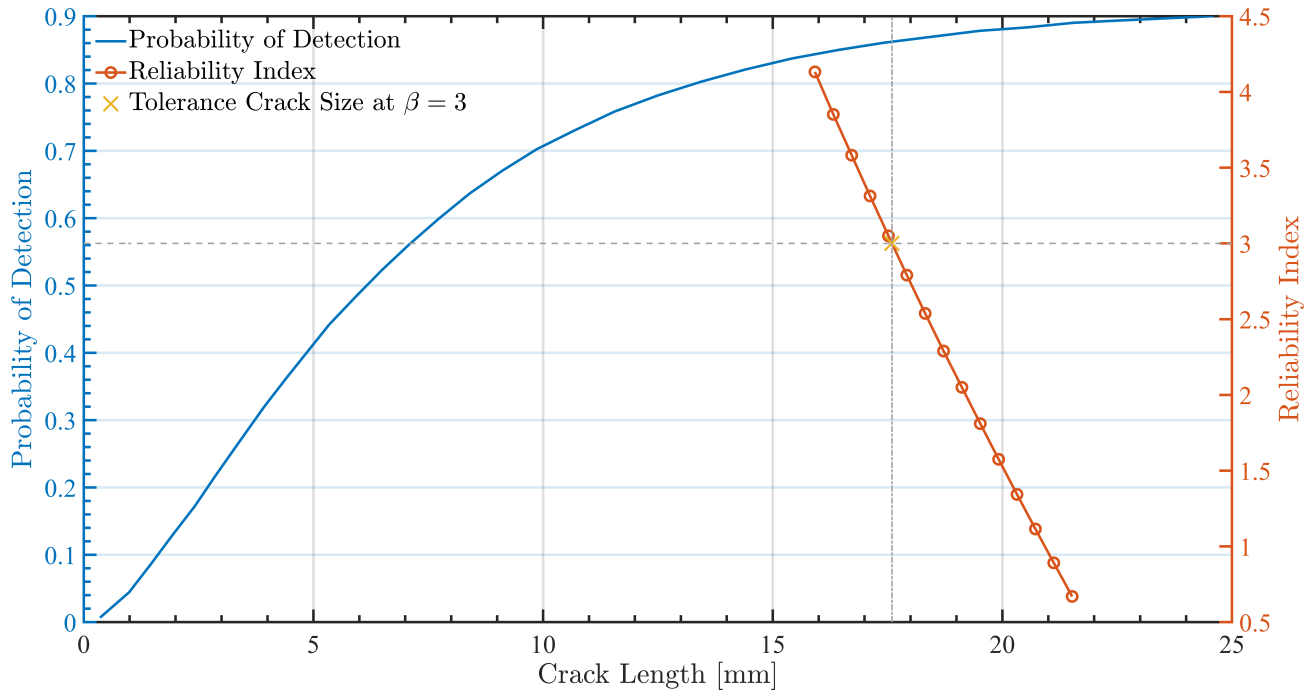


Figure 4.6: The graph shows the reliability index with variations in crack length (shown on the right y-axis). Additionally, an illustration of the probability of detection obtained from handheld eddy-current inspection is presented against the crack size (displayed on the left y-axis) [7]. The tolerable crack size was determined at a reliability index of $\beta = 3$, which corresponds to a crack length of $17.6mm$, as indicated by the cross on the graph. Notably, the corresponding probability of detection is measured at 86.3%.

The results of the reliability index with varying crack lengths are displayed in Fig.4.6, alongside by the probability of detection data of a handheld Eddy-Current inspection [7]. As anticipated, the reliability index displayed a decreasing trend as the crack size increased. The tolerable crack size $a_t = 17.6mm$ was determined to correspond to a reliability index of $\beta = 3$. At this chosen crack size, the Probability of Detection (POD) is of 86.3%, which is considered within an acceptable range. It's worth noting that in practical applications, the selection of targeting reliability and desired POD should encompass additional considerations, including factors such as inspection conditions and risk acceptance levels. For instance, components associated with potential catastrophic failure consequences should have a stricter tolerance design.

4.4.4 Fatigue Reliability Assessment

The second reliability analysis was performed with a limit state function defined by the service life of the structure and the cumulative loading cycles required to reach the determined permissible crack size a_t from the first reliability analysis. For the fatigue crack growth reliability analysis, the limit state function is defined as:

$$g(\mathbf{Z}) = N(\mathbf{Z}) - N_s \tag{4.34}$$

where $N(\mathbf{Z})$ represents the number of cycles required to reach the tolerable crack length a_t, while N_s denotes the service life in terms of the loading cycles experienced by the structure during its service duration. The set of uncertainties influencing fatigue crack growth is denoted by $\mathbf{Z}$, including variables $\mathbf{Z} = (r_1, b_1, \kappa_{11}, \kappa_{22}, h, t_2, p_2, q_3, C, m)$. The precise distribution of these uncertainties can be found in Table 4.2. It's important to note that the Paris law constants C and m are typically established through experimental assessment under specific loading conditions. Consequently, a dependency between the parameters linked to the loading situation and the Paris law constants was considered.

This analysis incorporates two limit state functions to isolate and examine the impact of loading conditions and Paris law constants. The first limit state function introduces uncertainties solely in loading conditions while treating the Paris law constants as deterministic. Conversely, the second limit state function introduces uncertainties in the Paris law constants while maintaining the loadings at their mean values in a deterministic fashion. For both scenarios, it is reasonable to anticipate that shorter service life durations would correspond to higher structural reliability. Two limit state functions were formulated as follows:

- Limit state function I

$$g(\mathbf{Z_1}) = N(\mathbf{Z_1}) - N_s, \quad \text{where } \mathbf{Z_1} = (r_1, b_1, \kappa_{11}, \kappa_{22}, h, t_2, p_2, q_3) \tag{4.35}$$

- Limit state function II

$$g(\mathbf{Z_2}) = N(\mathbf{Z_2}) - N_s, \quad \text{where } \mathbf{Z_2} = (r_1, b_1, \kappa_{11}, \kappa_{22}, h, C, m) \tag{4.36}$$

The fatigue life N of the structure was approximated by the Paris Law such that:

$$N = \int_{a_0}^{a} \frac{1}{C(\Delta K_{eff})^m} da \tag{4.37}$$

where $C = \frac{C_0}{(1-R)^{m(1-\gamma)}}$ and $\Delta K_{eff} = (1-R)K_{eff}$. The stress ratio is set at $R = 0.1$ and $\gamma = 0.68$ in this example. The derivatives of the fatigue life N can be derived in terms of the K_{eff}. This results in the following expressions for the derivatives of N with respect to the design variables:

$$N_{,g} = \int_{a_0}^{a_f} \frac{-m}{C} (\Delta K_{eff})^{-m-1} \Delta K_{eff,g} da \tag{4.38}$$

The derivatives of the effective SIF can be computed using $\Delta K_{eff,g} = (1-R)K_{eff,g}$ with a constant stress ratio R. The integration involved in Eq. (4.37), (4.38) was approximated using trapezoidal numerical integration. This same approach was employed to evaluate the sensitivity of N with respect to the curvature.

The results of the two limit state functions are presented in Fig.4.7 Both sets of results were compared against MCS consisting of N_{mcs} = 40,000 simulations to validate the accuracy of the proposed IDM formulations and their integration with FORM. It is worth noting that the number of MCS simulations was determined such that the mean of the distribution of N_s obtained from MCS converged with a difference of 0.1% and COV of 0.05.

The accuracy achieved an acceptable level, with a maximum difference of 3.67% for LSF I at 23000 *cycles* and 2.40% for LSF II at 16000 *cycles*. Notably, FORM demonstrated a high level of accuracy, particularly for high-reliability indexes that engineers commonly employ.

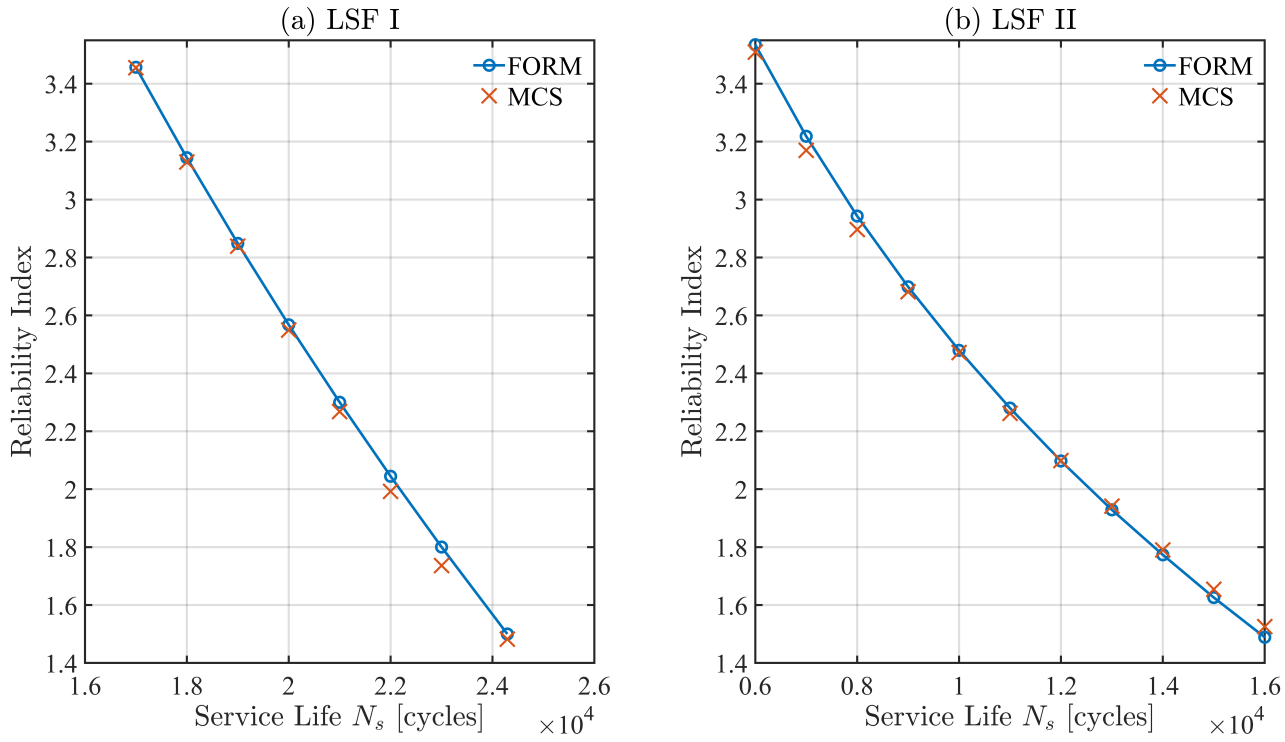


Figure 4.7: The reliability index against the number of loading cycles to which the structure has been exposed (service life) is shown for LSF I (a) and LSF II (b). The results of the Monte Carlo Simulation are illustrated for both LSFs. The highest difference observed in LSF I is at the value of 3.76% at 23000 *cycles*, while in LSF II it is found at 2.40% at 16000 *cycles*.

It is evident that when identical uncertainties in geometrical parameters are considered, the uncertainties in Paris law constants exert a more significant impact on the service life and reliability analysis. This observation underscores the need for more frequent inspections due to the variations in Paris law constants. The outcomes presented above illustrate the combined influence of parameters. To separate the effects of individual parameters, a parametric analysis was conducted, where a single parameter was treated as uncertain in the reliability analysis while the remaining parameters as deterministic.

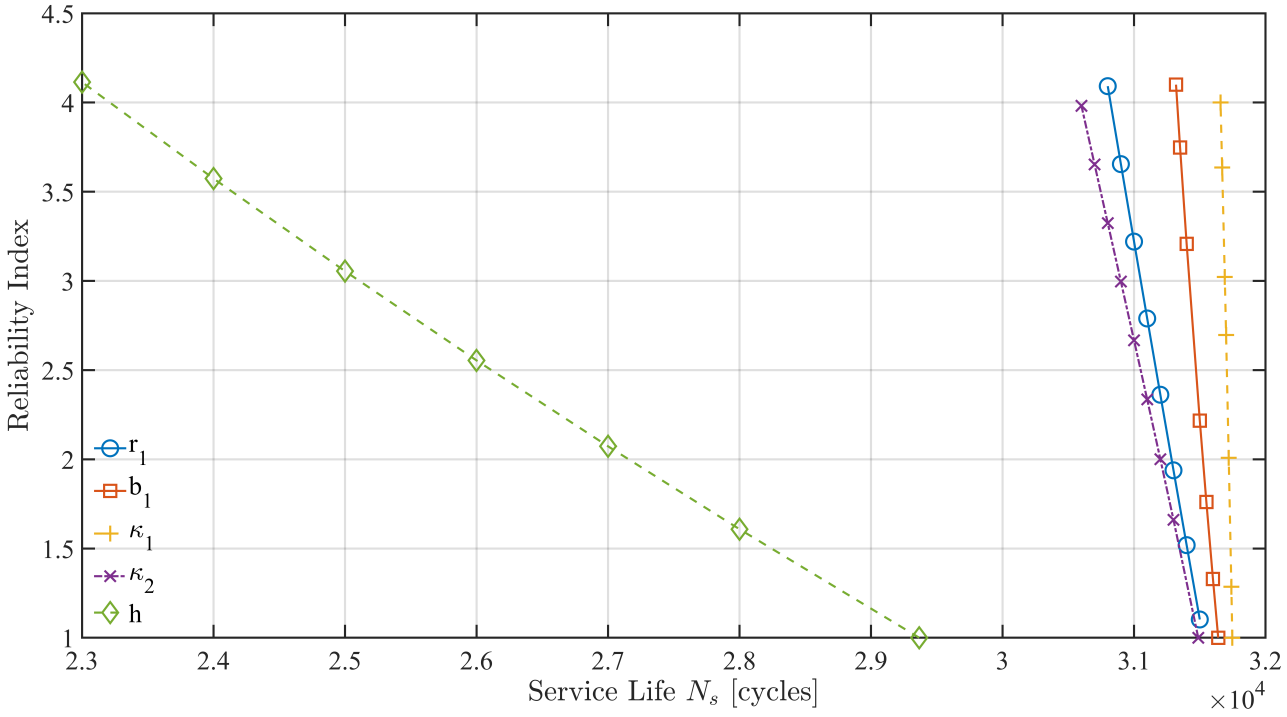


Figure 4.8: The parametric analysis investigated the influence of uncertainties in the geometrical parameters on the structure's reliability. Notably, uncertainties in the thickness exhibited a more pronounced impact on reliability. This is evident from the fact that the same reliability index corresponds to a shorter service life along the thickness line.

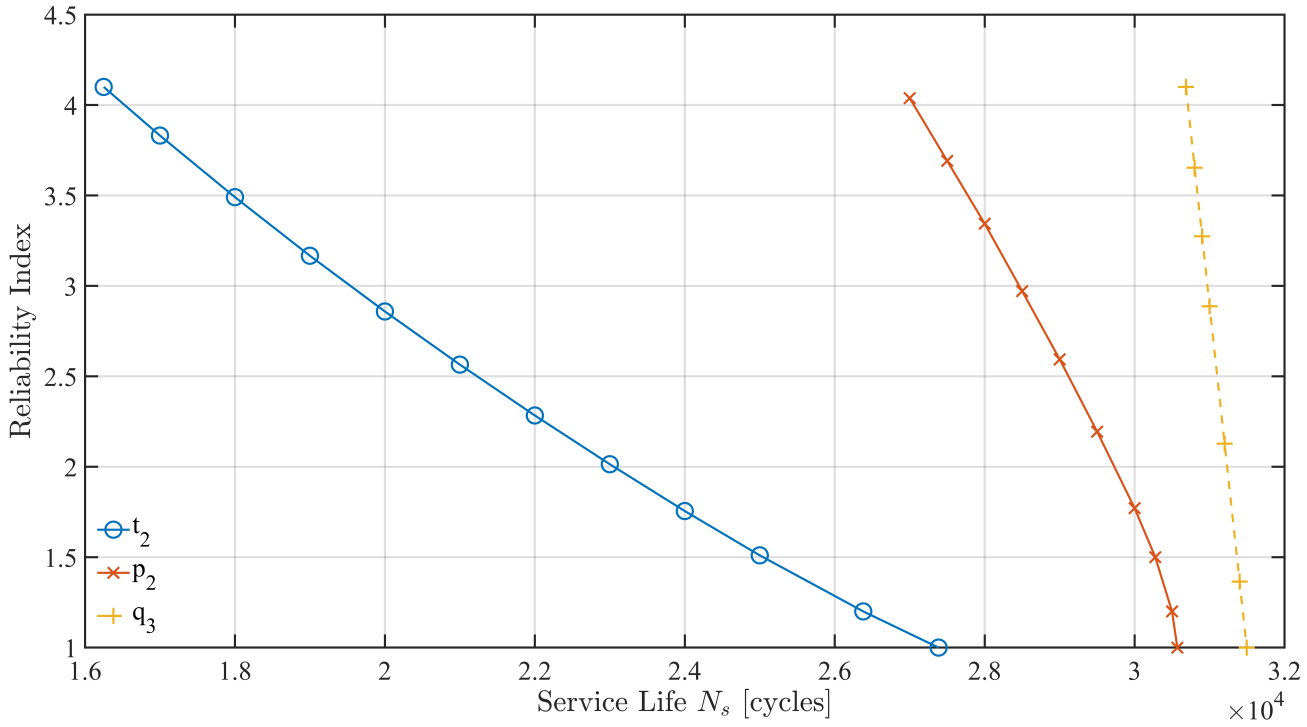


Figure 4.9: The Parametric analysis of the uncertainties in the loading parameters to the reliability of the structure. Notably, uncertainties in the tension exhibited a more pronounced impact on reliability.

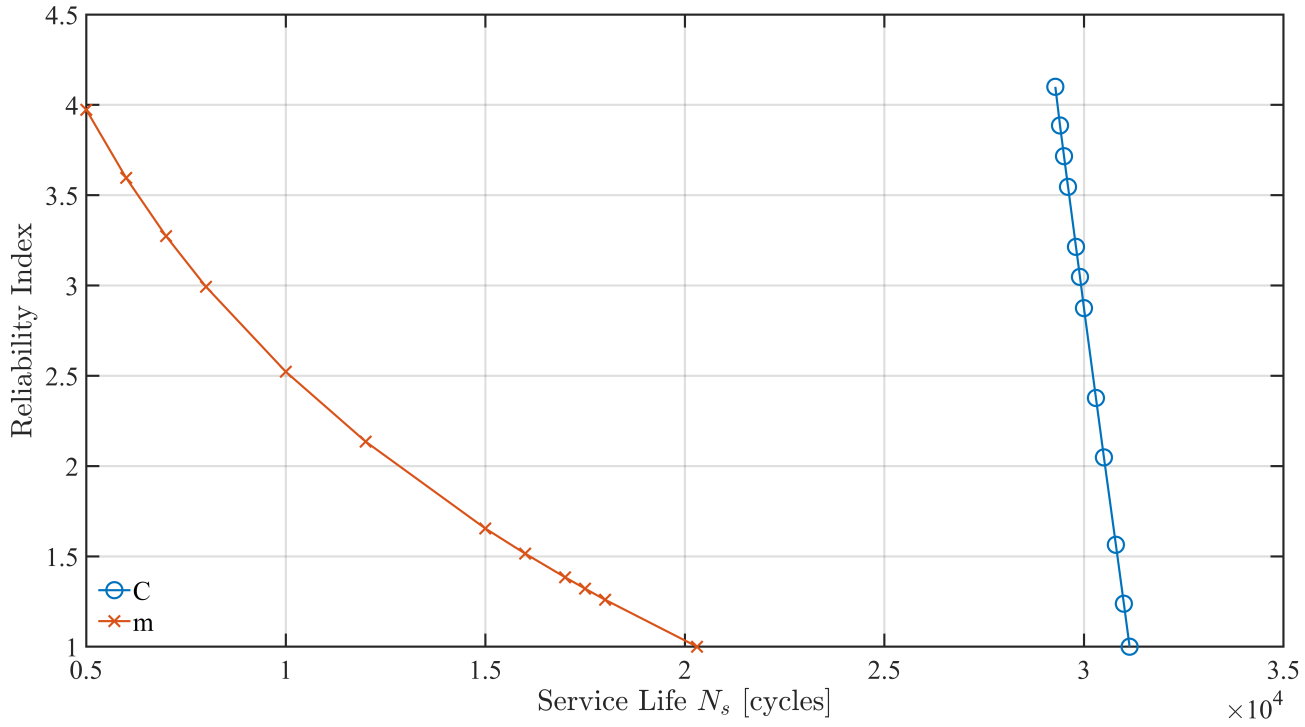


Figure 4.10: The Parametric analysis of the uncertainties in the Paris law constants to the reliability of the structure. Notably, uncertainties in the Paris law exponential term exhibited a more pronounced impact on reliability.

Figure 4.8 demonstrate the impact of uncertainties in geometrical parameters, it is evident that for a given reliability index, the curvature in the x-direction κ_1 leads to the longest service life and has a minor effect on reliability. This aligns with expectations as x-direction curvature is smaller and thus less influential compared to y-direction curvature. Conversely, uncertainties in the thickness exhibited a more pronounced impact on reliability. This is evident from the fact that the same reliability index corresponds to a shorter service life along the thickness line compared to other geometrical parameters.

The results for the influence of the loading conditions are shown in Figure 4.9. The result shows that the membrane traction force t_2 has a higher influence in determining a suitable service life while the domain pressure load has a minor effect on the service life.

In terms of Paris Law constants, Figure 4.10 shows that the Paris Law exponential term m as the only random variable results in the shortest service life among all parameters. This is within the expectation that the Paris Law exponent poses the largest impact on the reliability and hence service life as the number of cycles is highly dependent on the magnitude of the exponent.

The remaining parameters yield a relatively consistent range of service life when modelled as the only uncertainty. This highlights that service life is significantly impacted by thickness, membrane traction, and the Paris Law exponential term. Hence, design efforts should focus on accurately determining the variation of these parameters to achieve a longer service life.

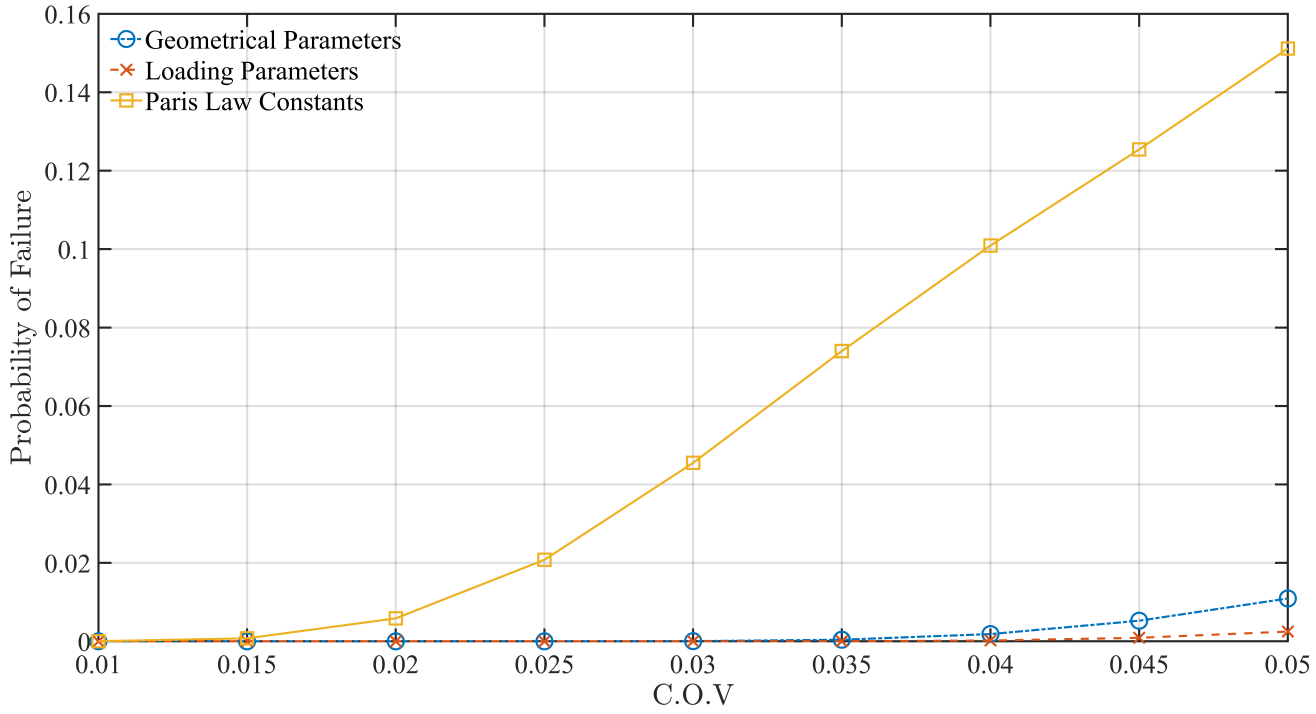


Figure 4.11: The parametric analysis of the combined effect of geometrical variables, loading parameters and Paris Law constants respectively with the same level of COV in the parameter.

A sensitivity test of the reliability index concerning the coefficient of variation (COV) was conducted. The uncertainties associated with geometrical parameters are conventionally standardized by the manufacturer with the same level of uncertainty (COV) for all parameters. The same principle applies to the loading parameters and Paris law constants, resulting in equal levels of uncertainty for all. This approach aims to investigate uncertainties across three distinct parameter categories: geometrical, loading, and Paris law constants. By increasing the COV within these three parameter groups, ranging from 0.01 to 0.05, the probability of failure increases. The results of the sensitivity test are shown in Figure 4.11. The findings underscore that a higher level of uncertainty in parameters corresponds to a higher failure probability, as expected. The impact of COV variations in geometrical and loading parameters has relatively minor effects on reliability, resulting in a 0.25% increase in the probability of failure for the loading parameter and a 1% in-

crease for the geometrical parameters. In contrast, variation in the uncertainty levels of the Paris law constants significantly increases the probability of failure. It is necessary to determine the variation in the Paris law constants in a more accurate way to maintain low COV in the uncertainty, hence decreasing the probability of failure.

4.5 Fatigue Reliability assessment of multi-site damage problem of the shell with three holes

A third numerical example was investigated, involving the assessment of fatigue reliability concerning a cylindrical shallow shell structure with multiple site damage. The geometry of the structure is presented in Figure 4.12. The geometry comprises three holes featuring two cracks each extending from opposing sides of each hole. The cracked section of the shell is denoted as region A, and specific structural dimensions are outlined in Table 4.3. The initial crack lengths a_0^i in C1 - C6 were treated as an uncertainty, where $i \in [1, 6]$. The shell is made of Aluminium 2024-T3, with Young's modulus of $E = 73780MPa$ and a Poisson's ratio of $\nu = 0.33$. The structure was discretized using 30 quadratic elements on the shell outer boundaries. Additionally, 8 quadratic elements were allocated to each hole, with 4 quadratic elements each on the upper and lower surfaces of the cracks. Overall, 102 quadratic elements were used. 70 DRM points were used and were uniformly distributed throughout the domain.

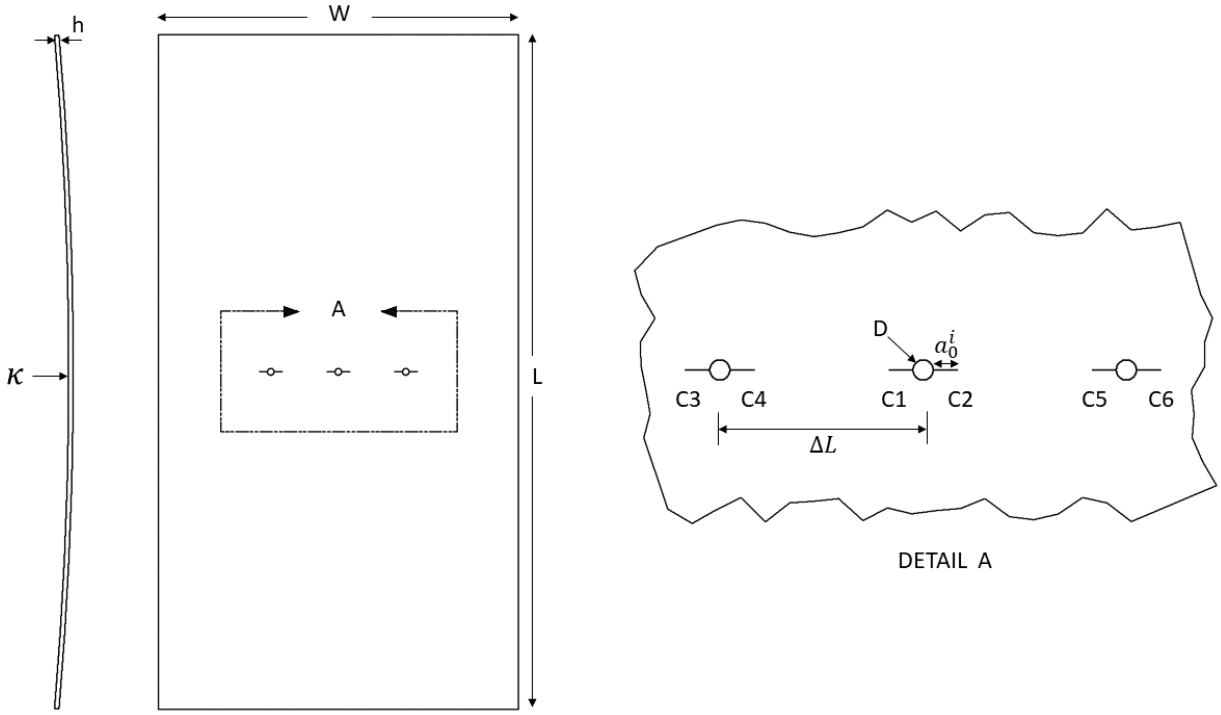


Figure 4.12: The geometry of the shallow shell used in the second reliability analysis. The geometry comprises three holes featuring two cracks extending from opposing sides of each hole. The cracked section is denoted as region A.

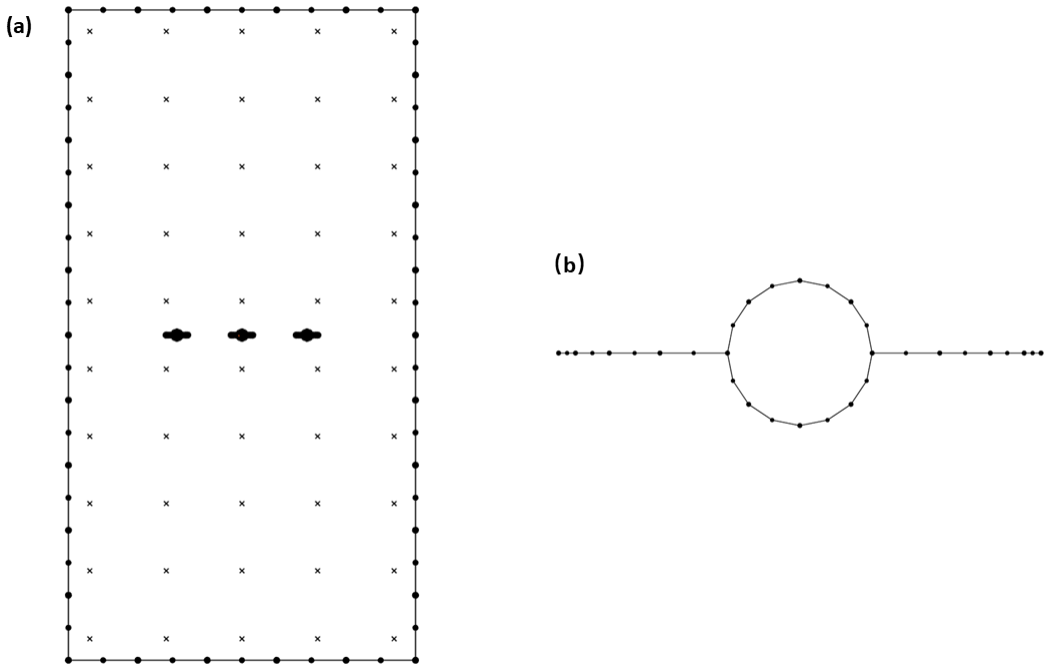


Figure 4.13: (a): The boundary element mesh of the shallow shell used in the second reliability analysis. (b): The mesh on the centre hole and crack. Only the mesh of the middle hole is shown here, the rest of the holes were meshed in the same way.

Table 4.3: Geometrical factors and uncertainties present in example 2.

Parameter	Description	Distribution	Mean	COV
W	Width of the shell	Deterministic	$160mm$	
L	Length of the shell	Deterministic	$300mm$	
κ	Curvature in y direction	Deterministic	Variable	
h	Thickness	Deterministic	$2mm$	
D	Diameter of the holes	Deterministic	$3mm$	
ΔL	Distance between the holes	Deterministic	$30mm$	
a_0	Initial crack length in $C1 - C6$	Lognormal	$3.5mm$	0.05
p	Pressure loading	Lognormal	$0.05MPa$	0.05
C	Paris Law constant	Lognormal	$2.839 \times 10^{-12} \frac{m/cycle}{(MPa\sqrt{m})^{m_p}}$	0.05
m_p	Paris Law exponent	Lognormal	4.6	0.02

In this example, the geometrical parameters remained constant except for the initial crack lengths at cracks $C1$ to $C6$, which were treated as uncertainties. The reliability analysis was conducted with varying curvature in the y direction ($\kappa_{11} = 0$, $\kappa_{22} = \kappa$). All cracks were grown to a final length of 8 mm, and the fatigue life of the structure is defined as the number of cycles required for the crack to reach this length. The reliability was evaluated on the crack with minimum fatigue life among all crack tips.

Four reliability analyses were conducted with curvature in y-direction taking the value of $\kappa = (1.0E-14, 0.01, 0.05, 0.1)m^{-1}$ to investigate the effect of curvature on the overall reliability, where the case of $\kappa = 1.0E-14m^{-1}$, the shell can be considered as a plate. The limit state function can be written as:

$$g(a_0^i, p, C, m, N_s) = N(a_0^i, p, C, m) - N_s \tag{4.39}$$

where $i \in [1, 6]$ for uncertainty in the initial crack length of crack $C1 - C6$. The derivatives of the fatigue life N can be found by differentiating the integral equation using trapezoidal numerical integration. The integration in Eq. (4.37) can be approximated by a trapezoidal rule with evenly spaced points such that:

$$N = \int_{a_0}^{a_f} f(a)da \approx \frac{a_f - a_0}{2N} \left[f(a_0) + 2f(a_1) + \cdots + 2f(a_N) + f(a_f)\right] \tag{4.40}$$

where $f(a) = \frac{1}{C(\Delta K_{eff}(a))^m}$. The derivatives with respect to the initial crack length can be found:

$$N_{,a_0} \approx \frac{a_f - a_0}{2N}\left[f'(a_0) + 2f'(a_1) + \cdots + 2f'(a_N) + f'(a_f)\right] - \frac{1}{2N}\left[f(a_0) + 2f(a_1) + \cdots + 2f(a_N) + f(a_f)\right] \tag{4.41}$$

The derivatives of the fatigue life N at crack tip j with respect to change in initial crack size a_0^i were calculated at each MPP iteration, using Eq. (4.41) for $j = i$ and Eq. (4.38) for $j \neq i$. It is expected that with increasing curvature, the structure exhibits higher resistance to crack propagation, consequently leading to longer fatigue life. The IDM-based FORM was used and the results of which were then compared with those of MCS.

Overall, 1×10^5 MCS iterations were conducted for each curvature value, and the results derived from both FORM and MCS are shown in Figure 4.14. The number of required MCS was determined in the same way as mentioned in the previous section. The outcomes generated through the FORM approach exhibit high consistency with the MCS results, with the maximum deviation of 3.49% recorded at $\beta = 2.23$ when $\kappa = 0.05$. The results show a larger error at a smaller reliability index. The reliability index illustrates substantial sensitivity to changes in shell curvature. Specifically, as curvature increases, longer service life can be achieved while maintaining the same reliability index, thereby reducing the probability of failure. The results agreed with the expectation. On average, four iterations in average for obtaining the converged reliability index. The computational time required to evaluate the FORM results for one curvature is 7.58×10^4 s. The computational time required for one DBEM simulation is 626.4 s. The total amount of computational time required by the MCS is, therefore, 6.26×10^7 s. The FORM requires significantly less computational effort while maintaining high accuracy. This shows the robustness and efficiency of the proposed formulation.

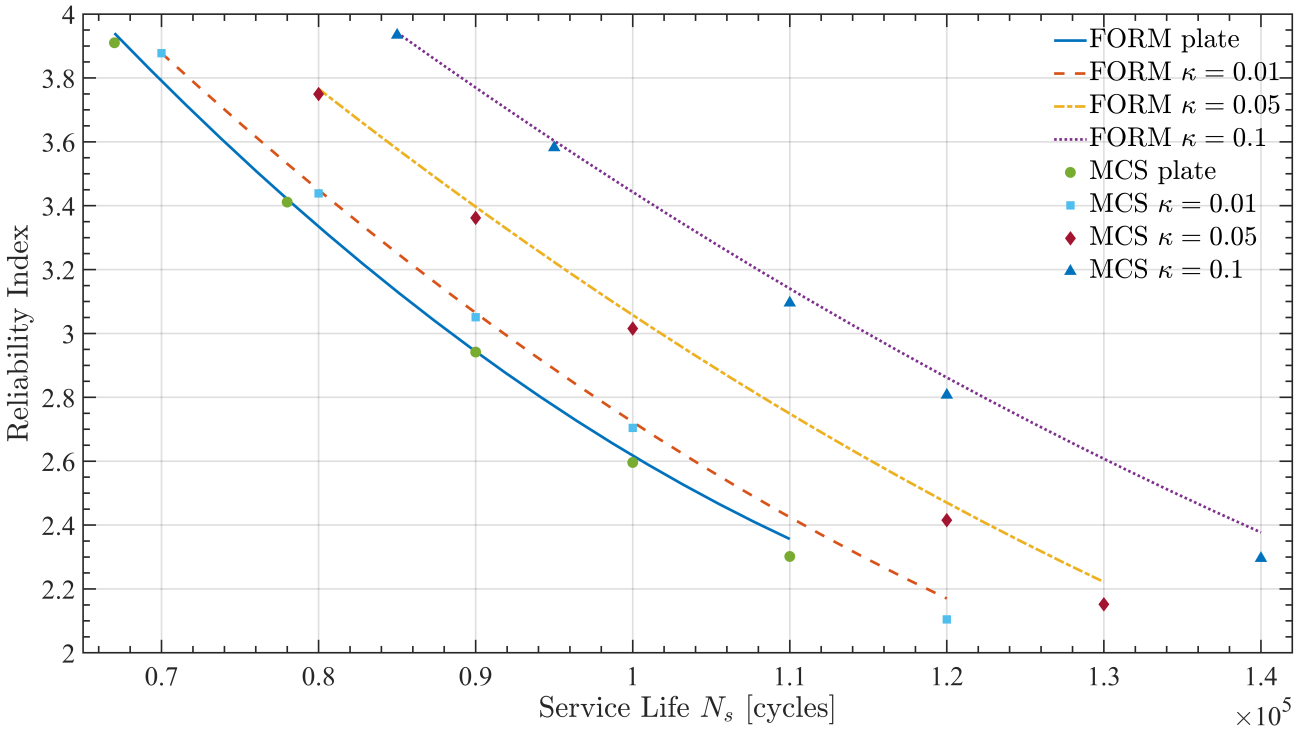


Figure 4.14: The reliability index concerning the structure's service life, influenced by different curvatures of the shell structure is shown in the figure. To validate the accuracy of the findings, the results of the Monte Carlo Simulation are included for comparison.

It is worth noting that in both numerical examples in this section, the difference between the FORM and MCS can be reduced by using the SORM, which approximates the LSF with a second-order Taylor expansion. This can significantly improve the accuracy of the estimated reliability index, especially for problems with highly nonlinear LSFs. When dealing with higher-dimensional problems that incorporate multiple uncertainties, there is a marked increase in the number of derivatives that need to be computed. This increase can lead to substantial computational challenges. In such situations, the application of MCS with surrogate modelling is preferential to mitigate these computational demands. This combination effectively reduces the overall computational burden while maintaining accuracy in the analysis of more complex, multi-variable systems.

4.6 Conclusion

This chapter introduces a novel methodology for performing reliability analyses of fatigue life through the newly developed Dual Boundary Element Method-based Implicit Differentiation Method

(DBEM-IDM) for shallow shell structures. The study has introduced DBEM-based formulations that enable the evaluation of stress intensity factor and fatigue lifetime sensitivities within shallow shell structures, concerning variations in geometrical variables and curvature. The proposed methodology holds the potential to significantly advance current capabilities in predicting the reliability of such structures under fatigue conditions, thereby enhancing their overall design and assessment processes.

The IDM formulations were derived by directly differentiating the BEM equations and were integrated with First Order Reliability Analysis (FORM) to assess the reliability index of shallow shell structures featuring multiple cracks, thus estimating the probability of failure. FORM offers a distinct advantage by significantly reducing computational demands while maintaining accuracy compared to the Monte Carlo Simulation (MCS). In order to demonstrate the effectiveness of the proposed approach, three numerical examples were presented.

In the first example, the investigation was conducted on a fuselage window structure featuring a crack subjected to membrane, bending, and uniform pressure loads. The fracture reliability of the structure was assessed, accounting for uncertainties in geometrical and loading parameters. By considering these uncertainties, the sensitivities of the crack tip stress intensity factors were derived. The reliability index was obtained by applying the Implicit Differentiation Method (IDM)-based First-Order Reliability Method (FORM). The results were compared with those obtained from Monte Carlo Simulation (MCS). As expected, the reliability of the structure decreases as the crack propagates, indicating an increased probability of failure, aligning with our expectations. The maximum difference between the results obtained from FORM and MCS was found to be 2.99% at a crack length of 0.0725 m, which demonstrates the reliability and accuracy of the proposed methodology. One of the significant advantages of using FORM is the substantial reduction in computational effort. The computational time required to evaluate one reliability index using FORM is merely 2475.2 seconds, whereas performing 40,000 MCS demands a significantly higher computational time of 3.0788×10^7 seconds. The practical applicability of reliability analysis is evident, as it enables engineers to determine a suitable inspection crack size while meeting safety requirements. Once the optimal inspection crack size is identified, the corresponding inspection technique can be deployed, ensuring the structural integrity of the shallow shell system.

In the second example, a shallow shell featuring a central hole and crack, subjected to membrane, bending, and uniform pressure loads, was investigated. The fracture reliability analysis was conducted and considered a limit state function formulated in terms of effective stress intensity factor K_{eff} and fracture toughness. The obtained reliability index results were coupled with the probability of detection from eddy current inspections, aiding in determining a critical crack length that would satisfy reliability requirements while allowing for inspectability.

Additionally, fatigue reliability assessments were carried out through limit state functions expressed in terms of fatigue life cycles. Two limit state functions were analysed to separate the impacts of loading conditions and Paris law constants. The results obtained from FORM were benchmarked against the results obtained from 40,000 MCS iterations, showing a maximum difference of only 3.67%. Furthermore, a parametric analysis was conducted on each design variable to identify the most influential factors on overall structural reliability. It was determined that thickness, membrane traction, and the Paris Law exponential term have a significant influence on service life, underscoring the need for precise determination of these parameters to achieve extended service life. The investigation further encompassed the influence of the coefficient of variation (COV). It was discovered that uncertainties associated with Paris law constants exerted a more substantial influence, prompting the need for enhanced precision in determining these constants to improve structural reliability and reduce the probability of failure.

A third numerical example investigated the fatigue reliability assessment of a cylindrical shallow shell structure with multiple-site damage, featuring six cracks with the initial crack lengths as variables. Varied curvature of the shell structure was used to investigate the effect of curvature on the reliability of the structure. Comparison of FORM results with those obtained from 1×10^5 MCS iterations revealed a maximum difference of only 3.49%. The computational time required for evaluating the reliability index for one curvature via FORM was around 7.58×10^4 s while achieving a converged distribution for the limit state function through MCS required a substantial 6.26×10^7 s. This comparison demonstrates the substantial efficiency of the IDM-based FORM in estimating the structural reliability index, particularly for higher-dimensional problems involving multiple random design variables, a scenario that typically requires a large amount of MCS. It is worth noting that the numerical examples presented in this study were assigned with a postulated initial crack size

in either a deterministic way or with uncertainties. In many real-world scenarios, determining the actual initial flaw size with high precision can be both challenging and economically expensive. This underscores the application of the concept of the Equivalent Initial Flaw Size (EIFS) such that it provides a starting point for the crack propagation model.

The accuracy of results achieved through FORM depends on the linearity or near-linearity of the limit state function within the variable space. To improve the precision of derived reliability indices, the application of the Second-Order Reliability Method (SORM) is usually employed. This method involves approximating the limit state function using a second-order Taylor expansion, with an associated increase in computational complexity due to the inclusion of second-order derivatives. However, it's worth noting that FORM has demonstrated both efficiency and accuracy across a broad spectrum of structural problems. Furthermore, FORM has exhibited significant accuracy in the context of static structures, underlining its robustness for these scenarios.

Chapter 5

Statistical Inference of Equivalent Initial Flaw Size for Engineering Structure

In the field of modern aviation, aircraft structures are primarily constructed using anisotropic materials, chosen for their advantageous properties of reduced weight and enhanced strength. As a consequence, this necessitates a fundamental requirement in the domain of structural integrity management — to accurately assess the fatigue life of anisotropic components, thereby mitigating the risk of structural failure. This quantitative evaluation of a structure's service life until the point of fatigue cracking under operational conditions is commonly referred to as durability analysis.

Durability analysis often commences with the evaluation of relatively small cracks, typically arising from material imperfections in the manufacturing process. While these initial flaws may not immediately pose safety concerns, they hold the potential to lead to catastrophic failure if they grow beyond a certain critical size. Consequently, durability analysis plays a crucial role in determining an optimal service life that maximizes operational time while minimizing maintenance costs [132]. The primary objective of durability analysis is to model the growth of cracks as a function of service time. This process comprises two essential steps:

1. The determination of the initial fatigue quantity (IFQ) of a structure.
2. The prediction of the probability that a crack will exceed the allowable length, based on the derived IFQ.

The second step can be effectively accomplished by employing methods such as the First-Order

Reliability Method (FORM) or Monte Carlo Simulation (MCS), as discussed in previous chapters with some known initial crack length. In the first step, IFQ is defined as the initial state of the structure immediately after manufacturing, taking into account potential material imperfections. The key parameter that represents IFQ is the initial flaw size, which forms the central focus of this chapter.

A noteworthy challenge in the estimation of the fatigue life of a structural component lies in the inherent difficulty of accurately measuring the initial flaw, which is often characterized by its very small size. Furthermore, the reliable modelling of the growth behaviour of these initial flaws poses a significant challenge, particularly in the context of anisotropic materials [16]. Traditionally, the initial flaw size has been treated as a deterministic parameter which equals the minimum detectable size of Non-Destructive Inspection (NDI) as prescribed in the US Air Force Military Specification [132]. This conventional practice tends to result in a conservative approach for estimating the fatigue life [133]. The consequence of this conservatism is often an over-engineered structure, which reduces the weight-saving advantages inherent in anisotropic materials.

An effective approach to estimating fatigue life, and overcoming the challenges outlined above, is the concept of the Equivalent Initial Flaw Size (EIFS). EIFS does not represent an actual physical quantity but rather functions as a model calibration parameter for long-crack growth models, such as the Paris law. Compared to the ideal method of estimating fatigue life, which involves tracking crack growth from the actual initial flaw size to the final crack size using a small crack growth model, the Equivalent Initial Flaw Size (EIFS) serves as a model calibration parameter. It is used in conjunction with the long crack growth model to ensure that the estimated fatigue life is the same as given in the ideal case. EIFS is assumed to exist before the commencement of service. Once EIFS is determined, it provides precise estimates for the fatigue life of the structural component, as well as similar components subjected to similar loading conditions. This approach mitigates the tendency to over-engineer the component, allowing engineers to maximize the weight-saving advantages inherent in anisotropic materials.

The durability analysis has suggested the treatment of Equivalent Initial Flaw Size (EIFS) as random variables, where EIFS values at different locations are governed by probabilistic distributions [132]. This perspective is particularly important when modelling anisotropic materials, which

are characterized by considerably higher levels of uncertainty compared to the modelling of traditional isotropic materials. These uncertainties arise from the inherently intricate manufacturing processes required for anisotropic materials. Additionally, the modelling of fracture in anisotropic materials necessitates a more extensive array of variables to accurately model fracture, in contrast to isotropic materials. The presence of these uncertainties considerably complicates the statistical inference of EIFS for anisotropic materials.

Taking a stochastic approach to the inference of Equivalent Initial Flaw Size (EIFS) introduces several challenges. Given the numerous uncertainties inherent in this context, relying on a single EIFS value becomes inadequate, necessitating the derivation of a distribution of EIFS (EIFSD) that encapsulates the inherent uncertainties. Generating such a distribution demands a substantial volume of data. However, obtaining statistical information on the initial flaw from Non-Destructive Inspection (NDI) proves to be economically impractical. As a result, EIFS values are often inferred from the distribution of final crack sizes, typically based on inspection data collected from a fleet of aircraft. Notably, within the same fleet, aircraft do not undergo inspection simultaneously, which results in field data encompassing varying crack sizes, each associated with a different number of flight cycles.

Within the research community, the estimation of Equivalent Initial Flaw Size (EIFS) for anisotropic materials has predominantly followed non-statistical approaches. Significantly, works primarily concentrated on isotropic materials have attracted more attention, with relevant research contributions found within the literature [134–138]. A comprehensive overview of various EIFS determination methods is presented in Steven Johnson's work [139]. One of the simplest methods for deriving EIFS involves fitting experimental data to determine the crack growth rate, allowing for a back extrapolation to the initial time point (t=0). For example, in Zheng et al.'s study [140], a range of EIFS values was systematically selected, and their corresponding fatigue life was numerically evaluated. Subsequently, these numerical results were compared with experimental data, with the most suitable EIFS value determined based on the highest correlation between the numerical and experimental outcomes. Nor Mohammed et al. [141] conducted fatigue crack growth testing on an anisotropic specimen, and the crack growth parameters were determined by plotting the stress-life (S-N) curve, thereby allowing for EIFS estimation through the back-extrapolation

method. Additionally, Li [142] proposed a modified Kitagawa-Takahashi diagram method that incorporates anisotropy in the material, providing an alternative method for EIFS determination.

Statistical approaches, specifically Maximum Likelihood Estimation (MLE) [143] and the Bayesian Updating Method, have found extensive applications in the field of fatigue analysis. Notably, the Bayesian Updating method has emerged as a successful tool in addressing fatigue-related issues that encompass uncertainties [144–149]. The Bayesian Updating approach allows for the continuous refinement of the estimation of the Equivalent Initial Flaw Size Distribution (EIFSD) as new data becomes available. This, coupled with the fact that EIFSD can be used for similar components under similar loading conditions, renders Bayesian Updating suitable for utilizing inspection data collected from a fleet of aircraft, enhancing its practicality. This approach also enables newer aircraft to benefit from the EIFSD inferences derived from older aircraft. Numerous examples within the literature illustrate the use of Bayesian Updating for EIFS inference. For instance, Salemi et al. [150] proposed a combined Bayesian and Finite Element Analysis (FEA) simulation approach to estimate EIFS and predict fatigue life, accounting for uncertainties in the fatigue process through a single noise term with a standard deviation of 10%. A noteworthy study by Sankararaman [8] included a numerical example featuring a cylindrical structure subjected to multi-axial loading. This work considered uncertainties related to crack growth, data accuracy, and modelling error, which were combined into a unified equation. The computationally expensive Finite Element Method (FEM) algorithm was replaced by surrogate modelling to obtain stress intensity factors. The study explored various methods, including Maximum Likelihood, Least Squares, and Bayesian Update, for EIFS inference, while also providing two approaches for the treatment of EIFSD parameters (mean and standard deviation) as deterministic with uncertainties. Furthermore, the paper proposed the importance of considering individual parameter uncertainties, leading to an extension of the study by the same author [149, 151] in which each source of uncertainty was assigned a probabilistic distribution rather than consolidating them into a single noise term.

Obtaining a substantial volume of real-world inspection data for a specific component poses significant challenges, and conducting experimental statistical analyses that account for uncertainties is often infeasible. Consequently, a valid numerical approach is needed. In this context, the Dual Boundary Element Method (DBEM) emerges as a highly efficient computational tool for fa-

tigue modelling challenges, used to model crack extension and perform fatigue life assessments for anisotropic structures. The DBEM requires only the modelling of the outer boundary of the structure, eliminates the need for re-meshing, and is able to automatically compute the path of crack growth [6]. When this robust numerical model is combined with a statistical approach, it enables the estimation of the EIFSD and the fatigue lifetime of the structure, even with limited real-world inspection data available. Previous applications of the DBEM in conjunction with EIFSD estimation can be found in works such as Morse (2017) [152], where the DBEM was employed as part of the EIFSD inference process for multiple-site damage in an isotropic aircraft lap-joint splice. Another example can be seen in the research by the same author [144], where the DBEM was utilized to model an isotropic assembled plate structure under complex loading conditions. The advantages of the DBEM in fatigue modelling can potentially be even more pronounced when applied to anisotropic structures. However, despite its merits, the DBEM has not yet been utilized for modelling anisotropic structures when inferring EIFSD. This represents one of the primary objectives of the present chapter.

In summary, the main novel contributions described in this chapter are:

- Expanding on previous work by Morse et al. [144] and develop a stochastic approach to the statistical inference of EIFSD for anisotropic materials.
- Extending previous DBEM formulations to predict the fatigue life of anisotropic materials.
- Expanding on previous work and developing a stochastic approach to the statistical inference of EIFSD for shallow shell structures.

Upon the successful inference of the Equivalent Initial Flaw Size Distribution (EIFSD) for a structural component, it serves as a valuable tool for determining the fatigue life of that component and for other components subjected to similar loading conditions. This information, in turn, assists in establishing optimal intervals for routine inspections. These inspection intervals are typically defined with the aim of ensuring that an undetected crack does not reach a critical length that endangers flight safety before the next scheduled inspection [153]. However, owing to the intricate challenge of accounting for uncertainties associated with crack growth, inspection intervals are often characterized by a conservative approach. This conservatism results in more frequent

inspections, thereby escalating costs, without necessarily corresponding safety enhancements. The EIFSD method offers a potentially more accurate and less conservative approach to determining inspection intervals for aircraft. An illustrative example of this approach can be found in the concluding section of this chapter.

This chapter is structured as follows: Section 5.1 provides an overview of the basic theory of the EIFS. Section 5.2 details the crack growth model utilized for modelling fatigue crack growth. Section 5.3 outlines the Bayesian updating approach employed for the inference of Equivalent Initial Flaw Size (EIFS). Section 5.4 introduces the surrogate model utilized to enhance the efficiency of the EIFS procedure. Finally, in Section 5.5.1 and 5.5.2, two numerical examples involving an anisotropic structure, encompassing multiple sources of uncertainty pertinent to anisotropic materials, are presented. Numerical example focusing on the shallow shell structure is demonstrated in Section 5.6.

5.1 Basic Theory of EIFS

A viable method for estimating and establishing an effective initial crack size is through the inference of EIFS. This inference approach offers a practical means to estimate the initial crack size without the need for experimental detection. The approximation of a short crack growth model using a long crack growth model with calibration has become a widely accepted method to ensure structural integrity [154].

Ideally, estimating the fatigue life of a structure requires growing the crack from its actual initial length to a critical crack size using an accurate model for short crack growth, denoted as $g_{short}(a)$, where a represents the crack size. However, determining the actual initial crack size is a challenging task, given that it is often smaller than the minimum detectable size achievable through Non-Destructive Inspection (NDI). Furthermore, the behaviour of short crack growth can be influenced by the material's microstructure [16] [155], making the application of such a crack growth model complex. To address these challenges, the EIFS approach is adopted, with the condition that the number of cycles taken from EIFS to reach a final crack size a_f is identical to what would be required for the actual initial flaw size to grow to the same final crack size a_f. This equivalence is visually demonstrated in Figure 5.1.

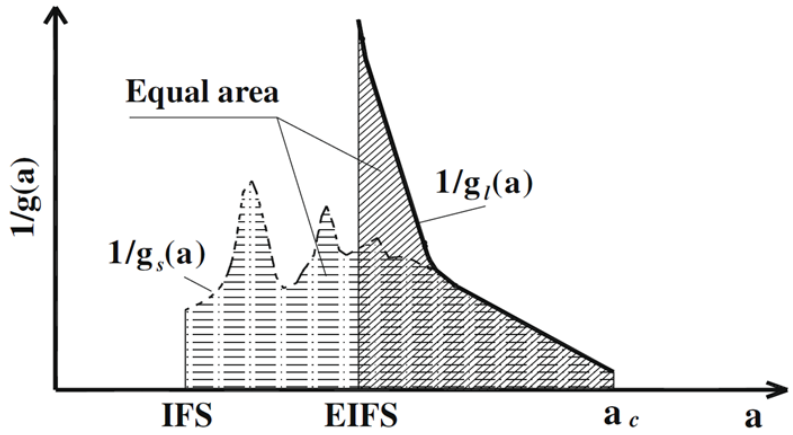


Figure 5.1: A graphic demonstration of the EIFS as a model calibration parameter for a long crack growth model $g_{long}(a)$ vs. the growth of an actual initial flaw size to a crack size a_f using a short crack growth model. The area under the curve represents the number of cycles required to grow a crack [8].

The area under the two curves in Fig. 5.1 gives the number of cycles required to grow from IFS or EIFS to a_c and is given by:

$$N = \int_{IFS}^{a_c} \frac{1}{g_s(a)} da = \int_{EIFS}^{a_c} \frac{1}{g_l(a)} da \tag{5.1}$$

This clarifies why the term EIFS is used, as it stands as the equivalent representation of the Initial Flaw Size (IFS) when a long-crack growth model is applied. Once the EIFS is inferred, it can be incorporated within the same long crack growth model to predict the number of cycles needed for the crack to extend to a maximum permissible size. Effectively, the EIFS can be regarded as a model calibration parameter for a long crack growth model.

5.2 Concept of Fatigue Crack Growth

Following the determination of all boundary displacements and tractions through the Dual Boundary Element Method (DBEM), the J-integral plays a pivotal role in computing the stress intensity factors at the crack tip. These stress intensity factors are subsequently employed within the DBEM for the modelling of the fatigue crack growth. Given that the inference of the EIFSD requires the utilization of a long-crack growth model, this study leverages the well-established Paris law [154]. In the context of fatigue modelling, the number of cycles N required to propagate the crack from

an initial size a_0 to a final crack size a can be computed as follows:

$$N = \int_{a_0}^{a} \frac{1}{da/dN} da \tag{5.2}$$

where da/dN is the crack growth rate that can be described using Paris law:

$$\frac{da}{dN} = C(\Delta K_{eff})^m \tag{5.3}$$

where C and m are the Paris law constants and exponent. ΔK_{eff} is the effective stress intensity factor range determined by the difference between the stress intensity factor evaluated at maximum stress level and minimum stress level ($K_{eff}^{max} - K_{eff}^{min}$). The effective stress intensity factor range can be expressed using a function of mode I and mode II SIF by [156]:

$$\Delta K_{eff} = \sqrt{\Delta K_I^2 + 2\Delta K_{II}} \tag{5.4}$$

where the mode I and mode II intensity range can be calculated by the J-integral.

To consider the influence of the stress ratio R on the crack growth rate, it is essential to incorporate the appropriate constant C that corresponds to the given stress ratio. This adjustment can be achieved by employing Walker's equation:

$$C = \frac{C_0}{(1-R)^{m(1-\gamma)}} \tag{5.5}$$

where γ is the coefficient of the Walker's equation, represents how strongly the stress ratio affects the crack growth rate and C_0 is the interception point when R=0.

5.3 Bayesian Updating Method

The statistical inference of the EIFSD through Bayesian updating entails initiating the process with a prior estimate for the EIFSD and subsequently updating this estimate with inspection data to derive a posterior estimate for the EIFSD. This section will offer a concise introduction to the formulations of Bayesian updating.

Denote Θ as the EIFSD where it follows the lognormal distribution, the likelihood that the testing pair of mean and standard deviation from $\Theta_{ij} \sim lnN(\hat{\mu}_i, \hat{\sigma}_j)$ is the 'true' distribution $\Theta_{true} \sim lnN(\mu, \sigma)$ for a given k_{th} inspection data N_k^{ins} is

$$\begin{aligned} L\left(\hat{\mu}_i, \hat{\sigma}_j \mid N_k^{ins}, \mathbf{Y}\right) &= f_{N|\hat{\mu}_i,\hat{\sigma}_j,\mathbf{Y}}\left(N_k^{ins} \mid \hat{\mu}_i, \hat{\sigma}_j, \mathbf{Y}\right) \\ &= \frac{1}{N_k^{ins}\sqrt{2\pi\beta_{ij}^2}} \exp\left(-\frac{\left[\log\left(N_k^{ins}\right) - \alpha_{ij}\right]^2}{2\beta_{ij}^2}\right) \end{aligned} \tag{5.6}$$

where α_{ij} and β_{ij} represent the location and shape parameters of a lognormal distribution. These parameters are estimated through Monte Carlo simulations using the EIFSD with specified mean and standard deviation. The variable $f_{N|\hat{\mu}_i,\hat{\sigma}_j,\mathbf{Y}}$ refers to the distribution of the number of cycles required for an EIFS to grow to 20 mm, given the EIFSD parameters $\hat{\mu}_i$ and $\hat{\sigma}_j$. The vector $\mathbf{Y}$ comprises uncertainties in parameters that influence crack growth. These parameters encompass the Paris law constants C_0 and m, the maximum applied stress σ_{max}, the stress ratio$R$, the ratio of Young's modulus ψ, and the angle of the anisotropic principal axis α.

As more values of N^{ins} are included to calculate the likelihood, the probability should be the product of the individual inspections. Assuming that there are l inspection data sets used, the likelihood of the test EIFSD Θ_{ij} given l inspections can be expressed as follows:

$$L\left(\hat{\mu}_i, \hat{\sigma}_j \mid \mathrm{N}_l^{ins}, \mathrm{Y}\right) = \prod_{k=1}^{l} L\left(\hat{\mu}_i, \hat{\sigma}_j \mid N_k^{ins}, \mathbf{Y}\right) \tag{5.7}$$

where N_l^{ins} contains all the available inspection data N_k^{ins}.
Eq.(5.7) represents the joint probability distribution of the tested $\hat{\mu}_i$ and $\hat{\sigma}_j$. The individual likelihood of $\hat{\mu}_i$ and $\hat{\sigma}_j$ is the 'true' mean and the standard deviation can be evaluated as:

$$\begin{aligned} L\left(\hat{\mu}_i \mid \mathbf{N}_l^{ins}, \mathbf{Y}\right) &= \int L\left(\hat{\mu}_i, \hat{\sigma} \mid \mathbf{N}_l^{ins}, \mathbf{Y}\right) f_{\hat{\Sigma}|\mathbf{N}_{l-1}^{ins},\mathbf{Y}}\left(\hat{\sigma} \mid \mathbf{N}_{l-1}^{ins}, \mathbf{Y}\right) d\hat{\sigma} \\ L\left(\hat{\sigma}_j \mid \mathbf{N}_l^{ins}, \mathbf{Y}\right) &= \int L\left(\hat{\mu}, \hat{\sigma}_j \mid \mathbf{N}_l^{ins}, \mathbf{Y}\right) f_{\hat{\mathrm{M}}|\mathbf{N}_{l-1}^{ns},\mathbf{Y}}\left(\hat{\mu} \mid \mathbf{N}_{l-1}^{ins}, \mathbf{Y}\right) d\hat{\mu} \end{aligned} \tag{5.8}$$

where $f_{\hat{\Sigma}|\mathbf{N}_{l-1}^{ins},\mathbf{Y}}$ and $f_{\hat{\mathrm{M}}|\mathbf{N}_{l-1}^{ns},\mathbf{Y}}$ represent the prior estimations. For the initial iteration of Bayesian Updating, an initial guess of the prior distribution is required. The trapezoidal rule is employed to approximate the integration, using evenly distributed ranges of μ and σ. The posterior term

can be iteratively updated from the prior terms.

It's worth noting that in Sankararaman's study [8], the mean and standard deviation of the EIFSD were treated as either deterministic values or as having uncertainties in their values, meaning they were represented with probability distributions. The research found that when treating the distribution parameters as deterministic values, the inferred mean of the EIFSD could achieve a good level of accuracy. However, the inferred standard deviation was observed to continuously decrease with more inspection data becoming available. On the other hand, when a distribution was assigned to both the mean and standard deviation, the estimation of both the mean and standard deviation was accurate. Therefore, this work adopts the latter approach, where the prior information of $f_{\hat{\Sigma}|\mathbf{N}_{l-1}^{ins},\mathbf{Y}}$ and $f_{\hat{\mathrm{M}}|\mathbf{N}_{l-1}^{ns},\mathbf{Y}}$ in Eq.(5.8) is represented with probability distributions. Note that in the case of treating the distribution parameters as deterministic values, the prior distribution is expressed as $f_{\hat{\Theta}|\mathbf{N}_{l-1}^{ins},\mathbf{Y}}$.

This posterior information is given as:

$$f_{\hat{\mathrm{M}}|\mathrm{N}_i^{ins},\mathbf{Y}}\left(\hat{\mu}_i \mid \mathrm{N}_l^{ins},\mathbf{Y}\right)=\frac{L\left(\hat{\mu}_i \mid \mathrm{N}_l^{ins},\mathbf{Y}\right) f_{\hat{\mathrm{M}}|\mathrm{N}_{l-1}^{ins},\mathbf{Y}}\left(\hat{\mu}_i \mid \mathrm{N}_{l-1}^{ins},\mathbf{Y}\right)}{\int L\left(\hat{\mu} \mid \mathrm{N}_l^{ins},\mathbf{Y}\right) f_{\hat{\mathrm{M}}|\mathrm{N}_{l-1}^{ins},\mathbf{Y}}\left(\hat{\mu} \mid \mathrm{N}_{l-1}^{ins},\mathbf{Y}\right) d\hat{\mu}} \tag{5.9}$$

$$f_{\hat{\Sigma}|\mathrm{N}_l^{ins},\mathbf{Y}}\left(\hat{\sigma}_j \mid \mathrm{N}_l^{ins},\mathbf{Y}\right)=\frac{L\left(\hat{\sigma}_j \mid \mathrm{N}_l^{ins},\mathbf{Y}\right) f_{\hat{\Sigma}|\mathrm{N}_{l-1}^{\mathrm{ins}},\mathbf{Y}}\left(\hat{\sigma}_j \mid \mathrm{N}_{i-1}^{\mathrm{ins}},\mathbf{Y}\right)}{\int L\left(\hat{\sigma} \mid \mathrm{N}_l^{\mathrm{ins}},\mathbf{Y}\right) f_{\hat{\Sigma}|\mathrm{N}_{l-1}^{\mathrm{ins}},\mathbf{Y}}\left(\hat{\sigma} \mid \mathrm{N}_{l-1}^{\mathrm{ins}},\mathbf{Y}\right) d\hat{\sigma}} \tag{5.10}$$

Where $f_{\hat{\mathrm{M}}|\mathrm{N}_i^{ns},\mathrm{Y}}$ and $f_{\hat{\Sigma}|\mathrm{N}_l^{ins},\mathrm{Y}}$ represent the posterior estimations of the distributions for $\hat{\mathrm{M}}$ and $\hat{\Sigma}$. The posterior distribution is computed for each pair of $\hat{\mu}_i$ and $\hat{\sigma}_j$. Once the posterior distribution for all possible pairs of $\hat{\mu}_i$ and $\hat{\sigma}_j$ is obtained, it becomes the prior distribution for the subsequent iteration when new inspection data N_k^{ins} is available. This process, spanning from Eq.(5.6) to(5.10), is repeated iteratively until no further inspection data is accessible.

As previously discussed, the distribution parameters themselves were treated as uncertain. It is assumed that the inferred means of both distributions represent the actual mean and standard deviation of the EIFSD. This implies:

$$\mu_l=\mathrm{E}(\hat{\mathrm{M}})=\int \hat{\mu} f_{\hat{\mathrm{M}}|\mathrm{N}_l^{\mathrm{ins}},\mathbf{Y}}\left(\hat{\mu} \mid \mathrm{N}_l^{\mathrm{ins}},\mathbf{Y}\right) d\hat{\mu} \tag{5.11}$$

$$\sigma_l = \mathrm{E}(\hat{\Sigma}) = \int \hat{\sigma} f_{\hat{\Sigma}|\mathrm{N}_l^{\mathrm{ins}},\mathbf{Y}} \left(\hat{\sigma} \mid \mathrm{N}_l^{\mathrm{ins}}, \mathbf{Y}\right) d\hat{\sigma} \tag{5.12}$$

It is expected that when more data of inspection l are used, the estimated μ_l and σ_l will approach to the 'true' values of μ and σ. The steps for conducting the EIFS inference can be summarized below [144]:

1. **Define the uncertainties Y in the crack growth model.** The uncertainties are assumed to have a lognormal distribution.

2. **Generate the simulated inspection data.** For the purpose of illustration, simulated inspection data was generated based on the Paris Law and the specified uncertainties. Initially, a dataset comprising the number of cycles to failure was generated as the source of inspection data, mimicking what would be obtained from a fleet of aircraft after routine inspections. The generation of this simulated inspection data was carried out using the DBEM while taking into account the associated uncertainties denoted as $\mathbf{Y}$. In this simulated dataset, each entry represents inspection data obtained after a routine inspection. For this illustrative exercise, the 'true' EIFSD was presumed to have to a lognormal distribution with parameters $\theta_{true} \sim \ln\mathcal{N}(\mu, \sigma)$. EIFS values were randomly sampled from this EIFSD and subsequently grown to a detectable size of $a_{det} = 20\ mm$, incorporating the uncertainties captured in $\mathbf{Y}$. The number of loading cycles required for the crack to reach this detectable size was recorded as inspection data.

3. **Monte Carlo Simulation (MCS).** A set of potential values for the mean and standard deviation of the Equivalent Initial Flaw Size Distribution (EIFSD) is defined as $\bar{M} = [\hat{\mu}_1, \hat{\mu}_2, ..., \hat{\mu}_{test}]$ and $\bar{\Sigma} = [\hat{\sigma}_1, \hat{\sigma}_2, ..., \hat{\sigma}_{test}]$, where the subscript $test$ signifies the number of possible mean and standard deviation pairs to be tested. In this study, there are a total of 60 test points, with each pair of mean and standard deviation being examined during the Bayesian updating process. To perform the Bayesian updating, Sobol sampling involving $N_{samp} = 1 \times 10^7$ samples for each uncertainty in $\mathbf{Y}$ and EIFS from the EIFSD was applied. These samples were grown to reach the detectable size of a_{det}. Subsequently, sets of the number of cycles to failure were recorded, and the distribution was denoted as $f_{N|\hat{\mu}_i,\hat{\sigma}_j,\mathbf{Y}}$. The parameters, mean α_{ij} and standard deviation β_{ij}, of the distribution in Eq.(5.6) were

obtained by fitting the distribution to a lognormal distribution. A visual representation of the Monte Carlo simulation (MCS) procedure is provided in Figure 5.2.

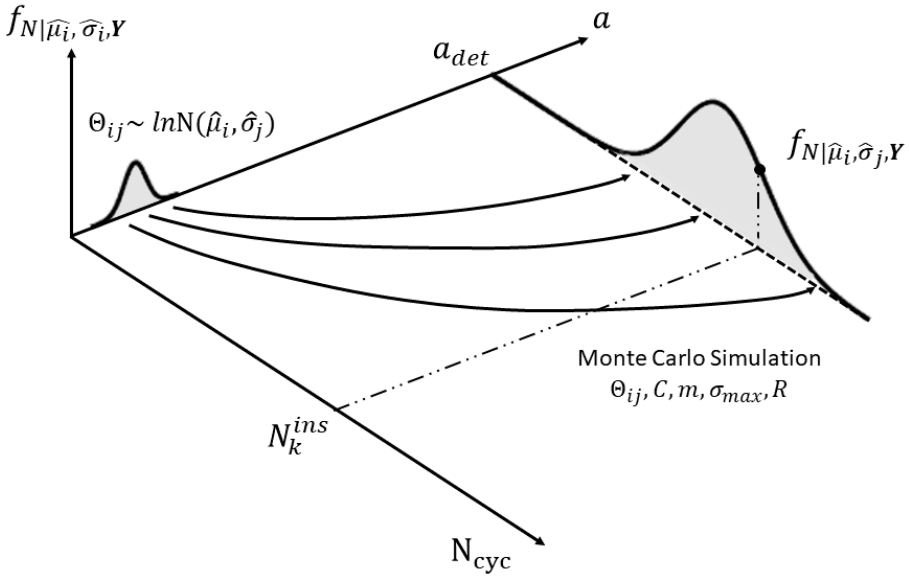


Figure 5.2: Monte Carlo Simulation procedure for obtaining the distribution $f_{N|\hat{\mu}_i,\hat{\sigma}_j,\mathbf{Y}}$ and hence the likelihood equation given in Eq.(5.6).

4. **Inference of EIFS using Bayesian Updating method.** Step 2 gives the values of N_k^{ins} and step 3 calculates the values of α_{ij} and β_{ij}. The likelihood of the tested EIFSD be the true EIFSD can be calculated by applying Eq.(5.6)-(5.10).

5.4 Surrogate Modelling

The Monte Carlo Simulation (MCS) outlined in step 3 of the previous section involves implementing the DBEM to determine the number of cycles required to reach the detectable crack size, denoted as a_{det}. However, this approach can be computationally expensive when dealing with numerous pairs of $\hat{\mu}_i$ and $\hat{\sigma}_j$ and a large number of sampling points. To address this challenge, surrogate modelling techniques can be employed. Several methods have been proposed for surrogate modelling, including polynomial functions, Kriging models, and neural networks. The choice of the most suitable method depends on the specific problem at analysis [157].

- Polynomial functions are straightforward to implement, but they require specifying the degree of the polynomial in advance and may be prone to overfitting.

- Neural networks are capable of handling complex problems with high-dimensional data and capturing non-linear relationships in the response surface. However, they can be computationally expensive and data-hungry, making them less ideal when only limited data is available.

- Kriging models, on the other hand, are a popular choice in structural analysis, especially for problems with dimensions less than 10. They require relatively less data to train the surrogate model. Kriging is employed in this work to replace the DBEM, with the aim of reducing computational costs. One limitation of the Kriging models is that the correlation matrix can become ill-conditioned if two training points are placed too close to each other. Therefore, Kriging models require a space-filling sampling method, such as Latin Hypercube sampling, to ensure that training data is evenly distributed in the input space [88].

Kriging models have demonstrated their effectiveness in predicting highly non-linear responses and tackling multi-dimensional problems, as highlighted in the work of Dhaene [158]. In this study, the SUMO toolbox [88] is utilized to create the Kriging model. A comprehensive understanding of the detailed formulations and construction of Kriging models is outlined in the book "Engineering Design via Surrogate Modelling" [157], as well as the technical report of surrogate modelling toolbox DACE [159]. To maintain conciseness, this section provides only a brief outline of the key equations.

The surrogate model was initially trained using the design dataset generated from the DBEM. In the training process, cross-validation was employed, and it was considered complete when the cross-validation error fell below 5%. Cross-validation involves partitioning the dataset into p equal subsets, with one of these subsets used to test the fitting results obtained from the remaining $p-1$ subsets. Once the Kriging model was trained, it was further tested using a separate testing dataset. This testing dataset was created by excluding the points that had been used in the training process. The trained Kriging model was then applied for use in the MCS obtaining the distribution parameter, as required for Bayesian updating.

Let's consider a set of existing data comprising n sets of design parameters denoted as $\mathbf{X} = \{\mathbf{x^1}, \mathbf{x^2}, ..., \mathbf{x^n}\}^T$. Each vector $\mathbf{x^n}$ consists of d design parameters. Corresponding to these design parameters, the outputs denoted as $\mathbf{Y} = \{y^1, y^2, \ldots, y^n\}^T$, where each y^i is a q-dimensional vector

for multiple outputs. In matrix form, $\mathbf{X}$ is represented as an $n \times d$ matrix as follows:

$$\boldsymbol{X} = \begin{bmatrix} x_1^1 & \cdots & x_d^1 \\ \vdots & \ddots & \vdots \\ x_1^n & \cdots & x_d^n \end{bmatrix} \tag{5.13}$$

The general form of the Kriging model response, denoted as $\hat{y}(\hat{x})$, at a new trial point $\hat{x}$ can be expressed as a linear regression model with an error term representing the difference between the predicted value and the true value, $y(\hat{x})$. This can be written as follows:

$$\hat{y}(\hat{x}) = \mathbf{F}\boldsymbol{\beta} + \boldsymbol{\epsilon}(\hat{x}) \tag{5.14}$$

where $\boldsymbol{\beta}$ is regression function. Types of the Kriging are defined by taking different forms of the regression function. The matrix $\mathbf{F}$ takes the form of:

$$\boldsymbol{F} = \begin{bmatrix} f_1(x_1^1) & \ldots & f_q(x_d^1) \\ f_1(x_1^2) & & f_q(x_d^2) \\ \vdots & \ddots & \vdots \\ f_1(x_1^n) & \cdots & f_q(x_d^n) \end{bmatrix} \tag{5.15}$$

The term $\boldsymbol{\epsilon}$ represents a stationary random process that follows a Gaussian distribution, $\boldsymbol{\epsilon(x)} \sim \mathcal{N}(0, \sigma)$, where $\mathcal{N}$ denotes a normal distribution. This process captures the deviation from the regression function representing the error of the prediction. The stationary random process $\epsilon(\mathbf{x})$ satisfies a correlation equation, which characterizes the relationships between different points in the design space. This correlation equation can be expressed as:

$$Cor[\boldsymbol{\epsilon}(\mathbf{x^i}), \boldsymbol{\epsilon}(\mathbf{x^l})] = \sigma^2 \mathbf{R}(\theta, \mathbf{x^i}, \mathbf{x^l}) \tag{5.16}$$

where $\mathbf{R}$ is the spatial correlation function between any point $\mathbf{x^i}$ and $\mathbf{x^l}$. This spatial correlation function is defined as:

$$\mathbf{R}(\theta, \mathbf{x^i}, \mathbf{x^l}) = exp(-\sum_{j=1}^{k} \theta_j \mid x_j^{(i)} - x_j^{(l)} \mid^{p_j}) \tag{5.17}$$

The parameter θ is often referred to as a hyperparameter, and it plays a crucial role in determining the range over which neighbouring samples have an influence on the current sample. A higher value of θ_j results in a narrower width for the influential range, meaning that only samples close to the current one will have a significant impact. This hyperparameter is especially valuable in high-dimensional problems where visualizing the interactions between parameters is challenging. By assessing θ_j, it can help identify the most important parameters and potentially lead to dimensionality reduction. The value of θ_j can be determined using global optimization methods such as genetic algorithms or simulated annealing. Another tunable parameter, denoted as p_j, affects the smoothness of the correlation function. When p_j is small, the correlation exhibits a sharp change, while a higher value of p_j results in a more smooth transition. In this work, a simplification is made by setting $p_j = 2$ with Matérn correlation function with $\nu = 5/2$ used in the training process where:

$$\mathbf{R}(\theta, \mathbf{x^i}, \mathbf{x^l}) = \left(1 + \sqrt{5}l + \frac{5l^2}{3}\right) exp(-\sqrt{5}l) \tag{5.18}$$

where $l = \sqrt{(\sum_{j=1}^{k} \theta_j \mid x_j^{(i)} - x_j^{(l)} \mid^{p_j})}$. The correlation matrix can be constructed by evaluating the correlation coefficients between each design site $\mathbf{x^1}$, which can be expressed as:

$$\mathbf{\Psi} = \begin{bmatrix} R(\theta, \mathbf{x^1}, \mathbf{x^1}) & R(\theta, \mathbf{x^1}, \mathbf{x^2}) & ... & R(\theta, \mathbf{x^1}, \mathbf{x^n}) \\ R(\theta, \mathbf{x^2}, \mathbf{x^1}) & R(\theta, \mathbf{x^2}, \mathbf{x^2}) & ... & R(\theta, \mathbf{x^2}, \mathbf{x^n}) \\ . & . & . & . \\ . & . & . & . \\ R(\theta, \mathbf{x^n}, \mathbf{x^1}) & R(\theta, \mathbf{x^n}, \mathbf{x^2}) & ... & R(\theta, \mathbf{x^n}, \mathbf{x^n}) \end{bmatrix} \tag{5.19}$$

The regression parameter β can be found by the generalized least squares solution such that

$$\boldsymbol{\beta^*} = (\mathbf{F}^T \mathbf{\Psi}^{-1} \mathbf{F})^{-1} \mathbf{F}^T \mathbf{\Psi}^{-1} \mathbf{Y} \tag{5.20}$$

The optimal variance σ can be found by the Maximum Likelihood estimates (MLE) such that

$$\sigma^2 = \frac{1}{n} (\mathbf{Y} - \mathbf{F}\boldsymbol{\beta^*})^T \mathbf{\Psi}^{-1} (\mathbf{Y} - \mathbf{F}\boldsymbol{\beta^*}) \tag{5.21}$$

once the parameters $\theta, \beta^*, \sigma^2$ are determined, the response of the Kriging model at a new trial point $\hat{\mathbf{x}}$ can be found by

$$\hat{y}(\hat{\mathbf{x}}) = \mathbf{r}(\hat{\mathbf{x}})^T \boldsymbol{\Psi}^{-1} \mathbf{Y} - (\mathbf{F}^T \boldsymbol{\Psi}^{-1} \mathbf{r}(\hat{\mathbf{x}}) - \mathbf{f}(\hat{\mathbf{x}}))^T \boldsymbol{\beta}^* \tag{5.22}$$

where the vector $\mathbf{r}(\hat{\mathbf{x}})$ contains the correlation coefficient between the new trial point $\hat{\mathbf{x}}$ and the data site points

$$\mathbf{r}(\hat{\mathbf{x}}) = \begin{bmatrix} R(\theta, \mathbf{x^1}, \hat{\mathbf{x}}) \\ R(\theta, \mathbf{x^2}, \hat{\mathbf{x}}) \\ . \\ . \\ R(\theta, \mathbf{x^n}, \hat{\mathbf{x}}) \end{bmatrix} \tag{5.23}$$

5.5 Inference of EIFS for 2D Anisotropic Structures

5.5.1 Inference of EIFS for an Anisotropic Plate Structure with Window Section

A numerical example featuring a crack emanating from a hole was employed to illustrate the proposed methodology for inferring the EIFSD in anisotropic structures. The problem under analysis involves a finite plate composed of anisotropic material, with an initial crack originating from a central hole. The mesh geometry is presented in Figure 5.3, and a close-up view of the central hole and the initial crack is shown in Figure 5.4. The plate is subjected to a constant-amplitude cyclic tensile stress σ on the top and bottom boundaries, with minimum stress σ_{min}, maximum stress σ_{max}, and a stress ratio $R = \sigma_{min}/\sigma_{max}$. The direction of the anisotropic principal axis is assumed to have an angle α relative to the horizontal direction. For this illustrative example, fictional material properties were employed. The Young's modulus ratio is denoted as $\psi = E_1/E_2$, Poisson's ratio as $\nu_{12} = 0.29$, shear modulus as $G_{12} = 789$ MPa, and the material constant in Walker's equation (Eq.(5.5)) is represented by $\gamma = 0.68$ [144]. The Young's modulus is expressed as $E_1 = G_{12}(\psi + 2\nu_{12} + 1)$ [25]. The location of the initial crack, with a size of a_0, is labelled as region B in Figure 5.3a), and it is assumed to have initiated along the E_1 direction. The angle

between the anisotropic principal axis and the global coordinate system is defined as α, as shown in Figure 5.3b).

The plate is subdivided into distinct regions, including an outer boundary, an inner boundary, and a crack region. The mesh used for this analysis comprises a total of 62 quadratic elements. Specifically, the outer straight edges consist of 4 elements each, while the curved corners, as depicted in Figure 5.3, are composed of 4 elements each. The horizontal straight inner edges given in Figure 5.4 are represented by 2 elements each. Notably, the right vertical straight inner edge is meshed with 22 elements, while the left vertical straight inner edge employs 4 elements in the mesh. The number of elements used in the mesh of the initial crack region varies depending on the initial crack length. For each growth increment, one element is added to the crack on each surface. As an example, if the initial crack length is 5 mm, the mesh for this initial crack consists of 5 elements for each surface of the crack. A visual representation of the mesh in the crack region is provided in Figure 5.4.

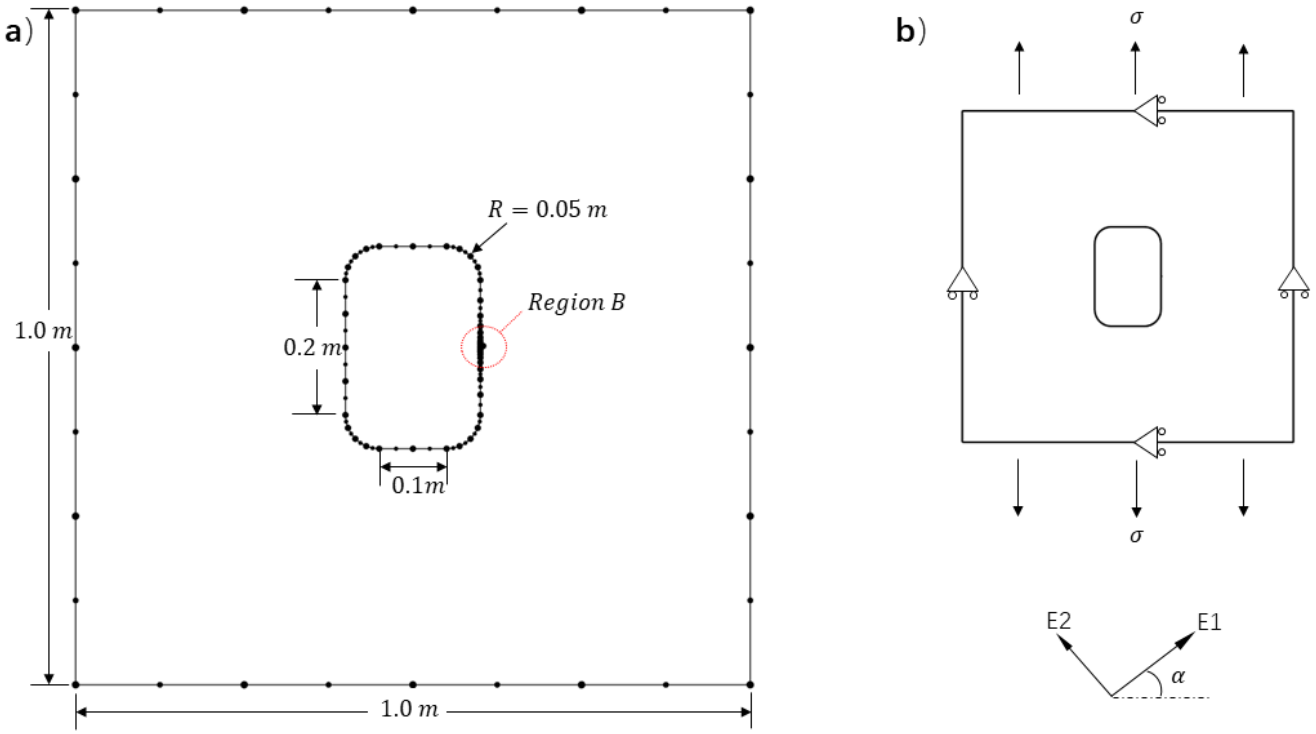


Figure 5.3: The BEM mesh (left) and boundary conditions (right) of the anisotropic plate used in the numerical example. The larger dots denote the end-nodes of the elements, while the smaller dots represent the centre-nodes. The initial crack is located at the middle of the right-most edge of the centre hole. The anisotropic principal axis exhibits an inclination angle denoted as α concerning the global horizontal direction. To emphasize, the region where the initial crack is situated has been demarcated as 'Region B'.

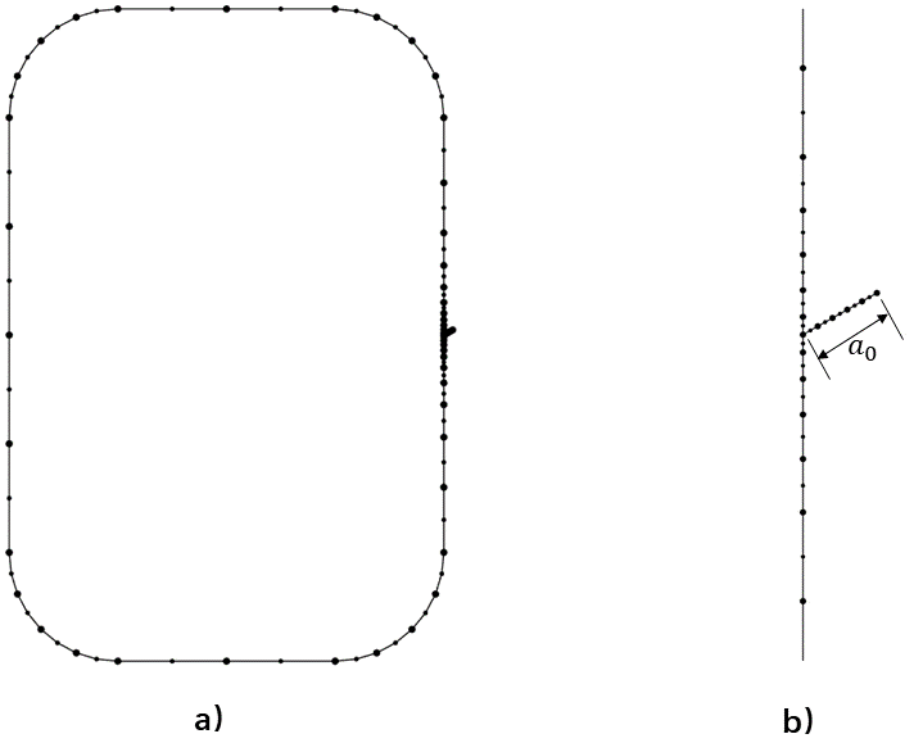


Figure 5.4: Sub-figure (a) shows the BEM mesh for the centre hole. Sub-figure (b) shows a zoomed-in view of the BEM mesh around the initial crack of length a_0 located at the middle of the right-most edge of the centre hole. To provide accurate results, elements were concentrated near the base of the crack.

5.5.1.1 Simulation of Inspection Data

The inspection data utilized in this study was assumed to originate from regular inspections of a specific component within an aircraft fleet. This inspection data was generated simulated data by progressively increasing the crack size from its initial length a_0 to its final length a_{det} using the DBEM. The number of cycles necessary for the crack to propagate from a_0 to a_{det} was recorded for each simulated inspection. It's important to note that the crack growth parameters were considered as stochastic variables following lognormal distributions. These parameters encompassed the material property ψ, the orientation angle of the principal direction denoted as α, the Paris Law constants C_0 and m, the maximum applied load σ_{max}, and the applied load ratio R, defined as the ratio of σ_{min} to σ_{max}. To assess the reliability and robustness of the methodology outlined in Section 5.3, two levels of uncertainty for each of the crack growth parameters were examined: low uncertainty and high uncertainty. Detailed information regarding these crack growth parameters is provided in Table 5.1:

Table 5.1: Uncertainties presented in the crack propagation.

				CoV	
Variable	Description	Distribution	Mean	Low	High
C_0	Paris law Constant	Lognormal	$1.027 \times 10^{-9} \frac{m/cycle}{(MPa\sqrt{m})^m}$	0.01	0.05
m	Paris law exponent	Lognormal	2.389	0.01	0.02
σ_{max}	Maximum applied stress	Lognormal	$30MPa$	0.01	0.05
R	Stress ratio	Lognormal	0.1	0.01	0.05
ψ	Ratio of Young's modulus	Lognormal	0.2	0.01	0.05
α	Angle of the anisotropic principal axis	Lognormal	30°	0.01	0.05

The accuracy of fatigue crack growth modelling depends upon the information available concerning the parameters influencing crack growth. The crack growth rate C in the Paris law may exhibit variations attributable to the loading environment and cycle frequency. Nevertheless, the value of m is typically less influenced by these factors and is often treated as a deterministic quantity, as indicated by the literature [160]. To assess the robustness of the proposed method, a slight Coefficient of Variation (CoV) of 0.02 is assigned to the parameter m, while a higher variation is assigned to the value of C_0. The Young's modulus E can also manifest variations depending on the measurement methodology employed. Generally, the value measured through a well-established standard method can vary within the range of 3-5% [161, 162], thereby contributing to the uncertainty in the value of ψ. Advanced measurement techniques, however, have the potential to reduce the uncertainty in E to as low as 0.36% [163]. Incorporating the uncertainty in the angle α is an essential consideration within this work, accounting for potential misalignments of the principal axis in anisotropic materials. The sources of misalignment contributing to this uncertainty are primarily associated with the manufacturing process, temperature variations, and packing procedures, among others. These misalignments could exert an influence on the overall geometry of the anisotropic structure [164]. For instance, Toft [165] has suggested that the fibre misalignment angle can vary within the range of 0.9 degrees to 2 degrees. Although this range is specifically relevant to composites, it serves as an illustrative example of a critical uncertainty inherent in anisotropic materials.

In order to evaluate the robustness of the proposed EIFS inference methodology, two levels of uncertainty were examined for each parameter detailed in Table 5.1: a state of low uncertainty and another characterized by high uncertainty.

For EIFSD inference, a dataset comprising a total of 500 simulated inspections has been generated. This dataset assumes its origin from a fleet of aircraft, thus obtaining 500 inspections a reasonable choice. Nonetheless, it remains possible that Bayesian updating might reach a state of convergence before incorporating data from all 500 inspections, rendering the utilization of the entire dataset potentially unnecessary. The parameters subjected to randomization across the simulated 500 inspections encompass:

1. **The initial crack size.** The true EIFSD is assumed to have the distribution parameter $\Theta_{true} \sim lnN(5, 0.5)$. The initial crack size for each inspection is randomly sampled from Θ_{true} with a mean of 5 mm and a standard deviation of 0.5 mm.

2. **The values of the crack growth parameters.** For each inspection, a single value for each of the crack growth parameters C_0, m, σ_{max}, R, ψ and α is randomly sampled from the distributions seen in Table 5.1.

5.5.1.2 Evaluation of the Surrogate Model

To estimate the distribution $f_{N|\hat{\mu}_i,\hat{\sigma}_j,\mathbf{Y}}$ as defined in Eq.(5.6), MCS was performed, involving the utilization of 1×10^7 samples. This extensive sample size was necessary to ensure a high degree of accuracy in the estimation. Given the computational demands of handling such a vast number of samples, direct employment of the DBEM proved unfeasible. Consequently, a Kriging model was established to serve as an approximation for the DBEM, facilitating the MCS process.

The surrogate model, in this case, provides the output, which is the effective stress intensity factor K_{eff}. This value plays a crucial role in the estimation of the number of cycles required for crack propagation, following the Paris Law outlined in Eq.(5.3). During the training of the Kriging model, essential information regarding the material properties ψ and α, as well as the crack sizes in the propagation (a_0 and a), were provided as the inputs to the model.

$$K_{eff} = f^{kriging}(\psi, \alpha, a_0, a) \tag{5.24}$$

Where $f^{kriging}$ represents the Kriging model employed to estimate the effective stress intensity factor at the crack tips. This estimation is conducted after the crack has grown from its initial

size, denoted as a_0, to reach a final size of a_{det}. As given in Figures 5.3 and 5.4, it is important to note that the initial crack is assumed to align with the anisotropic principal axis, characterized by an angle α relative to the global horizontal direction. Consequently, the crack propagation does not occur along a linear trajectory; instead, it follows a curved path. Furthermore, any alteration in the size of the initial crack, a_0, leads to a corresponding adjustment in the curvature of this path. Consequently, the effective stress intensity factor K_{eff} associated with the fully grown crack of size a also experiences a slight modification due to this change in a_0. Therefore, it is important to consider the initial crack length as an input parameter in the Kriging model and it can be observed that K_{eff} is a function of a_0 within the framework of this study. It is worth emphasizing that even a slight change in a_0 can result in a substantial alteration in the number of cycles N due to the Paris Law exponent, as will be presented in the subsequent figures presented in this section.

When developing the surrogate model, the range considered for the initial crack size, a_0, encompassed all possible combinations of trial points $(\hat{\mu}_i,\hat{\sigma}_j)$ as outlined in Section 5.3. In contrast, the training range for the final crack size, a, spanned from a_0 to $a_{det} = 20$ mm, where a_{det} symbolizes the typical minimum detectable crack size achievable through Non-Destructive Inspection (NDI) techniques. Additionally, a conditional sampling was applied such that the sampled final crack length a must be larger than the sampled initial crack size. The ranges chosen for the material properties, ψ, and the angle α, were established to encompass a slightly larger range specified by the lognormal distributions featured in Table 5.1 since it is often found that at the edges of the Kriging response surface, the error tends to be larger. Furthermore, during the training phase of the surrogate model, the maximum applied load was set to an average value of $30MPa$. This decision was grounded in the assumption that the stress intensity factor demonstrates linear proportionality to the applied stress, adhering to the principles of Linear Elastic Fracture Mechanics. For clarity, the training ranges are summarized in Table 5.2.

Table 5.2: The training ranges covered by the surrogate model.

Variable Name	Surrogate model training range
Initial crack size a_0	$2 - 8mm$
Final crack size a	$2 - 30mm$
Ratio of Young's modulus ψ	$0.18 - 0.21$
Fibre inclination angle α	$23° - 38°$

To construct an initial training dataset, an initial set of 50 sample points was chosen via the Latin Hypercube sampling method. Subsequently, a sequential design technique known as Delaunay triangulation sampling was employed to decide the optimal locations for all subsequent sample points. This strategy aimed to enhance the precision and reliability of the final surrogate model. Iteratively, the Kriging model was refined through sequential design until the Root-Relative Squared Error (RRSE) achieved a level of less than 5%, as determined via cross-validation. In total, 127 sample points were incorporated into the training of the Kriging model. The cumulative CPU time expended to train the surrogate model amounted to 44.8 minutes.

Upon obtaining the Kriging model for K_{eff}, the surrogate model for the number of cycles, denoted as N, is developed by substituting the mean values of the Paris law constants and the applied load into Eq.(5.3). The integration required in Eq.(5.2) is approximated using the Trapezoidal rule.

To assess the accuracy of the surrogate model, a set of 4725 testing points, distinct from those used during the surrogate model training, were generated via the DBEM. These points were then compared to the results provided by the surrogate model. The statistical errors between the Kriging model and the testing dataset results were evaluated, and the values are presented in Table 5.3 for both K_{eff} and N.

Tabulated in Table 5.3, the error between the surrogate model and DBEM is notably small. The Root-Relative Squared Error (RRSE), Mean-Absolute-Percentage-Error (MAPE), Mean-Absolute-Error (MAE), and Root-Mean-Square-Error (RMSE) all exhibit low values, indicating a high level of accuracy. Furthermore, the coefficient of determination (R^2) is in close proximity to 100%, underscoring the capacity of the surrogate model to effectively approximate the DBEM model.

For a visual representation of the accuracy, surface plots for K_{eff} and N are presented in Figures 5.5a) and 5.5b) respectively. Given that the surrogate model operates in a 5-dimensional space (four inputs and one output), only an illustrative 3D surface is displayed, at the value of $\psi = 0.19$ and $\alpha = 29.5°$. To emphasize accuracy, the surface plots can be effectively compared with the testing points, represented as black dots, as demonstrated in the figures.

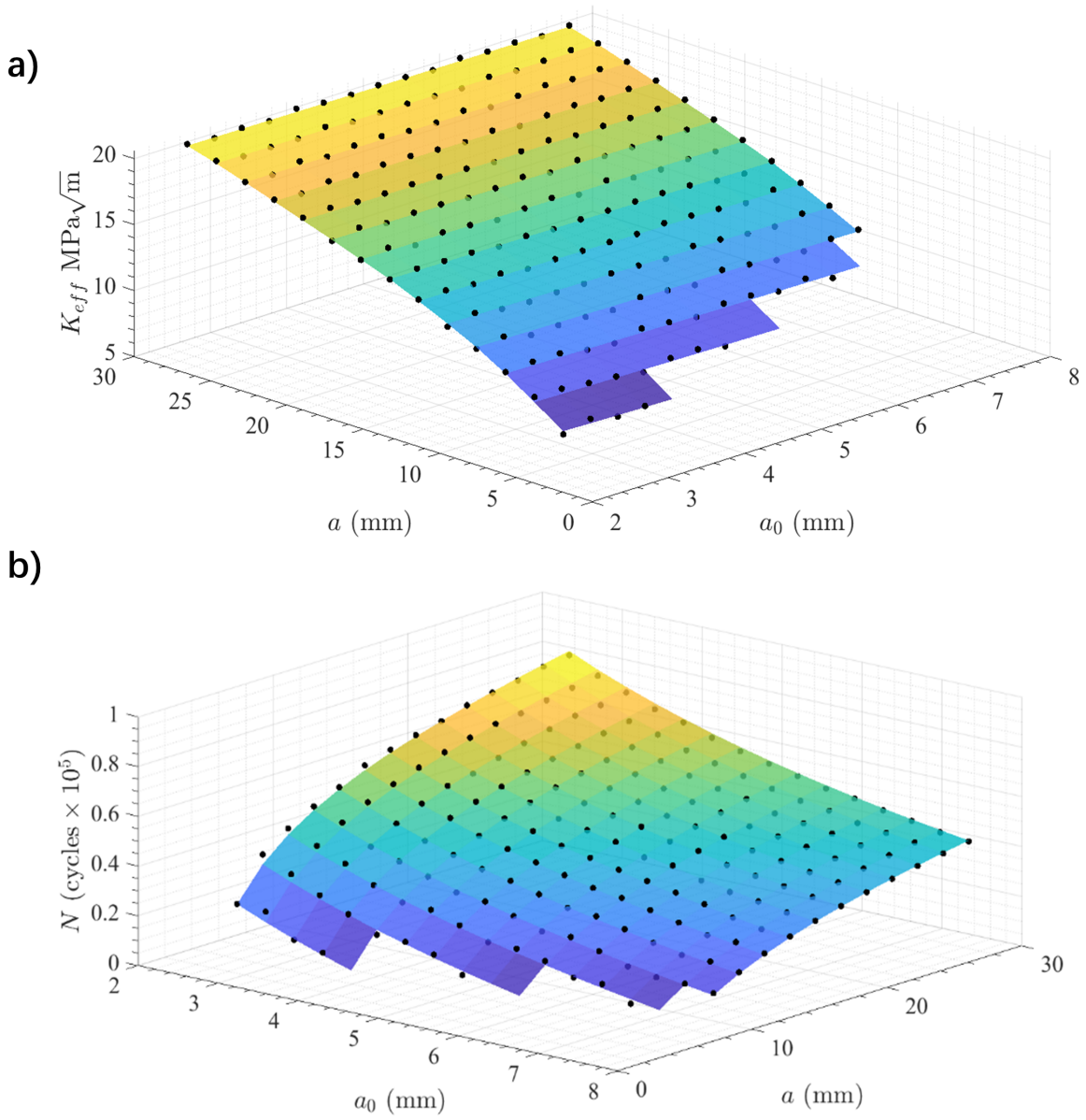


Figure 5.5: Surface plots showing the results evaluated from the Kriging models for the testing dataset when $\phi = 0.19$ and $\alpha = 29.5°$. The surfaces represent the results of the Kriging models over a range of initial and intermediate crack sizes. Sub-figure (a) shows the results of K_{eff} and sub-figure (b) shows the results of N.

Table 5.3: Model error of the K_{eff} and N surrogate models compared to the test dataset.

Model	RRSE(%)	MAPE(%)	MAE	RMSE	R^2 (%)
K_{eff}	4.73	0.95	0.13 $MPa\sqrt{m}$	0.16 $MPa\sqrt{m}$	99.8
N	7.68	3.17	1.01×10^3 $cycles$	1.25×10^3 $cycles$	98.2

The relatively higher RRSE observed in the surrogate model for N compared to K_{eff} can be attributed to the presence of the exponent m in the Paris law. This exponent magnifies the

error introduced in K_{eff}. However, it's essential to note that the primary region of interest lies near $a = 20$ mm. Within this region, specifically ranging from 17 mm to 23 mm, the RRSE is only approximately 4.82%. This implies that the surrogate model achieves an acceptable level of accuracy within the critical region of interest.

To gauge the efficiency of the proposed Kriging model, a comparative study was conducted to assess the CPU time required by the surrogate model in contrast to the DBEM when performing MCS. The results are summarized in Table 5.4. Notably, the surrogate model exhibits over 10,000 times higher efficiency than the DBEM in this specific application. For each combination of $\hat{\mu}_i$ and $\hat{\sigma}_j$, the MCS involved a total of 1×10^7 sampling points to estimate the distribution $f_{N|\hat{\mu}_i,\hat{\sigma}_j,\mathbf{Y}}$. The time required for generating 1×10^7 results using the DBEM is estimated to be 473 days. In contrast, the Kriging model completes the simulation in 340 seconds. This contrast underscores the substantial computational cost reductions made possible by implementing the proposed statistical inference methodology, demonstrating the effectiveness of the Kriging model as a highly efficient alternative to the DBEM model for this problem.

Table 5.4: Comparison of CPU time required by the kriging model and DBEM respectively.

Model	**CPU time per simulation** (s)
DBEM	4.09
Kriging model	3.4×10^{-5}

5.5.1.3 Inference of EIFSD

The proposed Bayesian updating methodology described in section 5.3 is applied for the inference of the EIFSD for the structure shown in Fig. 5.3. To test the robustness of this methodology for an anisotropic structure, two sources of variation are considered:

1. **The prior distribution:** In Eq.(5.8), an initial estimate is required in the form of an initial prior distribution for Bayesian updating. The accuracy of this initial guess, and how closely it approximates the 'true' distribution, largely depends on the engineer's judgment. To represent the quality of these initial guesses, three categories are utilized: 'good,' 'moderate,' and 'poor.' These quality levels reflect the proximity of the initial guess to the actual distribution. For instance, a 'poor' initial guess is significantly distant from the actual distribution,

whereas a 'good' guess closely aligns with it. When assessing the 'closeness' of an initial guess, greater emphasis has been placed on the standard deviation, as achieving convergence with the standard deviation is often more challenging than for the mean, as will be evident in the results presented later in this section. The specific means and standard deviations employed for these guesses are detailed in Table 5.5. Ideally, in a highly robust methodology, the quality of the initial guess should exert a diminishing influence on convergence as more inspection data is integrated into the analysis.

Table 5.5: Three levels of quality of the prior distribution that are used to represent 'good', 'moderate', and 'poor' engineering judgement.

Prior distribution	Distribution	Mean	Standard deviation
Poor	Lognormal	0.5 mm	1.5 mm
Moderate	Lognormal	10 mm	1 mm
Good	Lognormal	6 mm	0.6 mm

2. **The level of uncertainty associated with the material properties and the crack growth parameters:** The degree of uncertainty linked to the material properties and the parameters governing crack growth in the Paris law relies on the specific measurement techniques and manufacturing processes employed, as elaborated upon in the preceding section. Table 5.1 categorizes two distinct levels of uncertainty: a low level and a high level. Ideally, a highly robust methodology should exhibit decreased sensitivity to the level of uncertainty as more inspection data is incorporated into the analysis. This robustness would signify that the methodology's performance remains stable even in the presence of varying levels of uncertainty.

Figure 5.6 illustrates the convergence of EIFSD through Bayesian updating, incorporating data from 50, 100, 300, and 500 inspections. To maintain conciseness, only two cases are shown: a) In Figure 5.6a, convergence is observed for a scenario with low uncertainty and a 'good' initial guess. b) In Figure 5.6b, convergence is depicted for a scenario with high uncertainty and a 'poor' initial guess. In both cases, the posterior distribution gradually converges towards the actual EIFSD as data from additional inspections is incorporated. Notably, in Figure 5.6a, even when data from only 100 inspections is employed, the posterior distribution closely approximates the actual

EIFSD, and its shape remains relatively stable even with the inclusion of 300 or 500 inspections. In contrast, in Figure 5.6b, the posterior distribution after 100 inspections deviates more from the actual EIFSD compared to Figure 5.6a, indicating a slower convergence in this particular case.

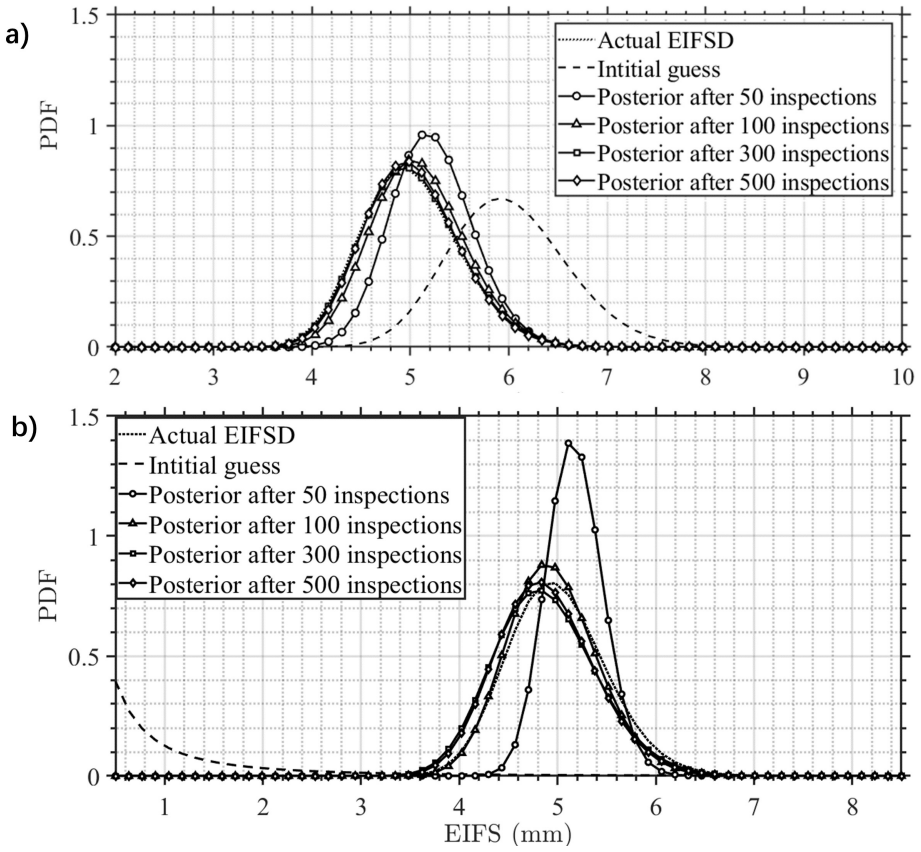


Figure 5.6: Convergence of the posterior distributions computed by Bayesian updating after using the data from 50, 100, 300, and 500 inspections. Sub-figure (a) shows the convergence for a 'good' initial guess and low uncertainties. Sub-figure (b) shows the convergence for a 'poor' initial guess and high uncertainties.

The convergence history of the mean and standard deviation is presented in Figure 5.7 and 5.8 for cases of low and high uncertainty, respectively. Detailed values of the mean and standard deviation are presented in Table 5.6 and 5.7. In the case of low uncertainty, as observed in Figure 5.7 and Table 5.6, the mean remains relatively stable after approximately 158 inspections. Convergence within ± 0.1 mm of the 'actual' mean (5 mm) is achieved with data from approximately 80 inspections. After 500 inspections, the error in the mean is merely 0.34%. The standard deviation exhibits a slight divergence from the actual standard deviation of 0.5 mm between 300 and 500 inspections, yet it remains very close to the actual value. After 500 inspections, the

error in the standard deviation is just 3.72%. It's notable that the quality of the initial guess significantly impacts convergence when data from fewer than 60 inspections are used, but its influence diminishes as more data is incorporated.

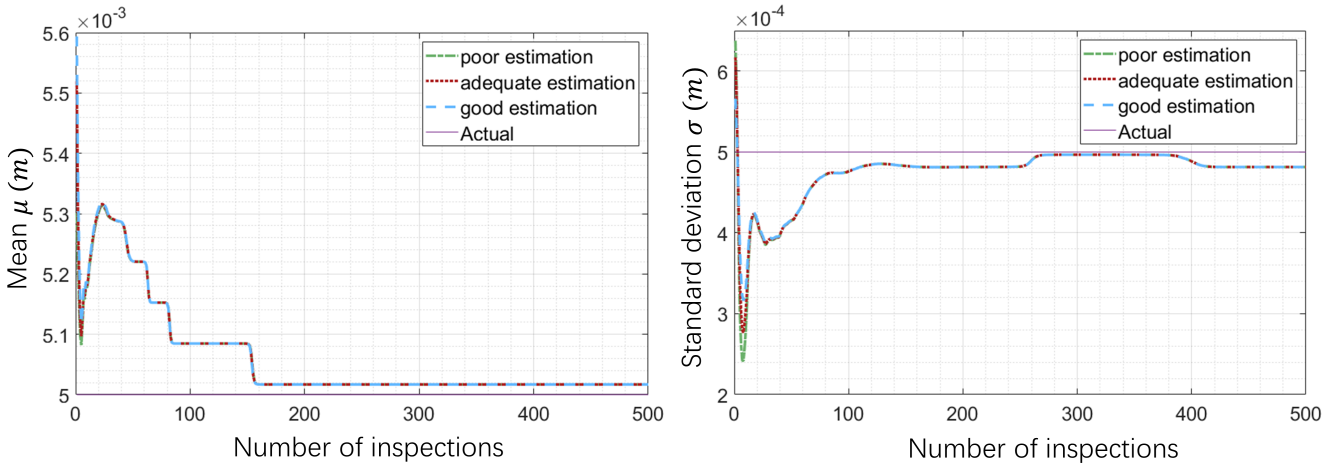


Figure 5.7: Convergence of the EIFSD mean and standard deviation from Bayesian Updating for the 'low' level of uncertainty.

Table 5.6: Convergence of the mean and standard deviation from Bayesian updating for the 'low' level of uncertainty.

	Mean μ (mm)				Standard deviation σ (mm)			
Inspection	50	100	300	500	50	100	300	500
Good	5.2213	5.0847	5.0169	5.0169	0.4158	0.4760	0.4966	0.4814
Moderate	5.2212	5.0847	5.0169	5.0169	0.4176	0.4764	0.4966	0.4814
Poor	5.2211	5.0847	5.0169	5.0169	0.4153	0.4761	0.4966	0.4814

Similar convergence behaviour is observed in the case of high uncertainty, as presented in Figure 5.8 and Table 5.7. Convergence within ±0.1 mm of the 'actual' mean (5 mm) is achieved with data from approximately 170 inspections, and the error after 500 inspections is 2.37%. It's important to note that the higher error in the high uncertainty case, compared to the low uncertainty case, is primarily due to the significantly greater uncertainties associated with the crack growth parameters. The standard deviation does not appear to fully converge within 500 inspections in the high uncertainty case but achieves an error of 0.22% when data from 500 inspections is used. The convergence of the mean is less affected by the quality of the initial guess, while the convergence of the standard deviation is more strongly impacted when data from a small number of inspections

(less than 100) is used. However, its impact diminishes with a higher number of inspections.

It's evident from Figures 5.7 and 5.8 and Tables 5.6 and 5.7 that even after a substantial number of inspections, Bayesian updating does not precisely converge to the actual mean of 5 mm and the actual standard deviation of 0.5 mm. This divergence is influenced by the parameter P^{trial}, representing the number of trial points used to model the posterior distributions as seen in Figure 5.6 and detailed in Section 5.3. When P^{trial} is set to a high value, the posterior distributions in Figure 5.6 are modelled with high resolution, enabling the mean and standard deviation shown in Figures 5.7 and 5.8 to achieve closer convergence to their actual values. In contrast, when P^{trial} is low, the posterior distributions in Figure 5.6 are modelled with lower resolution, leading to less accurate convergence of the mean and standard deviation. In this study, a value of $P^{trial} = 60$ was chosen, as it provided satisfactory convergence for the mean and standard deviation, as demonstrated in Figures 5.7 and 5.8, and Tables 5.6 and 5.7. For enhanced convergence, P^{trial} can be increased, though this would correspondingly increase the computational time required for Bayesian updating.

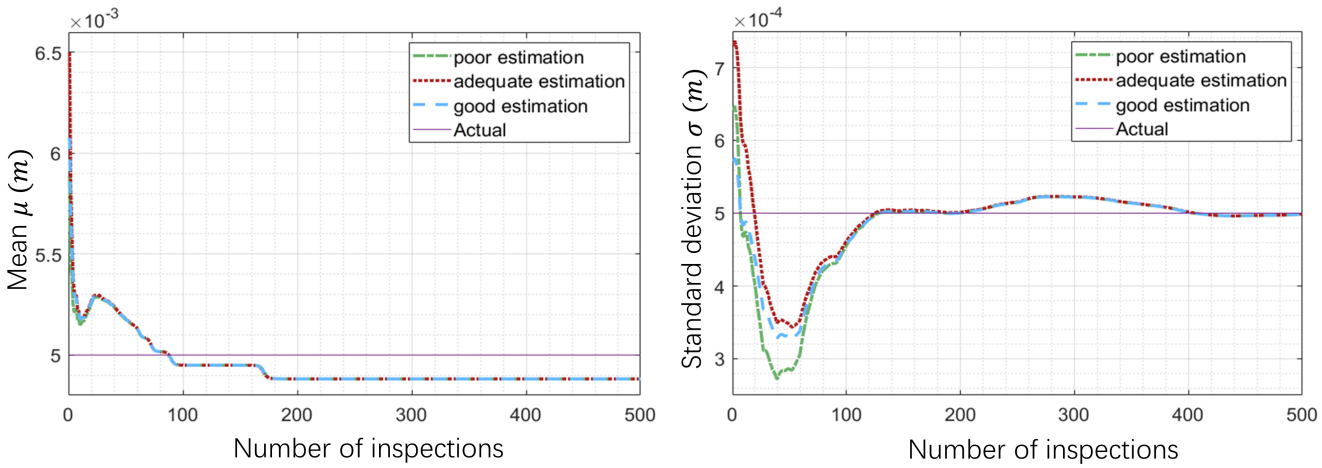


Figure 5.8: Convergence of the EIFSD mean and standard deviation from Bayesian Updating for the 'high' level of uncertainty.

Table 5.7: Convergence of the EIFSD mean and standard deviation from Bayesian Updating for the 'high' level of uncertainty.

	Mean $\mu(mm)$				Standard deviation $\sigma(mm)$			
Inspection	50	100	300	500	50	100	300	500
Good	5.1782	4.9494	4.8814	4.8814	0.3299	0.4568	0.5219	0.4989
Moderate	5.1791	4.9494	4.8814	4.8814	0.3470	0.4619	0.5224	0.4989
Poor	5.1754	4.9494	4.8814	4.8814	0.2857	0.4559	0.5220	0.4989

Figure 5.8 demonstrates that the standard deviation in the case of 'high' uncertainty did not fully converge within 500 inspections. To ensure its convergence, the number of inspections was extended to 1000, and the results are displayed in Figure 5.9. It's evident that convergence is reached at around 600 inspections, and after 1000 inspections, the error is around 2.53%. This extended analysis affirms that with a larger number of inspections, the standard deviation in the high uncertainty case converges as expected.

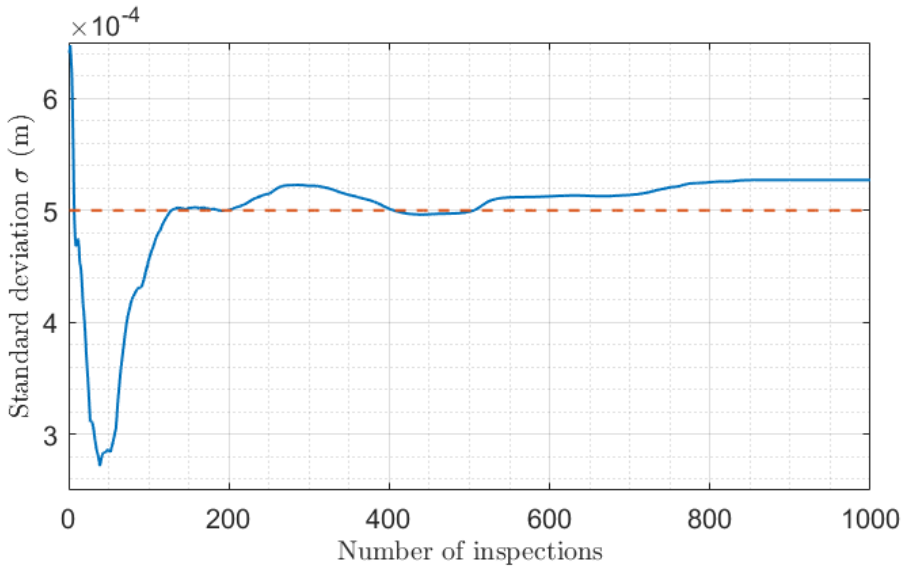


Figure 5.9: Convergence of the EIFS standard deviation estimation with respect to the number of inspection data that has been used in Bayesian Updating at high level of uncertainties. The Bayesian updating the 'poor' prior distribution is plotted only.

In summary, the presented convergence results highlight the substantial influence of the initial guess quality on the convergence process when a relatively small number of inspections is used (below 100). However, this influence diminishes as the number of inspections increases. Moreover, the results demonstrate that even in the case of 'high' uncertainty, convergence to within 3% can

be attained within 500-600 inspections. This underscores the high level of robustness inherent in the proposed EIFSD inference methodology.

5.5.1.4 Parametric Study for Convergence

A detailed investigation was conducted to assess the individual impact of each crack growth parameter's uncertainty on overall convergence. This study was structured such that the uncertainty in only one parameter was considered at a time, while the remaining parameters were treated as deterministic with fixed values at their mean. High uncertainty levels were employed for the parameter under investigation, and associated inspection data was simulated. The convergence results are visualized in Figure 5.10.

In the examination of convergence, it was determined that both the mean and standard deviation converged for each parameter within 500 inspections. However, there were notable differences in the convergence characteristics for different parameters: 1) ψ exhibited the largest error in standard deviation. 2) m required the most inspections to achieve convergence for standard deviation. 3) C_0 needed the most inspections to achieve convergence for the mean but converged quickly for the standard deviation. 4) α converged well for both the mean and standard deviation.

In summary, the overall convergence presented in Figure 5.6 could be most effectively improved by reducing the uncertainty associated with m and ψ. These parameters had a more substantial impact on convergence, particularly in terms of standard deviation, and addressing their uncertainties would enhance the rate of convergence of the EIFSD inference methodology.

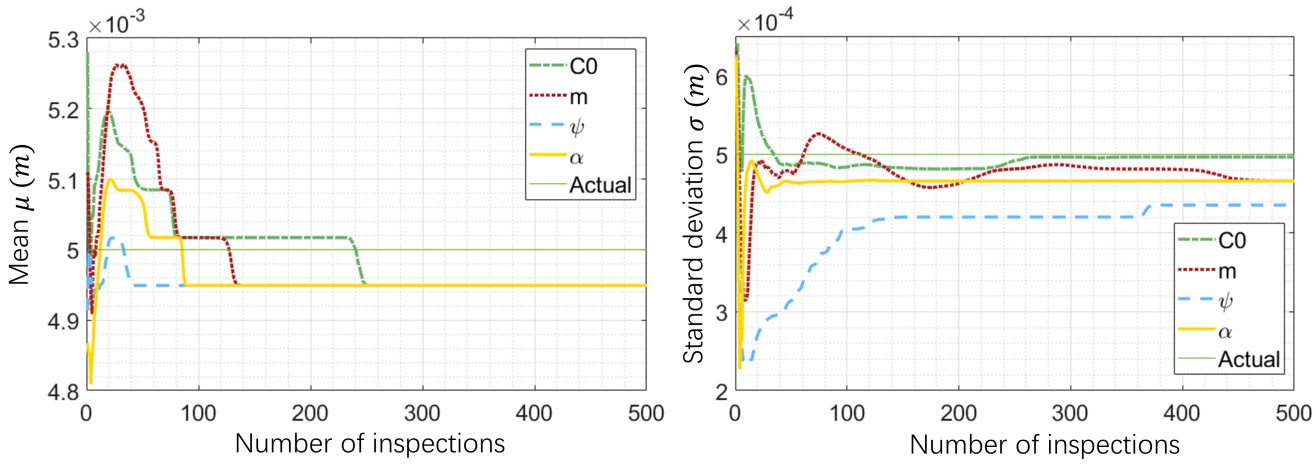


Figure 5.10: Convergence of mean and standard deviation when consider individual uncertainty.

5.5.1.5 Application of EIFSD to Maintenance

The routine inspections of aircraft components are crucial to prevent catastrophic failures. These inspections should be conducted at regular intervals, ideally before a crack reaches a critical size. To determine the appropriate inspection intervals, it's essential to estimate the fatigue life of the component. This estimation can be achieved by simulating the growth of a crack from its EIFSD to a critical size denoted as $a_{critical}$. The application of EIFSD inference plays a vital role in this process, as it provides insights into the distribution of fatigue life, aiding in making informed decisions regarding maintenance intervals and, consequently, enhancing the overall safety and reliability of the aircraft component.

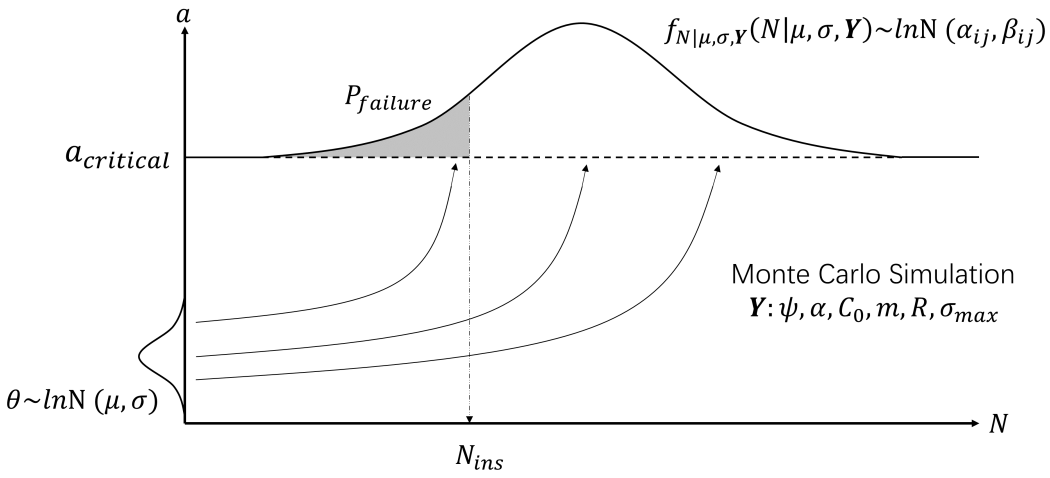


Figure 5.11: Graphical illustration of the estimation of the fatigue life distribution using the inferred EIFSD $\theta \sim lnN(\mu, \sigma)$.

The application of the EIFSD to determine fatigue life is exemplified using the same example as seen in Figure 5.3. This process is visually illustrated in Figure 5.11. The EIFSD results obtained in Section 5.5.1.3 can be utilized to estimate fatigue life. The surrogate model was retrained, extending the range of crack size a from 2 mm to 45 mm. Through MCS, single values of EIFS were sampled from the EIFSD, following a distribution $\theta \sim \ln N(\mu, \sigma)$. These values were grown to an arbitrary critical crack size of $a_{critical} = 40mm$ under the influence of uncertainties in $\mathbf{Y}$", and the number of cycles required was recorded. A total of 1×10^7 sampling points were used in MCS.

In the case of high uncertainty, the EIFSD is represented as $\theta_{high} \sim \ln N(4.8814, 0.4989)$, while

Table 5.8: The fatigue life distributions obtained using MCS with the EIFSD results from section 5.5.1.3, and with the actual EIFSD.

	Lognormal		Normal distribution	
EIFSD (mm)	α_{ij}	β_{ij}	μ $(\times 10^4 cycles)$	σ $(\times 10^4 cycles)$
$\theta_{low} \sim lnN(5.0169, 0.4814)$	11.065	0.093	6.4164	0.595
$\theta_{high} \sim lnN(4.8814, 0.4989)$	11.094	0.196	6.703	1.329
$\theta_{true_low} \sim lnN(5.0, 0.5)$	11.067	0.094	6.432	0.606
$\theta_{true_high} \sim lnN(5.0, 0.5)$	11.069	0.193	6.538	1.274

for the low uncertainty case, it is $\theta_{low} \sim \ln N(5.0169, 0.4814)$. Consequently, two fatigue life distributions were obtained: one for the high uncertainty case and another for the low uncertainty case. These fatigue life distributions were approximated as normal distributions. For comparison, the fatigue life distribution using the actual EIFSD, denoted as $\theta_{true} \sim \ln N(5.0, 0.5)$, was also determined. Detailed information on the fatigue life distributions is provided in Table 5.8.

As mentioned earlier, multiple criteria can be employed to determine the appropriate inspection interval. In this work, the chosen criterion such that the inspection interval should be scheduled after the component has undergone N_{ins} cycles, ensuring that there is less than a 2% chance of failure. This criterion is depicted in Figure 5.11. The fatigue life distributions obtained through the EIFSD inference can be employed to estimate the value of N_{ins}, and the results are presented in Table 5.9.

Table 5.9: Number of cycles to failure chance of 2%. EIFS distribution inferred from the Bayesian updating and actual EIFSD were used with different levels of uncertainties.

EIFSD (mm)	N_{ins} $(\times 10^4 cycles)$ required for $P_{failure} \leq 2\%$
$\theta_{low} \sim lnN(5.0169, 0.4814)$	5.284
$\theta_{high} \sim lnN(4.8814, 0.4989)$	4.398
$\theta_{true_low} \sim lnN(5.0, 0.5)$	5.278
$\theta_{true_high} \sim lnN(5.0, 0.5)$	4.316

Tab. 5.9 provides an intuitive insight into the impact of uncertainties in the crack growth model on inspection intervals. Higher uncertainties in the model result in shorter inspection intervals, necessitating more frequent routine inspections. Additionally, it's evident that in the case of low uncertainty, the difference in the number of cycles to failure when using the actual EIFSD versus the inferred EIFSD was merely 0.11%, while in the case of high uncertainty, this difference was

1.9%. This indicates that by reducing uncertainties in the model, the inspection interval can be estimated with greater accuracy, which is an expected outcome.

It's important to note that the procedure described assumes only one inspection will be performed before reaching the critical crack length. In practice, multiple inspections can be conducted regularly, such as at intervals of a fraction of the fatigue life. The EIFSD method can be adapted to help estimate the intervals for multiple routine inspections, providing a more fine-grained approach to maintenance scheduling.

However, it's essential to emphasize that the EIFSD, while a valuable tool, should not be solely relied upon to determine inspection intervals. Engineers must consider various factors, including manufacturing costs, required human effort, necessary equipment, and other practical considerations when establishing an effective inspection schedule.

5.5.2 Inference of EIFS for an Anisotropic Plate Structure with Crack emanating from a Circular Hole

This section provides a second numerical example, an anisotropic plate with a centred hole and a crack was analysed to illustrate the proposed method for inferring the EIFSD. The geometry is visualized in Figure 5.12. Uniform stresses were applied to the top and bottom boundaries. It was assumed that the principal axis of anisotropy is oriented at an angle α relative to the horizontal direction. The material property ψ was introduced, which is a function of the ratio between Young's moduli: $\psi = E_1/E_2$. The material properties used in the simulation included a Poisson's ratio $\nu_{12} = 0.29$, shear modulus $G_{12} = 789$ MPa, and a material constant $\gamma = 0.68$ [144]. Young's modulus was calculated as $E_1 = G_{12}(\psi + 2\nu_{12} + 1)$ [25].

The initial crack size, denoted as a_0, is located in region B and is assumed to be oriented along the E_1 direction. The 'true' EIFSD is postulated to have a lognormal distribution with parameters $\theta_{true} \sim lnN(6.0, 0.6)$ mm.

The structure under investigation is comprised of an outer boundary, an inner circular boundary, and the crack. The outer boundary is discretized into four elements per edge, while the inner circular boundary consists of 160 elements. The mesh configuration for the starting crack is depicted in Figure 5.12. The initial crack, denoted as a_0, has a length of 3 mm and is represented

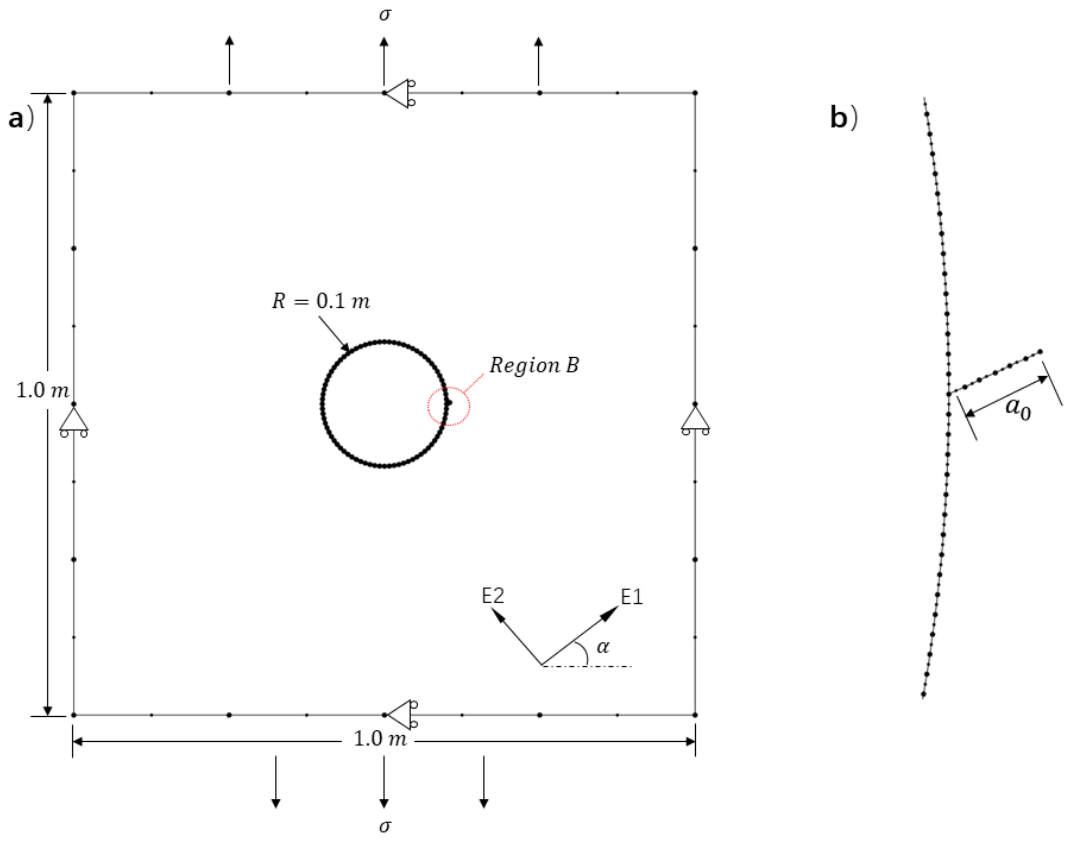


Figure 5.12: Sub-figure (a): The boundary element mesh of the structure and the boundary conditions. Sub-figure (b): The zoom-in demonstration of the starting crack.

by three elements on each crack surface. During the simulation of crack growth, one element is added to each crack surface at the crack tip with each incremental growth step.

In this study, inspection data is generated numerically using the DBEM. Several parameters influence the crack growth process, including the Young's modulus ratio ψ, the orientation of the axis of anisotropy α, Paris law constants C_0 and m, maximum loading stress σ_{max}, and the stress ratio $R = \sigma_{min}/\sigma_{max}$. These parameters are assumed to follow lognormal distributions. To assess the robustness of the proposed method, two levels of uncertainty are considered for each crack growth parameter: low and high. The distributions and coefficients of variation (COV) assigned to each crack growth parameter are provided in Table 5.10.

For each simulated inspection, the 'true' EIFSD is randomly sampled to determine the starting crack size and the values of the crack propagation parameters are randomly selected from their respective distributions. Subsequently, the number of cycles required to grow the starting crack size to a_{det} is recorded for each inspection. This process allows for the generation of inspection

data to be used in the EIFSD inference methodology.

Table 5.10: Uncertainties in the parameter presented in the fatigue crack growth.

				CoV	
Variable	Description	Distribution	Mean	Low	High
C_0	Paris law Constant	Lognormal	$1.027 \times 10^{-9} \frac{m/cycle}{(MPa\sqrt{m})^m}$	0.02	0.05
m	Paris law exponent	Lognormal	2.389	0.01	0.02
σ_{max}	Maximum applied stress	Lognormal	25 MPa	0.02	0.05
R	Stress ratio	Lognormal	0.3	0.02	0.05
ψ	Ratio of Young's modulus	Lognormal	0.15	0.02	0.05
α	Anisotropic axis orientation	Lognormal	25^o	0.02	0.05

5.5.2.1 Surrogate model

Similar to the previous example, a total of 60 trial pairs of mean and standard deviation were considered for use in MCS to estimate the distribution $f_{N|\hat{\mu}_i,\hat{\sigma}_j,\mathbf{Y}}$ as outlined in Eq. 5.6. To ensure accurate estimation, 1×10^6 samples were utilized for each trial pair. It's worth noting that simulating the structure using the DBEM for a large number of samples can be computationally expensive, hence surrogate model was used to replace the DBEM prior to the MCS. The output from this surrogate model is the effective Stress Intensity Factor (SIF), denoted as K_{eff}.

Once K_{eff} is determined, the number of cycles required for crack growth can be obtained by applying the Paris Law, as detailed in Eq. 5.3. When training the Kriging model, the values of the material property ψ, crack propagation lengths a_0 and a were provided as inputs. This ensures that the surrogate model can predict the effective SIF based on these input parameters.

$$K_{eff} = f^{kriging}(\psi, \alpha, a_0, a) \tag{5.25}$$

where $f^{kriging}$ is the surrogate model (Kriging model) that estimates the crack tip effective SIF when growing the crack from the starting length a_0 to a final length a. Once the surrogate model for the K_{eff} is obtained, the Paris Law can be applied to create the surrogate model for the fatigue cycles N to grow the crack from a_0 to a.

For the training of the surrogate model, a total of 342 data points were used for approximately 6.7 hours. To assess the accuracy of the surrogate model, a test was conducted by comparing the

results from the DBEM to those provided by the surrogate model. A total of 2700 testing points for both K_{eff} and N were generated directly from the DBEM, and their values were compared to the predictions of the surrogate model.

Given the complexity of the stochastic model with four inputs and one output, a 3-D example of the model is presented in Figure 5.13 for K_{eff} and N when $\psi = 0.18$ and $\alpha = 24°$. In this figure, the corresponding testing points are depicted as black dots. The statistical errors between the surrogate model and the testing points were assessed and are detailed in Table 5.11. The results demonstrate that the errors between the surrogate model and the DBEM are low, indicating the accuracy and reliability of the surrogate model.

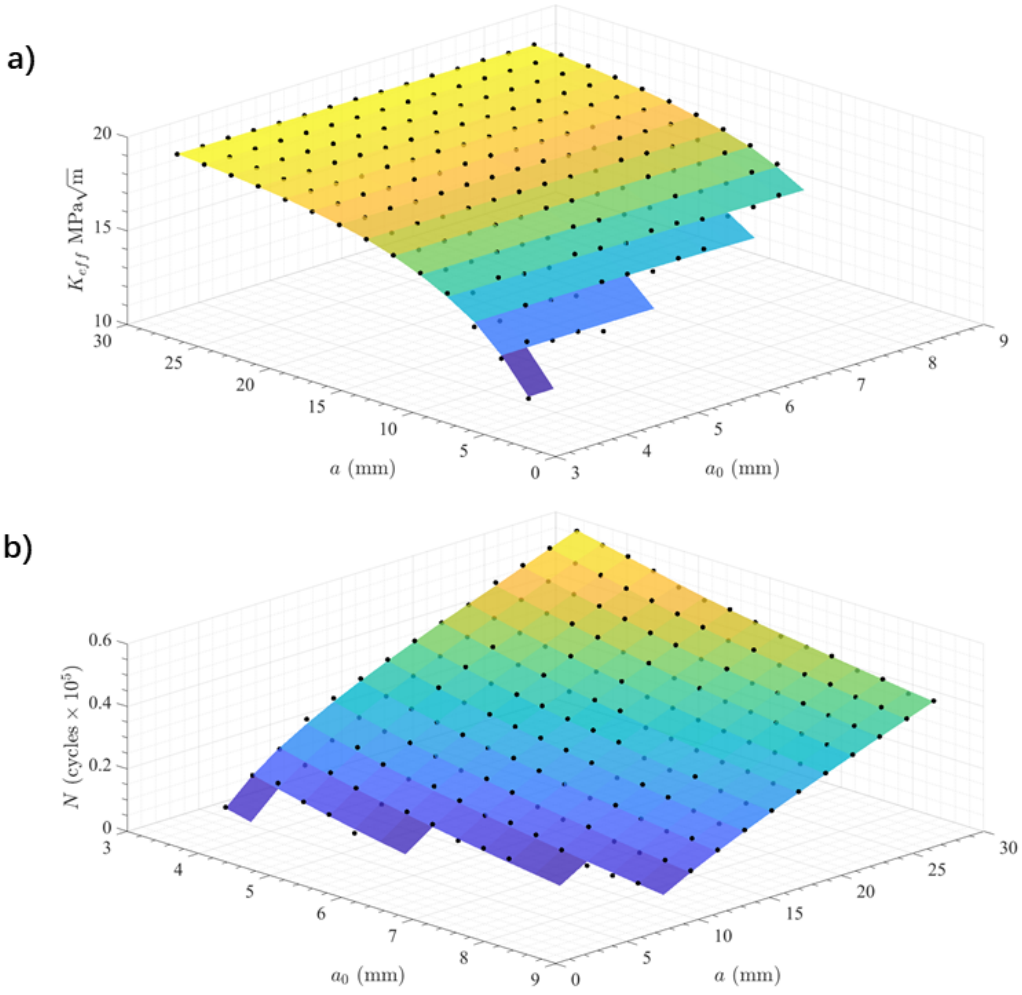


Figure 5.13: Surface plot showing the results of Kriging model evaluation comparing to the test dataset when $\psi = 0.18$ and $\alpha = 24°$. Sub-figure (a) surrogate model for K_{eff} and sub-figure (b) surrogate model for N.

To determine the efficiency of the surrogate model, a study was carried out. It was found that

Table 5.11: The statistical error in stress intensity factors and fatigue life between the actual DBEM and the surrogate model.

Model	RRSE(%)	MAPE(%)	MAE	RMSE	R^2 (%)
K_{eff}	4.59	0.35	0.058 $MPa\sqrt{m}$	0.089 $MPa\sqrt{m}$	99.7
N	6.33	2.74	494 $cycles$	599 $cycles$	99.6

the average CPU time required to estimate one value of K_{eff} was 3.73 s for the DBEM, while it was 0.0156 s for the surrogate model, a decrease by a factor of around 239.

5.5.2.2 Bayesian Inference of EIFS

Similar to the previous example, two sources of the uncertainties were considered during the EIFS inference:

1. **The quality of the prior distribution:** Two quality levels of the prior distributions were tested to show the robustness of the inference methodology. The quality levels are referred to here as 'good' and 'poor' prior distributions. The quality of a prior distribution is defined by its 'closeness' to the 'true' EIFSD. The 'good' prior distribution is $(5mm, 0.5mm)$, while 'poor' prior distribution is $(0.5mm, 1.5mm)$.

2. **The uncertainty level of the crack growth parameters:** Two levels of uncertainties, 'low' and 'high', are given in Tab. 5.10 in terms of the coefficient of variation (COV);

In the case of low uncertainty, as shown in Figure 5.14, the convergence behaviour of the mean and standard deviation can be observed. After utilizing data from 123 inspections, the mean converges to a value of approximately 5.97 mm. To bring the mean closer to the 'true' mean (around 6 $\pm$ 0.1 mm), data from around 77 inspections are required. The difference between the inferred mean and the 'true' mean is 0.56%. The standard deviation achieves convergence at approximately 265 inspections, resulting in an inferred standard deviation of 0.619 mm with an error of 3.11%. The quality of the prior estimation has a minor impact on the inferred value, and noticeable differences are observed only when a limited amount of inspections are available (less than 80 inspections).

In the case of high uncertainty, as shown in Figure 5.15, a similar convergence pattern is observed. The mean converges at about 183 inspections, with an error of $\pm$0.1 mm compared to

the 'true' mean of 6 mm. The values of the mean after 700 inspections reach the same value as in the 'low' uncertainty case. The standard deviation achieves an error of 4.83% (0.629 mm) after 790 inspections. The quality of the initial guess has a small effect on the convergence of the mean. However, the convergence behaviour for the standard deviation is significantly affected when a low number of inspections is used (under 170 inspections) but is less affected when more inspection data is available. It is expected that for a higher uncertainty level, more inspection data is needed to achieve convergence.

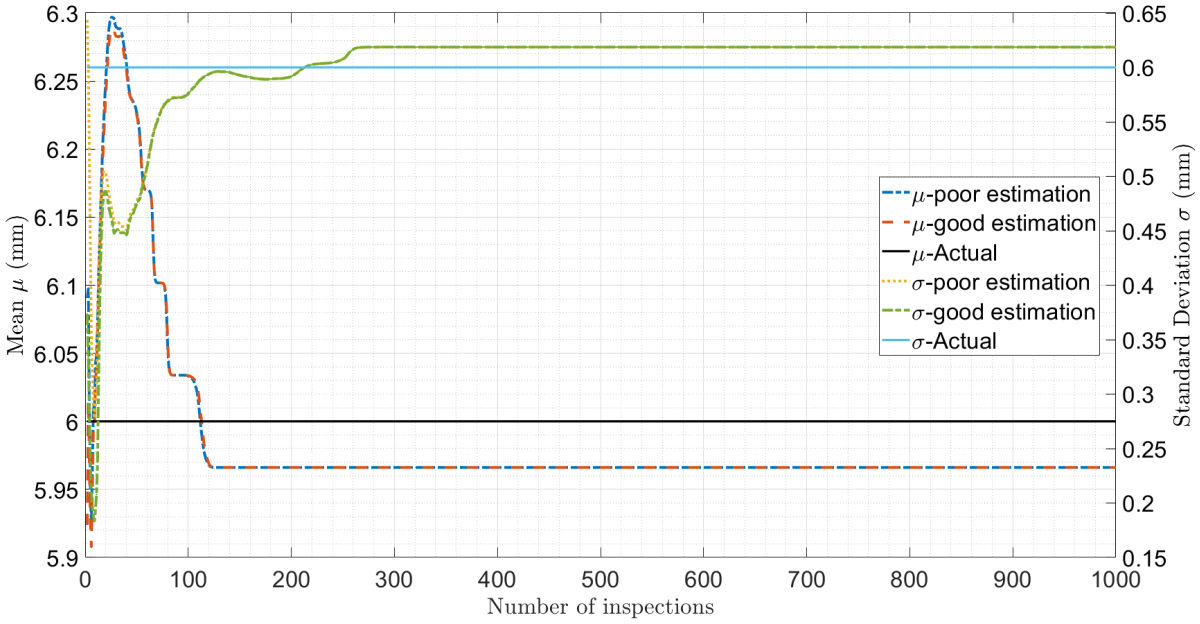


Figure 5.14: Convergence behaviour for the 'low' level of uncertainty.

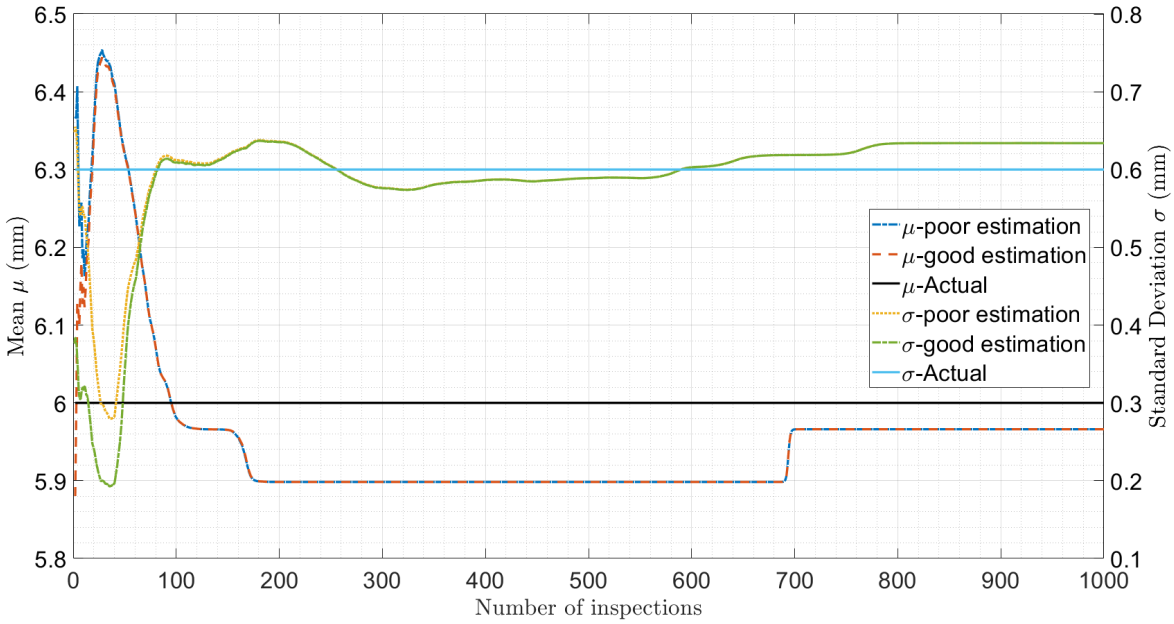


Figure 5.15: Convergence behaviour for the 'high' level of uncertainty.

5.5.2.3 Application of the inferred EIFSD

The application of the EIFSD to determine fatigue life is demonstrated using the same example as in Figure 5.12 and the same uncertainties in the fatigue crack growth parameters. The inferred EIFSD from Bayesian updating, as presented in the previous section, is applied to estimate fatigue life through MCS. In this demonstration, a critical crack size of $a_{critical} = 35$ mm is assumed, and the number of cycles required to grow the crack from its EIFSD to $a_{critical}$ is recorded. A total of 1×10^6 samples are used in MCS. The initial crack size, uncertainties in geometry, and parameters affecting crack growth are randomly sampled for each simulation. The location and shape parameters α and β can be determined by fitting the results obtained from the MCS to a lognormal distribution.

The results obtained from Bayesian updating under both 'high' and 'low' levels of uncertainty are used for MCS. The criteria for determining the inspection interval largely depend on engineering judgment. In this work, it is assumed that the component should be inspected at N_{ins} cycles so that the structural failure probability is less than 2%. The fatigue life distributions and the corresponding values of N_{ins} are provided in Table 5.12.

The results presented in Table 5.12 show that a reduced inspection interval is needed when

Table 5.12: The results of the distribution of the fatigue life in the form of $lnN(\alpha, \beta)$ obtained using the Monte Carlo simulation. Assuming that the structure needs to ensure that the failure chance of less than 2%.

Lognormal			
EIFSD (mm)	α	β	N_{ins} $(\times 10^4 cycles)$ required for $P_{failure} \leq 2\%$
$\theta_{low} \sim lnN(5.9661, 0.6186)$	11.211	0.0751	6.339
$\theta_{high} \sim lnN(5.9661, 0.6289)$	11.215	0.1868	5.059
$\theta_{true_low} \sim lnN(6.0, 0.6)$	11.209	0.0737	6.346
$\theta_{true_high} \sim lnN(6.0, 0.6)$	11.213	0.1853	5.077

there is a higher level of uncertainty in crack propagation. This implies that inspections should be conducted more frequently, leading to an increase in the overall cost of inspection. However, it's also evident that the number of cycles for failure is very similar between the case where the actual EIFSD is used and the case where the inferred EIFSD is used, with only a small difference of 0.12% at low uncertainty and 0.35% at high uncertainty. This demonstrates the accuracy of the proposed EIFSD inference methodology in estimating the true EIFSD and its capability to accurately determine inspection intervals.

5.5.3 Summary

This section presents a novel methodology for the statistical inference of the Equivalent Initial Flaw Size Distribution (EIFSD) using Bayesian Updating, specifically tailored for anisotropic materials. The EIFSD approach offers an alternative solution to overcome the challenges associated with modelling small crack growth, providing engineers with a means to accurately estimate the fatigue life of anisotropic aircraft components. This method can lead to less conservative designs, enabling engineers to harness the weight-saving benefits of anisotropic materials, potentially reducing aircraft weight, fuel consumption, and carbon emissions.

To demonstrate the methodology, the first numerical example involving an aircraft component made of an anisotropic material with an initial crack was explored. The Dual Boundary Element Method (DBEM) was employed to model crack growth, considering an inclined anisotropic principal axis. The DBEM's efficiency in modelling crack propagation without the need for re-meshing, using only boundary meshes, was highlighted. To enhance the efficiency of the EIFSD inference

methodology, a surrogate model in the form of a Kriging model was developed based on the DBEM. This surrogate model was over 10,000 times faster than the DBEM, improving the computational cost for EIFSD inference through Monte Carlo simulations (MCS).

The methodology was tested under different levels of uncertainty in crack growth parameters and anisotropic material properties, encompassing low and high-uncertainty scenarios. The results indicated that even in cases of high uncertainty, the estimated fatigue life based on the inferred EIFSD showed minimal errors, with only 0.11% error for low uncertainty and 1.9% error for high uncertainty, compared to the actual fatigue life. Similar results were observed in the second numerical example involving an anisotropic square plate with a crack demonstrated the effectiveness of this approach. Robustness testing with two levels of uncertainty showed that the EIFSD could be accurately inferred with an error of less than 5% for both levels of uncertainty.

The robustness of the methodology was also explored by examining the quality levels of the prior distribution in Bayesian updating for both examples. It was found that the quality of the prior distribution had a more noticeable impact when a small number of inspections were used (less than 100 inspections). However, with a larger amount of inspection data, the impact was significantly reduced, indicating the methodology's high level of robustness.

The proposed methodology demonstrates its adaptability to high levels of uncertainty while maintaining high accuracy. It has the potential to be applied for determining inspection intervals in anisotropic aircraft components, a critical consideration for aircraft maintenance, given the labour-intensive and equipment-dependent nature of inspections, as well as the complex disassembly of aircraft components.

5.6 Inference of EIFS for Shallow Shell Structure

To demonstrate the effectiveness of the proposed method for shallow shell structures, an analysis of a fuselage window structure with an initiating crack at the window's corner is presented. The structure is subjected to combined membrane, bending, and uniform pressure loads. The structure comprises Aluminium 2024-T3, having a Young's modulus of $E = 68.9\,\text{GPa}$ and a Poisson's ratio of $\nu = 0.33$. The structural geometry adheres to the specifications outlined in the previous chapter's example. Uncertainties in the geometrical parameters, loading conditions, and the parameters

governing Paris Law are presented in Table 5.13. The true EIFSD is designated as Θ_{true}, following a log-normal distribution with mean and standard deviation values of 5 mm and 0.5 mm, respectively, represented as $\Theta_{true} = \ln N(5, 0.5)$ mm.

Table 5.13: Details of the shell structure parameters and random variables used in the EIFS inference.

					COV	
Z_i	Parameter	Description	Distribution	Mean	Low	High
Z_1	W_2	Inner width	Lognormal	$0.5m$	0.01	0.02
Z_2	L_2	Inner length	Lognormal	$0.25m$	0.01	0.02
Z_3	R_2	Inner radius	Lognormal	$0.05m$	0.01	0.02
Z_4	h	Thickness	Lognormal	$0.05m$	0.01	0.02
Z_5	κ	Curvature	Lognormal	$0.1m^{-1}$	0.01	0.02
Z_6	N	Boundary traction	Lognormal	$0.8\ MNm^{-1}$	0.01	0.02
Z_7	M	Boundary moment	Lognormal	$0.01\ MN$	0.01	0.02
Z_8	P	Domain pressure	Lognormal	$0.05\ MNPa$	0.01	0.02
Z_9	C_0	Paris Law constant	Lognormal	$1.42 \times 10^{-11} \frac{m/cycle}{(MPa\sqrt{m})^m}$	0.01	0.02
Z_{10}	m	Paris Law exponent	Lognormal	$3.59\ m$	0.01	0.02

The determination of the Paris Law constants C_0 and m is inherently experimental, typically derived under specified loading conditions. This necessitates accounting for the interdependence between loading parameters and the Paris Law constants. To address this, the current analysis employs two distinct EIFS models, each tailored to evaluate the effects of the loading conditions and the Paris Law constants independently. The uncertainties in these models are categorized as follows: CASE II incorporates $[W_2, L_2, R_2, h, \kappa, C_0, m]$, and CASE II encompasses $[W_2, L_2, R_2, h, \kappa, M, N, P]$. Accordingly, two surrogate models are developed and trained to simulate the responses of the shallow shell structures using the Dual Boundary Element Method (DBEM) for CASE I and II, respectively.

5.6.1 Evaluation of the Surrogate Models

Model setup: In contrast to the anisotropic Boundary Element Method (BEM) employed in previous examples, the shallow shell BEM necessitates the uniform distribution of Dual Reciprocity Method (DRM) points within the domain. Additionally, the shell structure's deformation is characterized by five degrees of freedom, encompassing two rotational and displacements in three

directions. This complexity results in an expanded system matrix, leading to increased computational demands. To mitigate this, the study incorporates a Multi-fidelity modelling technique, specifically a co-Kriging model, for surrogate model construction. The co-Kriging model is predicated on analysing the correlation between models with coarse and fine meshes, thereby facilitating response prediction. Essentially, the co-Kriging model involves training two distinct Kriging models: the first model Y_c uses data from the coarse mesh, while the second model Y_d captures the residual difference between the coarse and fine meshes. The final prediction is a combination of responses from both Y_c and Y_d. This approach utilised training data from both low-fidelity (coarse mesh) and a smaller subset from high-fidelity (fine mesh) models, reducing computational efforts relative to a high-fidelity Kriging model without compromising accuracy. The High-fidelity and Low-fidelity models were developed using MATLAB's Regression Learner, while the Co-Kriging models were constructed with the ooDACE toolbox [166], all employing the Matérn correlation function with $\nu = 5/2$.

The finer mesh model consists of 88 boundary elements and 76 DRM points evenly distributed in the domain. The coarser mesh model consists of 58 boundary elements and 36 DRM points. The detail of the mesh is shown in Figure. 5.16.

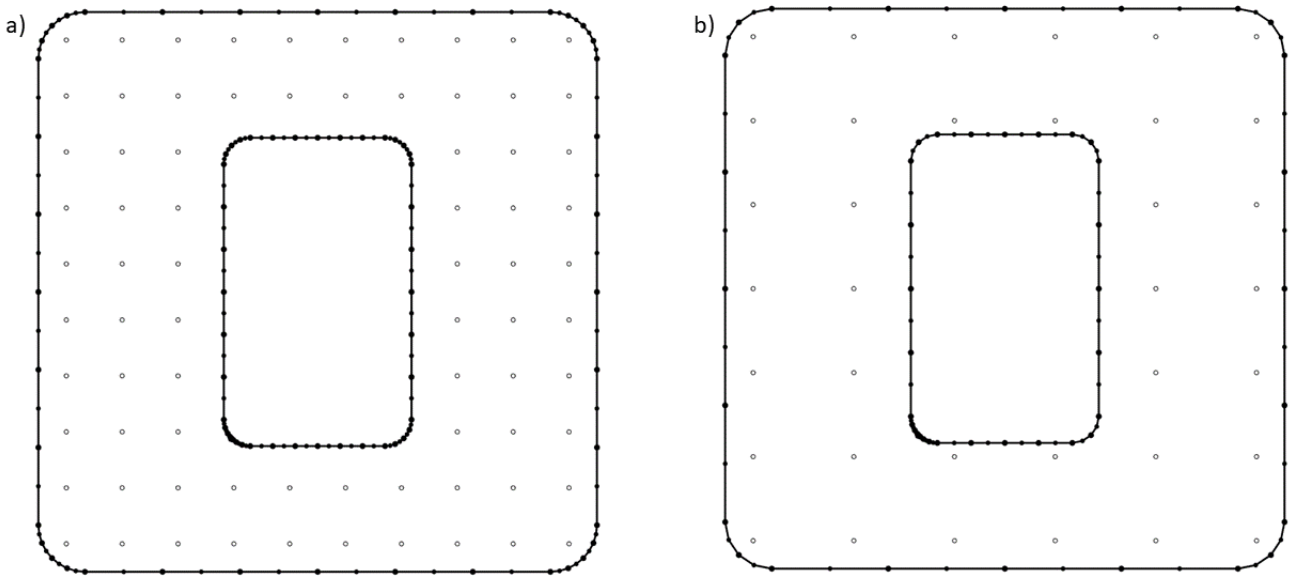


Figure 5.16: a) The mesh of the high-fidelity model. b) The mesh of the low-fidelity model

Sampling plan: It is important to mention that the training approach for the surrogate models does not consist of a sequential sampling strategy; rather, the sampling points were established in

advance. The sampling points were predetermined using the iterative sampling method outlined in [157], aimed at optimizing the sampling plan layout. Given the high dimensionality of the modelling challenge, it is imperative to necessitate a well-crafted sampling plan to ensure that the model can be trained effectively using a manageable number of samples that possess space-filling characteristics. Consider a sampling plan $\mathbf{X}$ characterized by a set of unique distances between sampling points, denoted as $d_1, d_2, \ldots, d_m$, and variables $J_1, J_2, \ldots, J_m$ represent the count of these distances. Specifically, J_j indicates the number of pairs of sampling points separated by a distance d_j. The parameter $\Phi_q(\mathbf{X})$, introduced by Morris [167], serves as a criterion to evaluate the space-filling quality of a sampling plan $\mathbf{X}$,a s follows:

$$\Phi_q(\mathbf{X}) = \left(\sum_{j=1}^{m} J_j d_j^{-q} \right)^{1/q} \tag{5.26}$$

In the design of the sampling plan, a range of values for q, specifically $\{1, 2, 5, 10, 20, 50, 100\}$ as suggested in the literature, were considered to optimize the sampling distribution. The objective was to achieve a plan that maximizes the distances d_j between sampling points while concurrently minimizing the corresponding J_j of these distances. Sampling plans for different q values were systematically evaluated and ranked based on their $\Phi_q(\mathbf{X})$ values. The plan yielding the lowest value of $\Phi_q(\mathbf{X})$ was selected as the most suitable for the training of the surrogate models. This approach ensures an optimized distribution of sampling points, crucial for the effectiveness and efficiency of the surrogate modelling process.

For each cases, a set of three distinct surrogate models were developed and assessed for accuracy against testing data. These models comprise the High-Fidelity (HF) model, the Low-Fidelity (LF) model, and the Multi-Fidelity (MF) model. The selection of training points for these models adhered to the sample and rank method previously described. Notably, the number of sampling points designated for training each surrogate model was consistent across all models. The following is a summary detailing the uncertainties involved in constructing the surrogate model, as well as the number of training and testing points used:

- Case I: 208 training points, 3740 testing points

$$K_{eff} = f_I^{kriging}(W_2, L_2, R_2, h, \kappa, a_0, a), \quad N_{cyc} = f_I^{kriging}(K_{eff}, C_0, m) \tag{5.27}$$

- Case II: 229 training points, 3857 testing points

$$K_{eff} = f_{II}^{kriging}(W_2, L_2, R_2, h, \kappa, M, N, P, a_0, a), \quad N_{cyc} = f_{II}^{kriging}(K_{eff}) \tag{5.28}$$

To evaluate the accuracy of the surrogate models, a distinct set of testing points, separate from those utilized in the training process, was generated using the DBEM employing the finer mesh configuration. The results obtained from the surrogate models were then compared against these testing points to assess model accuracy. For each case, the statistical errors between the three types of surrogate models (HF, LF, and MF) and the respective testing data were evaluated. Furthermore, a comparison of the average CPU time required for generating training data from DBEM for each model was performed. Details of the statistical error and the CPU time comparison are tabulated in Table 5.14.

Table 5.14: Model error of the K_{eff} for surrogate models compared to the test dataset. MAE $[MPa\sqrt{m}]$, RMSE $[MPa\sqrt{m}]$.

		Training Points	RRSE(%)	MAPE (%)	MAE	RMSE	R^2	CPU Time (s)
I	HF	208	2.78	0.35	0.043	0.074	1.0	4.32e+04
	LF	208	5.77	0.84	0.11	0.15	0.997	8.11e+03
	MF	172 LF+36HF	1.83	0.24	0.031	0.051	1.0	1.42e+04
II	HF	229	4.04	0.81	0.1	0.15	0.997	4.76e+04
	LF	229	8.17	1.24	0.16	0.24	0.993	8.92e+03
	MF	189 LF+40HF	3.17	0.45	0.057	0.091	0.999	1.57e+04

The discrepancy between the surrogate models and the DBEM results is notably minimal for both the High-Fidelity (HF) and Multi-Fidelity (MF) models. In contrast, the Low-Fidelity (LF) model exhibits the largest error, attributable to its reliance on training data generated from a coarser mesh configuration. The statistical errors, including the Root-Relative Squared Error (RRSE), Mean-Absolute-Percentage Error (MAPE), Mean-Absolute Error (MAE), and Root-Mean-Square Error (RMSE) for the co-Kriging (MF) model, demonstrate low values. This indicates a commendable accuracy level of the MF model. Additionally, the coefficient of determination (R^2)

closely approaches unity, suggesting that the MF model's predicted responses are highly correlated with the actual values. The employment of an increased proportion of Low-Fidelity (LF) data relative to High-Fidelity (HF) data in the Multi-Fidelity (MF) model has led to a notable reduction in the CPU time needed for creating training samples, in comparison to using the HF model exclusively. This strategy has proven to be highly efficient, achieving around a 67% reduction in CPU time for both cases examined. This significant decrease in computational time demonstrates the efficiency of the MF model in training sample generation, enabling a faster training process while maintaining accuracy in the model.

Figures 5.17 provide a visual demonstration of the Multi-Fidelity (MF) model's accuracy, showcasing surface plots for the effective stress intensity factor(K_{eff}) in CASE I and CASE II. Considering the high-dimensional nature of the surrogate models, the 3D surfaces displayed correspond to the mean values of the geometrical and loading parameters. For a clear indication of accuracy, these surface plots are overlaid with testing points, represented as black dots. This comparative visualization aids in demonstrating the model's precision, as evident in the figures.

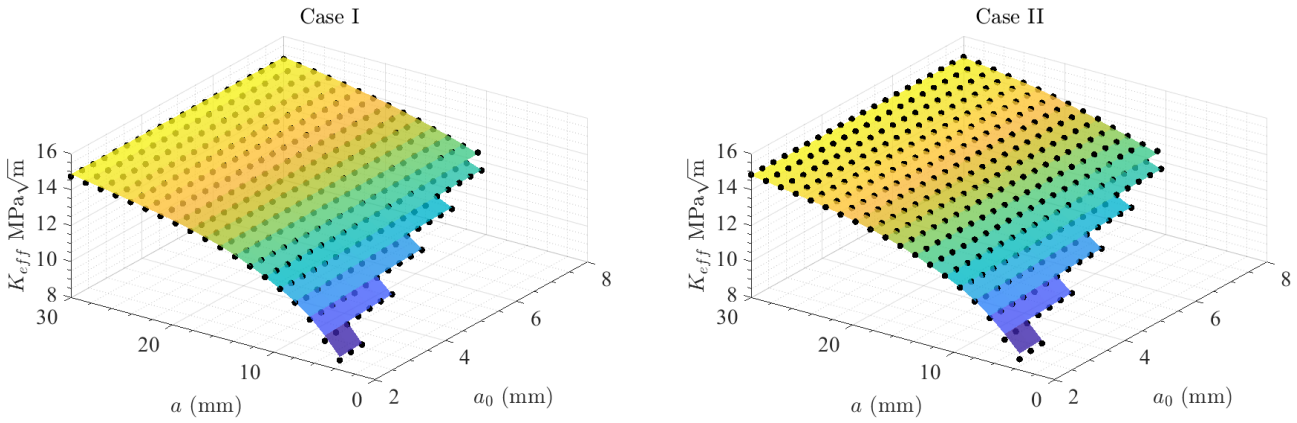


Figure 5.17: The surfaces represent the results of the K_{eff} constructed from the MF model over a range of initial and intermediate crack sizes versus the testing points (black dots) for CASE I (left) and CASE II (right).

Following the establishment of surrogate models for the effective stress intensity factor K_{eff}, the subsequent step involves developing a surrogate model for the number of cycles N. This model is formulated by incorporating the mean values of the Paris Law constants and the applied load into Eq.(5.2). For the integral computation in Eq.(5.2), the Trapezoidal rule is employed as an approximation method. The training points utilized for this model are consistent with those used

in the development of the K_{eff} surrogate models, and the average CPU time remains comparable. As such, only the statistical errors associated with this model are detailed in Table 5.15.

Table 5.15: Model error of the N for surrogate models compared to the test dataset.

		RRSE(%)	MAPE (%)	MAE [*cycles*]	RMSE [*cycles*]	R^2
I	HF	7.77	4.10	4688.78	8052.07	0.994
	LF	8.96	3.94	4586.90	9291.50	0.992
	MF	5.64	2.64	3276.99	6322.46	0.997
II	HF	10.70	5.78	7972.78	14153.55	0.989
	LF	11.53	7.16	8965.02	15241.31	0.987
	MF	6.21	3.93	4805.55	8201.27	0.996

The Root-Relative Squared Errors (RRSEs) associated with the surrogate models for N are observed to be generally higher than those for the K_{eff} models. This increased error is attributed to the exponent in the Paris Law, which tends to amplify the errors inherent in modelling K_{eff}. Despite this, the Multi-Fidelity (MF) model shows a high level of accuracy in relation to the testing data, which is reflected in its low RRSE values and a strong R^2 correlation. Visual representations of the surrogate model's performance using the MF approach are depicted in Figure 5.18 for both Case I and Case II.

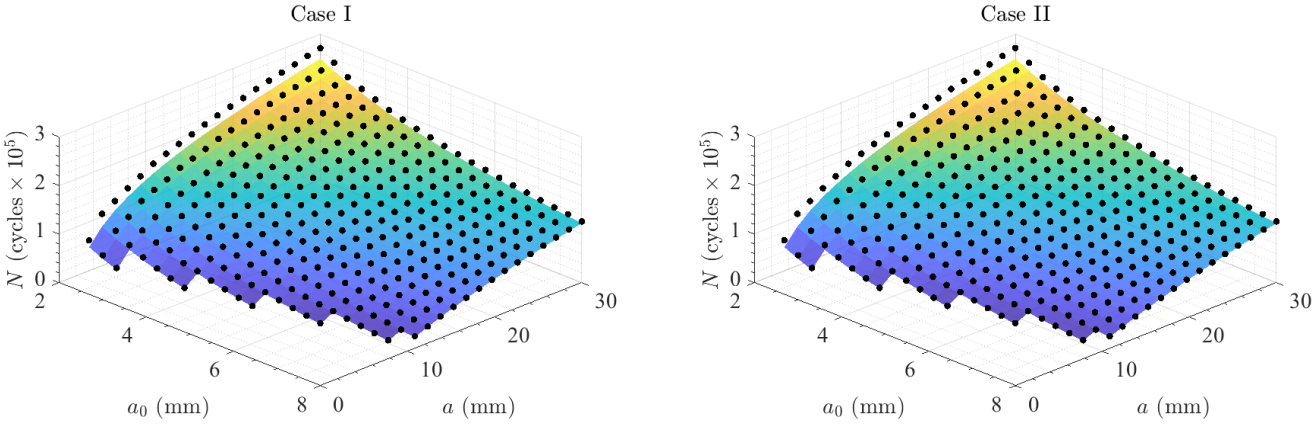


Figure 5.18: The surfaces represent the results of the number of cycles N constructed from the MF model over a range of initial and intermediate crack sizes versus the testing points (black dots) for case I (left) and case II (right).

It is noteworthy that at the boundaries of the surrogate model, a larger differences between the testing data and the model predictions is observed. This phenomenon, commonly encountered in surrogate modelling, suggests that edge regions typically exhibit higher errors, which significantly

contribute to the evaluated statistical error. Nonetheless, the accuracy within the crucial region of interest, particularly around $a = 20\,\text{mm}$ where the crack is assumed to be detectable during inspection, remains commendably high.

Comparing the errors across models for Case I and Case II, it is evident that all models in Case II exhibit greater errors. This is attributable to the increased complexity inherent in the higher-dimensional problem defined for training the Case II models. Enhancing model accuracy could be achieved by incorporating a more extensive set of training data, particularly through the use of the Latin Hypercube sampling method. Furthermore, in the training of the Multi-Fidelity (MF) models, the combination of Multi-Fidelity and Low-Fidelity points was determined manually. The optimal balance of these points was established by incrementally adding MF points until no further reduction in error was observed in the Co-Kriging model. Employing sequential sampling could potentially offer a more efficient strategy for selecting training points, and maintaining similar accuracy levels while utilizing fewer data points.

5.6.2 Inference of EIFSD

Simulation of Inspection data Variables listed in Table 5.13 were randomized for simulations to determine the required number of cycles for crack propagation to a detectable size. The variables randomized for these simulations include: (1) the size of the actual Equivalent Initial Flaw Size (EIFS); (2) geometrical parameters; and (3) Paris Law parameters in CASE I / loading variables in CASE II. The detectable crack length is assumed to be $a_{\text{det}} = 20\,\text{mm}$. A comprehensive dataset, comprising over 2000 inspection data points, was generated under both low and high uncertainty conditions for each of these variables across both cases. The scattering of the generated inspection data is shown in Figure 5.19.

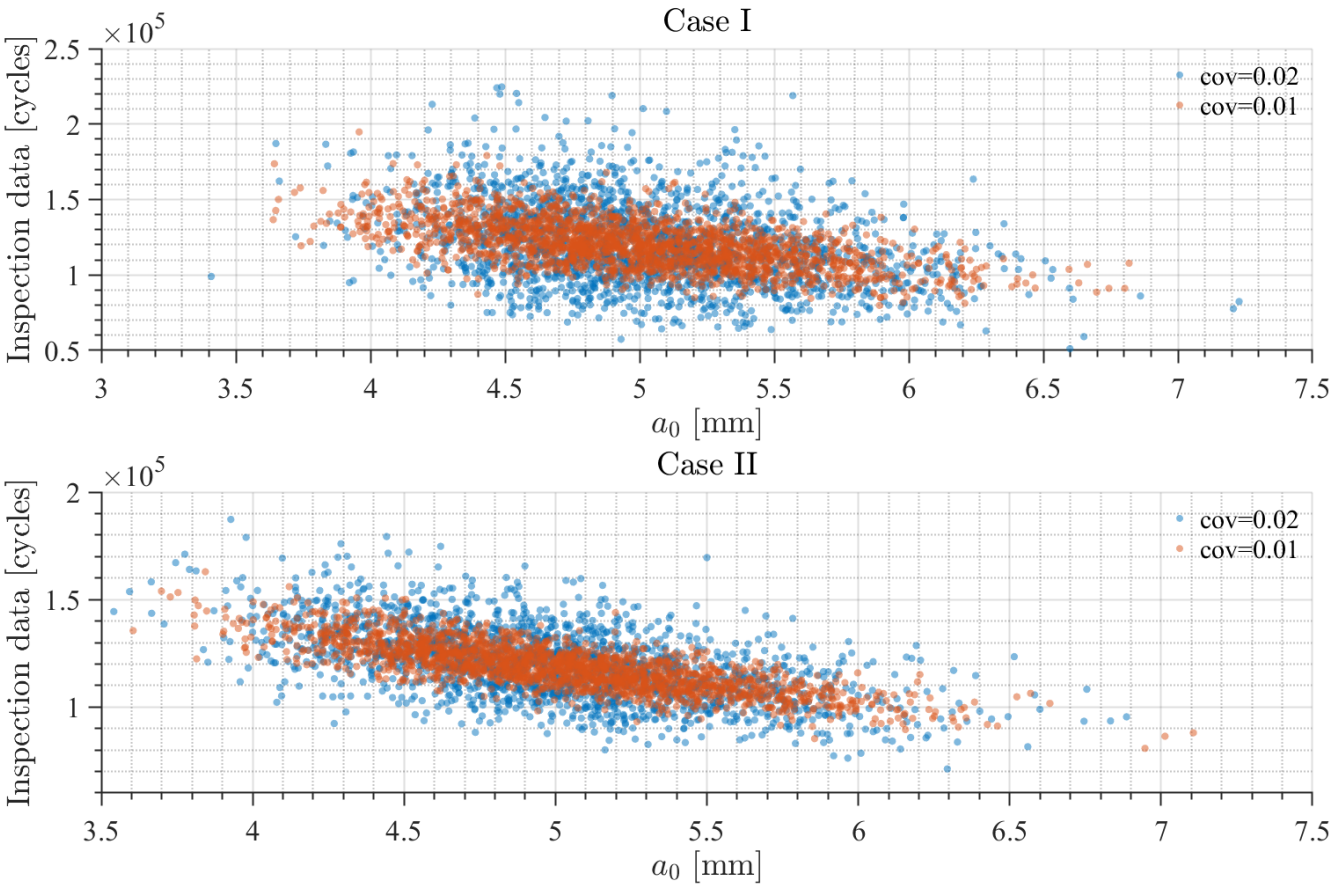


Figure 5.19: Simulated inspection data generated from actual EIFS vs the number of cycles required to grow the crack to $a_{det} = 20mm$.

Bayesian Inference The shape parameters α_{ij} and β_{ij} in Eq.(5.6) were derived using the Monte Carlo Simulation (MCS) with the Co-Kriging and Kriging models developed in Section 5.6.1. To evaluate the method's robustness in the context of shallow shell structures, two primary sources of variation were considered: (1) The accuracy of the initially guessed prior distributions. Three distinct guessed prior distributions, as detailed in Table 5.16, were examined. The distribution most closely aligning with the true EIFSD is classified as the 'good' prior. (2) The degree of uncertainty associated with the parameters. Ideally, a robust methodology would demonstrate diminishing sensitivity to uncertainty levels and prior distribution as more inspection data is integrated into the analysis. Such robustness is indicative of the method's stability under various levels of uncertainty.

Table 5.16: Three levels of quality of the prior distribution that are used to represent 'good', 'moderate', and 'poor' engineering judgement.

Prior distribution	Distribution	Mean	Standard deviation
Poor	Lognormal	1 mm	1.5 mm
Moderate	Lognormal	8 mm	0.8 mm
Good	Lognormal	6 mm	0.6 mm

CASE I

Figure 5.20 provides a graphical representation of the Bayesian updating process for the EIFSD, incorporating inspection data from 50, 600, 900, and 1500 instances. For brevity, only two cases analysed using the Co-Kriging model are depicted: (a) a scenario with low uncertainty and a 'good' initial guess (Figure 5.20 a), and (b) a scenario with high uncertainty and a 'poor' initial guess (Figure 5.20 b). In both instances, the posterior EIFSD progressively approximates the actual distribution as more inspection data is accumulated. Notably, Figure 5.20 a) exhibits a posterior distribution that closely matches the actual EIFSD with data from merely 50 inspections, and this accuracy is maintained with the addition of further data. Conversely, Figure 5.20 b) displays a considerable initial difference from the actual EIFSD, which, despite improvements, still shows a noticeable variance after 1500 inspections.

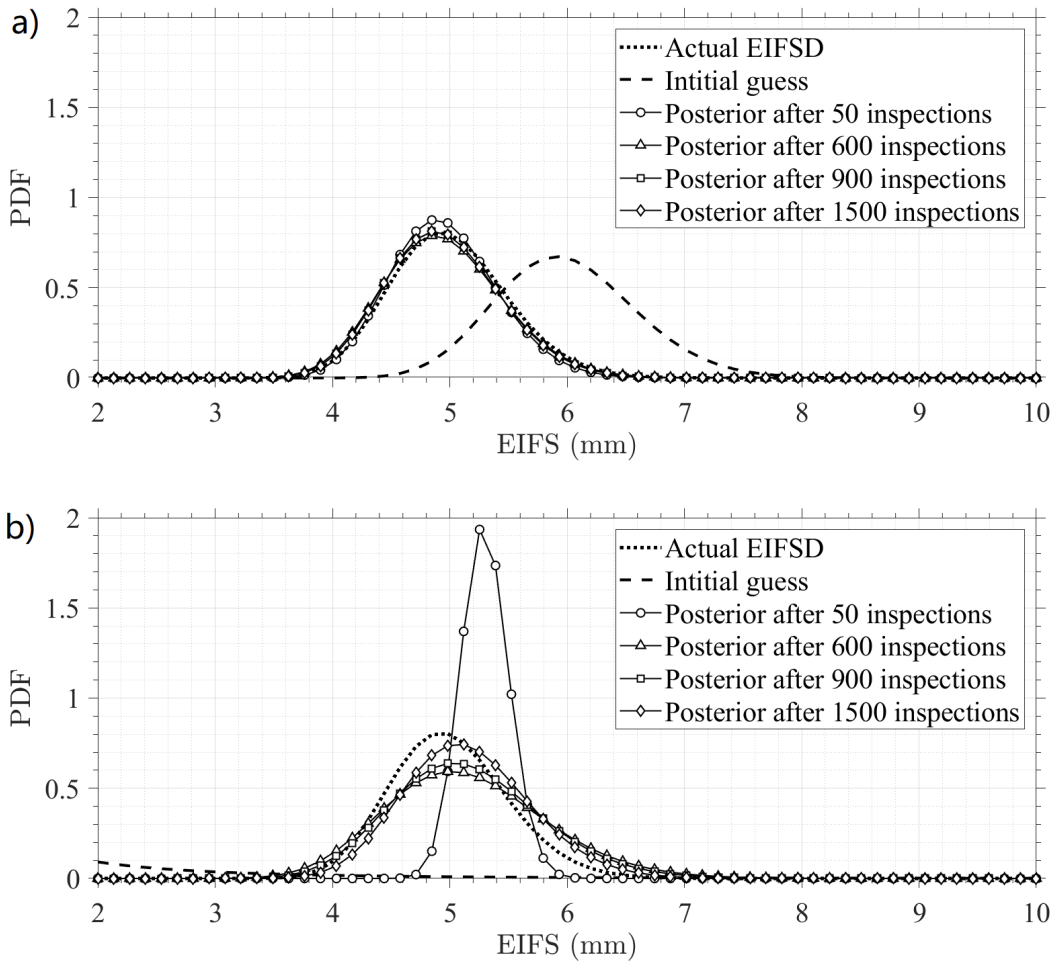


Figure 5.20: CASE I: Convergence of the posterior distributions computed by Bayesian updating using the Co-Kriging model after using the data from 50, 600, 900, and 1500 inspections. a): the figure shows the convergence for a 'good' initial guess and low uncertainties (COV = 0.01). b): the figure shows the convergence for a 'poor' initial guess and high uncertainties (COV = 0.02).

Figures 5.21 and 5.22 illustrate the convergence history of mean and standard deviation values under low and high uncertainty conditions, respectively. In each figure, the convergence paths for both Kriging and Co-Kriging models are presented. The impact of the prior distribution's quality is primarily evident with a limited amount of inspection data, as detailed in the 'zoom-in' portions of the figures. Notably, the convergence of the standard deviation is more significantly impacted by the initial guess, requiring around 200 inspection data points for the posterior distribution curves to align, indicating the diminishing effect of the initial guess.

In the low uncertainty scenario shown in Figure 5.21, the mean value rapidly approaches conver-

gence with a limited number of inspections: approximately 100 inspections for the Kriging model and 500 for the Co-Kriging model. For both models, the posterior mean estimation reaches within ± 0.2 mm of the actual mean (5 mm) at around 100 inspections. The standard deviation, as estimated by the Kriging model, attains an error of ± 0.02 mm from the 'actual' standard deviation (0.5 mm) at about 550 inspections, while the Co-Kriging model achieves this accuracy level around 490 inspections. By the end of 1500 inspections, both models reached a same accuracy level, with the Co-Kriging model exhibiting slightly faster convergence.

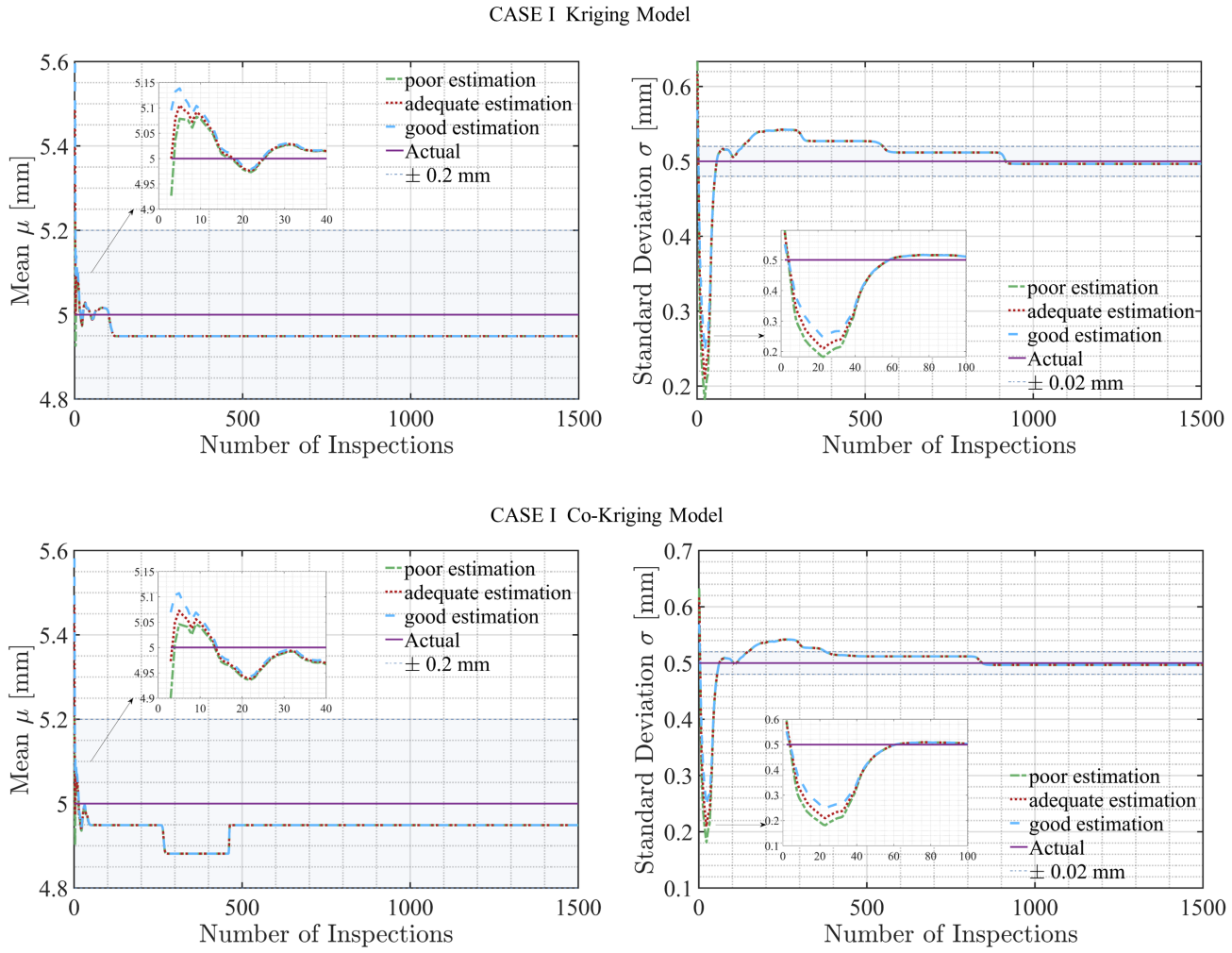


Figure 5.21: CASE I: Convergence of the EIFSD mean and standard deviation from Bayesian Updating for the 'low' level of uncertainty using Kriging and Co-Kriging model.

In the high uncertainty scenario, achieving convergence in standard deviation proved challenging even after 1500 inspections, prompting the use of 3000 inspection data points to better assess convergence. As depicted in Figure 5.22, the Co-Kriging model achieves convergence more rapidly,

at around 300 inspections, in contrast to the Kriging model which reaches convergence around 1500 inspections. A similar pattern is observed for the standard deviation, where an error margin of ±0.02 mm is achieved after about 1900 inspections using the Kriging model and 1800 inspections with the Co-Kriging model. By the end of 3000 inspections, both models exhibit comparable accuracy levels, with the Co-Kriging model showing a marginally faster convergence rate.

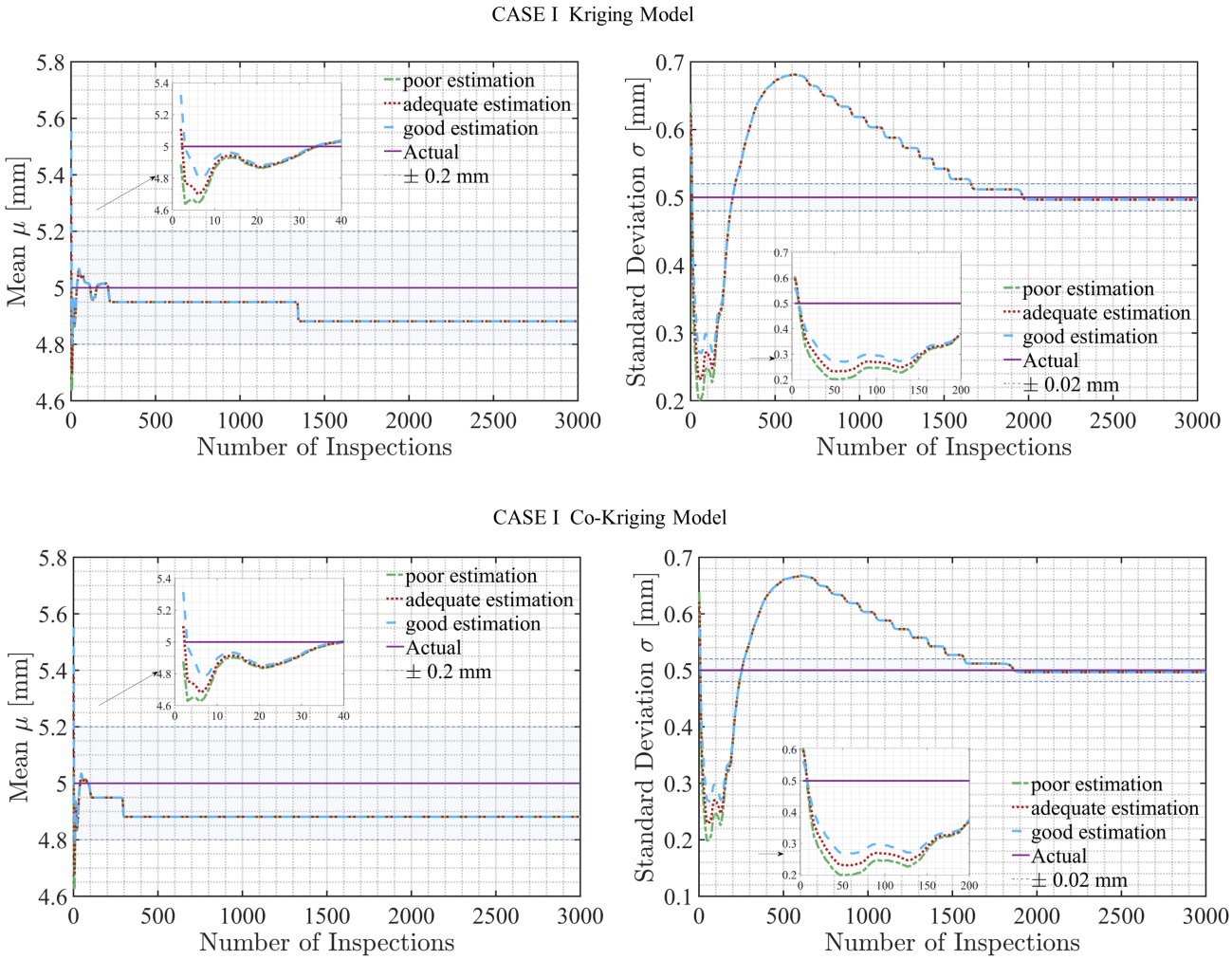


Figure 5.22: CASE I: Convergence of the EIFSD mean and standard deviation from Bayesian Updating for the 'high' level of uncertainty using Kriging and Co-Kriging model.

Table 5.17 summarizes the converged values of the estimated mean and standard deviation for both the low uncertainty case (using 1500 inspection data) and the high uncertainty case (utilizing 3000 inspection data). Additionally, the table presents the error between these inferred values and the true values. As highlighted in the preceding discussion, while different models attained similar accuracy levels, the Co-Kriging model demonstrated a more efficient convergence rate.

Table 5.17: Convergence of the mean and standard deviation from Bayesian updating for CASE I.

		cov=0.01 (1500 inspections)		cov=0.02 (3000 inspections)	
		mean	standard deviation	mean	standard deviation
Kriging Model	Value [mm]	4.95	0.497	4.88	0.497
	Error [%]	1.02	0.678	2.37	0.678
Co-Kriging Model	Value [mm]	4.95	0.497	4.88	0.497
	Error [%]	1.02	0.678	2.37	0.678

CASE II

Figure 5.23 provides the Bayesian updating process for the EIFSD, based on inspection data collected at intervals of 50, 600, 900, and 1500 inspections. To maintain conciseness, the figure highlights two specific cases evaluated using the Co-Kriging model: (a) a low uncertainty case with an accurate initial guess (Figure 5.23 a), and (b) a high uncertainty case with an inaccurate initial guess (Figure 5.23 b). In both scenarios, the posterior distributions progressively approximate the actual EIFSD as more inspection data is integrated. Notably, the impact of the initial guess becomes negligible after the first 50 inspections in both cases, as evidenced by the posterior distributions closely distributions closely align with the actual EIFSD and remain relatively stable with the inclusion of additional data. This stability continues despite the introduction of more data, although Figure 5.23 b) exhibits slightly higher deviation from the actual EIFSD compared to the scenario in Figure 5.23 a).

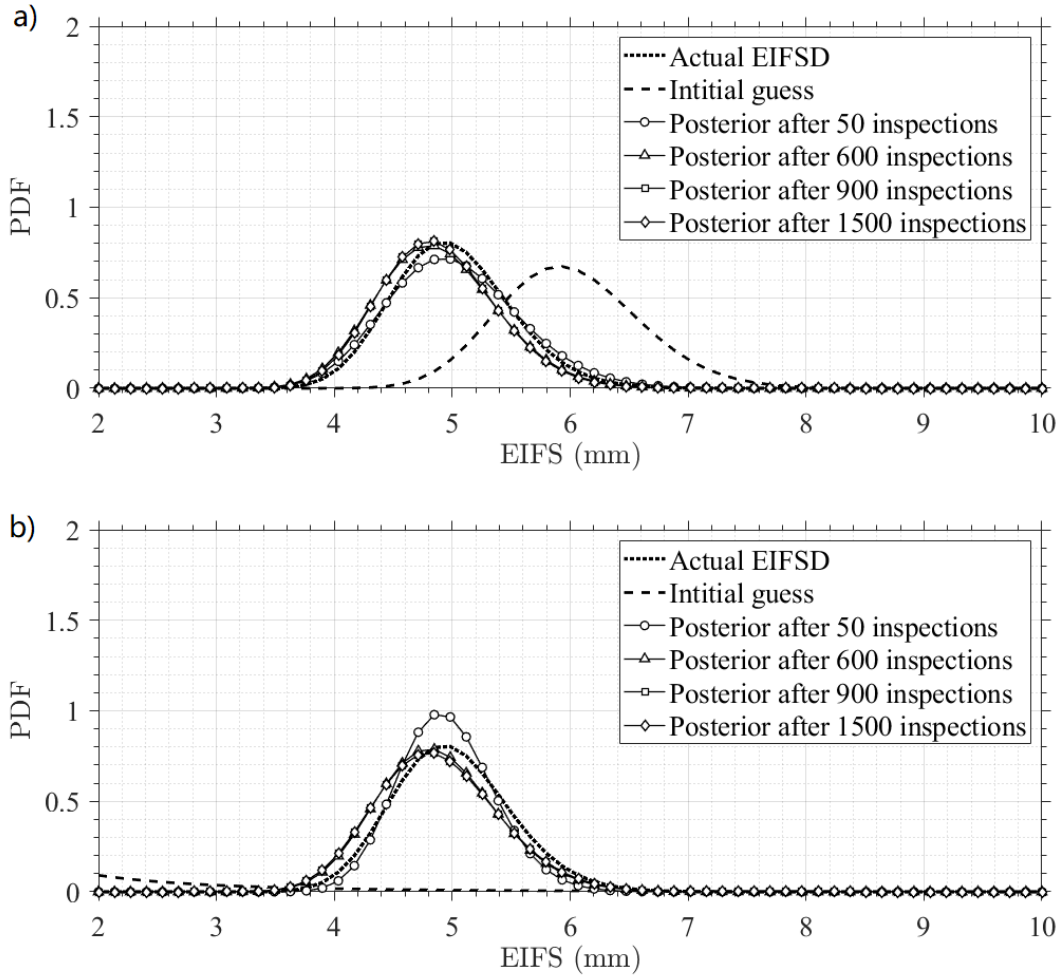


Figure 5.23: CASE II: Convergence of the posterior distributions computed by Bayesian updating using the Co-Kriging model after using the data from 50, 600, 900, and 1500 inspections. a): The figure shows the convergence for a 'good' initial guess and low uncertainties (COV = 0.01). b): The figure shows the convergence for a 'poor' initial guess and high uncertainties (COV = 0.02).

Figures 5.24 and 5.25 display the convergence history of mean and standard deviation for CASE II with low and high uncertainties, respectively. In each case, the convergence trends using both Kriging and Co-Kriging models are illustrated. The initial quality of the prior distribution is seen to affect convergence predominantly in the initial phase with limited inspection data, as indicated in the 'zoom-in' portions of the figures. After 40 inspections, the impact of the initial guess becomes less significant.

In the low uncertainty scenario, as shown in Figure 5.24, the mean value converges with fewer inspections, needing 750 inspections for the Kriging model and 400 inspections for the Co-Kriging

model. In both models, convergence within ±0.2 mm of the 'actual' mean (5 mm) is achieved around 100 inspections. The standard deviation, as estimated by the Kriging model, reaches a ±0.02 mm error from the 'actual' standard deviation (0.5 mm) at about 750 inspections, while the Co-Kriging model achieves this level of accuracy around 400 inspections. Comparatively, the Co-Kriging model demonstrates a faster convergence rate and more precise results in terms of both mean and standard deviation than the Kriging model.

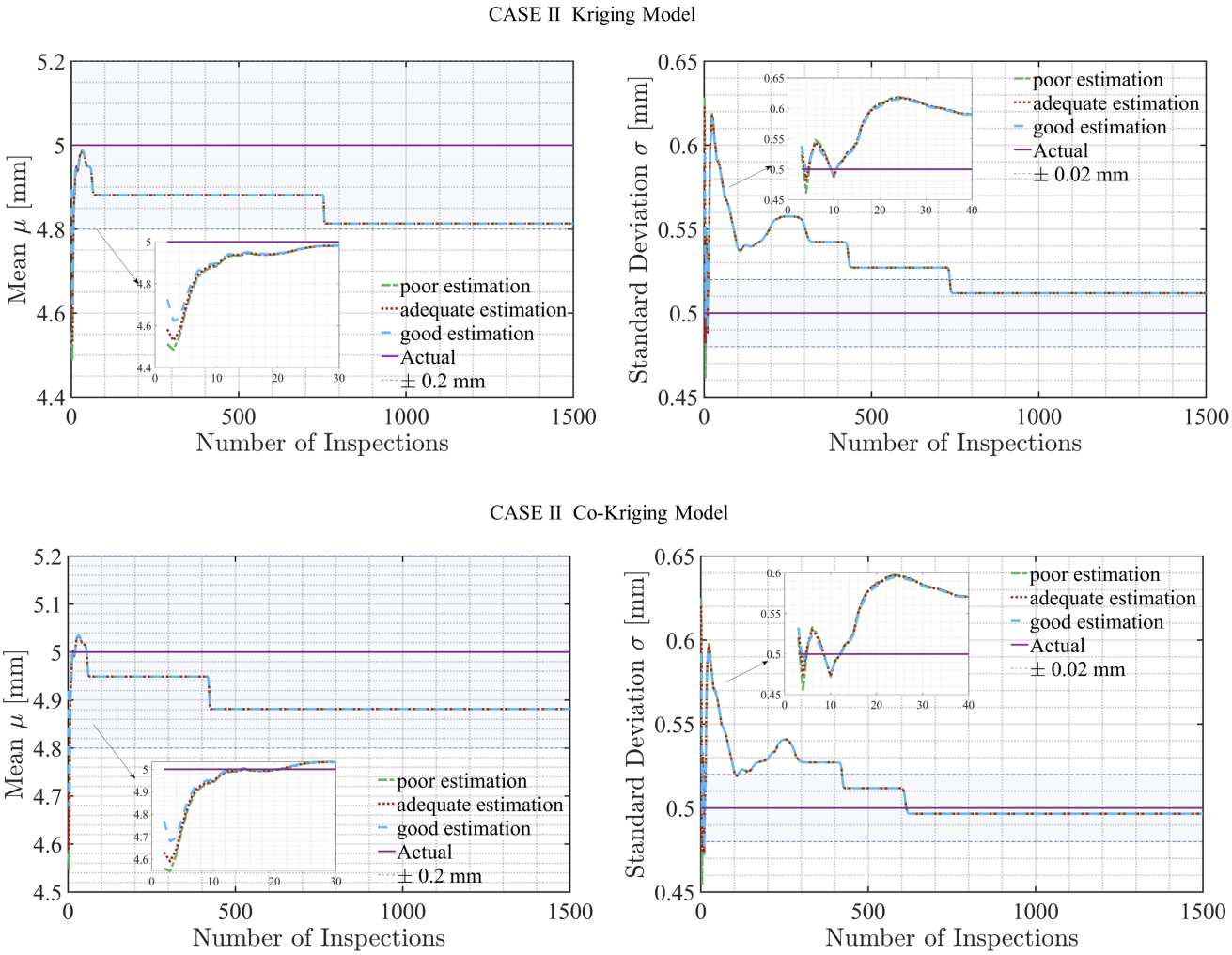


Figure 5.24: CASE II: Convergence of the EIFSD mean and standard deviation from Bayesian Updating for the 'low' level of uncertainty using Kriging and Co-Kriging model.

Similarly to CASE I, In CASE II with high uncertainty, a more substantial amount of inspection data was necessary to attain an acceptable level of accuracy in the standard deviation. Therefore, 3000 inspection data points were employed to thoroughly analyse the convergence. As depicted in Figure 5.25, the posterior estimations of the mean for both the Kriging and Co-Kriging models

converged at approximately 200 inspections, with the Co-Kriging model demonstrating a smaller error in the estimated mean. For standard deviation, convergence within error of ±0.02 mm was observed at around 2900 inspections for Kriging model while Co-Krignig model offers faster convergence at around 2000 inspections.By the end of 3000 inspections, the Co-Kriging model provided a more accurate estimation of mean value in contrast to the larger error observed with the Kriging model, both models show the same level of accuracy in the estimated standard deviation.

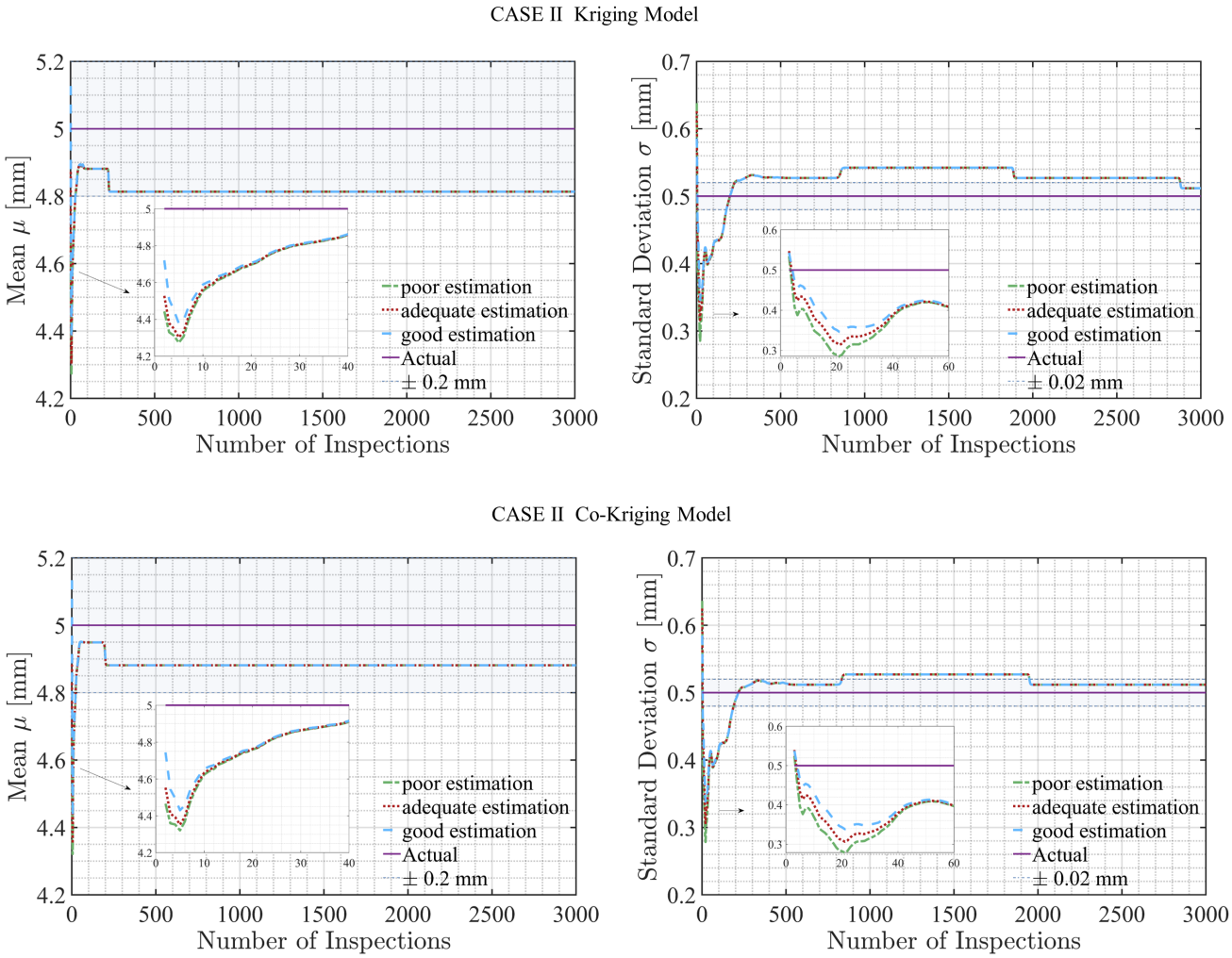


Figure 5.25: CASE II: Convergence of the EIFSD mean and standard deviation from Bayesian Updating for the 'high' level of uncertainty using Kriging and Co-Kriging model.

Table 5.18 provides a summary of the converged estimates for mean and standard deviation in both low and high uncertainty scenarios in CASE II, utilizing 1500 and 3000 inspection data points, respectively. Additionally, the table includes the errors between these estimated values and their respective true values. As previously discussed, the application of the Co-Kriging model has

been instrumental in achieving enhanced accuracy in the estimations. This model demonstrates its effectiveness by producing results with smaller errors in comparison to the true values, especially under conditions of high uncertainty.

Table 5.18: Convergence of the mean and standard deviation from Bayesian updating for CASE II.

		cov=0.01 (1500 inspections)		cov=0.02 (3000 inspections)	
		mean	standard deviation	mean	standard deviation
Kriging Model	Value [mm]	4.81	0.512	4.81	0.512
	Error [%]	3.73	2.37	3.73	2.37
Co-Kriging Model	Value [mm]	4.88	0.497	4.88	0.512
	Error [%]	2.37	0.678	2.37	2.37

The presented convergence findings highlight the critical impact of surrogate model accuracy on the overall convergence process. Similar to earlier observations, the influence of the initial guess on convergence outcomes reduces as more inspection data is incorporated. By implementing a more accurate surrogate model can facilitate both improved accuracy and swifter convergence. In scenarios of low uncertainty, both mean and standard deviation achieve convergence with minimal error. Conversely, in high uncertainty scenarios, convergence proves to be more arduous, with noticeable error reduction observed only after applying 3000 inspection data points. Particularly in CASE I, the standard deviation demonstrates significant deviation during the convergence process. This discrepancy is likely due to the introduction of uncertainty in the Paris Law exponent, which profoundly affects the convergence, especially in terms of standard deviation. Addressing the uncertainties more rigorously could substantially enhance the effectiveness and convergence rate of the EIFSD inference methodology.

5.6.3 Summary

This section introduces a novel approach for statistical inference of the Equivalent Initial Flaw Size Distribution (EIFSD) in shallow shell structures, employing Bayesian Updating.

The methodology was demonstrated through a numerical example involving a fuselage window structure with an initial crack at the window corner, under multi-axial loading. The Dual Boundary Element Method (DBEM) was employed for modelling crack growth. To improve the efficiency of the EIFSD inference process, surrogate models were developed, including a Kriging model with

High-fidelity data and a Co-Kriging model incorporating both High-fidelity and Low-fidelity data, based on the DBEM. The Co-Kriging model has been found to have around 67% reduction in the CPU time required for generating the training data sets. The Co-Kriging model outperformed the Kriging model in terms of error reduction and required less computational effort in generating the training data.

The effectiveness of the methodology was tested under different uncertainty levels, involving crack growth parameters, geometrical factors, and loading. Two distinct cases were examined: CASE I, which dealt with uncertainties in geometrical variables and Paris Law parameters, and CASE II, which focused on uncertainties in geometrical variables and loading conditions. Results indicated that the Co-Kriging model could achieve commendable accuracy in high-uncertainty situations, with a 2.37% error in the inferred mean for CASE I and 2.37% for CASE II. The study also demonstrated that a more accurate surrogate model could significantly enhance the convergence speed and accuracy.

Additionally, the robustness of the methodology was assessed by examining the impact of prior distribution quality in the Bayesian updating process. It was observed that the quality of the prior distribution had a notable influence when only a few inspection data points were used. However, this influence diminished with the inclusion of a larger dataset, underscoring the robustness of the proposed methodology.

Once the EIFS is inferred, the durability of the structure can be evaluated by taking the structure to a fatigue crack length.

5.7 Conclusion

This chapter introduces innovative methodologies for the statistical inference of the Equivalent Initial Flaw Size Distribution (EIFSD) in both anisotropic materials and shallow shell structures using Bayesian Updating. The methods emphasize the modelling of small crack growth and the estimation of fatigue life, crucial for aircraft component durability.

For anisotropic materials, the methodology utilizes the Dual Boundary Element Method (DBEM) to model crack growth, incorporating an inclined anisotropic principal axis. A notable innovation is the use of a Kriging model as a surrogate to the DBEM, significantly reducing computational

costs. This approach was validated under varying levels of uncertainty, proving highly accurate in estimating fatigue life with minimal errors, and demonstrating robustness, especially when larger datasets are available for Bayesian updating.

In the context of shallow shell structures, such as fuselage window structures under multi-axial loading, the methodology similarly employs the DBEM. However, it introduces a Co-Kriging model integrating both High-fidelity and Low-fidelity data, showing a considerable reduction in computational time and improved error reduction over the Kriging model alone. Tested under different uncertainty scenarios, the Co-Kriging model exhibited good accuracy.

Both methodologies share a common foundation in the statistical inference of EIFSD using Bayesian Updating and DBEM, with unique adaptations to their specific structural contexts.

Chapter 6

Conclusion and Future Works

This chapter outlines the general conclusions and potential future works.

6.1 Conclusion

As outlined in Chapter 1, the fundamental objective of this study was the development of a Boundary Element Method (BEM)-based approach for conducting reliability analyses and assessing the fatigue life of complex engineering structures. These structures encompass shallow shell structures and composite materials featuring anisotropic material properties. Detailed discussions on the methodology associated with the BEM were presented in Chapter 2 and corresponding results were outlined in Chapters 3 and 4, where the details of the reliability analysis were introduced and numerical examples were presented. Chapter 5 focuses on the comprehensive assessment of fatigue durability through the inference of the Equivalent Initial Flaw Size (EIFS).

In Chapter 3, the presented work is pursued towards achieving the following objectives: **To develop an Implicit Differentiation-Based (IDM) Reliability Analysis for Shallow Shell Structures using the Boundary Element Method (BEM)**. Within the confines of this chapter, the Implicit Differentiation Method (IDM) of the BEM formulation was proposed, which serves as a pivotal tool for evaluating the sensitivity of the shallow shell structure's response to diverse design parameters. Specifically, the focus was on the determination of sensitivity with respect to geometrical design parameters, curvature, and thickness, which influence boundary

stress resultants and, consequently, the Von Mises Stress. The chapter itself can be subdivided into four primary sections:

1. **Analytical Validation.** The validation of the accuracy of the BEM-IDM formulations for sensitivity calculations represents a pivotal requirement in the study. To initiate the validation process, the results were first compared the results obtained from IDM with those derived analytically, utilizing a hemispherical shell subjected to normal pressure as the test case. The evaluation focused on sensitivities of the out-of-plane displacement at the centre of the shell concerning the shell's radius (curvature) and thickness. In parallel, the Finite Difference Method (FDM) was employed to derive sensitivity values for the shell structure. The comparative analysis reveals that IDM and FDM results exhibit only minor differences, signifying that IDM offers a level of accuracy comparable to that of the FDM. Furthermore, when compared with the analytical solution, the deviations between IDM and the analytical results are negligible, with differences of less than 1% for sensitivity concerning curvature and less than 3% for sensitivity concerning thickness. These findings underscore the effective validation of IDM formulations against analytical solutions, affirming the accuracy and robustness of the proposed formulations.

2. **Reliability Analysis.** The IDM-BEM formulations find application in First-Order Reliability Analysis, enabling the evaluation of structural reliability while accounting for inherent uncertainties in diverse design parameters. A primary emphasis is placed on the serviceability limit state, which is defined in terms of the Von Mises stress. To illustrate the proposed methodology, a numerical example featuring a clamped circular shallow spherical shell was employed. This case study specifically explored the impact of uncertainty in the curvature parameter, given the shell structure's proficiency in transmitting load through membrane stresses, which is directly influenced by curvature. It is noteworthy that an increase in uncertainty corresponds to a decrease in the reliability of the structure. This observation underscores the correlation between heightened uncertainties and an elevated probability of structural failure. In terms of computational efficiency, a comparative analysis between IDM-FORM and FDM-FORM revealed only minor disparities, with the most substantial difference observed at 0.11%. IDM outperforms the FDM by being 35% faster in terms of

CPU time when assessing sensitivity with respect to a specific parameter.

3. **Sensitivity Analysis.** An important advantage of reliability analysis lies in its capacity to facilitate sensitivity analyses, thereby aiding in the identification of the most influential design parameters for enhancing structural reliability and, subsequently, achieving dimensional reduction. To pinpoint the significance of each random variable, the percentage importance of these variables was computed, leading to the identification of those with the most pronounced impact on reliability. The results of this analysis underscore the need to prioritize considerations related to curvature and thickness. These parameters emerge as key factors significantly affecting the probability of structural failure, and they also offer a relatively higher degree of controllability in comparison to non-geometric factors, such as the applied pressure. Furthermore, it becomes evident that obtaining a more precise quantification of uncertainties associated with the applied pressure load is imperative, given that variations in the pressure load's standard deviation have a notable impact on the failure probability. Originally, the structure encompassed four geometrical design parameters. However, the sensitivity analysis has revealed that one of these parameters does not wield a substantial influence on the overall reliability. As a result, it is advisable to allocate less focus and attention to this particular parameter in future considerations.

4. **Optimisation** To underscore the practical applicability of IDM formulations, two optimization examples were conducted:

   1) The initial optimization effort focused on the structure used in the sensitivity analysis. This optimization concentrated exclusively on the critical parameters identified in the sensitivity analysis. The primary objective of this optimization was to minimize the mass of the shell structure while considering various materials, including Aluminum 6061-T6, 2024-T4, 7075-T6, and 7075-T7. Notably, the optimization process succeeded in reducing the volume of the structure compared to its initial design. The outcomes prominently highlight that employing materials with higher yield strength, such as Aluminum 7075-T6, leads to the optimised final design with a lighter mass.

   2) The second example serves as a practical demonstration of the application of BEM-IDM

in Reliability-Based Design Optimization (RBDO). Here, the optimization goal remained the minimization of mass. However, this optimization methodology differed from the first numerical example in that it introduced a constraint, mandating the achievement of a specified reliability level for the structure. The limit state of Von Mises stress was utilized, and a range of targeting reliability indices, spanning from 2 to 6, was considered. The results achieved a successful agreement to the reliability targets, with a maximum error of only 0.47%. Notably, as the targeting reliability index increases, the optimal design necessitates increased thickness and curvature, along with a larger radius for the fillet and a reduction in the 'window' section. Consequently, in this scenario, the optimal design results in higher mass compared to the initial design to meet the specified requirements for structural integrity.

In Chapter 4, the work presented aims to meet the objectives: **Develop the IDM formulation for cracked shell structure and perform fatigue reliability assessment using FORM.** This chapter is dedicated to the comprehensive exploration of fatigue crack propagation within the shell structure, and as a result, it introduces the utilization of the Dual Boundary Element Method (DBEM) in conjunction with the IDM, giving rise to the IDM-DBEM formulation. The main point of this analysis is the stress intensity factor (SIF), recognized as the most pivotal parameter characterizing the stress field at the crack tip. In the context of fatigue reliability assessment, the sensitivity of the crack tip SIF concerning geometrical parameters and curvatures was derived. The chapter can be divided into two sections of main topics:

1. **Fracture Reliability Analysis.** Two numerical examples, with the first one involving the examination of a cracked fuselage window structure and the second example on a shallow shell featuring a central hole and two cracks used to demonstrate the practical application of the proposed IDM-DBEM formulation in reliability analysis. In these analyses, a limit state function was formulated taking into account crack tip stress intensity factors and fracture toughness. It also considered the presence of potential anti-symmetric in the structure, involving uncertainties in the x-location of the central hole. The reliability analysis was conducted over a range of crack lengths. The results underscore a critical observation: as the cracks propagate, the structural reliability decreases. This emphasizes the significance of fracture reliability analysis in the context of determining tolerance crack size, with a

focus on achieving a specified reliability level. Additionally, the second example taking into account the probability of detection, underscores the importance of certain Non-Destructive Inspection techniques such as Eddy-Current inspection, ensuring that the tolerance crack size is sufficiently large to be detected while remaining small enough to preserve the structure's reliability.

2. **Fatigue Reliability Assessment.** In the context of fracture reliability analysis, the primary objective is to establish a suitable tolerance crack size. Conversely, fatigue reliability assessment focuses on determining the structural reliability concerning the required service life to reach the specified tolerance crack size. Two numerical examples were considered:

   1) For the modelling of fatigue crack growth, the Paris Law was employed, with the Paris Law constants and exponent considered as sources of uncertainties. The sensitivity of service life concerning geometry and curvature was derived and subsequently applied during the reliability analysis. A crucial concept in this reliability analysis is the independence of parameters among each other. Consequently, the applied loading and Paris Law parameters were treated separately in two distinct limit state functions. The FORM was conducted over a range of service life. The results from the FORM were compared to the results obtained from Monte Carlo Simulation (MCS) involving 40,000 simulations. The results demonstrate the high accuracy of FORM, with a maximum difference of 3.67%, particularly evident at higher reliability indexes typically employed by engineers. Additionally, a parametric study was conducted to explore the impact of uncertainties within three distinct parameter categories: geometrical parameters, loading conditions, and Paris Law constants. The findings underscore the relationship of higher parameter uncertainty and a decreased failure probability.

   2) A third numerical example focused on the assessment of fatigue reliability within a cylindrical shallow shell structure, accounting for multiple site damage and initial crack length as uncertainties. This investigation encompassed various curvatures across different service life durations. The results showcased good agreement with MCS, featuring a maximum difference of 3.49%. Importantly, the computational time required in FORM was 7.58×10^4 s, while one DBEM simulation took 626.4 s. In contrast, the total computational time required by MCS

amounted to 6.26×10^7 s. These results clearly illustrate that FORM demands significantly less computational effort while maintaining a high level of accuracy. This underscores the robustness and efficiency of the proposed formulation.

In Chapter 5, the work presented aims to meet the objectives: **Develop formulation for the inference of EIFS for anisotropic structures and shallow shell structure through Bayesian Updating.** In this chapter, a novel methodology for inferencing the initial fatigue quantity, specifically the EIFS, is presented. The EIFS serves as a critical foundation within the fatigue crack growth model, facilitating the estimation of the durability of an engineering structure. Notably, the previous chapters encompassed reliability assessments, where numerical examples were assigned with postulated initial crack sizes, either in a deterministic manner or with uncertainties. However, in many real-world scenarios, ascertaining the actual initial flaw size with a high degree of precision can be a challenging and economically demanding task. This underscores the practical application of the concept of the EIFS, which provides a starting point for the crack propagation model. To illustrate the proposed methodology, two numerical examples were investigated with anisotropic materials. The anisotropic properties were expressed in terms of Young's Modulus ratio in two principal directions. To further illustrate the practical application of the proposed methodology, a numerical example involving a shallow shell structure was employed. This example incorporated uncertainties in the geometrical parameters. Additionally, the effects of varying loading conditions and Paris Law constants were examined in separate scenarios. This approach allowed for a comprehensive evaluation of the methodology's effectiveness in addressing different aspects of uncertainty, thereby demonstrating its applicability and robustness in modelling complex structural behaviours under varied conditions. The chapter can be divided into three main topics:

1. **Surrogate Modelling.** While the BEM offers substantial advantages in reducing computational costs, when a large number of simulations, such as in Monte Carlo Simulation (MCS), are required, it can still pose computational expenses. To mitigate these costs, surrogate models were developed to replace the DBEM for the evaluation of crack tip stress intensity factors and the number of cycles to detectable crack size in the MCS. This involves:

   1) For anisotropic structures, surrogate models in the form of Kriging were developed. The training of the Kriging model involved incorporating a total of 127 sample points. The cu-

mulative CPU time used for training the surrogate model was 44.8 minutes. To assess the accuracy of the surrogate model, a separate set of 4725 testing points, distinct from those used for surrogate model training, was generated using the DBEM. Subsequently, the results from the surrogate model were compared to those from the DBEM. This comparative analysis revealed that within the region of interest, the maximum Root-Relative Squared Error was approximately 4.82%. In terms of computational efficiency, the surrogate model exhibited remarkable advantages, with over 10,000 times higher efficiency than the DBEM for this specific application. To provide further context, the time required for generating 1×10^7 results using the DBEM was estimated at 473 days. In contrast, the Kriging model completed the same simulation in a mere 340 seconds. This significant disparity underscores the substantial cost reductions in terms of computational resources made possible by the integration of a surrogate model.

2) For the analysis of shallow shell structures, surrogate models employing Kriging and Co-Kriging methodologies were developed. The Co-Kriging model, in particular, implements data from both high-fidelity (finer mesh model) and low-fidelity (coarser mesh model) sources to predict the structural response. This approach is advantageous given the complex formulation and high computational demands of the shallow shell DBEM. The Co-Kriging model proved to be markedly more efficient, achieving a reduction of approximately 67% in CPU time required for training data generation, and exhibited enhanced performance over the Kriging model in terms of error reduction and computational resource utilization.

2. **Infernce of EIFSD via Bayesian Updating method.** The statistical inference of the EIFSD through Bayesian updating entails initiating the process with a prior estimate for the EIFSD and subsequently updating this estimate with inspection data to derive a posterior estimate for the EIFSD. The robustness of this methodology was meticulously investigated, with a focus on two key aspects: 1) Two levels of uncertainty in crack growth parameters and anisotropic material properties were examined. In cases with low uncertainty, convergence within a range of approximately ± 0.1 mm from the 'actual' mean (5 mm) was achieved with data from approximately 80 inspections. After 500 inspections, the error in the mean convergence with an error of 0.34%. In scenarios characterized by high uncertainty, conver-

gence within the same ±0.1 mm range from the 'actual' mean was achieved with data from around 170 inspections, and the error following 500 inspections was 2.37%. Likewise, the standard deviation achieved convergence after 500 inspections with an error of 3.72% for low uncertainties and approximately 2.53% for high uncertainties after 600 inspections.

2) The quality of the prior distribution in Bayesian updating, notably its closeness to the true EIFSD, was also examined. The results underscore the substantial impact of the initial guess distribution on the convergence process when a relatively limited number of inspections (below 100) is employed. However, this influence tends to diminish as the number of inspections increases.

The parametric study further revealed that the most effective improvement in overall convergence could be achieved by reducing the uncertainty associated with the Paris Law exponent and anisotropic ratio. These parameters held a more substantial influence on convergence, particularly in terms of standard deviation. Addressing uncertainties in these parameters would enhance the EIFSD inference methodology's convergence rate.

For the analysis of shallow shell structures, the methodology's effectiveness was evaluated under various uncertainty levels, focusing on crack growth parameters, geometrical factors, and loading. Two cases were studied: CASE I, examining uncertainties in geometrical variables and Paris Law parameters, and CASE II, focusing on uncertainties in geometrical variables and loading conditions. The Co-Kriging model showed high accuracy in these high-uncertainty scenarios, with a 2.37% error in inferred mean for CASE I and 2.37% for CASE II. The study concluded that a more accurate surrogate model can greatly improve both the speed and accuracy of convergence.

3. **Application of EIFSD.** Inspection intervals are commonly defined as a fraction of the fatigue life, and the EIFSD plays a pivotal role in providing a more accurate estimation of a structure's failure life. Consequently, it can be employed to determine an appropriate inspection interval. In practice, a postulated critical crack size is assigned, and the fatigue life distribution is simulated through Monte Carlo Simulation (MCS). The inspection interval is selected with the criterion that there should be less than a 2% chance of failure at the time

of inspection.

In scenarios characterized by low uncertainty, the difference in the number of cycles to failure when utilizing the actual EIFSD in contrast to the inferred EIFSD was a mere 0.11%. In contrast, in cases with high uncertainty, this difference increased to 1.9%. Nevertheless, it's worth noting that, as mentioned previously, in the context of reliability analysis, the EIFSD can be employed as a substitute for a postulated initial crack size, emphasizing its significance in enhancing the accuracy of structural assessments.

6.2 Future Works

Potential works in terms of improved methodology and more complicated geometry are shown below.

- The use of shell structures in aircraft fuselages is a common application. To enhance the modelling accuracy of fuselage panels, it's important to incorporate stiffeners. Additionally, the phenomenon of crack arresting should be considered when stiffeners are introduced. This necessitates the inclusion of crack propagation direction as one of the parameters in reliability analysis. Future work can focus on developing an IDM formulation with respect to the local coordinate system to account for directional changes in the crack path.

- Another approach to model the fuselage panels could involve developing a plate-shell assembly BEM formulation. This approach would embrace the concept of system reliability, particularly for structures with multiple members. In such cases, reliability may be defined by more than one limit state function, meaning that different components within the structure can have different failure modes. This approach often considers that the failure of two or more components results in an overall structural failure. Consequently, instead of defining the failure probability for one component as $P(F_i)$ where i represents a failure mode, the structural failure probability could be considered as the multiplication of multiple limit states that satisfy $g_{ni} < 0$. This can be expressed in terms of the probability as $P(F_{1i} \cap F_{2i}, ..., F_{ni})$, where n is the number of components that have failed.

- In terms of inspection, a more realistic assumption is that not all inspections may successfully detect a crack. Moreover, when a crack is detected, it can be repaired, and a new reliability analysis is performed. Future work could involve incorporating the updating of inspection information into the reliability analysis to account for these dynamic changes in the structure's condition.

- The concept of multi-site damage can be considered in the context of inferring the EIFSD. The EIFS was originally proposed for lap joint panels where multiple cracks may be present. In each inspection, different numbers of cracks can be detected, and these cracks may be located in different positions. To address this scenario, future work could involve training multiple surrogate models that correspond to all possible combinations of crack numbers and locations, allowing for a more comprehensive assessment of multi-site damage scenarios.

Bibliography

[1] B. Derode. In-situ experimental study of the seismic signatures of the role of fluids in the rupture of fault zones: Application to large rockslides failure studies. *UNIVERSITE DE NICE-SOPHIA ANTIPOLIS*, :, 2013.

[2] M.H. Aliabadi and P. Sollero. Crack growth analysis in homogeneous orthotropic laminates. *Composites Science and Technology*, 58(10):1697–1703, 1998.

[3] T Lucht and M.H. Aliabadi. Correction to the crack extension direction in numerical modelling of mixed mode crack paths. *International Journal of Fracture*, 143(2):195–202, 2007.

[4] . Civil aircraft accident: Report of the court of inquiry into the accidents to gomet g-alyp on 10th january 1954 and comet g-alyy on 8th april 1954, 1955.

[5] Screams, then silence: The story of flight 243's miracle landing. https://www.nzherald.co.nz/world/screams-then-silence-the-story-of-flight-243s-miracle-landing/BDV7QVFFX2K23KKZDEOUWZGI54/. Accessed: 2022-06-26.

[6] M. H. Aliabadi. *The Boundary Element Method: Applications in solids and structures*, volume 2. John Wiley and Sons, 2002.

[7] G Georgiou. Pod curves, their derivation, applications and limitations. *Insight*, 49:409–414, 07 2007.

[8] S. Sankararaman, Y. Ling, and S. Mahadevan. Statistical inference of equivalent initial flaw size with complicated structural geometry and multi-axial variable amplitude loading. *International Journal of Fatigue*, 32(10):1689–1700, 2010.

[9] ASM Aerospace Specification Metals. Asm handbooks online. Report, ASM Aerospace Specification Metals, Inc., .

[10] A. Portela, M. H. Aliabadi, and D. P. Rooke. The dual boundary element method: Effective implementation for crack problems. *International Journal for Numerical Methods in Engineering*, 36(6):1269–1287, 1992.

[11] E.L. Albuquerque, P. Sollero, W.S. Venturini, and M.H. Aliabadi. Boundary element analysis of anisotropic kirchhoff plates. *International Journal of Solids and Structures*, 43(14):4029–4046, 2006.

[12] T. Dirgantara and M. H. Aliabadi. Crack growth analysis of plates loaded by bending and tension using dual boundary element method. *International Journal of Fracture*, 105(1):27–47, 2000.

[13] T. Dirgantara and M. H. Aliabadi. A new boundary element formulation for shear deformable shells analysis. *International Journal for Numerical Methods in Engineering*, 45(9):1257–1275, 1999.

[14] P. C. Miedlar, A. P. Berens, A Gunderson, and J.P. Gallagher. Analysis and support initiative for structural technology (asist). Technical report, USAF Damage Tolerant Design Handbook: Guidelines For the Analysis and Design of Damage Tolerant Aircraft Structures, 2002.

[15] S. A. Barter, P. K. Sharp, G. Holden, and G. Clark. Initiation and early growth of fatigue cracks in an aerospace aluminium alloy. *Fatigue & Fracture of Engineering Materials & Structures*, 25(2):111–125, 2002.

[16] A. Navarro and E. R. de los Rios. Short and long fatigue crack growth: A unified model. *Philosophical Magazine A*, 57(1):15–36, 1988.

[17] David Percy. Rooke and David John. Cartwright. *Compendium of stress intensity factors*. H.M.S.O., London, 1976.

[18] C.L. TAN and Y.L. GAO. Boundary integral equation fracture mechanics analysis of plane orthotropic bodies. *International Journal of Fracture*, 53:343–365, 1992.

[19] A. Portela, M. H. Aliabadi, and D. P. Rooke. The dual boundary element method: Effective implementation for crack problems. *International Journal for Numerical Methods in Engineering*, 33(6):, 1992.

[20] Heider de Castro e Andrade and Edson Denner Leonel. The multiple fatigue crack propagation modelling in nonhomogeneous structures using the dbem. *Engineering Analysis with Boundary Elements*, 98:296–309, 2019.

[21] Thiago A.A. Oliveira, Gilberto Gomes, and Francisco Evangelista Jr. Multiscale aircraft fuselage fatigue analysis by the dual boundary element method. *Engineering Analysis with Boundary Elements*, 104:107–119, 2019.

[22] F.R.M. Romlay, H. Ouyang, A.K. Ariffin, and N.A.N. Mohamed. Modeling of fatigue crack propagation using dual boundary element method and gaussian monte carlo method. *Engineering Analysis with Boundary Elements*, 34(3):297–305, 2010.

[23] Supriyono and M H Aliabadi. Dual boundary element method for elastoplastic fracture mechanics of shear deformable plate. *Engineering Analysis with Boundary Elements*, 117:132–142, 2020.

[24] J. Li, Z. Sharif Khodaei, and M. H. Aliabadi. Dynamic fracture analysis of kane–mindlin plates using the dual boundary element method. *Engineering Analysis with Boundary Elements*, 106:217–227, 2019.

[25] P. Sollero and M.H. Aliabadi. Fracture mechanics analysis of anisotropic plates by the boundary element method. *International Journal of Fracture*, 64:269–284, 1993.

[26] T. Dirgantara and M.H. Aliabadi. Dual boundary element formulation for fracture mechanics analysis of shear deformable shells. *International Journal of Solids and Structures*, 38(44):7769–7800, 2001.

[27] T. W. Clyne and D. Hull. *General Introduction*, page 1–8. Cambridge University Press, 3 edition, 2019.

[28] M. Piry and W. Michaeli. Stiffness and failure analysis of smc components considering the anisotropic material properties. *Macromolecular Materials and Engineering*, 284-285(1):40–45, 2000.

[29] Tomonari Furukawa and John G. Michopoulos. Computational design of multiaxial tests for anisotropic material characterization. *International Journal for Numerical Methods in Engineering*, 74(12):1872–1895, 2008.

[30] Tatsuki Ohji, Kiyoshi Hirao, and Shuzo Kanzaki. Fracture resistance behavior of highly anisotropic silicon nitride. *Journal of the American Ceramic Society*, 78(11):3125–3128, 1995.

[31] Chia-Huei Tu, C.-S. Chen, and T.-T. Yu. Fracture mechanics analysis of multiple cracks in anisotropic media. *International Journal for Numerical and Analytical Methods in Geomechanics*, 35(11):1226–1242, 2011.

[32] E.L. Albuquerque, P. Sollero, and P. Fedelinski. Free vibration analysis of anisotropic material structures using the boundary element method. *Engineering Analysis with Boundary Elements*, 27(10):977–985, 2003.

[33] Azam Tafreshi. Simulation of crack propagation in anisotropic structures using the boundary element shape sensitivities and optimisation techniques. *Engineering Analysis with Boundary Elements*, 35(8):984–995, 2011.

[34] L. Rodríguez-Tembleque, F. García-Sánchez, and A. Sáez. Crack-face frictional contact modelling in cracked piezoelectric materials. *Computational Mechanics*, 64():1655–1667, 2019.

[35] P. Sollero, M. H. Aliabadi, and D.P. Rooke. Anisotropic analysis of cracks emanating from circular holes in composite laminates using the boundary element method. *Engineering Fracture Mechanics*, 49(2):213–224, 1994.

[36] G. R. Irwin. Analysis of stresses and strains near the end of a crack traversing a plate. *Journal of Applied Mechanics-Transactions of the ASME*, E24:351–369, 1957.

[37] C.C. Sih, P.C. Paris, and G.R. Irwin. On cracks in rectilinearly anisotropic bodies. *International Journal of Fracture Mechanics*, 3:189–203, 1965.

[38] . Aircraft accident report – aloha airlines, flight 243, boeing 737-200, n73711, near maui, hawaii, april 28, 1988, 1988.

[39] V. V. Novozhilov. The theory of thin elastic shells. *P. Noordhoff Ltd, Groningen*, 1964.

[40] E. Reissner. Stress strain relations in the theory of thin elastic shells. *Journal of Mathematics and Physics*, 31:109–119, 1952.

[41] P. Wen, M.H. Aliabadi, and A. Young. Transformation of domain integrals to boundary integrals in bem analysis of shear deformable plate bending problems. *Computational Mechanics*, 24:304–309, 1999.

[42] C. Di Pisa and M. H. Aliabadi. Fatigue crack growth analysis of assembled plate structures with dual boundary element method. *Engineering Fracture Mechanics*, 98:200–213, 2013.

[43] P.M. Baiz and M. H. Aliabadi. Buckling analysis of shear deformable shallow shells by the boundary element method. *Engineering Analysis with Boundary Elements*, 31(4):361–372, 2007.

[44] E.L. Albuquerque and M.H. Aliabadi. A boundary element analysis of symmetric laminated composite shallow shells. *Computer Methods in Applied Mechanics and Engineering*, 199(41):2663–2668, 2010.

[45] Brizeida Gámez, Eduardo Divo, Alain Kassab, and Miguel Cerrolaza. Evaluation of fatigue crack growing in cortical bone using the bem. *International Journal of Healthcare Technology and Management*, 11, 07 2010.

[46] T. Dirgantara and M. H. Aliabadi. Numerical simulation of fatigue crack growth in pressurized shells. *International Journal of Fatigue*, 24(7):725–738, 2002.

[47] J. Useche. Fracture dynamic analysis of cracked reissner plates using the boundary element method. *International Journal of Solids and Structures*, 191-192:315–332, 2020.

[48] P. M. Naghdi. Note on the equations of shallow elastic shells. *Quarterly of Applied Mathematics*, 14:331–333, 1956.

[49] P. Lu Pin and M. Huang. Boundary element analysis of shallow shells involving shear deformation. *International Journal of Solids and Structures*, 29(10):1273–1282, 1992.

[50] P. M. NAGHDI. On the theory of thin elastic shells. *Quarterly of Applied Mathematics*, 14(4):369–380, 1957.

[51] F. Vander Weeën. Application of the boundary integral equation method to reissner's plate model. *International Journal for Numerical Methods in Engineering*, 18(1):1–10, 1982.

[52] P. H. Wen, M. H. Aliabadi, and A. Young. Plane stress and plate bending coupling in bem analysis of shallow shells. *International Journal for Numerical Methods in Engineering*, 48(8):1107–1125, 2000.

[53] Yossi Mi and M.H. Aliabadi. Discontinuous crack-tip elements: Application to 3d boundary element method. *International Journal of Fracture - INT J FRACTURE*, 67, 06 1994.

[54] Robert E. Melchers and Andre T. Beck. *Structural reliability analysis and prediction*. Wiley, Chichester, third edition. edition, 2018.

[55] Andrzej S. Nowak and Kevin R. Collins. *Reliability of structures*. CRC Press, Boca Raton, second edition. edition, 2013.

[56] A. Ghaderi, E. Ghavanloo, and S.A. Fazelzadeh. Reliability analysis of carbon nanotube-based nano-truss under various loading conditions. *Iranian Journal of Science and Technology, Transactions of Mechanical Engineering*, 45:1123–1131, 2021.

[57] B. Keshtegar, M.E. Amine, S. Zhu, R. Abbassi, and N. Trung. Reliability analysis of corroded pipelines: Novel adaptive conjugate first order reliability method. *Journal of Loss Prevention in the Process Industries*, 62:103986, 2021.

[58] M.S. Chowdhury, C. Song, W. Gao, and C. Wang. Reliability analysis of homogeneous and bimaterial cracked structures by the scaled boundary finite element method and a hybrid random-interval model. *Structural Safety*, 59:53–66, 2016.

[59] X. Yuan, J. Gu, and S. Liu. Sensitivity of sample for simulation-based reliability analysis methods. *Computer Modeling in Engineering & Sciences*, 126(1):331–357, 2021.

[60] B. Q. Li and D. G. Lu. Comparisons of three meta-models for structural reliability analysis: Rsm, ann and svr. In *55th AIAA Structures, Structural Dynamics, and Materials Conference*, 02 2013.

[61] G. H. Besterfield, W. K. Liu, M. A. Lawrence, and T. B. Belytschko. Brittle fracture reliability by probabilistic finite elements. *Journal of Engineering Mechanics*, 116(3):642–659, 1990.

[62] K. Yoo, O. Bacarreza, and M.H. Aliabadi. A novel multi-fidelity modelling-based framework for reliability-based design optimisation of composite structures. *Engineering with Computers*, 38:595–608, 2022.

[63] C. Zheng, W. Zhao, H. Gao, L. Du, Y. Zhang, and C. Bi. Sensitivity analysis of acoustic eigenfrequencies by using a boundary element method. *The Journal of the Acoustical Society of America*, 149(3):2027–2039, 2021.

[64] M. A. Fahmy and M. O. Alsulami. Boundary element and sensitivity analysis of anisotropic thermoelastic metal and alloy discs with holes. *Materials (Basel, Switzerland)*, 15(5):1828, 2022.

[65] A. Tafreshi. Shape sensitivity analysis of composites in contact using the boundary element method. *Engineering Analysis with Boundary Elements*, 33(2):215–224, 2009.

[66] G.K. Sfantos and M.H. Aliabadi. A boundary element sensitivity formulation for contact problems using the implicit differentiation method. *Engineering Analysis with Boundary Elements*, 30(1):22–30, 2006.

[67] C. Su and J. Xu. Reliability analysis of reissner plate bending problems by stochastic spline fictitious boundary element method. *Engineering Analysis with Boundary Elements*, 51:37–43, 2015.

[68] D. Kim and B Kwak. Reliability-based shape optimization of two-dimensional elastic problems using bem. *Computers Structures*, 60(5):743–750, 1996.

[69] A. Canelas, J. Herskovits, and J.C.F. Telles. Shape optimization using the boundary element method and a sand interior point algorithm for constrained optimization. *Computers Structures*, 86(13):1517–1526, 2008. Structural Optimization.

[70] A Tafresh. Shape optimization of two-dimensional anisotropic structures using the boundary element method. *The Journal of Strain Analysis for Engineering Design*, 38(3):219–232, 2003.

[71] Z Kala. Probability based global sensitivity analysis of fatigue reliability of steel structures. *IOP Conference Series: Materials Science and Engineering*, 668(1):012015, 2019.

[72] O. Lee and D. H. Kim. Reliability of fatigue damaged structure using form, sorm and fatigue model. In *World Congress on Engineering*, 2007.

[73] R. E. Melchers and M Ahammed. A fast approximate method for parameter sensitivity estimation in monte carlo structural reliability. *Computers & Structures*, 82:55–61, 2004.

[74] G.H. Besterfield, W Liu, M.A. Lawrence, and T Belytschko. Fatigue crack growth reliability by probabilistic finite elements. *Computer Methods in Applied Mechanics and Engineering*, 86(3):297–320, 1991.

[75] Dong Won Kim and Byung Man Kwak. Reliability-based shape optimization of two-dimensional elastic problems using bem. *Computers Structures*, 60(5):743–750, 1996.

[76] X. Huang and M.H. Aliabadi. A boundary element method for structural reliability. *Key Engineering Materials*, 627:453–456, 01 2015.

[77] X. Huang, M.H. Aliabadi, and Z. Sharif Khodaei. Fatigue crack growth reliability analysis by stochastic boundary element method. *Computer Modeling in Engineering & Sciences*, 102(4):291–330, 2014.

[78] L. Morse, Z. Sharif Khodaei, and M.H. Aliabadi. Multi-fidelity modeling-based structural reliability analysis with the boundary element method. *Journal of Multiscale Modelling*, 08:1740001, 2017.

[79] L. Morse and M. H. Mallardo, V.and Aliabadi. Manufacturing cost and reliability-based shape optimization of plate structures. *International Journal for Numerical Methods in Engineering*, 123(10):2189–2213, 2022.

[80] B. Potrzeszcz-Sut. Reliability analysis of shell truss structure by hybrid monte carlo method. *Journal of Theoretical and Applied Mechanics*, 58(2):469–482, 2020.

[81] H. Liu and N. Li. Reliability analysis of autonomous underwater vehicle aft pressure shell for optimal design and strength. *Ocean Engineering*, 249:110906, 2022.

[82] Sandipan N., S. Chakraborty, and C. Ray. Reliability analysis of laminated composite shells by response surface method based on hsd. *Structural Engineering and Mechanics*, 72(2):203–216, 2019.

[83] L. Morse, Z. Sharif Khodaei, and M.H. Aliabadi. A dual boundary element based implicit differentiation method for determining stress intensity factor sensitivities for plate bending problems. *Engineering Analysis with Boundary Elements*, 106:412–426, 2019.

[84] L. Morse, V. Mallardo, Z. Sharif-Khodaei, and F.M.H. Aliabadi. Shape optimisation of assembled plate structures with the boundary element method. *Aerospace*, 9:381, 2022.

[85] Marissa Renardy, Louis R. Joslyn, Jess A. Millar, and Denise E. Kirschner. To sobol or not to sobol? the effects of sampling schemes in systems biology applications. *Mathematical Biosciences*, 337:108593, 2021.

[86] Nishant Dige and Urmila Diwekar. Efficient sampling algorithm for large-scale optimization under uncertainty problems. *Computers Chemical Engineering*, 115:431–454, 2018.

[87] Sergei S. Kucherenko, Daniel Albrecht, and Andrea Saltelli. Exploring multi-dimensional spaces: a comparison of latin hypercube and quasi monte carlo sampling techniques. *arXiv: Applications*, 2015.

[88] D. Gorissen, I. Couckuyt, P. Demeester, T. Dhaene, and K. Crombecq. A surrogate modeling and adaptive sampling toolbox for computer based design. *Journal of Machine Learning Research*, 11:2051–2055, 2010.

[89] *Measures of Structural Reliability*, chapter 1, pages 1–29. John Wiley Sons, Ltd, 2017.

[90] Abraham M. Hasofer and Niels C. Lind. Exact and invariant second-moment code format. *Journal of the Engineering Mechanics Division*, 100(1):111–121, 1974.

[91] Rüdiger Rackwitz and Bernd Flessler. Structural reliability under combined random load sequences. *Computers & Structures*, 9:489–494, 1978.

[92] Mohamed Abdelsabour Fahmy. Shape design sensitivity and optimization for two-temperature generalized magneto-thermoelastic problems using time-domain drbem. *Journal of Thermal Stresses*, 41(1):119–138, 2018.

[93] G.K. Sfantos and M.H. Aliabadi. A boundary element sensitivity formulation for contact problems using the implicit differentiation method. *Engineering Analysis with Boundary Elements*, 30(1):22–30, 2006.

[94] Mengke Zhuang, Llewellyn Morse, Zahra Sharif Khodaei, and M.H. Aliabadi. Implicit differentiation-based reliability analysis for shallow shell structures with the boundary element method. *Engineering Analysis with Boundary Elements*, 156:223–238, 2023.

[95] S.C. Mellings and M.H. Aliabadi. Three-dimensional flaw identification using inverse analysis. volume 34, pages 453–469, 1996.

[96] S. C. Mellings and M. H. Aliabadi. Flaw identification using the boundary element method. *International Journal for Numerical Methods in Engineering*, 38(3):399–419, 1995.

[97] Maria Radwanska. *Plate and shell structures : selected analytical and finite element solutions*. John Wiley Sons, Inc., Chichester, West Sussex, United Kingdom, 2017.

[98] Jia G. and X. Du. Reliability sensitivity analysis with random and interval variables. *International Journal for Numerical Methods in Engineering*, 78(13):1585–1617, 2009.

[99] A. (Andrea) Saltelli, K. (Karen) Chan, and E. Marian. Scott. *Sensitivity analysis*. Wiley series in probability and statistics. Wiley, Chichester, 2000.

[100] X. Niu, R. Wang, D. Liao, S. Zhu, X. Zhang, and B. Keshtegar. Probabilistic modeling of uncertainties in fatigue reliability analysis of turbine bladed disks. *International Journal of Fatigue*, 142:105912, 2021.

[101] J. Romero and N. Queipo. Reliability-based and deterministic design optimization of a FSAE brake pedal: a risk allocation analysis. *Journal of Mechanical Design*, 56():681–695, 07 2017.

[102] Liu Du, K. K. Choi, Byeng D. Youn, and David Gorsich. Possibility-Based Design Optimization Method for Design Problems With Both Statistical and Fuzzy Input Data. *Journal of Mechanical Design*, 128(4):928–935, 11 2005.

[103] Byeng D. Youn, Kyung K. Choi, and Young H. Park. Hybrid Analysis Method for Reliability-Based Design Optimization . *Journal of Mechanical Design*, 125(2):221–232, 06 2003.

[104] André Teófilo Beck and Wellison José de Santana Gomes. A comparison of deterministic, reliability-based and risk-based structural optimization under uncertainty. *Probabilistic Engineering Mechanics*, 28:18–29, 2012. Computational Stochastic Mechanics — CSM6.

[105] Fatma Abid, Abdelkhalak El Hami, Tarek Merzouki, Lassaad Walha, and Mohamed Haddar. An approach for the reliability-based design optimization of shape memory alloy structure. *Mechanics Based Design of Structures and Machines*, 49(2):155–171, 2021.

[106] Soo-Chang Kang, Hyun-Moo Koh, and Jinkyo Choo. Reliability-based design optimisation combining performance measure approach and response surface method. *Structure and Infrastructure Engineering*, 7:477–489, 07 2011.

[107] Paul H Wirsching. Fatigue reliability. *Progress in Structural Engineering and Materials*, 1(2):200–206, 1998.

[108] K. Sobczyk and B.F. Spencer. *Random Fatigue: From Data to Theory.* Elsevier Science, 2012.

[109] R Masoudi Nejad, Z. Liu, W Ma, and F Berto. Fatigue reliability assessment of a pearlitic grade 900a rail steel subjected to multiple cracks. *Engineering Failure Analysis*, 128:105625, 2021.

[110] Ni P, J Li, H Hao, W Yan, X Du, and H Zhou. Reliability analysis and design optimization of nonlinear structures. *Reliability Engineering System Safety*, 198:106860, 2020.

[111] R Teixeira, M Nogal, and A O'Connor. Adaptive approaches in metamodel-based reliability analysis: A review. *Structural Safety*, 89:102019, 2021.

[112] Erdem Acar, Amit A. Kale, and Mehmet A. Akgün. Reliability-based design and inspection scheduling optimization of an aircraft structure containing multiple site damage. 2004.

[113] Amit A. Kale, Raphael T. Haftka, and Bhavani V. Sankar. Efficient reliability-based design and inspection of stiffened panels against fatigue. *Journal of Aircraft*, 45(1):86–97, 2008.

[114] P. D. White. Review of methods and approaches for the structural risk assessment of aircraft. 2006.

[115] R. Masoudi Nejad, Z. Liu, W. Ma, and F. Berto. Reliability analysis of fatigue crack growth for rail steel under variable amplitude service loading conditions and wear. *International Journal of Fatigue*, 152:106450, 2021.

[116] Gilberto Gomes, Thiago A A Oliveira, and Francisco Evangelista. A probabilistic approach in fuselage damage analysis via boundary element method. *Advances in Fatigue and Fracture Testing and Modelling [Working Title]*, 2021.

[117] Cheng Su and Chun Zheng. Probabilistic fracture mechanics analysis of linear-elastic cracked structures by spline fictitious boundary element method. *Engineering Analysis with Boundary Elements*, 36(12):1828–1837, 2012.

[118] Jian Yang Yong Liu, Gaoshun Jia and L.H. Liang. Stochastic inverse boundary element method for defect and structural reliability parameter prediction. *Journal of the Chinese Institute of Engineers*, 23(3):289–297, 2000.

[119] Edson Denner Leonel, Alaa Chateauneuf, and Wilson Sergio Venturini. Probabilistic crack growth analyses using a boundary element model: Applications in linear elastic fracture and fatigue problems. *Engineering Analysis with Boundary Elements*, 36(6):944–959, 2012.

[120] X. Huang and M.H. Aliabadi. Probabilistic fracture mechanics by the boundary element method. *International Journal of Fracture*, 171(1):51–64, 2011.

[121] Zhao Wangwen. *Reliability analysis of fatigue and fracture under random loading*. PhD thesis. Imperial College London, 1989.

[122] S. Abdullah, S. Beden, and A. K. Ariffin. *Fatigue Crack Growth Simulation of Aluminium Alloy under Cyclic Sequence Effects*. 02 2011.

[123] P. Lopes, H. Gomes, and A.M. Awruch. Reliability analysis of laminated composite structures using finite elements and neural networks. *Composite Structures*, 92:1603–1613, 06 2010.

[124] H. Tang, X. Guo, and S. Xue. Uncertainty quantification in small-timescale model-based fatigue crack growth analysis using a stochastic collocation method. *Metals*, 10(5), 2020.

[125] Pengpeng Zhi, Yonghua Li, Bingzhi Chen, and Shanshan Shi. Bounds-based structure reliability analysis of bogie frame under variable load cases. *Engineering Failure Analysis*, 114:104541, 2020.

[126] Ning Li, De-Quan Zhang, Hai-Tao Liu, and Tie-Jun Li. Optimal design and strength reliability analysis of pressure shell with grid sandwich structure. *Ocean Engineering*, 223:108657, 2021.

[127] Ouk Lee and Dong Kim. Reliability of fatigue damaged structure using form, sorm and fatigue model. *Lecture Notes in Engineering and Computer Science*, 2166, 07 2007.

[128] Masoud Rais-Rohani. Reliability analysis and reliability-based design optimization of circular composite cylinders under axial compression. *NASA Langley Research Center*, 05 2000.

[129] V. Dubourg, J.-M. Bourinet, and B. Sudret. Reliability-based design optimization of shells with uncertain geometry using adaptive kriging metamodels. 2017.

[130] H. O. Madsen. *Methods of structural safety*. Dover Publications, Mineola, NY, dover ed. edition, 2006 - 1986.

[131] Peyman Amirafshari, Feargal Brennan, and Athanasios Kolios. A fracture mechanics framework for optimising design and inspection of offshore wind turbine support structures against fatigue failure. *Wind Energy Science*, 6:677–699, 05 2021.

[132] James W. Provan, editor. *Probabilistic Fracture Mechanics and Reliability*. Engineering Applications of Fracture Mechanics. Springer Dordrecht, 1987.

[133] W. S. Johnson. The history, logic and uses of the equivalent initial flaw size approach to total fatigue life prediction. *Procedia Engineering*, 2(1):47–58, 2010.

[134] P. White, L. Molent, and S. Barter. Interpreting fatigue test results using a probabilistic fracture approach. *International Journal of Fatigue*, 27(7):752–767, 2005.

[135] Pedro M.G.P. Moreira, Paulo F.P. de Matos, and Paulo M.S.T. de Castro. Fatigue striation spacing and equivalent initial flaw size in al 2024-t3 riveted specimens. *Theoretical and Applied Fracture Mechanics*, 43(1):89–99, 2005.

[136] Andrew Makeev, Yuri Nikishkov, and Erian Armanios. A concept for quantifying equivalent initial flaw size distribution in fracture mechanics based life prediction models. *International Journal of Fatigue*, 29(1):141–145, 2007.

[137] Kaushik Kethamukkala, Changyu Meng, Jie Chen, and Yongming Liu. Crack growth-based life prediction for additively manufactured metallic materials considering surface roughness. *International Journal of Fatigue*, 176:107914, 2023.

[138] Y. Liu and S. Mahadevan. Probabilistic fatigue life prediction using an equivalent initial flaw size distribution. *International Journal of Fatigue*, 31(3):476–487, 2009.

[139] W. Steven Johnson. The history, logic and uses of the equivalent initial flaw size approach to total fatigue life prediction. *Procedia Engineering*, 2(1):47–58, 2010. Fatigue 2010.

[140] B. Zheng and M. Dawood. Fatigue crack growth analysis of steel elements reinforced with shape memory alloy (sma)/fiber reinforced polymer (frp) composite patches. *Composite Structures*, 164:158–169, 2017.

[141] S. A. Nor Mohamed, E. S. Zainudin, S. M. Sapuan, M. A. Md. Deros, and A. M.T. Arifin. Crack growth analysis for rice husk reinforced polypropylene composite using equivalent initial flaw size concept. *BioResources*, 16(3):4963–4985, 2021.

[142] Fei Li, Zhixun Wen, Ziyan Wu, Haiqing Pei, and Zhufeng Yue. Fatigue life assessment of nickel-based single crystals considering equivalent initial flaw size model and anisotropy. *International Journal of Fatigue*, 160:106886, 2022.

[143] Shankar Sankararaman and Sankaran Mahadevan. Likelihood-based approach for uncertainty propagation in multidisciplinary analysis. 2012. Cited by: 0.

[144] L. Morse, Z. S. Khodaei, and M. H. Aliabadi. Statistical inference of the equivalent initial flaw size for assembled plate structures with the dual boundary element method. *Engineering Fracture Mechanics*, 238:107271, 2020.

[145] J. Chiachío, M. Chiachío, A. Saxena, S. Sankararaman, G. Rus, and K. Goebel. Bayesian model selection and parameter estimation for fatigue damage progression models in composites. *International Journal of Fatigue*, 70:361–373, 2015.

[146] Shankar Sankararaman and Sankaran Mahadevan. Bayesian methodology for diagnosis uncertainty quantification and health monitoring. *Structural Control and Health Monitoring*, 20(1):88 – 106, 2013. Cited by: 68; All Open Access, Bronze Open Access.

[147] J. Chiachio, M. Chiachio, S. Sankararaman, A. Saxena, and K. Goebel. A robust modeling approach for fatigue damage in composites based on bayesian model class selection. 2014. Cited by: 0.

[148] Llewellyn Morse, Zahra Sharif Khodaei, and M.H. Aliabadi. A multi-fidelity modelling approach to the statistical inference of the equivalent initial flaw size distribution for multiple-site damage. *International Journal of Fatigue*, 120:329–341, 2019.

[149] S. Sankararaman, Y. Ling, C. Shantz, and S. Mahadevan. Inference of equivalent initial flaw size under multiple sources of uncertainty. *International Journal of Fatigue*, 33:75–89, 2011.

[150] M. Salemi and H. Wang. Fatigue life prediction of pipeline with equivalent initial flaw size using bayesian inference method. *Journal of Infrastructure Preservation and Resilience*, 1(1):2, 2020.

[151] S. Sankararaman, L. You, C. Shantz, and S. Mahadevan. Uncertainty quantification in fatigue crack growth prognosis. *International Journal of Prognostics and Health Management*, 2, 2011.

[152] L. Morse, Z. S. Khodaei, and M. H. Aliabadi. Multi-fidelity modeling-based structural reliability analysis with the boundary element method. *Journal of Multiscale Modelling*, 08(03n04):1740001, 2017.

[153] V. Giurgiutiu. *Structural Health Monitoring with Piezoelectric Wafer Active Sensors*. Academic Press, 2 edition, 2014.

[154] K. Walker and W. Hu. A critical review of three models for short and long fatigue crack growth. In *Conference: Proceedings of twenty-fourth 2007 ICAF Symposium*, Naples, Italy, 2007.

[155] Fernand Ellyin. *Fatigue Damage, Crack Growth and Life Prediction*. Springer Dordrecht, 1 edition, 1997.

[156] K. Tanaka. Fatigue crack propagation from a crack inclined to the cyclic tensile axis. *Engineering Fracture Mechanics*, 6(3):493–507, 1974.

[157] Alexander I. J. Forrester, Andras. Sobester, and A. J. Keane. *Engineering design via surrogate modelling : a practical guide /*. John Wiley Sons, Ltd., Chichester, 2008.

[158] Karel Crombecq. Surrogate modeling of computer experiments with sequential experimental design. In *PhD dissertation University of Antwerp*, Antwerp, Belgium, 01 2011.

[159] Hans Bruun Nielsen, Søren Nymand Lophaven, and Jacob Søndergaard. Dace - a matlab kriging toolbox, 2002.

[160] British Standards Institution. Guide to methods for assessing the acceptability of flaws in metallic structures., 2005.

[161] F.H. Newmann and V.H.L. Searle. *The general properties of matter*. Edward Arnold, 1962.

[162] ASTM E. Standard test method for dynamic young´s modulus, shear modulus, and poisson´s ratio by sonic resonance. Technical report, ASTM International, 2013.

[163] J. Nunn. Measuring young's modulus the easy way, and tracing the effects of measurement uncertainties. *Physics Education*, 50, 2015.

[164] Y. Arao, J. Koyanagi, S. Utsunomiya, and H. Kawada. Effect of ply angle misalignment on out-of-plane deformation of symmetrical cross-ply cfrp laminates: Accuracy of the ply angle alignment. *Composite Structures*, 93(4):1225–1230, 2011.

[165] H. S. Toft, K. Branner, L. Mishnaevsky, and J. D. Sørensen. Uncertainty modelling and code calibration for composite materials. *Journal of Composite Materials*, 47(14):1729–1747, 2013.

[166] Selvakumar Ulaganathan, Ivo Couckuyt, Dirk Deschrijver, Eric Laermans, and Tom Dhaene. A matlab toolbox for kriging metamodelling. *Procedia Computer Science*, 51:2708–2713, 2015. International Conference On Computational Science, ICCS 2015.

[167] Max D. Morris and Toby J. Mitchell. Exploratory designs for computational experiments. *Journal of Statistical Planning and Inference*, 43(3):381–402, 1995.

Appendices

Appendix A

Fundamental Solutions and Kernels of the Boundary Element Method for Shell Structure

This chapter presents the fundamental solutions W^*_{ij}, P^*_{ij}, $U^*_{\theta\alpha}$ and $T^{*(i)}_{\theta\alpha}$ in the boundary integral equations in Eq. 2.52-2.53, and the kernels $W^*_{i\beta k}$, $P^*_{i\beta k}$, $U^*_{\alpha\beta\gamma}$ and $T^{(i)*}_{\alpha\beta\gamma}$ in the stress resultant equations Eq. 2.73- 2.75. The fundamental solutions and kernels were first derived in the work by Weeen [51].

A.1 Fundamental Solutions

The fundamental solution for rotational and out-of-plane displacements W^*_{ij} is

$$\begin{aligned} W^*_{\alpha\beta} &= \frac{1}{8\pi D(1-\nu)}\left\{[8B(z)-(1-\nu)(2\ln z-1)]\delta_{\alpha\beta}\right. \\ &\quad \left.-[8A(z)+2(1-\nu)]r_{,\alpha}r_{,\beta}\right\} \\ W^*_{\alpha 3} &= -W^*_{3\alpha} = \frac{1}{8\pi D}(2\ln z-1)rr_{,\alpha} \\ W^*_{33} &= \frac{1}{8\pi D(1-\nu)\lambda^2}\left[(1-\nu)z^2(\ln z-1)-8\ln z\right] \end{aligned} \tag{A.1}$$

The fundamental solution for bending and shear tractions P^*_{ij}

$$\begin{aligned}
P^*_{\gamma\alpha} &= \frac{-1}{4\pi r}\left[(4A(z)+2zK_1(z)+1-\nu)\left(\delta_{\alpha\gamma}r_{,n}+r_{,\alpha}n_\gamma\right)\right.\\
&\quad \left.+(4A(z)+1+\nu)r_{,\gamma}n_\alpha-2\left(8A(z)+2zK_1(z)+1-\nu\right)r_{,\alpha}r_{,\gamma}r_{,n}\right]\\
P^*_{\gamma 3} &= \frac{\lambda^2}{2\pi}\left[B(z)n_\gamma - A(z)r_{,\gamma}r_{,n}\right]\\
P^*_{3\alpha} &= \frac{-(1-\nu)}{8\pi}\left[\left(2\frac{(1+\nu)}{(1-\nu)}\ln z-1\right)n_\alpha+2r_{,\alpha}r_{,n}\right]\\
P^*_{33} &= \frac{-1}{2\pi r}r_{,n}
\end{aligned} \tag{A.2}$$

where

$$\begin{aligned}
A(z) &= K_0(z)+\frac{2}{z}\left[K_1(z)-\frac{1}{z}\right]\\
B(z) &= K_0(z)+\frac{1}{z}\left[K_1(z)-\frac{1}{z}\right]
\end{aligned} \tag{A.3}$$

where r is the absolute distance between the source and field points such that $r_\alpha = x_\alpha(x)-x_\alpha(x')$. The derivatives $r_{,\alpha}=r_\alpha/r$ and $r_{,n}=r_{,\alpha}n_\alpha$. $K_0(z)$ and $K_1(z)$ are the modified Bessel functions of the second kind with $z=\lambda r$, where λ is the shear factor $\lambda=\sqrt{10}/h$.

In the case of constant domain load in Eq. 2.55, the fundamental solution can be written as

$$\begin{aligned}
V^*_{\alpha,\beta} &= \frac{r^2}{128\pi D}\left[(4\ln z-5)\delta_{\alpha\beta}+2(4\ln z-3)r_{,\alpha}r_{,\beta}\right]\\
V^*_{3,\beta} &= \frac{-rr_{,\beta}}{128\pi D(1-\nu)\lambda^2}\left[32(2\ln z-1)-z^2(1-v)(4\ln z-5)\right]
\end{aligned} \tag{A.4}$$

The fundamental solutions for in-plane displacements $U^*_{\theta\alpha}$

$$U^*_{\theta\alpha} = \frac{1}{4\pi B(1-\nu)}\left[(3-4\nu)\ln(\frac{1}{r})\delta_{\theta\alpha}+(1+\nu)r_{,\theta}r_{,\alpha}\right] \tag{A.5}$$

The fundamental solutions for membrane tractions $T^{*(i)}_{\theta\alpha}$

$$T^{*(i)}_{\theta\alpha} = -\frac{1}{4\pi r}\left[r_{,n}((1-\nu)\delta_{\theta\alpha}+2(1+\nu)r_{,\theta}r_{,\alpha})+(1-\nu)(n_\theta r_{,\alpha}-n_\alpha r_{,\theta})\right] \tag{A.6}$$

A.2 Kernels

The kernels $W^*_{i\beta k}$ and $P^*_{i\beta k}$ are determined through the first derivative of the fundamental solution W^*_{ij} and P^*_{ij}.

$$\begin{aligned}
W^*_{\alpha\beta\gamma} &= \frac{1}{4\pi r}\left[\left(4A(z)+2zK_1(z)+1-\nu\right)\left(\delta_{\beta\gamma}r_{,\alpha}+\delta_{\alpha\gamma}r_{,\beta}\right)\right.\\
&\quad \left.-2\left(8A(z)+2zK_1(z)+1-\nu\right)r_{,\alpha}r_{,\beta}r_{,\gamma}+\left(4A(z)+1+\nu\right)\delta_{\alpha\beta}r_{,\gamma}\right]\\
W^*_{\alpha\beta 3} &= \frac{-(1-\nu)}{8\pi}\left[\left(2\frac{(1+\nu)}{(1-\nu)}\ln z-1\right)\delta_{\alpha\beta}+2r_{,\alpha}r_{,\beta}\right]\\
W^*_{3\beta\gamma} &= \frac{\lambda^2}{2\pi}\left[B(z)\delta_{\gamma\beta}-A(z)r_{,\gamma}r_{,\beta}\right]\\
W^*_{3\beta 3} &= \frac{1}{2\pi r}r_{,\beta}\\
P^*_{\alpha\beta\gamma} &= \frac{D(1-\nu)}{4\pi r^2}\left\{\left(4A(z)+2zK_1(z)+1-\nu\right)\left(\delta_{\gamma\alpha}n_\beta+\delta_{\gamma\beta}n_\alpha\right)\right.\\
&\quad +\left(4A(z)+1+3\nu\right)\delta_{\alpha\beta}n_\gamma-\left(16A(z)+6zK_1(z)+z^2K_0(z)+2-2\nu\right)\\
&\quad \times\left[\left(n_\alpha r_{,\beta}+n_\beta r_{,\alpha}\right)r_{,\gamma}+\left(\delta_{\gamma\alpha}r_{,\beta}+\delta_{\gamma\beta}r_{,\alpha}\right)r_{,n}\right]\\
&\quad -2\left(8A(z)+2zK_1(z)+1+\nu\right)\left(\delta_{\alpha\beta}r_{,\gamma}r_{,n}+n_\gamma r_{,\alpha}r_{,\beta}\right)\\
&\quad \left.+4\left(24A(z)+8zK_1(z)+z^2K_0(z)+2-2\nu\right)r_{,\alpha}r_{,\beta}r_{,\gamma}r_{,n}\right\}\\
P^*_{\alpha\beta 3} &= \frac{D(1-\nu)\lambda^2}{4\pi r}\left[\left(2A(z)+zK_1(z)\right)\left(r_{,\beta}n_\alpha+r_{,\alpha}n_\beta\right)\right.\\
&\quad \left.-2\left(4A(z)+zK_1(z)\right)r_{,\alpha}r_{,\beta}r_{,n}+2A(z)\delta_{\alpha\beta}r_{,n}\right]\\
P^*_{3\beta\gamma} &= \frac{-D(1-\nu)\lambda^2}{4\pi r}\left[\left(2A(z)+zK_1(z)\right)\left(\delta_{\gamma\beta}r_{,n}+r_{,\gamma}n_\beta\right)\right.\\
&\quad \left.+2A(z)n_\gamma r_{,\beta}-2\left(4A(z)+zK_1(z)\right)r_{,\gamma}r_{,\beta}r_{,n}\right]\\
P^*_{3\beta 3} &= \frac{D(1-\nu)\lambda^2}{4\pi r^2}\left[\left(z^2B(z)+1\right)n_\beta-\left(z^2A(z)+2\right)r_{,\beta}r_{,n}\right]
\end{aligned} \tag{A.7}$$

and for the case of uniform domain load

$$\begin{aligned}
Q^*_{\alpha\beta} &= \frac{-r}{64\pi}\left\{\left(4\ln z-3\right)\left[\left(1-\nu\right)\left(r_{,\beta}n_\alpha+r_{,\alpha}n_\beta\right)+\left(1+3\nu\right)\delta_{\alpha\beta}r_{,n}\right]\right.\\
&\quad \left.+4\left[\left(1-\nu\right)r_{,\alpha}r_{,\beta}+\nu\delta_{\alpha\beta}\right]r_{,n}\right\}\\
Q^*_{3\beta} &= \frac{1}{8\pi}\left[\left(2\ln z-1\right)n_\beta+2r_{,\beta}r_{,n}\right]
\end{aligned} \tag{A.8}$$

The kernels $U^*_{\alpha\beta\gamma}$ and $T^{(i)*}_{\alpha\beta\gamma}$ are derived from the first derivative of the fundamental solution $U^*_{\theta\alpha}$ and $T^{(i)*}_{\theta\alpha}$.

$$\begin{aligned}
U^*_{\alpha\beta\gamma} =& \frac{1}{4\pi r}\left[(1-\nu)\left(\delta_{\gamma\alpha}r_{,\beta}+\delta_{\gamma\beta}r_{,\alpha}-\delta_{\alpha\beta}r_{,\gamma}\right)+2(1+\nu)r_{,\alpha}r_{,\beta}r_{,\gamma}\right] \\
T^{(i)*}_{\alpha\beta\gamma} =& \frac{B(1-\nu)}{4\pi r^2}\left\{2r_{,n}\left[(1-\nu)\delta_{\alpha\beta}r_{,\gamma}+\nu\left(\delta_{\gamma\alpha}r_{,\beta}+\delta_{\gamma\beta}r_{,\alpha}\right)-4(1+\nu)r_{,\alpha}r_{,\beta}r_{,\gamma}\right]\right. \\
&+2\nu\left(n_\alpha r_{,\beta}r_{,\gamma}+n_\beta r_{,\alpha}r_{,\gamma}\right)+(1-\nu)\left(2n_\gamma r_{,\alpha}r_{,\beta}+n_\beta\delta_{\alpha\gamma}+n_\alpha\delta_{\beta\gamma}\right) \\
&\left.-(1-3\nu)n_\gamma\delta_{\alpha\beta}\right\}
\end{aligned} \tag{A.10}$$

Appendix B

Particular Solutions for the Dual Reciprocity Method

This chapter presents the particular solutions derived and the detailed derivations are presented in [41]. The particular solutions were used for transforming the domain integral equations into the boundary integral equations in Eq. 2.52-2.53, and Eq. 2.73- 2.75 through the Dual Reciprocity Method (DRM). Only the necessary formulations are provided here as in the Implicit Differentiation Method (IDM), the corresponding derivatives with respect to the design parameters are required to be computed. The coefficients are:

$$\begin{aligned} B &= Eh/(1-\nu^2) \\ D &= Eh^3/12(1-\nu^2) \\ CW &= 45(1-\nu)\lambda^2 D \\ \lambda &= \sqrt{(10)}/h \end{aligned} \tag{B.1}$$

and the distance between the source and field point

$$r = \sqrt{(x_1 - x_1')^2 + (x_2 - x_2')^2} \tag{B.2}$$

B.1 Particular Solutions for Plane Stress

The particular solutions $\hat{u}^{\gamma}_{m\alpha}$, $\hat{t}^{\gamma}_{m\alpha}$ were derived from solving the Galerkin vector for 2D plane stress.

$$\begin{aligned}\hat{u}^{1}_{m1} &= -\frac{2}{(1-\nu)B}\left[\frac{rx_1}{3} - \frac{1+\nu}{30}\left(\frac{x_1^3}{r} + 3x_1 r\right)\right] \\ \hat{u}^{1}_{m2} &= \frac{(1+\nu)}{15(1-\nu)B}\left(\frac{x_1^2 x_2}{r} + x_2 r\right)\end{aligned} \tag{B.3}$$

the in-plane strain can be related to the displacement as $\epsilon_{\alpha\beta} = \frac{1}{2}(u_{\alpha,\beta} + u_{\beta,\alpha})$, hence, the particular solution for the strain can be found as

$$\begin{aligned}\hat{\varepsilon}^{1}_{m11} &= -\frac{2}{(1-\nu)}\left[\left(\frac{x_1^2}{r} + \frac{r}{3}\right) - \frac{1+\nu}{30}\left(-\frac{x_1^4}{r^3} + \frac{6x_1^2}{r} + 3r\right)\right] \\ \hat{\varepsilon}^{1}_{m12} &= -\frac{2}{(1-\nu)}\left[\frac{x_1 x_2}{6r} - \frac{1+\nu}{30}\left(-\frac{x_1^3 x_2}{r^3} + \frac{3x_1 x_2}{r}\right)\right] \\ \hat{\varepsilon}^{1}_{m22} &= \frac{2}{(1-\nu)}\frac{1+\nu}{30}\left(-\frac{x_1^2 x_2^2}{r^3} + 2r\right)\end{aligned} \tag{B.4}$$

the membrane stress resultant can be found by substitute stress resultant-displacement relationship in Eq. 2.51

$$\begin{aligned}\hat{N}^{1}_{m11} &= B\left[(1-\nu)\hat{\varepsilon}^{1}_{m11} + \nu\hat{\varepsilon}^{1}_{m\alpha\alpha}\right] \\ \hat{N}^{1}_{m12} &= B(1-\nu)\hat{\varepsilon}^{1}_{m12} \\ \hat{N}^{1}_{m22} &= B\left[(1-\nu)\hat{\varepsilon}^{1}_{m22} + \nu\hat{\varepsilon}^{1}_{m\alpha\alpha}\right]\end{aligned} \tag{B.5}$$

the particular solution for traction $\hat{t}^{1}_{m\alpha}$ is therefore

$$\hat{t}^{1}_{m\alpha} = \hat{N}^{1}_{m\alpha\beta} n_{\beta} \tag{B.6}$$

The same procedure can be applied to deriving the particular solutions using $\hat{t}^{2}_{m\alpha}$ where

$$\begin{aligned}\hat{u}^{2}_{m1} &= \frac{(1+\nu)}{15(1-\nu)B}\left(\frac{x_2^2 x_1}{r} + x_1 r\right) \\ \hat{u}^{2}_{m2} &= -\frac{2}{(1-\nu)B}\left[\frac{rx_2}{3} - \frac{1+\nu}{30}\left(\frac{x_2^3}{r} + 3x_2 r\right)\right]\end{aligned} \tag{B.7}$$

and by applying the strain-displacement and stress resultant-displacement relationship

$$\begin{aligned}
\hat{\varepsilon}^2_{m11} &= \frac{2}{(1-\nu)}\frac{1+\nu}{30}\left(-\frac{x_1^2x_2^2}{r^3}+2r\right)\\
\hat{\varepsilon}^2_{m12} &= -\frac{2}{(1-\nu)}\left[\frac{x_1x_2}{6r}-\frac{1+\nu}{30}\left(-\frac{x_2^3x_1}{r^3}+\frac{3x_1x_2}{r}\right)\right]\\
\hat{\varepsilon}^2_{m22} &= -\frac{2}{(1-\nu)}\left[\left(\frac{x_2^2}{r}+\frac{r}{3}\right)-\frac{1+\nu}{30}\left(-\frac{x_2^4}{r^3}+\frac{6x_2^2}{r}+3r\right)\right]
\end{aligned} \tag{B.8}$$

and for membrane stress resultants:

$$\begin{aligned}
\hat{N}^2_{m11} &= B\left[(1-\nu)\hat{\varepsilon}^2_{m11}+\nu\hat{\varepsilon}^2_{m\alpha\alpha}\right]\\
\hat{N}^2_{m12} &= B(1-\nu)\hat{\varepsilon}^2_{m12}\\
\hat{N}^2_{m22} &= B\left[(1-\nu)\hat{\varepsilon}^2_{m22}+\nu\hat{\varepsilon}^2_{m\alpha\alpha}\right]
\end{aligned} \tag{B.9}$$

the particular solution for traction $\hat{t}^2_{m\alpha}$ is therefore

$$\hat{t}^2_{m\alpha} = \hat{N}^2_{m\alpha\beta}n_\beta \tag{B.10}$$

B.2 Particular Solutions for Plate Bending

The particular solutions $\hat{w}^i_{m\alpha}$, $\hat{p}^i_{m\alpha}$ were derived from the governing equation of shear deformable plate bending problems, implemented by using the radial basis functions.

The particular solution for rotation and deflection is

$$\begin{aligned}
\hat{w}^3_{m1} &= -\left(\frac{1}{16}+\frac{r}{45}\right)\frac{x_1r^2}{D}\\
\hat{w}^3_{m2} &= -\left(\frac{1}{16}+\frac{r}{45}\right)\frac{x_2r^2}{D}\\
\hat{w}^3_{m3} &= -\left(\frac{1}{2}+\frac{2r}{9}\right)\frac{r^2}{(1-\nu)\lambda^2D}+\left(\frac{1}{64}+\frac{r}{225}\right)\frac{1}{D}
\end{aligned} \tag{B.11}$$

the bending stress resultant $M_{\alpha\beta}$ can be found in terms of the displacement by substituting the above formulations into Eq.2.49. Similarly, the shear stress resultant Q_α can be found with Eq.2.50,

hence the particular solutions for $\hat{M}_{m\alpha\beta}$ and $\hat{Q}_{m\beta}$ are

$$\begin{aligned}
\hat{M}^3_{m11} &= -\left[\left(\frac{1}{8}+\frac{r}{15}\right)\left(x_1^2+\nu x_2^2\right)+(1+\nu)\left(\frac{r^2}{16}+\frac{r^3}{45}\right)\right] \\
\hat{M}^3_{m12} &= -(1+\nu)\left(\frac{1}{8}+\frac{r}{15}\right)(x_1x_2) \\
\hat{M}^3_{m22} &= -\left[\left(\frac{1}{8}+\frac{r}{15}\right)\left(\nu x_1^2+x_2^2\right)+(1+\nu)\left(\frac{r^2}{16}+\frac{r^3}{45}\right)\right] \\
\hat{Q}^3_{m1} &= -\frac{x_1}{2}\left(1+\frac{2r}{3}\right) \\
\hat{Q}^3_{m2} &= -\frac{x_2}{2}\left(1+\frac{2r}{3}\right)
\end{aligned} \tag{B.12}$$

the particular solutions $\hat{w}^1_{mk}$ are

$$\begin{aligned}
\hat{w}^1_{m1} &= -\left(3x_1^2+r^2\right)\frac{r}{45D} \\
\hat{w}^1_{m2} &= -\frac{x_1x_2r}{15D} \\
\hat{w}^1_{m3} &= -\left[30-(1-\nu)\lambda^2r^2\right]\frac{rx_1}{45(1-\nu)\lambda^2D}
\end{aligned} \tag{B.13}$$

similarly, by applying the stress resultant-displacement relationship, the particular solutions for $\hat{M}_{m\alpha\beta}$ and $\hat{Q}_{m\beta}$ are

$$\begin{aligned}
\hat{M}^1_{m11} &= -\frac{x_1}{15}\left[\nu\left(\frac{x_1^2}{r}+3r\right)+\left(\frac{x_2^2}{r}+r\right)\right] \\
\hat{M}^1_{m12} &= -(1-\nu)\frac{x_2}{15}\left(\frac{x_1^2}{r}+r\right) \\
\hat{M}^1_{m22} &= -\frac{x_1}{15}\left[\nu\left(\frac{x_1^2}{r}+3r\right)+\left(\frac{x_2^2}{r}+r\right)\right] \\
\hat{Q}^1_{m1} &= -\frac{1}{3}\left(\frac{x_1^2}{r}+r\right) \\
\hat{Q}^1_{m2} &= -\frac{1}{3}\frac{x_1x_2}{r}
\end{aligned} \tag{B.14}$$

for $\alpha = 2$, the particular solutions $\hat{w}^2_{mk}$ are

$$\begin{aligned}
\hat{w}^2_{m1} &= -\frac{x_1x_2r}{15D} \\
\hat{w}^2_{m1} &= -\left(3x_2^2+r^2\right)\frac{r}{45D} \\
\hat{w}^2_{m3} &= -\left[30-(1-\nu)\lambda^2r^2\right]\frac{rx_2}{45(1-\nu)\lambda^2D}
\end{aligned} \tag{B.15}$$

hence,

$$\begin{aligned}
\hat{M}^2_{m11} &= -\frac{x_2}{15}\left[\nu\left(\frac{x_1^2}{r}+r\right)+\left(\frac{x_2^2}{r}+3r\right)\right] \\
\hat{M}^2_{m12} &= -(1-\nu)\frac{x_1}{15}\left(\frac{x_2^2}{r}+r\right) \\
\hat{M}^2_{m22} &= -\frac{x_2}{15}\left[\nu\left(\frac{x_1^2}{r}+r\right)+\left(\frac{x_2^2}{r}+3r\right)\right] \\
\hat{Q}^2_{m1} &= -\frac{1}{3}\frac{x_1 x_2}{r} \\
\hat{Q}^2_{m2} &= -\frac{1}{3}\left(\frac{x_2^2}{r}+r\right)
\end{aligned} \tag{B.16}$$

Appendix C

Probablistic Distributions and Derivatives of Limit State Function

This chapter presented the distributions that have been used in the numerical examples for accounting for the uncertainties in the parameters. The derivatives of the limit state function are hence associated with the distribution type of the design parameters.

C.1 Probablistic Distributions

A general introduction of the probabilistic distribution can be found in any statistical book. This section provides only the relevant expressions of each distribution. There are two main types of distributions that were considered in this work, namely, normal distributions and lognormal distributions.

C.1.1 Normal Distribution

Consider a random variable x follows a normal distribution with mean μ_x and standard distribution σ_x such that $x \sim N(\mu_x, \sigma_x)$, the *probability density function* (PDF) is defined as

$$f_X(x) = \frac{1}{\sigma_x\sqrt{2\pi}} exp\left[-\frac{1}{2}\left(\frac{x-\mu_x}{\sigma_x}\right)^2\right] \tag{C.1}$$

the *cumulative distribution function* (CDF) is defined by the total summation of the PDF corresponding to a value less or equal to x, hence, the CDF can be expressed by:

$$F_X(x) = P(X \leq x) = \int_{-\infty}^{x} f_X(\zeta) d\zeta \tag{C.2}$$

The standard normal distribution is defined when $x \sim N(0,1)$. The PDF for a variable z that follows the standard normal distribution can be written as:

$$f_U(u) = \frac{1}{\sqrt{2\pi}} exp\left[-\frac{1}{2}(u)^2\right] \tag{C.3}$$

the CDF can be computed by the equation given in Eq. C.2 and the notation for the standard normal CDF is $\Phi(u)$.

For any normal distribution, the CDF can be computed in terms of the CDF in the standard normal space $\Phi(u)$. Consider the variable $X = \mu_x + U\sigma_x$, the following relationship can be derived:

$$F_X(x) = P(X \leq x) = P(\mu_x + U\sigma_x \leq x) = P(U \leq \frac{x-\mu_x}{\sigma_x}) = \Phi(\frac{x-\mu_x}{\sigma_x}) \tag{C.4}$$

C.1.2 Lognormal Distribution

The variable x is considered to follow the lognormal distribution if $Y = ln(x)$ is a normal distribution. This also means that all x is a positive number. Following the relationship given in Eq.C.4

$$F_X(x) = P(X \leq x) = P(ln(X) \leq ln(x)) = P(Y \leq y) \tag{C.5}$$

such that

$$F_X(x) = \Phi(\frac{y-\mu_y}{\sigma_y}) = \Phi\left(\frac{ln(x)-\mu_{lnx}}{\sigma_{lnx}}\right) \tag{C.6}$$

where $Y \sim N(\mu_{lnx}, \sigma_{lnx})$ follows normal distribution. Given that the variable $x \sim lnN(\mu_x, \sigma_x)$, the mean and standard deviation for Y can be found by

$$\begin{aligned} \sigma_{lnx}^2 &= ln\left(\frac{\sigma_x^2}{\mu_x^2} + 1\right) \\ \mu_{lnx} &= ln(\mu_x) - \frac{1}{2}\sigma_{lnx}^2 \end{aligned} \tag{C.7}$$

the PDF for a lognormal distribution can be found as

$$f_X(x) = \frac{1}{x\sigma_{lnx}\sqrt{2\pi}} exp\left[-\frac{1}{2}\left(\frac{ln(x)-\mu_{lnx}}{\sigma_{lnx}}\right)^2\right] \tag{C.8}$$

C.2 Derivatives of the Limit State Function

The limit state function $g(\mathbf{Z})$ takes the form of structure resistance R and structure demand $G(\mathbf{X})$, where X contains the parameters that can affect the value of the limit state function (LSF) excluding the variable R. The failure region is defined such that the demand is larger than the resistance as $g(\mathbf{Z}) < 0$.

$$g(\mathbf{Z}) = R - G(\mathbf{X}) \tag{C.9}$$

In performing the First-Order Reliability analysis (FORM), the first-order derivatives of the LSF with respect to the design parameters X are required to be computed as

$$\frac{\partial g(\mathbf{Z})}{\partial X_i} = \frac{\partial R}{\partial X_i} - \frac{\partial G(\mathbf{X})}{\partial X_i} = -\frac{\partial G(\mathbf{X})}{\partial X_i} \tag{C.10}$$

where X_i is design parameters and $i \in [1, n]$ when n parameters are considered to affect the LSF. In the case when X_i follows a normal distribution with $X_i = \mu_i + U_i\sigma_i$, the derivatives in terms of U can be found $\partial X_i/\partial U_i = \sigma_i$. Hence, Eq. C.10 can be rewrite as:

$$\frac{\partial G(\mathbf{X})}{\partial U_i} = \sigma_i \frac{\partial G(\mathbf{X})}{\partial X_i} \tag{C.11}$$

In the case when x follows a lognormal distribution such that $X_i = exp(\mu^i_{lnx} + U_i\sigma^i_{lnx})$, the derivatives with respect to U is $\partial X_i/\partial U_i = X_i\sigma^i_{lnx}$. Hence, Eq. C.10 can be rewrite as:

$$\frac{\partial G(\mathbf{X})}{\partial U_i} = X_i\sigma^i_{lnx} \frac{\partial G(\mathbf{X})}{\partial X_i} \tag{C.12}$$

Similarly, the derivative of the LSF with respect to U_R when $R = \mu_R + U_R\sigma_R$ follows a normal distribution can be found as

$$\frac{\partial g(\mathbf{Z})}{\partial U_R} = \frac{\partial g(\mathbf{Z})}{\partial R}\frac{\partial R}{\partial U_R} = \sigma_R \tag{C.13}$$

and for lognormal distribution $R = exp(\mu_{lnx}^R + U_R \sigma_{lnx}^R)$

$$\frac{\partial g(\mathbf{Z})}{\partial U_R} = R\sigma_{lnx}^R \tag{C.14}$$

Appendix D

Derivatives of the Particular Solutions

D.1 Derivatives of the particular solutions with respect to geometry variables

The derivation and detailed expressions for the particular solutions used in the DRM method can be found in [26] for the transformation of the domain integral to the boundary integral. The derivatives of the particular solutions with respect to some geometry variables Z_g are derived for the first time in this work and are shown below.

The distance between the field point and collocation point can be found by:

$$r = \sqrt{(x_1 - x_1')^2 + (x_2 - x_2')^2} \tag{D.1}$$

where x_1 and x_2 represent the x and y coordinates of the nodal points respectively. Therefore, the derivatives of r can be found by:

$$r_{,g} = \left((x_1 - x_1')(x_{1,g} - x_{1,g}') + (x_2 - x_2')(x_{2,g} - x_{2,g}')\right)/r \tag{D.2}$$

D.1.1 Derivatives of the particular solutions for 2D plane stress with respect to a geometrical variable

The derivatives of the particular solution for displacement are:

$$\begin{aligned}
\hat{u}^1_{m1,g} &= -\frac{2}{(1-\nu)B}\left[\frac{1}{3}\left(r_{,g}x_1 + r x_{1,g}\right) - \frac{1+\nu}{30}\left(\frac{1}{r^2}\left(3x_1x_{1,g}r - x_1^3 r_{,g}\right)\right.\right. \\
&\left.\left. +3x_{1,g}r + 3x_1 r_{,g}\right)\right] \\
\hat{u}^1_{m2,g} &= \frac{(1+v)}{15(1-v)B}\left[\frac{1}{r^2}\left(2x_1x_{1,g}x_2r + x_1^2x_{2,g}r - r_{,g}x_1^2x_2\right) + x_{2,g}r + x r_{,g}\right] \\
\hat{u}^2_{m1,g} &= \frac{1+\nu}{15(1-\nu)B}\left[\frac{1}{r^2}\left(2x_2x_{2,g}x_1r + x_2^2x_{1,g}r - r_{,g}x_2^2x_1\right) + x_{1,gr} + x r_{,g}\right] \\
\hat{u}^2_{m2,g} &= -\frac{2}{(1-\nu)B}\left[\frac{1}{3}\left(r_{,g}x_2 + r x_{2,g}\right) - \frac{1+\nu}{30}\left(\frac{1}{r^2}\left(3x_2^2x_{2,g}r\right.\right.\right. \\
&\left.\left.\left. -{x_2}^3 r_{,g}\right) + 3x_{2,g}r + 3x r_{,g}\right)\right]
\end{aligned} \tag{D.3}$$

The derivatives of the particular solutions for the strains are:

$$\begin{aligned}
\hat{\varepsilon}^1_{m11,g} &= -\frac{2}{(1-\nu)}\left[\frac{1}{r^2}\left(2x_1x_{1,g}r - r_{,g}x_1^2\right) + \frac{1}{3}r_{,g} - \frac{1+\nu}{30}\left(-\frac{1}{r^6}\left(4x_1^3x_{1,g}r^3\right.\right.\right. \\
&\left.\left.\left. -3r^2r_{,g}x_1^4\right) + \frac{1}{r^2}\left(12x_1x_{1,g}r - 6x_1^2r_{,g}\right) + 3r_{,g}\right)\right] \\
\hat{\varepsilon}^1_{m12,g} &= -\frac{2}{(1-\nu)}\left[\frac{1}{6r^2}\left(x_{1,g}x_2r + x_1x_{2,g}r\right) - \frac{(1+\nu)}{30}\left(-\frac{1}{r^3}\left(3x_1^2x_{1,g}x_2r^3\right.\right.\right. \\
&\left.\left.\left. +x_1^3x_2, gr^3\right) + \frac{3}{r^6}x_1^3x_2r^2r_1g + \frac{1}{r^2}\left(3x_1, gx_2r + 3x_1x_2, gr - 3x_1x_2r_{,g}\right)\right] \\
\hat{\varepsilon}^1_{m22,g} &= \frac{(1+\nu)}{15(1-\nu)}\left[-\frac{1}{r^6}\left(2x_1x_{1,g}x_2^2r^3 + 2x_1^2x_2x_{2,g}r^3 - 3x_1^2x_2^2r^2r_{,g}\right) + 2r_{,g}\right] \\
\hat{\varepsilon}^2_{m11,g} &= \frac{(1+\nu)}{15(1-\nu)}\left[-\frac{1}{r^6}\left(2x_1x_{1,g}x_2^2r^3 + 2x_1^2x_2x_{2,g}r^3\right.\right. \\
&\left.\left. -3r^2r_{,g}{x_1}^2{x_2}^2\right) + 2r_{,g}\right] \\
\hat{\varepsilon}^2_{m12,g} &= -\frac{2}{(1-\nu)}\left[\frac{1}{6r^2}\left(x_{1,g}x_2r + x_1x_{2,g}r\right) - \frac{1+\nu}{30}\left(-\frac{1}{r^6}\left(3x_2^2x_{2,g}x_1r^3\right.\right.\right. \\
&\left.\left.\left. +{x_2}^3x_{1,g}r^3 - 3x_2^3x_1r^2r_{,g}\right) + \frac{1}{r^2}\left(3x_{1,g}x_2r + 3x_1x_{2,g}r - 3x_1x_2r_{,g}\right)\right] \\
\hat{\varepsilon}^2_{m22,g} &= -\frac{2}{1-\nu}\left[\frac{1}{r^2}\left(2x_2x_{2,g}r - r_{,g}x_2^2\right) + \frac{1}{3}r_{,g} - \frac{1-\nu}{30}\left(-\frac{1}{r^6}\left(4x_2^3x_{2,g}r^3\right.\right.\right. \\
&\left.\left.\left. +3x_2^4r^2r_{,g}\right) + \frac{1}{r^2}\left(12x_2x_{2,g}r - 6x_2^2r_{,g}\right) + 3r_{,g}\right)\right]
\end{aligned} \tag{D.4}$$

The derivatives of the particular solution for the membrane stress are: resultant $\hat{N}_{m\alpha\beta}$

$$\begin{aligned}
\hat{N}^{ii}_{m11,g} &= B\left[(1-v)\hat{\varepsilon}^{ii}_{m11,g} + v\hat{\varepsilon}^{ii}_{m11,g} + v\hat{\varepsilon}^{ii}_{m22,g}\right] \\
\hat{N}^{ii}_{m12,g} &- B(1-\nu)\hat{\varepsilon}^{ii}_{m12,g} \\
\hat{N}^{ii}_{m22,g} &= B\left[(1-\nu)\hat{\varepsilon}^{ii}_{m22,g} + \nu\hat{\varepsilon}^{ii}_{m11,g} + \nu\hat{\varepsilon}^{ii}_{m22,g}\right]
\end{aligned} \tag{D.5}$$

The particular solutions for traction can be found by multiplying the membrane stress resultant with the unit outward normal such that $\hat{t}_{m\alpha} = \hat{N}_{m\alpha\beta}n_\beta$. The derivatives of the traction can be found by:

$$\hat{t}^{ii}_{m\alpha,g} = \hat{N}^{ii}_{m\alpha\beta,g}n_\beta + \hat{N}^{ii}_{m\alpha\beta}n_{\beta,g} \tag{D.6}$$

In the above equation, superscript ii can take values of 1 or 2.

D.1.2 Derivatives of the particular solutions for plate bending with respect to a geometrical variable

From the bending stress resultant-displacement relationship, the tractions on the boundary can be found by the bending moment stress resultants $\hat{M}_{m\alpha\beta}$ and shear force stress resultants $\hat{Q}_{m\alpha}$ such that:

$$\hat{p}_{m\alpha} = \hat{M}_{m\alpha\beta}n_\beta, \quad \hat{p}_{m3} = \hat{Q}_{m\alpha}n_\alpha \tag{D.7}$$

The derivatives of the tractions can be found by:

$$\hat{p}_{m\alpha,g} = \hat{M}_{m\alpha\beta,g}n_\beta + \hat{M}_{m\alpha\beta}n_{\beta,g}, \quad \hat{p}_{m3,g} = \hat{Q}_{m\alpha,g}n_\alpha + \hat{Q}_{m\alpha}n_{\alpha,g} \tag{D.8}$$

For the function $F_{,\alpha} = x_\alpha/r$, the derivatives of the particular solution when $\alpha = 1$ can be calculated as:

$$\begin{aligned}
\hat{w}^1_{m1,g} &= -\left(r_{,g}\left(3x_1^2 + r^2\right) + r\left(6x_1x_{1,g} + 2rr_{,g}\right)\right)\frac{1}{45D} \\
\hat{w}^1_{m2,g} &= -\left(x_1x_2r_{,g} + x_1x_{2,g}r + x_{1,g}x_2r\right)\frac{1}{15D} \\
\hat{w}^1_{m3,g} &= -\left[30 - (1-\nu)\lambda^2\right]\frac{r_{,g}x_1 + rx_{1,g}}{45(1-\nu)\lambda^2 D} + \left[(1-\nu)\lambda^2 2rr_{,g}\right]\frac{rx_1}{45(1-\nu)\lambda^2 D}
\end{aligned} \tag{D.9}$$

where bending stiffness $D = Eh^3/[12(1-\nu^2)]$ and $\lambda = \sqrt{10}/h$. the derivatives for the particular solutions of moments $\hat{M}_{\alpha\beta}$ and shear forces $\hat{Q}_\beta$ are:

$$\begin{aligned}
\hat{M}^1_{m11,g} &= S^1_{11}g + \nu S^1_{22,g} \\
\hat{M}^1_{m12,g} &= (1-\nu) S^1_{12,g} \\
\hat{M}^1_{m22,g} &= \nu S^1_{11,g} + S^1_{22,g}
\end{aligned} \tag{D.10}$$

where:

$$\begin{aligned}
S^1_{11,g} &= -\frac{1}{15}\left[\frac{1}{r^2}\left(3x_1^2 x_{1,g} r - x_1^3 r_{,g}\right) + 3r_{,g}x_1 + 3r x_{1,g}\right] \\
S^1_{12,g} &= -\frac{1}{15}\left[\frac{1}{r^2}\left(2x_1 x_{1,g} x_2 r + x_1^2 x_{2,g} r - x_1^2 x_2 r_{,g}\right) + r_{,}g x_2 + r x_{2,g}\right] \\
S^1_{22,g} &= -\frac{1}{15}\left[\frac{1}{r^2}\left(2r x_2 x_{2,g} x_1 + r {x_2}^2 x_{1,g} - x_2^2 x_1 r_{,g}\right) + r_{,g}x_1 + r x_{1,g}\right]
\end{aligned} \tag{D.11}$$

$$\begin{aligned}
\hat{Q}^1_{m1,g} &= -\frac{1}{3}\left(r_{,g} + 2x_1 x_{1,g}\frac{1}{r} - x_1^2 r_{,g}\frac{1}{r^2}\right) \\
\hat{Q}^1_{m2,g} &= -\frac{1}{3}\left(\frac{1}{r}x_1 x_{2,g} + \frac{1}{r}x_2 x_{1,g} - \frac{1}{r^2}x_1 x_2 r_{,g}\right).
\end{aligned} \tag{D.12}$$

For $\alpha = 2$, the derivatives of the particular solutions are:

$$\begin{aligned}
\hat{w}^2_{m_1,g} &= -\frac{1}{15D}\left(x_{1,g}x_2 r + x_1 x_{2,g} r + x_1 x_2 r_{1,g}\right) \\
\hat{w}^2_{m2,g} &= -\frac{1}{45D}\left[\left(6x_2 x_{2,g} + 2r r_{,g}\right) r - \left(3x_2^2 + r^2\right) r_{,g}\right] \\
\hat{w}^2_{m3,g} &= -\left[30 - (1-\nu)\lambda^2 r^2\right]\frac{r_g x_2 + r x_{2,g}}{45(1-\nu)\lambda^2 D} + (1-\nu)\lambda^2 2 r r_{,g}\frac{r x_2}{45(1-\nu)\lambda^2 D}
\end{aligned} \tag{D.13}$$

The derivatives for the particular solutions of moments $\hat{M}_{\alpha\beta}$ and shear forces $\hat{Q}_{beta}$ are:

$$\begin{aligned}
\hat{M}^2_{m11,g} &= S^2_{11,g} + \nu S^2_{22,g} \\
\hat{M}^2_{m12,g} &= (1-\nu) S^2_{12,g} \\
\hat{M}^2_{m22,g} &= \nu S^2_{11,g} + S^2_{22,g}
\end{aligned} \tag{D.14}$$

where:

$$
\begin{aligned}
S^2_{11,g} &= -\frac{1}{15D}\left[\frac{1}{r^2}\left(2x_1x_{1,g}x_2r + x_1^2x_{2,g}r - x_1^2x_2r_{,g}\right) + r_{,g}x_2 + rx_{2,g}\right] \\
S^2_{12,g} &= -\frac{1}{15D}\left[\frac{1}{r^2}\left(x_{1,g}x_2^2r + 2x_1x_2x_{2,g}r - x_1x_2^2r_{,g}\right) + r_{,g}x_1 + rx_{1,g}\right] \\
S^2_{22,g} &= -\frac{1}{15D}\left[\frac{1}{r^2}\left(3x_2^2x_{2,g}r - x_2^3r_{,g}\right) + 3rx_{2,g} + 3r_{,g}x_2\right]
\end{aligned}
\tag{D.15}
$$

$$
\begin{aligned}
\hat{Q}^2_{m1,g} &= -\frac{1}{3}\left[\frac{1}{r}\left(x_1x_{2,g}\right) + \frac{1}{r}x_2x_{1,g} - \frac{1}{r^2}x_1x_2r_{,g}\right] \\
\hat{Q}^2_{m2,g} &= -\frac{1}{3}\left(r_{,g} + 2x_2x_{2,g}\frac{1}{r} - x_2^2r_{,g}\frac{1}{r^2}\right).
\end{aligned}
\tag{D.16}
$$

For the radial basis function $F(r) = 1 + r$, the derivatives of the rotations and deflection can be calculated by:

$$
\begin{aligned}
\hat{w}^3_{m1,g} &= -\frac{1}{D}\left(\frac{1}{16} + \frac{r}{45}\right)\left(x_{1,g}r^2 + 2rr_{,g}x_1\right) - \frac{1}{45D}\left(r_{,g}x_1r^2\right) \\
\hat{w}^3_{m2,g} &= -\frac{1}{D}\left(\frac{1}{16} + \frac{r}{45}\right)\left(x_{2,g}r^2 + 2rr_{,g}x_2\right) - \frac{1}{45D}x_2r^2r_{,g} \\
\hat{w}^3_{m3,g} &= -\left(\frac{1}{2} + \frac{2r}{9}\right)\frac{2rr_{,g}}{(1-\nu)\lambda^2D} - \frac{2r_{,g}}{9}\frac{r^2}{(1-\nu)\lambda^2D} + \frac{r_{,g}}{225D}
\end{aligned}
\tag{D.17}
$$

The derivatives of the particular solutions of moment $\hat{M}_{m\alpha\beta}$ can be derived:

$$
\begin{aligned}
\hat{M}^3_{m11,g} &= -\left[\frac{r_{,g}}{15}\left(x_1^2 + \nu x_2^2\right) + \left(\frac{1}{8} + \frac{r}{15}\right)\left(2x_1x_{1,g} + 2\nu x_2x_{2,g}\right)\right. \\
&\quad \left.+(1+\nu)\left(\frac{1}{8}rr_{,g} + \frac{1}{15}r^2r_{,g}\right)\right] \\
\hat{M}^3_{m12,g} &= -(1+\nu)\frac{1}{15}r_{,g}x_1x_2 - (1+\nu)\left(\frac{1}{8} + \frac{r}{15}\right)\left(x_{1,g}x_2 + x_1x_{2,g}\right) \\
\hat{M}^3_{m22,g} &= -\left[\frac{1}{15}r_{,g}\left(\nu x_1^2 + x_2^2\right) + \left(\frac{1}{8} + \frac{r}{15}\right)\left(20\nu x_1x_{1,g} + 2x_2x_{2,g}\right)\right. \\
&\quad \left.+(1+\nu)\left(\frac{1}{8}rr_{,g} + \frac{1}{15}r^2r_{,g}\right)\right]
\end{aligned}
\tag{D.18}
$$

The derivatives of the shear forces $\hat{Q}_{m\beta}$ are:

$$
\begin{aligned}
\hat{Q}^3_{m1,g} &= -\frac{x_{1,g}}{2}\left(1 + \frac{2r}{3}\right) - \frac{1}{3}x_1r_{,g} \\
\hat{Q}^3_{m2,g} &= -\frac{x_{2,g}}{2}\left(1 + \frac{2r}{3}\right) - \frac{1}{3}x_2r_{,g}
\end{aligned}
\tag{D.19}
$$

D.2 Derivatives of the particular solutions with respect to thickness

The derivatives of the particular solutions with respect to the thickness are needed in the DRM for transforming the domain integral into a boundary integral. The derivatives of the BEM membrane and bending fundamental solutions with respect to the thickness were proposed in the previous literature [79]. Here, only the derivatives of the particular solutions for shell BEM is presented. The coefficient related to the BEM integrals are defined as:

$$\begin{aligned} B &= Eh/(1-\nu^2) \\ D &= Eh^3/12(1-\nu^2) \\ CW &= 45(1-\nu)\lambda^2 D \\ \lambda &= \sqrt{(10)}/h \end{aligned} \tag{D.20}$$

The derivatives with respect to the thickness are:

$$\begin{aligned} B_{,h} &= B/h \\ D_{,h} &= 3D/h \\ CW_{,h} &= 45(1-\nu)(D_{,h}\lambda^2 + 2D\lambda\lambda_{,h}) \\ \lambda_{,h} &= -\lambda/h \end{aligned} \tag{D.21}$$

D.2.1 Derivatives of the particular solutions for 2D plane stress with respect to thickness

The derivatives of the particular solution for displacement:

$$\begin{aligned}
\hat{u}^1_{m1,h} &= \frac{2B_{,h}}{(1-\nu)B^2}\left[\frac{rx_1}{3} - \frac{1+\nu}{30}\left(\frac{x_1^3}{r} + 3x_1 r\right)\right] \\
\hat{u}^1_{m2,h} &= -\frac{(1+\nu)B_{,h}}{15(1-\nu)B^2}\left(\frac{x_1^2 x_2}{r} + x_2 r\right) \\
\hat{u}^2_{m1,h} &= -\frac{(1+\nu)B_{,h}}{15(1-\nu)B^2}\left(\frac{x_2^2 x_1}{r} + x_1 r\right) \\
\hat{u}^2_{m2,h} &= \frac{2B_{,h}}{(1-\nu)B^2}\left[\frac{rx_2}{3} - \frac{1+\nu}{30}\left(\frac{x_2^3}{r} + 3x_2 r\right)\right]
\end{aligned} \tag{D.22}$$

The derivatives of the particular solution for the membrane stress resultant

$$\begin{aligned}
\hat{N}^{ii}_{m11,g} &= B_{,h}\left[(1-\nu)\hat{\varepsilon}^{ii}_{m11} + \nu\hat{\varepsilon}^{ii}_{m11} + \nu\hat{\varepsilon}^{ii}_{m22}\right] \\
\hat{N}^{ii}_{m12,g} &= B_{,h}(1-\nu)\hat{\varepsilon}^{ii}_{m12} \\
\hat{N}^{ii}_{m22,g} &= B_{,h}\left[(1-\nu)\hat{\varepsilon}^{ii}_{m22} + \nu\hat{\varepsilon}^{ii}_{m11} + \nu\hat{\varepsilon}^{ii}_{m22}\right]
\end{aligned} \tag{D.23}$$

where the superscript ii can take a value of 1 or 2.

D.2.2 Derivatives of the particular solution for plate bending with respect to thickness

The derivatives of the particular solution when $\alpha = 1$ are:

$$\begin{aligned}
\hat{w}^1_{m1,h} &= \left(3x_1^2 + r^2\right)\frac{rD_{,h}}{45D^2} \\
\hat{w}^1_{m2,h} &= \frac{x_1 x_2 r D_{,h}}{15D^2} \\
\hat{w}^1_{m3,h} &= \left[30 - (1-\nu)\lambda^2 r^2\right]\frac{rx_1 \cdot CW_{,h}}{CW^2} + (2x_1 r^3 \lambda\lambda_{,h}(1-\nu))\frac{1}{CW}
\end{aligned} \tag{D.24}$$

For $\alpha = 2$:

$$\begin{aligned}
\hat{w}^2_{m1,h} &= \frac{x_1 x_2 r D_{,h}}{15D^2} \\
\hat{w}^2_{m2,h} &= \left(3x_2^2 + r^2\right) \frac{r D_{,h}}{45D^2} \\
\hat{w}^2_{m3,h} &= \left[30 - (1-\nu)\lambda^2 r^2\right] \frac{x_2 r C W_{,h}}{C W^2} + (2x_2 r^3 \lambda \lambda_{,h}(1-\nu)) \frac{1}{CW}
\end{aligned} \tag{D.25}$$

For $\alpha = 3$:

$$\begin{aligned}
\hat{w}^3_{m1,h} &= \left(\frac{1}{16} + \frac{r}{45}\right) \frac{x_1 r^2 D_{,h}}{D^2} \\
\hat{w}^3_{m2,h} &= \left(\frac{1}{16} + \frac{r}{45}\right) \frac{x_2 r^2 D_{,h}}{D^2} \\
\hat{w}^3_{m3,h} &= -\left(\frac{1}{64} + \frac{r}{225}\right) \frac{D_{,h}}{D^2} + \left(\frac{1}{2} + \frac{2r}{9}\right) \frac{r^2 D_{,h}}{(1-\nu)\lambda^2 D^2} + \left(\frac{1}{2} + \frac{2r}{9}\right) \frac{2r^2 \lambda_{,h}}{(1-\nu)\lambda^3 D}
\end{aligned} \tag{D.26}$$

Appendix E

Derivatives of the Boundary Stress Resultants and Stress Intensity Factors

E.1 Derivatives of the Boundary Stress Resultants

The detailed formulations for the derivatives of the boundary stress resultants are given in this section with respect to geometrical parameters, curvature and thickness, respectively.

E.1.1 Bending stress resultant derivatives

(1) With respect to g:

$$\begin{aligned}
&\hat{M}_{11,g} = \hat{p}_{1,g}, \quad \hat{M}_{12,g} = \hat{p}_{2,g} \\
&\hat{M}_{22,g} = \nu \hat{M}_{11,g} + D\left(1-\nu^2\right)\hat{\chi}_{22,g} \\
&\hat{\chi}_{22,g} = \frac{1}{J(\zeta)}\left[e_{2\alpha,g}\sum\left(\hat{w}_\alpha\left(\frac{dN(\zeta)}{d\zeta}\right)\right) - J_{,g}(\zeta)\hat{\chi}_{22} + e_{2\alpha}\sum\left(\hat{w}_{\alpha,g}\left(\frac{dN(\zeta)}{d\zeta}\right)\right)\right.
\end{aligned} \tag{E.1}$$

(2) With respect to K:

$$\begin{aligned}
&\hat{M}_{11,\rho} = \hat{p}_{1,\rho} \quad \hat{M}_{12,\rho}\rho = \hat{p}_{2,\rho} \\
&\hat{M}_{22,\rho} = \nu \hat{M}_{11,\rho} + D\left(1-\nu^2\right)\hat{\chi}_{22,\rho} \\
&\hat{\chi}_{22,\rho} = \frac{e_{2\alpha}}{J(\zeta)}\sum\left(\hat{w}_{\alpha,\rho}\left(\frac{dN(\zeta)}{d\zeta}\right)\right)
\end{aligned} \tag{E.2}$$

(3) With respect to h:

$$\begin{aligned} &\hat{M_{11,h}} = \hat{p}_{1,h} \quad \hat{M}_{12,h} = \hat{p}_{2,h} \\ &\hat{M_{22,h}} = \nu\hat{M_{11,h}} + D_{,h}\left(1-\nu^2\right)\hat{\chi}_{22} + D\left(1-\nu^2\right)\hat{\chi}_{22,h} - \frac{2\lambda_{,h}q_3 v}{\lambda^3} \end{aligned} \tag{E.3}$$

E.1.2 shear stress resultant derivatives

(1) With respect to g:

$$\begin{aligned} &\hat{Q}_{1,g} = \hat{p}_{3,g} \\ &\hat{Q}_{2,g} = \frac{D(1-\nu)\lambda^2}{2}\left[w_{2,g} + \frac{1}{J(\zeta)}\sum\left(w_{3,g}\left(\frac{dN(\zeta)}{d\zeta}\right)\right) - \frac{J_{,g}(\zeta)}{J^2(\zeta)}\sum\left(w_3\left(\frac{dN(\zeta)}{d\zeta}\right)\right)\right] \end{aligned} \tag{E.4}$$

(2) With respect to k:

$$\begin{aligned} &\hat{Q}_{1,\rho} = \hat{p}_{3,\rho} \\ &\hat{Q}_{2,\rho} = \frac{D(1-\nu)\lambda^2}{2}\left[w_{2,\rho} + \frac{1}{J(\zeta)}\sum\left(w_{3,\rho}\left(\frac{dN(\zeta)}{d\zeta}\right)\right)\right] \end{aligned} \tag{E.5}$$

(3) With respect to h:

$$\begin{aligned} &\hat{Q_{1,h}} = \hat{p_{3,h}} \\ &\hat{Q}_{2,h} = \frac{D_{,h}(1-\nu)\lambda^2}{2}\left[w_2 + \frac{1}{J(\zeta)}\sum\left(w_3\left(\frac{dN(\zeta)}{d\zeta}\right)\right)\right)] \\ &+ \frac{2D(1-\nu)\lambda\lambda_{,h}}{2}\left[w_2 + \frac{1}{J(\zeta)}\sum\left(w_3\left(\frac{dN(\zeta)}{d\zeta}\right)\right)\right] \\ &+ \frac{D(1-\nu)^2}{2}\left[w_{2,h} + \frac{1}{J(\zeta)}\sum\left(w_{3,h}\left(\frac{dN(\zeta)}{d\zeta}\right)\right)\right] \end{aligned} \tag{E.6}$$

E.2 Derivatives of the Stress Intensity Factor

The derivatives of the stress intensity factor with respect to geometry variables Z_g are given in Sec.4.2.3. A similar approach was used for deriving the derivatives of SIF with respect to curvature Z_ρ and thickness Z_h. The formulations are given in this section.

For simplification, denote that $T_\kappa = [1+\frac{h}{4}(\frac{1}{R_1}+\frac{1}{R_2})]^{-1} = [1+\frac{h}{4}(\kappa_{11}+\kappa_{22})]^{-1}$ and the corresponding

derivatives $T_{\kappa,\rho} = -\left[1+\frac{h}{4}\left(\kappa_{11}+\kappa_{22}\right)\right]^{-2}\frac{h}{4}\left(\kappa_{11,\rho}+\kappa_{22,\rho}\right)$. The derivatives of the maximum SIF can be found by:

$$\begin{aligned} K_{I,\rho}^{max} &= \left(\frac{1}{h}K_{1m,\rho}+\frac{6}{h^2}K_{1b,\rho}\right)T_\kappa + \left(\frac{1}{h}K_{1m}+\frac{6}{h^2}K_{1b}\right)T_{\kappa,\rho} \\ K_{II,\rho}^{max} &= \left(\frac{1}{h}K_{2m,\rho}+\frac{6}{h^2}K_{2b,\rho}\right)T_\kappa + \left(\frac{1}{h}K_{2m}+\frac{6}{h^2}K_{2b}\right)T_{\kappa,\rho} \\ K_{III,\rho}^{max} &= \left(\frac{3}{2h}K_{3b,\rho}\right)T_\kappa + \left(\frac{3}{2h}K_{3b}\right)T_{\kappa,\rho} \end{aligned} \tag{E.7}$$

similarly, the derivatives of T_κ is $T_{\kappa,h} = \frac{\partial T_\kappa}{\partial h} = -\left[1+\frac{h}{4}\left(\kappa_{11}+\kappa_{22}\right)\right]^{-2}\frac{1}{4}\left(\kappa_{11}+\kappa_{22}\right)$, hence the sensitivity of the maximum SIF with respect to the thickness is:

$$\begin{aligned} K_{I,h}^{max} &= \left(\frac{1}{h}K_{1m,h}+\frac{6}{h^2}K_{1b,h}-\frac{1}{h^2}K_{1m}-\frac{12}{h^3}K_{1b}\right)\cdot T_\kappa + \left(\frac{1}{h}K_{1m}+\frac{6}{h^2}K_{1b}\right)\cdot T_{\kappa,h} \\ K_{II,h}^{max} &= \left(\frac{1}{h}K_{2m,h}+\frac{6}{h^2}K_{2b,h}-\frac{1}{h^2}K_{2m}-\frac{12}{h^3}K_{2b}\right)\cdot T_\kappa + \left(\frac{1}{h}K_{2m}+\frac{6}{h^2}K_{2b}\right)\cdot T_{\kappa,h} \\ K_{III,h}^{max} &= \left(\frac{3}{2h}K_{3b,h}-\frac{3}{2h^2}K_{3b}\right)\cdot T_\kappa + \left(\frac{3}{2h}K_{3b}\right)\cdot T_{\kappa,h} \end{aligned} \tag{E.8}$$

where $()_{,h}$ represents the derivatives with respect to the thickness h. Once the sensitivity of the individual SIF is obtained, the evaluation of the K_{eff} can be performed using the same equations given in Eq.4.30, 4.31.